Model Lipid Membranes To Assess The Organization And Photophysical Properties Of Synthetic Pigments And Light-Harvesting Proteins

Sophie A. Meredith

Submitted in accordance with the requirements for the degree of Doctor of Philosophy
on the programme of the "BBSRC White Rose DTP in Mechanistic Biology"

University of Leeds

School of Physics and Astronomy
Faculty of Biological Sciences

September 2021

Declaration

The candidate confirms that the work submitted is her own, except where work has formed part of jointly authored publications. The contribution of the candidate and the other authors to this work has been explicitly indicated below. The candidate confirms that appropriate credit has been given within the thesis where reference has been made to the work of others.

The work discussed in chapter 4 of this thesis has appeared in publication as follows: Meredith S. A., Yoneda T., Hancock A. M., Connell S. D., Evans S. D., Morigaki K. Adams P. G. (2021), *Model Lipid Membranes Assembled from Natural Plant Thylakoids into 2D Microarray Patterns as a Platform to Assess the Organization and Photophysics of Light-Harvesting Proteins*, Small, DOI:10.1002/smll.202006608.

S. A. Meredith was responsible for the preparation of membrane samples, acquisition of FLIM data, acquisition of AFM data, the analysis and presentation of data, and for writing the first drafts of the manuscript. The contribution of other authors involved sample preparation, collection of solution-based spectroscopy data, collection and epifluorescence data. All authors revised the manuscript.

The work discussed in chapter 5 (section 5.2) of this thesis has appeared in publication as follows: Hancock A. M., Meredith S. A., Connell S. D. A., Jeuken L. J. C., Adams P. G. (2019), *Proteoliposomes as energy transferring nanomaterials: enhancing the spectral range of light-harvesting proteins using lipid-linked chromophores*, Nanoscale, DOI:10.1039/C9NR04653D.

S. A. Meredith was responsible for the acquisition and analysis of FLIM data and presentation of FLIM images. A. M. Hancock performed purification of the LHCII protein, co-reconstitution of LHCII alongside lipid-tethered Texas Red (TR) chromophores into proteoliposomes, acquisition and analysis of solution-based spectroscopy and wrote the first drafts of the manuscripts. All authors revised the manuscript.

Acknowledgements

First and foremost, I would like to thank my supervisor, Pete Adams. You are a talented and rigorous scientist with an infectious enthusiasm. Working with you has made me a methodical and self-assured scientist and your outstanding tutelage will continue to influence my career for many years. It has been an enormous privilege to have your support and guidance, and I wish you the best of luck in your future projects (though I am sure you do not need it). I would also like to thank my other supervisors, Simon Connell and Steve Evans for your insightful discussions and for always reminding me of the bigger picture. You have added enormous value to our research and to my time in Leeds. I also wish to thank Ashley Hancock for your consistently good advice, for always being willing to discuss ideas and for many long experiments. I cannot think of anyone better to have spent so much time in the lab with and I owe you approximately one million pints. I am also fortunate to have had the opportunity to work with some extremely talented collaborators, and I am particular grateful for the productive collaboration with Takuro Yoneda, Yuka Kusunoki and Kenichi Morigaki from the University of Kobe. This research would not have been possible without their contributions and hard work.

Above all, I would also like to collectively thank all the people in MNP who have made my time in Leeds so special and so memorable. There is something truly unique about the atmosphere and comradery within MNP and my life is vastly improved by the humour, support and friendship I have found within this group. Most important of all, MNP gave me my best friend. Thank you, Jordan, for always unapologetically being your absurd self, for being my support at home and bringing out the best in me. Whilst I am extremely proud of everything we have accomplished in the last four years, it is small compared to the joy of getting to know you and how much you mean to me now. I look forward to the future knowing that you will be with me every step of the way.

Outside of MNP, I would like to thank the members of LUUSAC for keeping me grounded and reminding me to find joy outside of science. In particular, Yas and Jake, for adopting us into your house for the last few months. Writing a thesis is a long, arduous process, so thank you for putting up with me, and for putting a roof over my head, whilst I did.

My final thanks are to my family, in particular for my mum and dad. I often joke that I took physics at undergraduate in spite of having two teachers for parents, but it is because of you and your seemingly endless support that I have made it this far. Every step I have taken to get here is the result of your encouragement.

Abstract

Photosynthetic thylakoid membranes contain a complex and adaptable network of proteins and lipids that regulate the light-harvesting, energy transfer and photoprotective abilities of land plants. It can be challenging to disentangle and understand the numerous interactions that control photosynthetic processes, however, it is possible to use simplified model systems to interrogate or manipulate components from the biological system in a controllable manner. This thesis describes the development and application of a range of model lipid membranes to: (i) enhance the absorption cross-section of photosynthetic proteins for applications in light-harvesting nanotechnologies, (ii) to characterise the energy transfer and quenching processes that occur between freely-diffusing organic fluorophores, and (iii) to quantify the quenching interactions that can occur between thylakoid proteins to improve our understanding of how their photophysical properties may be important in photoprotection. The model systems developed throughout this thesis led to a more comprehensive understanding of the photophysical interactions that may occur between synthetic fluorophores and photosynthetic proteins and how these interactions may modulate photoprotective processes in land plants.

Table of contents

List of abbreviations and acronyms

α-DDM: n-dodecyl α-D-maltoside

ADP/ATP: Adenosine diphosphate/ Adenosine triphosphate

AFM: Atomic Force Microscopy

BOD/Bodipy: N-(4,4-Difluoro-5,7-Dimethyl-4-Bora-3a,4a-Diaza-s-Indacene-3-Propionyl)

C: concentration

CCD: Charge coupled device

Chl: chlorophyll

CM: Contact Mode

Cyt b_6f: Cytochrome b_6f complex

DHPE: 1,2-dihexadecanoyl-sn-glycero-3-phosphoethanolamine

Diyne-PC: 1,2-bis(10,12-tricosadiynoyl)-*sn*-glycero-3-phosphocholine

DGDG: Digalactosyldiacylglycerol

DLS: Dynamic Light Scattering

DMBQ: 2,6-Dimethoxybenzoquinone

DOPC: 1,2-dioleoyl-sn-glycero-3-phosphocholine

Em: Emission

ETE: Energy Transfer Efficiency

Ex: Excitation

Fd: Ferrodoxin

FLIM: Fluorescence Lifetime Imaging Microscopy

FNR: Ferredoxin $NADP^+$ reductase

FRAP: Fluorescence Recovery After Photobleaching

FRET: Förster Resonance Energy Transfer

FWHM: Full-Width at Half-Maximum

HEPES: 4-(2-hydroxyethyl)-1-piperazineethanesulfonic acid

IRF: Instrument Response Function

LED: Light-emitting Diode

LDH: Laser Diode Head

LH: Light-Harvesting

LHCI: Light-Harvesting Complex I

LHCII: Light-Harvesting Complex II

MOU: Main Optical Unit

MGDG: Monogalactosyldiacylglycerol

MW: Molecular Weight

NA: Numerical Aperture

NADH/NADPH: Nicotinamide adenine dinucleotide/ Nicotinamide adenine dinucleotide phosphate

NBD: N-(7-nitro-2-1,3-benzoxadiazol-4-yl)

ND: Neutral Density

NPQ: Non-photochemical quenching

OEC: Oxygen-Evolving Complex

PC: Plastocyanin

PDL: Pulsed Diode Laser

PDMS:

PFT: Peak Force Tapping

PIE: Pulsed Interleaved Excitation

PMT: Photon Multiplier Tube

PQ: Plastoquinone

PQH^+: Platoquinol

PS: Photosystem

QE: Quenching efficiency

RC: Reaction centre

SDS: Sodium dodecyl sulphate

SLB: Supported Lipid Bilayers

SPAD: Single Photon Avalanche Detector

SPM: Scanning Probe Microscopy

SSA: Singlet-singlet annihilation

SQDG: Sulphoquinovosyldiacylglycerol

T: Temperature

t: Time

TCSPC: Time Correlated Single Photon Counting

TEM: Transmission electron microscopy

TR: Texas Red (also termed “sulforhodamine 101”)

TTTR: Time-Tagged Time-Resolved

TRIS: Tris(hydroxymethyl)aminomethane

List of Figures

List of Tables

1 Introduction

This chapter will introduce the concepts of photosynthesis, light-harvesting, energy transfer and the functions of various proteins in higher-order plants. The chapter will outline the current challenges and questions faced within the field of photosynthetic research. The use of model systems and model lipid membranes to interrogate photosynthesis will be reviewed, with the aim of discussing the pros and cons of each approach and outlining potential areas for development. This will provide context for the motivation of the new research described in this thesis.

1.1 Motivation for studying photosynthesis

Photosynthesis is the primary or secondary source of energy for almost every living organism on the planet. It is defined as the biological process in which energy provided by light from the Sun is converted into chemical energy which can be stored and used[1]. The majority of the solar light that reaches the Earth's surface is in the wavelength range from 380 to 700 nm and photosynthetic absorption in this region provides the primary source of energy for plants, algae and cyanobacteria[2]. Other so-called purple and green photosynthetic bacteria may absorb light in the near-infrared (up to 1000 nm)[3]. The initial photosynthetic processes of energy capture, transfer, and stabilisation are far more efficient than any equivalent renewable human-fabricated process[1]. For this reason, understanding the nature of photosynthesis on both molecular and macro levels is hugely important for the development of renewable energy systems which are necessary to alleviate the worldwide demand for non-renewable fossil fuels[4]. In addition, the demand for food and biofuels is steadily increasing, whilst gains in the yield of many major food crops (through traditional breeding and natural variation) have plateaued and large portions of fertile land are predicted to become arid by the middle of this century[5]. It has been suggested that enhancing the photosynthetic process, by increasing either light-harvesting or the efficiency of photochemical processes could increase crop yields by up to 50%[6]. It is crucial to develop innovative carbon-neutral and sustainable solutions if we are to limit the environmental effects and humanitarian costs of climate change[5].

1.2 Photosynthesis and the role of light-harvesting proteins

1.2.1 The structure of the thylakoid membrane

In plants, the primary reactions of photosynthesis takes place within organelles called chloroplasts. These organelles share many features with, and are thought to have evolved from, prokaryotic cyanobacteria which perform photosynthesis with a similar mechanism to plants[7]. Contained within the chloroplast is a complex system of bio-membranes called the thylakoid (**Figure 1.1a**), which is the location of solar energy capture, transfer, and initial chemical stabilisation (the "light-reactions" of photosynthesis)[8]. Within the chloroplast and surrounding the thylakoids is a fluid called the stroma, which contains many soluble proteins crucial for the latter stages of photosynthesis and so-called "dark-reactions" in which energy is converted to sugars for long-term storage (i.e. carbon fixation, etc). Light and dark reactions of photosynthesis are given below, where ΔG° is the free energy change of the reaction. The positive sign of ΔG° means that the reaction requires energy (from light-absorption) to take place[9].

Light-induced reactions:

$$2H_2O + \text{light (4 photons)} \rightarrow O_2 + 4H^+ + 4e^- \quad (\Delta G^{\circ} = +317\ \text{kJ} \cdot \text{mol}^{-1})$$

Dark reactions (where $(CH_2O)_n$ represents long-chain sugars):

$$CO_2 + 4H^+ + 4e^- \rightarrow (CH_2O) + H_2O \quad (\Delta G^{\circ} = +162\ \text{kJ} \cdot \text{mol}^{-1})$$

Overall:

$$H_2O + \text{light} + CO_2 \rightarrow (CH_2O) + O_2 \quad (\Delta G^{\circ} = +479\ \text{kJ} \cdot \text{mol}^{-1})$$

Thylakoids are made up of an interconnected membrane which encapsulates an inner space, termed the lumen, and separates the lumen from the stromal liquid. The thylakoid is laterally-differentiated into densely-packed stacks of discs, called grana, and single layered regions, called stromal lamellae, that connect between the grana stacks. The heterogeneous membrane structure is accompanied by an uneven distribution of membrane proteins within the thylakoid membrane, such that the light-harvesting complex II (LHCII) and photosystem II (PSII) are primarily concentrated in the grana, while photosystem I (PSI) and the chloroplast adenosine triphosphate (ATP) synthase are localized in the stromal lamellae[10] (**Figure 1.1b**). This "lateral heterogeneity" results in functional differences between the grana and

stromal lamellae, allowing many processes to take place in various regions of the membrane simultaneously[11]. The structure of the thylakoid membrane changes in response to high or low light conditions[10]. The diameter of grana, number of layers and number of grana per chloroplast can vary on the time scale of minutes[12], and it is hypothesized that these changes may regulate light-harvesting and energy transfer through the membrane[13, 14], or may alter the distribution of proteins (e.g., electron transfer complexes or electron carriers) to regulate electron transfer pathways[15-17].

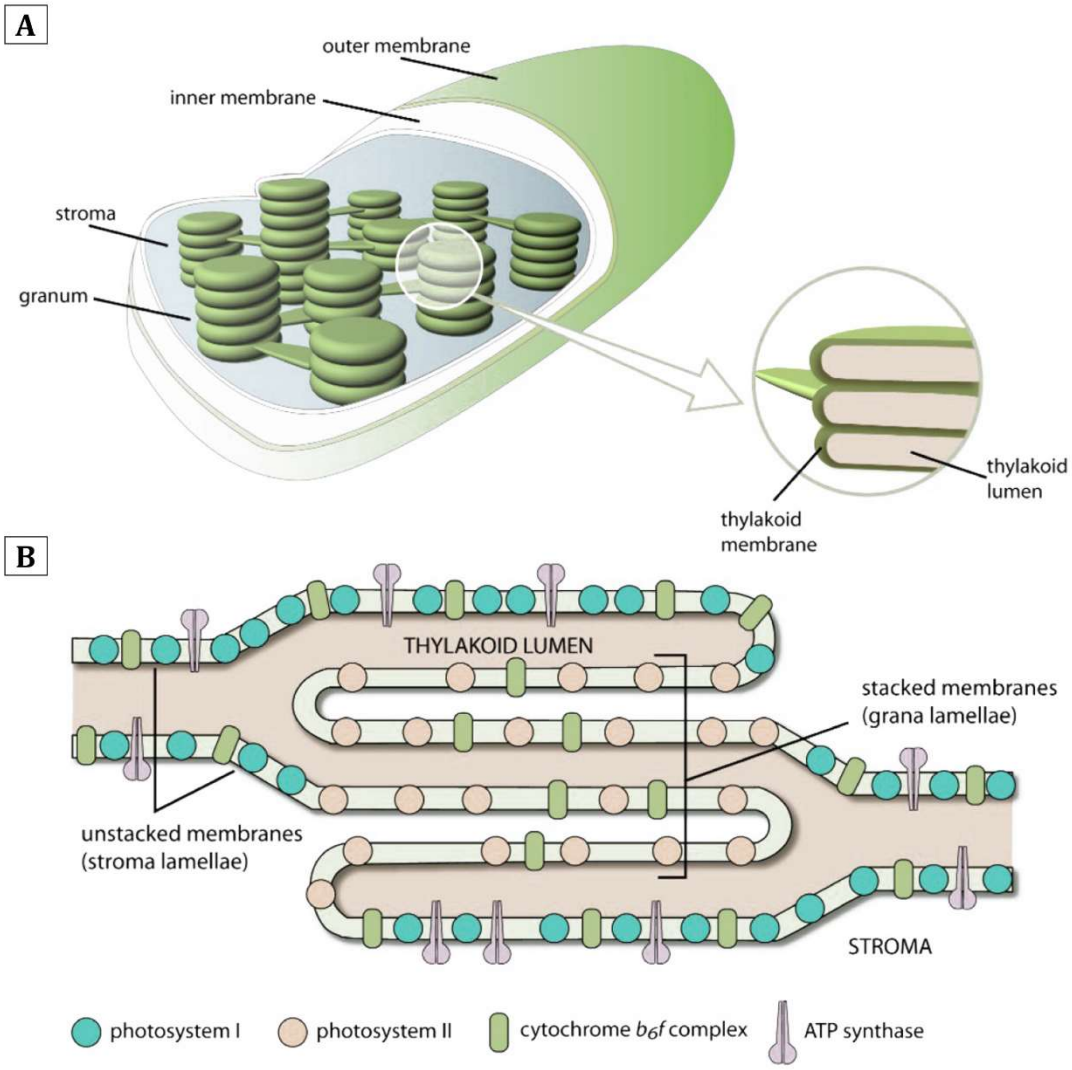

Figure 1.1: Schematic of a plant chloroplast and thylakoid membrane. **(A)** Cartoon showing the cross-section of a chloroplast and thylakoid membrane. **(B)** Schematic of a thylakoid membrane showing the cross section and protein composition of grana stacks and interconnecting stromal lamellae. Adapted from Mirkovic et al (2017).[18]

1.2.2 Energy transduction in chloroplasts

The energy pathway within photosynthetic chloroplasts is shown in **Figure 1.2**. Energy is initially absorbed by photosynthetic proteins confined within grana regions of the thylakoid membrane. Both PSII and LHCII contain numerous chlorophyll molecules that can absorb an incident photon and form an excited electronic state, or "exciton". PSII and LHCII can arrange into a large connected network of proteins, called "supercomplexes", that increases the overall area for light-harvesting and funnel excitons, through a series of energy transfer processes, towards the central PSII reaction centre (RC) on the luminal side of the thylakoid membrane. The core PSII reaction centre consists of a "special pair" of chlorophyll molecules, called P680 (with an associated absorption relating to photons of 680 nm), in close proximity to monomeric chlorophylls and pheophytins (like a chlorophyll pigment lacking the central magnesium ion). The light energy absorbed by PSII causes P680 to undergo charge separation to form an extremely oxidizing form of $P680^+$, which has a redox potential sufficient to oxidize water. The water splitting reaction requires four electrons, and therefore four separate charge separations of P680 (turnovers of PSII) are required to drive the formation of one O_2 molecule from two H_2O molecules. To replenish the lost electron from $P680^+$ a cluster of manganese ions within the oxygen-evolving complex (OEC) can donate electrons to "reset" P680. Manganese is a transition metal that can exist in range of oxidation states, from +1 to +5, and therefore accumulates positive charges derived from each light-induced turnover of P680. After the fourth turnover of P680, sufficient positive charge has built up on the OEC to allow the water splitting reaction to take place, in which two water molecules (H_20) are split into molecular oxygen (O_2), four protons (H^+) and four electrons[19]. The protons produced in this reaction build up on the luminal side of the thylakoid membrane, creating a proton gradient across the membrane required for ATP synthesis, whereas electrons are used to regenerate the original state of the manganese cluster so that future water splitting reactions can take place. Plastoquinone (PQ) is a water-soluble electron carrier that resides within the membrane and transfers two electrons and two protons from PSII to the cytochrome b_6f complex (cyt b_6f). PQ gains two electrons from the electrons yielded from P680 during charge separation (two PSII turnovers are required) and takes up two protons from the stroma during the formation of

plastoquinol (PQH_2). The protonated plastoquinone then joins a pool of PQH_2 molecules in the thylakoid membrane, transfers electrons to the cytochrome b6f complex (cyt b_6f) and which then transfers electrongs to water-soluble plastocynanin (PC) to continue the light-dependant reactions. PC then binds with the membrane protein PSI in the stromal lamellae region of the thylakoid membrane and the electrons are transferred through an electron transfer chain to the soluble protein ferredoxin (Fd) on the stoma side of the membrane[1].

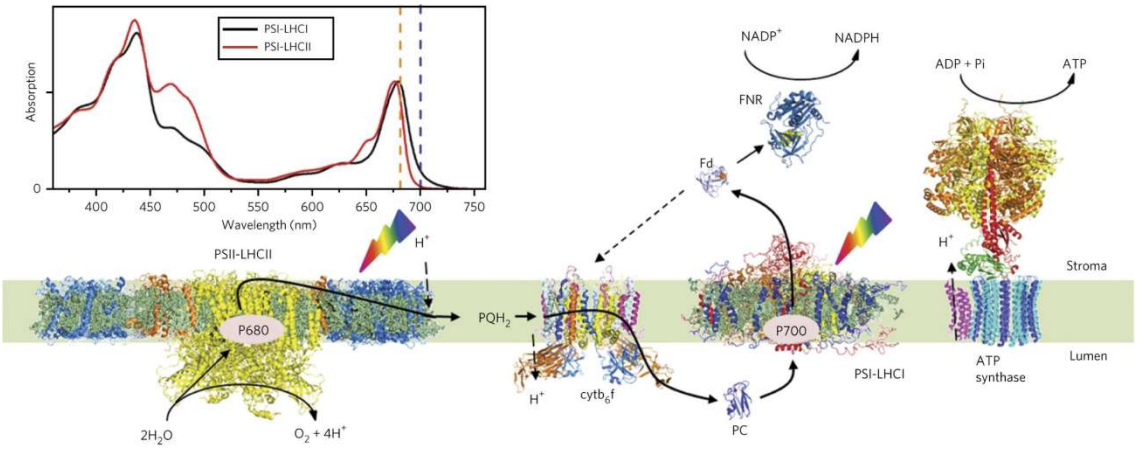

Figure 1.2: Schematic of membrane proteins found in the thylakoid membrane and chemical pathways for energy transduction. Adapted from Croce et al (2014).[20]

The electron transport from plastocyanin to ferredoxin via PSI requires additional energy provided by the absorption of photons by the PSI or its associated antenna proteins LHCI. Similarly to PSII, PSI contains a reaction centre that consists of a 'special pair' of chlorophylls with a corresponding absorption wavelength of 700 nm (P700). After photon absorption, the excited P700 is a strong reductant that donates an electron to reduce ferredoxin (Fd) which, in turn, is required to generate nicotinamide adenine dinucleotide phosphate (NADPH). The $P700^+$ is restored to P700 for further reactions by accepting electrons from PC. The reduced Fd is then oxidised by the enzyme ferredoxin-$NADP^+$ reductase (FNR), which utilises the electrons in ferredoxin to produce NADPH by reducing $NADP^+$ in the stroma. NADPH is a stable reducing agent used in many cellular reactions including molecular synthesis and the 'dark reactions' of photosynthesis. This includes the Calvin cycle, where long-chain sugars are formed to store chemical energy in plants. The proton gradient formed by protons being produced on the lumen side of the membrane, via

the oxidation of plastoquinol and the water splitting reaction, is utilised by the protein ATP synthase which is located in the lamella stroma region of the thylakoid. ATP synthase uses the energy from the protein gradient to convert ADP to ATP which is used as the standard 'energy currency' in cells for processes such as the Calvin cycle and complex molecule synthesis[1].

1.2.3 Light absorption and fluorescence in photosynthetic systems

The very first stage of photosynthesis involves the absorption of photons by a number of different pigments in both photosystems and their associated light-harvesting proteins. Absorbance occurs when a photon interacts with an atom, or molecule, and transfers energy to an electron, causing the electron to enter an excited vibrational state. Generally, a photon can be absorbed by an atom, or molecule, if its energy corresponds to the gap between the molecule's ground state energy level (S_0) and the energy level of the first (S_1) or second (S_2) electronic excited states. It is also possible for higher energy photons to excite electrons from the ground state (S_0) into higher excitonic states ($S_0 \rightarrow S_n$, n = 1, 2, 3…), but this typically corresponds to photons with a wavelength outside the visible range. For fluorescent molecules with multiple interacting atoms and molecular orbitals, each electronic energy state (S_1, S_2, etc) may actually consist of many vibrational sub-states that greatly broaden the energy levels available. An electron may be excited to a high vibrational sub-state by photon absorption, and due to the small energy gap between these sub-states, will rapidly return to the lowest vibrational sub-state (within a given electronic state) though a process called "vibrational relaxation" which dissipates excess energy to the environment as heat. It is also possible that the vibrational sub-states of one electronic orbital may overlap with the vibrational sub-states of another electronic orbital, allowing non-radiative transitions between them (also known as "internal conversion"). From the lowest-vibrational state of the S_1 excited state, there may be relaxation to the ground electronic state (often via associated higher-energy vibrational sub-states) through the re-emission of an absorbed photon, commonly termed "fluorescence" (a type of photoluminescence). The combined loss of energy due to vibrational relaxation and internal conversion results in an overall loss of energy, and the vibrational relaxation during S0-S1-S0

transition manifests as a red-shift (termed the "Stoke's shift") in the wavelength of the emitted photon relative to the absorbed photon.

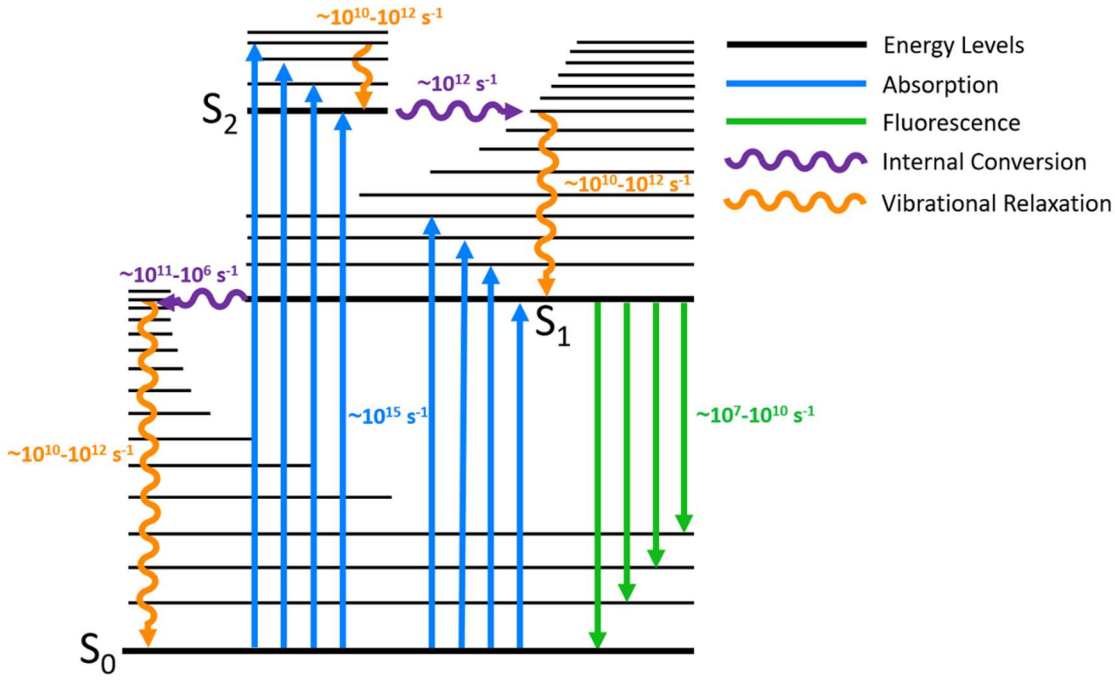

Figure 1.3: A typical Jablonksi diagram showing excited states of a fluorescent molecule and possible routes for internal conversion and vibrational relaxation. Adapted from Edinburgh instruments F980 fluorescence spectrometer manual.

LHCII, the major light-harvesting antenna of photosystem II, is the primary source of photon-absorption in thylakoid membranes and has been shown to act as the antenna protein for the water splitting PSII[21]. Since its discovery, the structure of LHCII has been obtained with a resolution of up to 2.5 Å (top and side views of an LHCII trimer are shown in **Figure 1.4a,b**)[22-24]. In nature, LHCII functions both in a monomeric and in a trimeric form. Both are found in the dimeric PSII-LHCII supercomplex, with monomers labelled CP29, CP26 and CP24[25]. Each monomer of LHCII contains three transmembrane alpha helices, 8 chlorophyll *a*, 6 chlorophyll *b*, 4 carotenoids and 2 bound lipids[22].

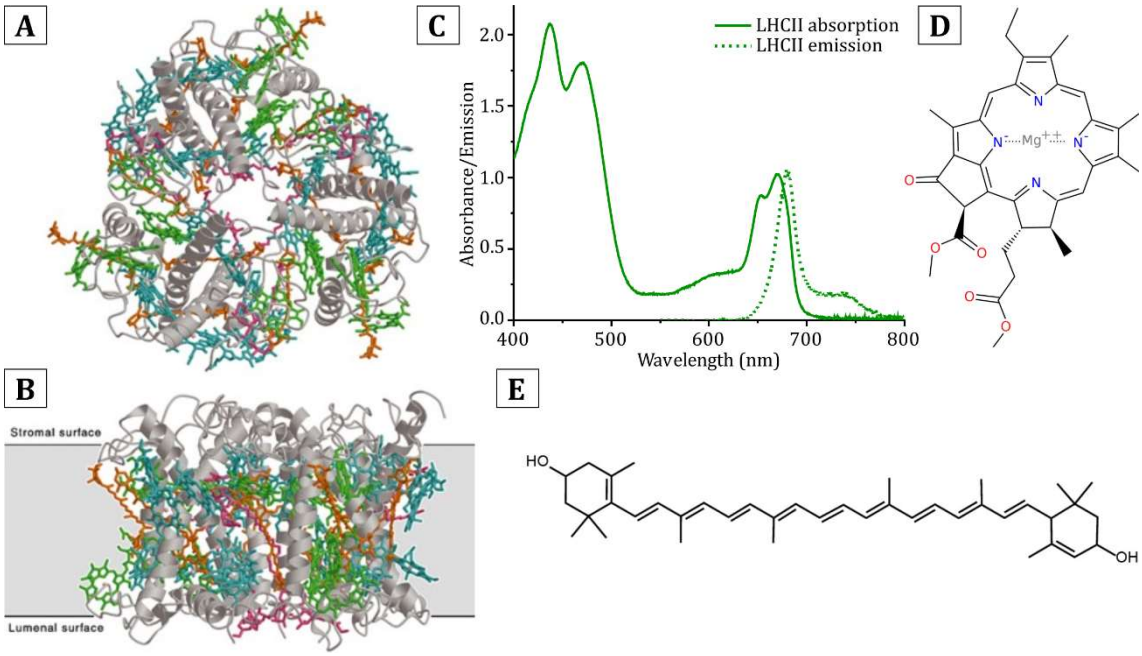

Figure 1.4: Structure of LHCII trimers and chlorophyll and carotenoid pigments and the resulting emission spectra of LHCII. **(A) + (B)** Top and side views of an LHCII trimer complex respectively; the membrane has a thickness of 35Å. *Grey*; polypeptide chain, *Cyan*; chlorophyll *a*, *Green*; chlorophyll *b*, *Orange*; Carotenoids, *Red*; Lipids. Adapted from Standfuss et al (2005)[22]. **(C)** Absorption and emission spectra of isolated LHCII in detergent. **(D)** Chemical structure of chlorophyll *a*. **(E)** Chemical structure of a lutein molecule.

Chlorophyll (Chl) *a* is the most common chlorophyll in nature and absorbs strongly in the visible wavelength regions of 380 – 450 nm (termed "Soret" band) and 625 - 725 nm (termed Q_y), as well as a weaker absorption peak between 550 – 600 nm (termed Q_x). Electrons in the Q_y (S_1) excited state are relatively stable and persist for several nanoseconds (lifetime ~4 ns), making it effective for the onwards transfer of excitation energy to other pigments. In contrast, the higher-energy Soret and Q_x excited electronic states are unstable and typically transition to the Q_y state by rapid internal conversion within picoseconds. Chlorophyll molecules consist of a planar 'head group', which have a magnesium atom at the centre ligated by four nitrogen atoms, and a hydrocarbon 'tail' which provides stability and allows the pigment to be incorporated into complex structures such as proteins, as shown the chemical structure of Chl *a* in **Figure 1.4d**. The chemical structure of lutein, the most common carotenoid found in plant light-harvesting proteins, is shown in **Figure 1.4e**. Carotenoids typically absorb strongly in the 400-500 nm range of the visible spectrum related to a strong $S_0 - S_2$ transition and associated vibrational manifold

(the S_0 – S_1 transition is "forbidden"). Carotenoids have multiple roles in photosynthetic systems: first, energy absorbed by carotenoids in the blue part of the visible spectrum can be transferred to chlorophylls for eventual use in photochemical reactions. Second, the ability of carotenoids to quickly dissipate electron energy as heat through internal conversion and vibrational relaxation (because the carotenoid S_2 excited state lifetime is <300 fs, which is very short compared to the chlorophylls) make them crucial for the rapid quenching of potentially damaging chlorophyll triplet states which can form if photosynthetic proteins are excited by multiple photons in a short time period. Thirdly, carotenoids have important structural roles in stabilizing the 3D structure of many pigment-protein complexes[1].

Absorption and emission spectra of LHCII isolated in detergent are shown in **Figure 1.4b**. The densely packed arrangement of pigments within an LHCII monomer gives the complex strong absorption in the blue region of the visible spectrum (400 -500 nm), due to the combined absorption bands of the chlorophyll Soret and carotenoid S_2 transitions, and it also has a strong absorption in the red (650 – 700 nm) due to the Q_y transitions of chlorophyll *a* and *b*. Energy absorbed by any of the pigments in LHCII is transferred to the lowest-energy ('terminal') chlorophyll *a* molecules, corresponding to a wavelength of ~680 nm, ready for either fluorescence or transfer to another protein. In the natural membranes, under normal conditions, the majority of energy is transferred to PSII in a few picoseconds on average[26]. The energy rapidly directed to a 'terminal' chlorophyll *a* results in a single fluorescence emission peak for isolated LHCII trimers at 681 nm corresponding to emission from a single type of pigment. This fluorescence band has moderate breadth (FWHM ~ 50 nm) and a minor shoulder at ~710-750 nm due to the various vibrational sub-states.

1.2.4 Resonance energy transfer and light-harvesting systems

The initial stages of photosynthesis involve photons being absorbed by a number of different pigments in both photosystems and their associated light-harvesting proteins. For productive photosynthesis, these "excitons" must be transferred to specific chlorophyll pairs located within the reaction centres of PSII and PSI in order to perform photochemistry. The principal mode of energy transportation between pigments in photosynthetic proteins is through a process called Förster Resonance

Energy Transfer (FRET)[27], in which energy can be transferred from one fluorophore to another via dipole-dipole coupling. Dipole-dipole coupling occurs (due to Coulombic interactions[18]) when two electromagnetic dipoles, such as vibrational electronic dipoles in chlorophylls, are aligned with each other and are in close proximity (e.g., within 10 nm). An energy level diagram of this general process is shown in **Figure 1.5a** with the electronic states of the donor fluorophores, and of the acceptor. After initial absorption of a photon by the donor molecule an electron is excited to some vibrational state of the S_1 electronic state, which then returns to the lowest vibration state of S_1 through vibrational relaxation. If the dipoles are of a similar frequency then the vibronic dipoles can become coupled and the energy of the excited state in the donor is transferred to the acceptor. In this process, the excited electron in the donor molecule relaxes to the ground state without photon emission. Simultaneously an electron is excited from acceptor molecule ground state to an S_1 excited electronic state without photon absorption. This coupled donor-acceptor process represents non-radiative transfer of excitation energy. Photon emission (fluorescence) or some other relaxation process can then occur from the acceptor. There are multiple requirements for FRET to occur between fluorescent molecules: (i) overlapping energetic states (overlapping spectra) and a downhill energy transfer (as net energy cannot be increased), (ii) the donor and acceptor must have parallel (or close to) transition dipole orientation, and (iii) the fluorophores must be in close enough spatial proximity to allow dipole-dipole coupling[28].

The conditions for energy transfer can be defined by the donor molecule emission spectrum and acceptor molecule absorption spectrum. The peak representing the possible wavelengths (energy levels) of photon emission from the donor must overlap with the possible photon absorption wavelengths (energy levels) of the acceptor; this condition must be met so that the energies of vibronic states are sufficiently similar to allow dipole-dipole coupling. This overlap of donor emission and acceptor absorption can be defined by a spectral overlap factor, *J*. The overlap factor *J* correlates to the area of overlap the donor's fluorescence emission spectra and the acceptor's absorption spectra, which is the integral with respect to wavelength of the molar extinction coefficient of the acceptor, $\varepsilon(\lambda)$, and the

normalised emission spectrum of the acceptor, $F_D(\lambda)$. The equation for the overlap integral (in $M^{-1}cm^{-1}nm^4$) is given by:

$$J = \int \varepsilon(\lambda) F_D(\lambda)\, \lambda^4 d\lambda \qquad \text{Eq. 1.1}$$

where λ is the wavelength (in nm), $\varepsilon(\lambda)$ is the molar extinction coefficient of the acceptor as a function of wavelength (in $M^{-1}cm^{-1}$) and $F_D(\lambda)$ is the normalised emission spectrum of the donor as a function of wavelength. A spectral representation is shown in **Figure 1.5b** (B, grey shaded area).

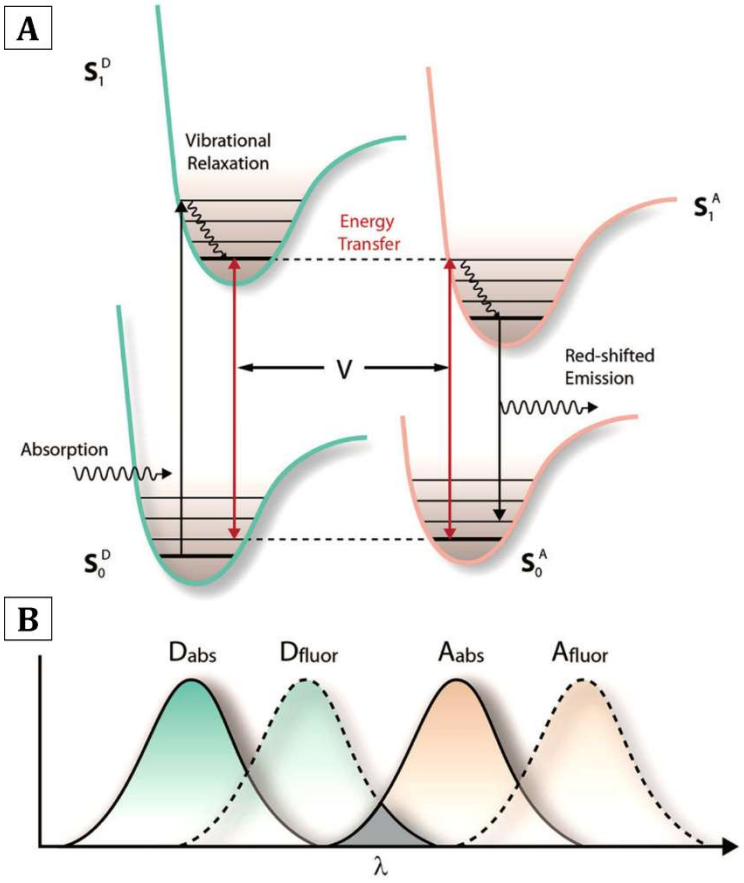

Figure 1.5: Jablonksi diagram showing donor-acceptor FRET and required spectral overlap. (**A)** Energy level diagram for donor to acceptor FRET. **(B)** Spectral conditions needed for donor to acceptor FRET to take place. The grey shaded area is the overlap defined by the overlap integral J. Adapted from Mirkovic et al (2017).[18]

The orientation of dipoles relative to each other is also crucial to the efficiency of energy transfer; if the dipoles are parallel then energy transfer will be most effective due to maximised Coulombic interactions, whereas if they are perpendicular coupling is not possible. The orientation of dipoles relative to one another is given by an orientation factor, κ:

$$\kappa^2 = (\cos\alpha - 3\cos\beta_1 \cos\beta_2)^2 \qquad \text{Eq. 1.2}$$

Where α is the angle between planes of dipoles and β is the angle between the dipole direction and a vector linking to the other dipole. For randomly oriented dipoles (e.g. fluorophores in a lipid bilayer), the interaction factor has an average value of $2/3$[1, 29].

The rate of energy transfer ($k_{D\rightarrow A}$) can be calculated by defining a critical distance between two pigments where energy transfer is 50 % efficient (R_0). The critical distance considers the rate of fluorescence of the donor dipole in the absence of energy transfer (k_f) (which is equal to 1/donor fluorescence lifetime (τ_D)). The value of R_0 between a donor and acceptor pair can be calculated from:

$$R_0^6 = 8.79 \times 10^{(-5)}\, J\, \kappa^2\, n^{-4}\, \phi \qquad \text{Eq. 1.3}$$

where n is the optical refractive index of the medium, and ϕ is the fluorescence quantum yield of the FRET donor. The value for R_0 varies from pigment to pigment but is generally between 60 Å and 100Å[30]. Molecules must be separated by at least 10Å for FRET to take place, due to the Pauli Exclusion Principle which limits massive particles from occupying the same space and comes into effect at sub-nanometre separation[1].

The rate of energy transfer in a system can also be defined by the rate of fluorescence of the donor (k_D), donor–acceptor dipole separation (r_{DA}) and the critical distance (R_0):

$$k_{D\rightarrow A} = k_D (R_0/r_{DA})^6 \qquad \text{Eq. 1.4}$$

The rate of energy transfer is proportional to r^{-6} meaning that FRET is extremely sensitive to distance between molecules, this has been utilised in many nanotechnological applications which involve measuring when two molecules are sufficiently close for FRET to occur[31].

Finally, the energy transfer efficiency (ETE) between donor and acceptor molecules can be defined by the relative rates of energy transfer from the donor due to dipole-dipole coupling ($k_{D\rightarrow A}$) and the rate of natural donor fluorescence (k_D). This can be combined with Equation 1.4 for the rate of energy transfer defined by donor-acceptor separation (r_{DA}) and R_0 to give energy transfer efficiency in these terms:

$$ETE = \frac{k_{D\rightarrow A}}{k_{D\rightarrow A} + k_D} = \frac{R_0^6}{R_0^6 + r_{DA}^6} \qquad \text{Eq. 1.5}$$

In photosynthetic systems, LH antenna proteins and PSII are arranged in such a way to increase the spatial and optical area for light-harvesting and to funnel this energy, via FRET, to the photosynthetic reaction centre subunits. Calculations show that solar energy is relatively dilute, and that individual chlorophyll molecules in PSII absorb a photon once every ~100 μs[1]. Since multiple cycles of photon absorption, photochemistry and electron transfer are required in the PSII RC for the water splitting reaction to take place, relying on the absorption of these chlorophylls alone would result in a rate of water splitting that well below the maximum rate that reaction centres are capable of (once every 300 ps)[32]. Instead, antenna proteins and photosystems are organised into large light-harvesting supercomplexes (typically 4 LHCII trimers and a PSII dimer) together with a larger pool of loosely associated LHCII trimers, in which energy is transferred to the RC at a rate that allows regular photochemistry to take place. Within the supercomplexes, the outermost carotenoid pigments absorb the highest energy photons (lowest, blue wavelengths) and excitons are transferred to the orange and then red-absorbing pigments, chlorophyll b and a, respectively, before reaching the reaction centre 'special pair' of chlorophyll a molecules with an associated energy of 680 nm. In reality, at room temperature the energy funnel is extremely shallow and thermal energy from the local environment, k_BT, can provide additional energy to excitons which allows them to transfer to pigments with higher corresponding energies. For this reason, excitons are effectively de-localised across multiple pigments allowing them to "hop" via FRET to eventually reach the central reaction centres[18,33].

1.2.5 The regulation and mechanism of non-photochemical quenching

The antenna of PSII is highly efficient, with ~85 % of the photo-induced excitation being delivered to the RC and leading to photosynthetic charge separation[34]. In low light this efficiency ensures an optimal rate of energy delivery to PSII RCs. In high light, however, a highly efficient antenna network can lead to saturation of the RCs, a build-up of chlorophyll triplet states within the antenna[35] and the formation of highly reactive oxygen states that will oxidise molecules in their immediate vicinity and damage the protein[36]. This damage, known as photoinhibition, can take several hours to reverse and can impact the viability of the organism long term. However, plants have evolved the ability to cope with intense illumination, through a variety of adaptive mechanisms and "feedback loops".

In the most rapid photoprotective mechanism the rate of photoinhibition reduced by the regulation of energy transfer pathways within the PSII antenna, LHCII, and the formation of dissipative pathways that reduce the "excitation pressure" on the overburdened reaction centres[37-39]. This so called "non-photochemical quenching" (NPQ) manifests itself as the quenching of chlorophyll fluorescence, i.e. a reduction in the fluorescence emission and lifetime of the Chl excited state. In 2012, Ruban and co-workers established a description of NPQ that consists of four key stages, namely: (i) the trigger, (ii) the site, (iii) the quencher and (iv) the mechanism[40]. The trigger is the primary event that brings about the formation of the dissipative pathways, and acts upon the site (i.e., the location of the quencher). The mechanism is the precise physical change that forms the quencher, i.e., the molecular state (or states) that accept and dissipate excess energy. For the rest of this subsection, we will discuss what is and is not known about each of these aspects, and the highlight the outstanding questions regarding NPQ.

1.2.5.1 Trigger

Whilst there is still controversy, most researchers agree that the LHCII trimer is the primary protein that brings about the formation of dissipative pathways and that site (i.e., the quenching pigments) resides within LHCII. There is extensive evidence

that an increase in the transmembrane pH gradient (ΔpH), due to the accumulation of photons from higher rates of water-splitting reactions and latter processes under intense sunlight, may act as a feedback loop and initiate quenching[40-42]. There is also causal evidence to suggest that the "xanthophyll cycle", i.e., the enzymatic conversion of antenna-associated carotenoids, also contributes to quenching[41, 43-45]. Under high-light conditions, the carotenoid LHCII violaxanthin is converted to the carotenoid zeaxanthin and results in quenching of fluorescence within LHCII either by acting as the main quenching site or by some stabilisation of the quenched state[39]. Finally, numerous researchers have identified a link between the presence of the PsbS protein in the thylakoid membrane and the amount of fluorescence quenching[46-49]. It is likely the case that the aforementioned trigger for NPQ is a combination of all three of these factors.

1.2.5.2 Site

Since the early 1980s numerous lines of evidence have emerged which suggest that the site of NPQ resides within the LHCII antenna. Early spectroscopy measurements of the quenched state in thylakoid extracts found that the quencher preferentially quenches LHCII emission bands at 680 nm and 700 nm[42]. Plant mutants lacking a majority of their LHCII were found to display strongly reduced NPQ[50, 51]. It has since been suggested that the aggregation of LHCII (termed the "LHCII aggregation model"), i.e., the clustering of LHCII proteins within the thylakoid membranes, causes a quenching of fluorescence even in the absence of other photosynthetic proteins, suggesting that inter-protein interactions, specifically those involving LHCII, may lead to energy dissipation[41,42,43]. LHCII trimers have been shown to rapidly reorganise in order to balance excitation levels between the two photosystems and divert excess energy away from the one which is energetically saturated and unable to utilise excitons. Both LHCII and PSII have been demonstrated to aggregate during NPQ to change organisation from LHCII-PSII supercomplexes that are highly efficient at transferring excitation energy to a state where proteins are more closely aggregated and pigments within the proteins are capable of energy dissipation[52, 53]. In addition, in both extracted thylakoids and model systems (e.g. protein aggregates in solution and protein reconstituted into liposomes) LHCII has been shown to undergo concentration-dependant quenching,

manifesting as a reduced fluorescence emission and lifetime, apparently based on the extent of LHCII-LHCII associations[54-56]. Hence it is now widely accepted that LHCII contains the quenching site, and modulates energy pathways and dissipation through the membrane.

1.2.5.3 Quencher

In recent years there is growing concensus that carotenoid (Cars) pigments, specifically lutiens, are responsible for quenching excitons within LHCII. Cars have an absorption maximum at the wavelengnths where Chls have a near-minimum[1], and the optically bright S_2 state of cars can rapidly transfer energy to lower Chl energy states. In addition to the bright S_2 state, cars posess a low-lying "dark" state, S_1 (and associated vibrational states S^*), that is optically forbidden and therefore cannot be directly absorb or emit photons but are accessible by energy transfer from other fluorophores. These dark states posesses an extremely short lifetime (~10 ps) due to the proximity of S_1 with the ground state and a high probability of internal conversion. This short lifetime and the close proximity of the S_1 state to the lowest excited state of Chl makes cars extremely effective quenchers[40]. Multiple researchers have used transient absorption spectroscopy measurements to reveal the timescales of energy transfer between pigments within LHCII (isolated in detergent or in nanodiscs) and suggest that the quenching mechanism of LHCII relies on energy transfer from chlorophylls to this rapidly decaying "dark" carotenoid state[57-60]. Croce et al identified that, due to the downward energy funnel of LHCII, a likely candidate for quenching is a carotenoid located in the proximity of the lowest energy chlorophyll, termed *a*612. Chlorophyll *a*612 is the nearest neighbour of a lutein site L620 (**Figure 1.6**), in addition to being part of a cluster of three strongly coupled, low energy chlorophylls (*a*610-*a*611-*a*612)[61]. Since this identification, it has been observed that the spectral signatures associated with NPQ are absent in LHCII monomers lacking *a*612 Chls[57], and theoretical modelling of pigments within LHCII identify strong coupling and rapid energy transfer from Chl pigments to L620, whereas the strength of coupling between Chls and other carotenoids was significantly weaker[61]. These findings, and a variety of other experimental[59, 62] and theoretical evidence[63], strongly suggest that lutein is the site of the quencher in LHCII and that a transfer pathway from *a*612 to L620 is opened or closed due to conformational changes of the protein[64-66].

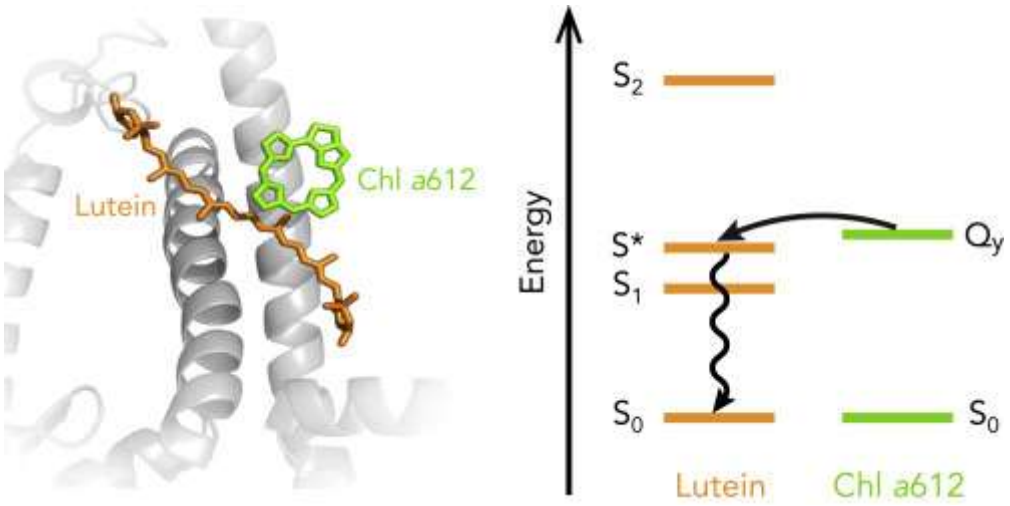

Figure 1.6: Schematic showing the location of the lowest energy chlorophyll, *a*612, relative to the lutein molecule, L620, and potential pathway of exciton quenching. Excitons are quenched by the transfer of energy from the Q_y band of chl excitation to an optically "dark" S^* or S_1 Lutein state, wherein it rapidly decays (~30 ps) to the ground state without the emission of a photon. Reprinted from Son et al (2019)[58].

1.2.5.4 Mechanism

The exact molecular mechanism of quenching is still under scrutiny. The LHCII aggregation model suggests that the ΔpH trigger results in the in-membrane aggregation of LHCII which is linked to a conformational change within the complex that forms the quencher (as shown in **Figure 1.7**)[41]. However, recent evidence has suggested that aggregation is not a requirement for fluorescence quenching and that isolated trimers may switch between a light-harvesting and energy dissipative state either due to the application of external forces (e.g. hydrostatic pressure[54]) or intermittently due to seemingly random fluctuations of the light harvesting state[67-69]. In all cases quenched isolated trimers exhibited spectral similarities to aggregation-induced quenching[41]. It has been proposed that this "blinking" can be explained by the conformational switching between two distinct conformational states[70], though this has since been complicated by single-molecule spectroscopy measurements suggesting that LHCII may actually possess multiple quenching conformations and therefore multiple quenching mechanisms[65]. The formation of quenched states of LHCII in the absense of aggregation leads to the question of the exact role of aggregation and macromolecular reorganisation within the membrane

and it has been suggested that aggregation may merely be a thermodynamic consequence of the conformational change, rather than actively stabilising the dissipative state of LHCII[71]. In either case, thylakoid membrane reorganisation, LHCII aggregation *and* the blinking of isolated trimers[68, 69] have all been shown to be sensitive to a variety of local physiochemical conditions, and it is apparent that the precise mechanism of trap formation is the combination of numerous complex interactions between LHCII proteins and the surrounding thylakoid environment. A significant challenge for future photosynthetic researchers is to delineate these effects.

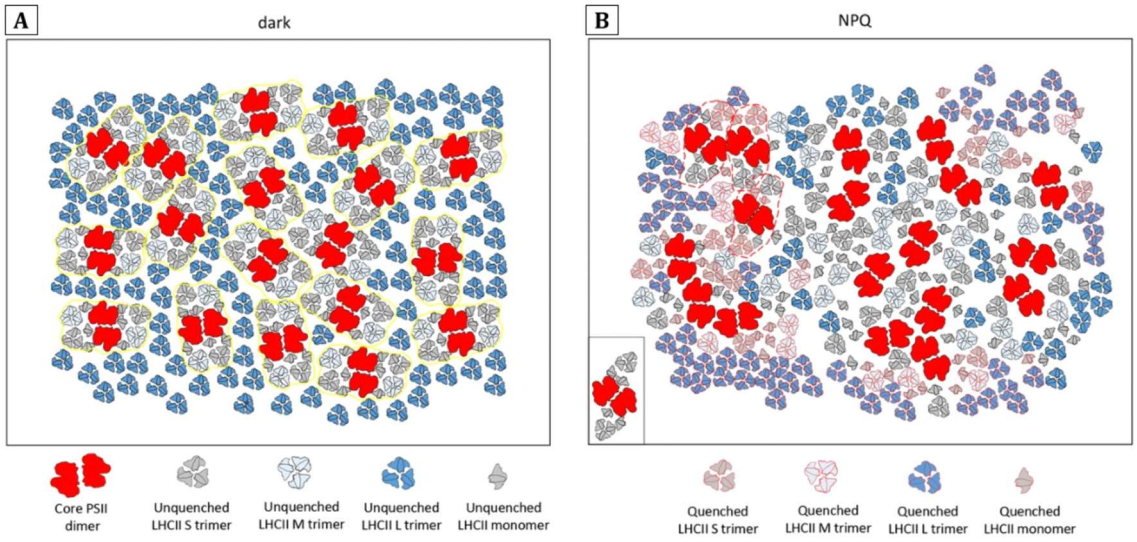

Figure 1.7: Schematic showing the reorganization of PSII/LHCII supercomplexes and peripheral LHCII during NPQ in the dark **(A)** and light states **(B).** Adapted with from Ruban (2016).[36]

1.2.6 Structural techniques to study non-photophysical quenching in photosynthetic membranes

Recent studies have already made significant progress towards delineating various structural and photophysical effects. Structural microscopy methods such as atomic force microscopy or electron microscopy have been used by numerous authors to directly visualise the reorganisation of thylakoid membranes and photosynthetic proteins in lipid bilayers in reponse to various conditions[72-76]. Atomic force microscopy (AFM) in particular has the advantage that the technique can be performed in aqeuous environements and using gentle imaging forces to directly image the organisation and topography of membranous samples. Recently, Zhao et

al were able to visualise structural changes in bacterial thylakoid membrane extracts with exceptionally high lateral and vertical resolution (~1-2 nm and 0.1 nm respectively). These topographs (**Figure 1.8a**) reveal the dense aggregation of proteins within the thylakoids under high light conditions and structural heterogeneity that may bear similarities to the photoprotection that occurs in plant thylakoids. Other AFM applications include the recent innovation of affinity-mapping AFM which measures the interaction forces between targeted proteins and a chemically altered AFM tip, as well as providing topographic information. This approach was recently applied by Johnson et al to determine the precise location of cyt b_6f dimers within thylakoid extracts and to reveal the strucutres of nanodomains within the membrane (**Figure 1.8b**). By chemically altering the AFM probe to selectively interact with other proteins, it may be possible to map protein rearrangement and native thylakoid compositon in a range of conditions. The study by Johnson et al is also notable for the application of the extremely high vertical resolution of AFM (typically ~0.1 nm) to identify specific types of proteins within the thylakoid, by measuring their protrustion from the bilayer and comparing that to the known crystal structures of each protein. In addition to AFM, electron microscopy is commonly employed to reveal the structure of large areas of membrane as well as smaller protein complexes. An advantage of this approach is the ability to visualise the 3D organisation of the membrane, for example, it was recently observed that PSII/LHCII complexes are more highly ordered in stacked thylakoid membranes (**Figure 1.8c**) and may register (be aligned) between multiple layers of stacked membranes, suggesting that protein organisation may play a large structural role in the stability of the thylakoid grana.

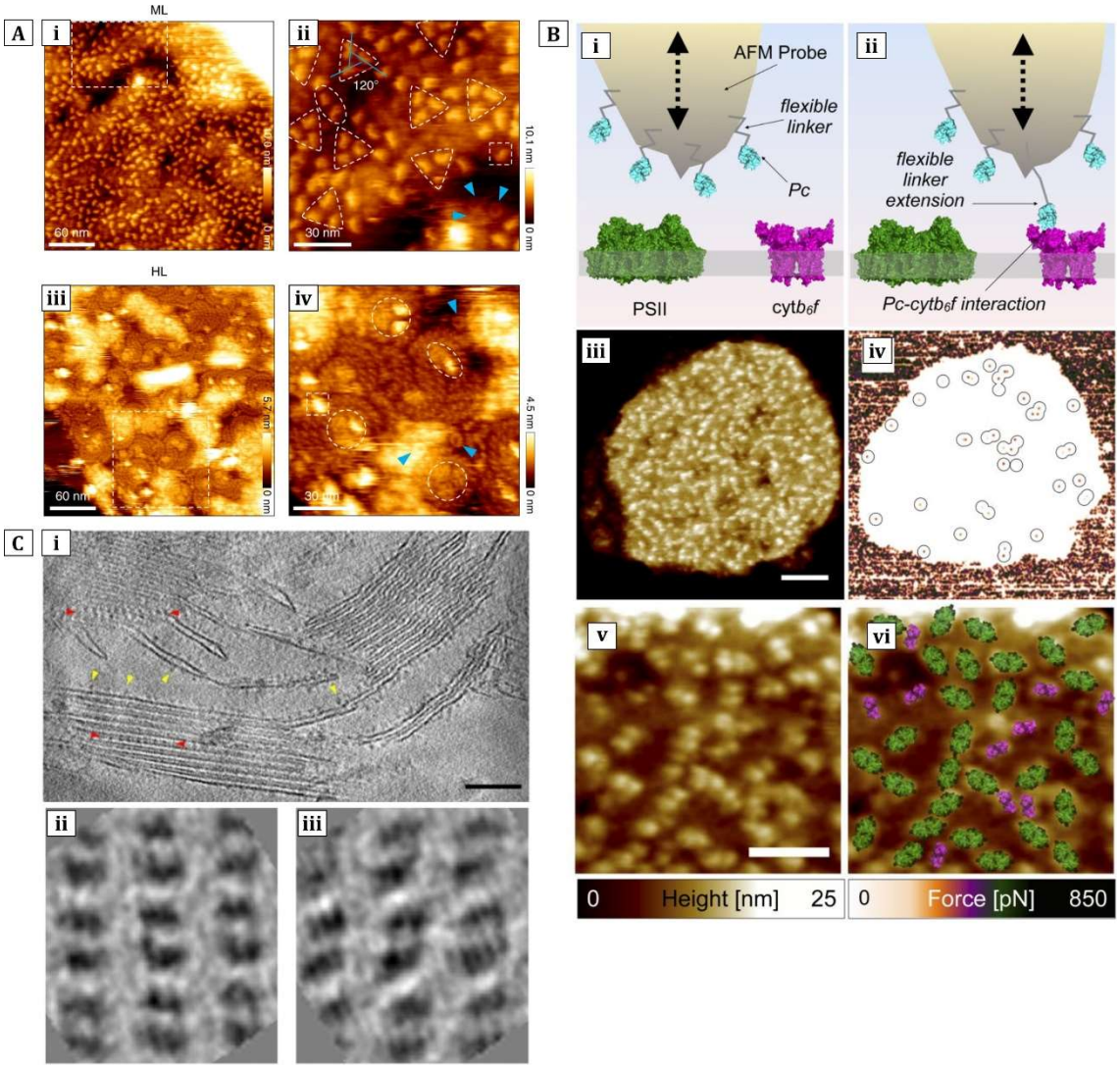

Figure 1.8: AFM and electron microscopy reveal the organisation of photosynthetic proteins within the thylakoid. **(A)** AFM topographs of bacterial thylakoid extracts grown in moderate-light **(i)-(ii)** and high-light **(iii)-(iv)** conditions. The high resolution (1-2 nm) reveals membrane heterogeneity and tightly packed protein aggregates that may contribute to photoprotection. Adapted from Zhao et al (2020)[77]. **(B) (i)-(ii)** Affinity-mapping AFM schematic showing the functionalisation of the probe and interactions that the linker molecule may have with a targeted protein (in this case cyt b_6f). **(iii)** A topographic map of a thylakoid extracted from spinach and **(iv)** the associated force map that reveals the location of cyt b_6f in the membrane. **(v)** A topographic map of protein clusters within a thylakoid extract, overlaid with protein crystal structures in **(vi)** that correspond with the membrane topography. Adapted from Johnson et al (2014)[72]. **(C)** Freeze-fracture electron microscopy measurements of thylakoid extracts showing **(i)** the 3D structure of a large area consisting of stacked and unstacked thylakoid membranes (scale bar = 100 nm). **(ii)** and **(iii)** The organisation of proteins in stacked membranes showing the registration between proteins between two stacked lipid bilayers. Adapted from Daum et al (2010)[78].

Fluorescence lifetime measurements are another technique that is popular in the photosynthetic community, due to the ability to assess the photophysical properties or interactions between proteins as indicated by their fluorescent lifetime. Multiple authors have identified fluorescence quenching (lifetime shortening) and NPQ-like spectral signatures in LHCII aggregates and isolated trimers in a variety of conditions. Fluorescence lifetime measurements have been obtained by Natali et al[79] of LHCII reconstituted into proteoliposomes, wherein it was identified that proteoliposomes with a greater protein:lipid ratio have shorter fluorescence lifetimes (shown in **Figure 1.9a** as steeper gradients in the fluorescence decay curves). This work took advantage of the modularity of model proteoliposomes to generate a series of proteoliposomes with different LHCII/DOPC ratios and detailed the relationship between protein crowding and function within a lipid environment. One limitation of the work, is that one cannot observe the structural arrangement of individual proteins within the membrane so this could not be directly correlated to the fluorescence changes. As a result, some researchers have tended towards fluorescence lifetime measurements of LH proteins on solid surfaces, to directly observe the spatial organisation of proteins or any sample heterogeneity correlated to differences in the fluorescence lifetime. This has the additional advantage that proteins may be arranged into desired structures. In an example by Vasilev et al[80] LHCII proteins were arranged into thin stripes <100 nm wide (**Figure 1.9bi**) and FLIM measurements on these patterned complexes show the fluorescence lifetime could be reversibly shortened or elongated in response to aggregating or disaggregating the proteins using detergent (**Figure 1.9bii**). More recently, researchers have combined both FLIM and AFM measurements, to provide high-resolution structural information that is correlated to fluorescence lifetime data. Application of this combined technique is still relatively rare, due to the time-consumption and technical complexity of collecting both data forms. However, a notable example by Adams et al[56] demonstrates the application of AFM to determine the position of proteins within a few nanometers (**Figure 1.9ci-ii**), combined with FLIM measurements to determine their photophysical state (**Figure 1.9ciii**). It was observed that increasing the average distance between proteins within aggregates (by introducing lipids) resulting in lifetime elongation and unquenching, and strongly suggests that the protein-protein interactions may modulate the onset of photosynthetic NPQ.

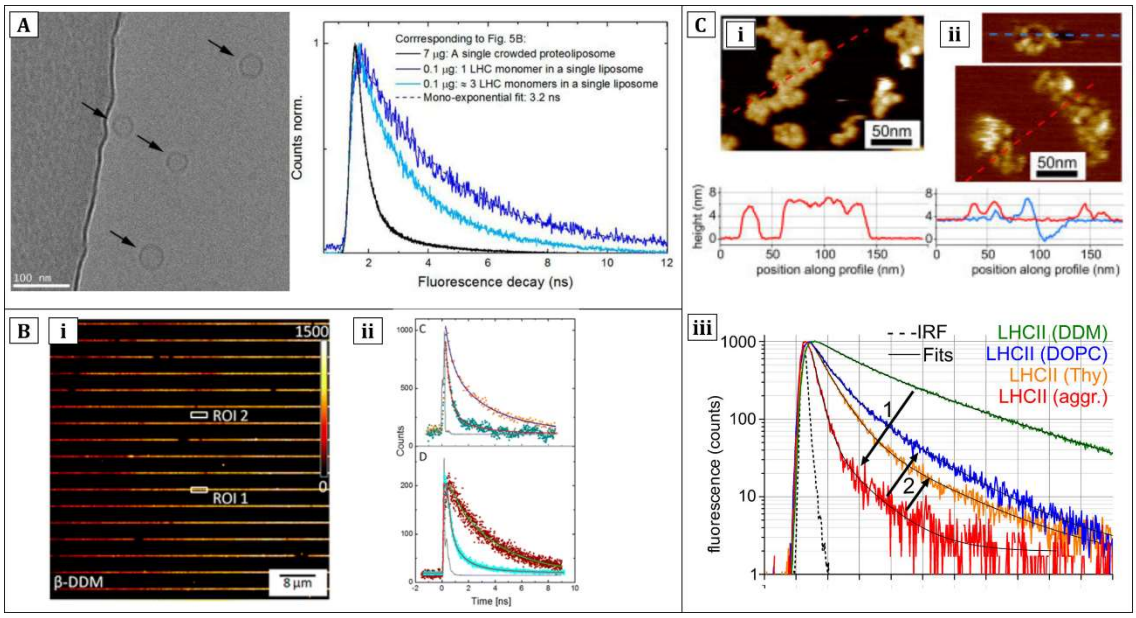

Figure 1.9: FLIM measurements can report on the photophysical properties and function of photosynthetic proteins in a variety of samples. **(A)** Electron microscopy measurements of LHCII reconstituted into proteoliposomes and accompanying fluorescence decay curves of different proteoliposome populations varying lipid:protein ratio. Adapted from Natali et al (2016)[79]. **(B)(i)** Fluorescence image of LHCII trimers deposited onto solid substrates in thin 2D arrays. **(ii)** Fluorescence decay curves of the sample in (i) showing the result of aggregation (*blue*) and disaggregation (*red*) of the proteins by removal or addition of detergent. Adapted from Vasilev et al (2014)[80]. **(C)** A combined AFM and FLIM study of LHCII deposited on mica substrates. **(i)** AFM topograph of LHCII deposited onto mica, that has self-assembled into a series of aggregates. The trace below shows the height of the proteins from the substrate, and can be used to determine the separation of proteins with high resolution. **(ii)** AFM topograph of the sample in (i) but after it has been incubated in a solution of DOPC liposomes. A supported lipid bilayer forms surrounding the protein aggregates and between individual proteins to reduce the extent of protein aggregation. **(iii)** Fluorescence decay curves obtained from LHCII in a variety of aggregated states. *Red*: obtained from a sample similar to (i). *Orange*: obtained from a sample similar to (ii) but "backfilled" with thylakoid lipids. *Blue:* obtained from a sample similar to (ii) backfilled with DOPC lipids. *Green:* obtained from LHCII in detergent solution, representing an entirely non-aggregated state. Adapted from Adams et al (2018)[56].

1.3 Using model systems to mimic or interrogate natural processes

In natural systems, biological lipid bilayers are often densely packed with transmembrane proteins which have crucial biological functions such as molecular transport, molecular synthesis and signalling[1]. In photosynthetic thylakoid bilayers, membrane proteins such as those involved in solar energy capture (introduced in section 1.1.1), are estimated to make up ~70 % of membrane surface area[8]. The large number of proteins performing a multitude of functions in biological membranes make it extremely difficult to study the properties of the lipid bilayer itself or any specific protein in the system. To delineate the complex photosynthetic machinery, many researchers have developed and utilised "model" systems, which typically consist of fewer components (e.g. proteins, lipids, etc.) in controlled or well-characterised systems, to interrogate specific photosynthetic processes. This section will provide an overview on some of the model systems previously developed, as well as discussing the pros and cons of each approach.

1.3.1 Bio-membrane extracts

Photosynthesis researchers have utilised natural membranes extracted from chloroplasts to investigate the structure and role of the thylakoid membrane since as early as the 1960s[81, 82]. Thylakoid membranes are typically isolated from chloroplasts after mechanically disrupting the organelles (by sonication or French press) followed by ultracentrifugation and/or further treatment with detergents[83, 84]. It is possible to purify a largely intact network of thylakoid membranes, often consisting of multi-layered structures and densely-packed protein supercomplexes[8]. In many ways, thylakoid extracts are an ideal material for studying photosynthesis since they provide a close to native membrane composition and contain many of the protein types found in *in vivo* membranes required for the early stages of photosynthesis[84, 85]. It is possible to study the structure of thylakoid extracts by adsorbing thylakoids onto support grids for electron microscopy measurements[52, 86-88] or by adhering thylakoids onto flat substrates (e.g. mica or etched glass) for atomic force microscopy measurements[72, 89, 90]. These measurements have been invaluable to determine the 3D structure of thylakoid membranes and the organisation of proteins within the membrane, both of which

are key aspects when considering the interactions between proteins required for effective photosynthesis. Nonetheless, challenges remain, and recent studies have shown that the use of typical detergents (DDM) during this thylakoid extraction process can disrupt the protein arrangement, but it is possible to purify thylakoids with more gentle detergents (digitonin)[91] or to avoid detergents entirely[73].

Thylakoid extracts are one of the most biologically relevant model systems in which to study photosynthesis, however, a direct consequence of their complexity is the additional challenge of delineating specific effects. To assess the effects of specific proteins or physiochemical conditions on the thylakoid structure and function, it is possible to alter the composition of the extract thylakoids by selectively breeding plant mutants[92, 93], modifying plant growth conditions[92, 94, 95] or by comparing thylakoid membranes from different plant species[96, 97]. However, a "simple" change (e.g. protein knockout) may often result in a combination changes to the overall membrane structure and function. For example, a previous study comparing wild-type rice plants with a PsbS knock-out mutant reported a multitude of differences in the thylakoid, including changes to the concentration of protein supercomplexes, variations in the overall protein concentration, greater LHCII phosphorylation, *and* a suppression of the NPQ response[92]. Whilst it was obvious that PsbS plays a significant role in modulating the structure and the photoprotective ability of the thylakoid, it was not clear if/how these multiple effects were linked or the precise differences in protein interactions that lead to such widespread differences. Numerous other studies using thylakoid extracts result in similarly complicated observations[92-95] and the associated difficulty of interpreting numerous, interlaced effects in a heterogeneous system.

1.3.2 Protein-only models

An alternative "bottom-up" approach to understanding photosynthesis is to accumulate knowledge in a piecewise fashion using simplified model systems. These model systems typically consist of one or two photosynthetic components (e.g. LHCII, PSII, thylakoid lipids, etc.) incorporated into a modular system where specific effects can be interrogated. Multiple researchers have generated protein-only systems as models to investigate energy transfer and quenching between pigments within a single protein, or energy transfer and interactions between multiple

proteins in the absence of other membrane components[47, 56, 68, 69, 80]. Typically proteins are purified from grana membranes by solubilising the grana with high concentrations of detergents and centrifugation. The supernatant (containing a variety of solubilised proteins) is then fractionated through ultracentrifugation through a sucrose gradient, and can be further purified using size exclusion chromatography to separate membrane components based upon their mass[56, 80, 98]. SDS-PAGE, native-page and absorption spectroscopy are among the variety of biochemical tools available to characterize the protein purity, oligermisation state and the extent of any protein denaturation.

An obvious target for protein-only studies was the determination of the protein structure of LHCII and LHCII/PSII super-complexes to a high resolution (2.5 Å)[24, 99, 100] which has led to the development of numerous theoretical models of energy transfer between inter/intra protein chlorophylls and a better understanding of the photophysical and structural properties of the membrane components[39, 61, 71, 101, 102]. Other studies of protein-only models have allowed ensemble solution spectroscopy measurements of proteins in solution[55, 103], and single molecule spectroscopy measurements of proteins immobilised onto substrates[66, 104, 105], that have been used to elucidate the pathways and rates of energy transfer between specific pigments and to identify various photophysical states of LHCII/PSII in response to physiochemical conditions (pH, temperature, detergent, etc.). Additional methodologies include the immobilization of proteins onto substrates[106, 107], as patterned arrays[80] or into solid gel systems[47] for high-resolution microscopy or spectroscopy measurements. An advantage of this approach is that the distance between proteins can be precisely controlled and measured, and the result on the fluorescent properties of the proteins can be assessed. In addition, protein-only models are highly adaptable, and it is relatively straight forward to change the protein concentration or environmental conditions to determine the photophysical or functional implications of similar changes within the thylakoid membranes. A notable disadvantage of protein-only studies is the removal of proteins from their native-like lipid environment, which has been shown to help stabilise proteins from denaturation and conformational changes[74, 108] and alter the spectroscopic properties of LHCII trimers[62, 109]. Due to the limited number of components these

systems may not always provide biologically relevant insight into the processes and interactions that occur in natural thylakoids.

1.3.3 Model lipid bilayers and membrane protein reconstitution

To effectively study the properties of lipids and/or membrane proteins in a native-like lipid environment, model lipid membranes can be formed *in vitro*. Lipid bilayers can be prepared from specifically selected lipids that self-assemble into nanoscale structures which are stable in aqueous solutions. This is often achieved by the gradual hydration of lipids dried onto a surface[110], through disrupting aggregates of liposomes in solution by applying a force through sonication[111], or by solubilising lipids into detergent micelles and gently removing the detergent[112]. All of these methods involve breaking up any preformed aggregates of lipids and allowing lipids to self-assemble into various structures. In solution, this typically results in the formation of liposomes or micelles, i.e. approximately spherical structures wherein the hydrophobic moieties of the lipids are protected from unfavourable interactions with polar water molecules. Liposomes, which consist of two layers of lipids that are fully enclosed, can be studied in solution or deposited onto hydrophilic surfaces to form "supported lipid bilayers (SLBs) (see **Figure 1.10b**). This has the advantage that SLBs consist of a far larger flat area than liposomes (10-100s of microns) and the capacity to be studied via microscopy techniques. SLBs can be formed on solid surfaces such as glass or mica by vesicle fusion and spreading methods (incubation of a clean hydrophilic substrate with a solution of liposomes)[113]. Lipid-tagged or lipophilic fluorophores are often utilised in both liposomes and supported lipid bilayers, allowing these bilayers to be labelled and also be environmentally sensitive to changes in local conditions[114]. Dyes are often directly covalently-tagged to lipid head or tail groups which will either freely diffuse laterally in the bilayer or be localised to specific lipid types or phases[115].

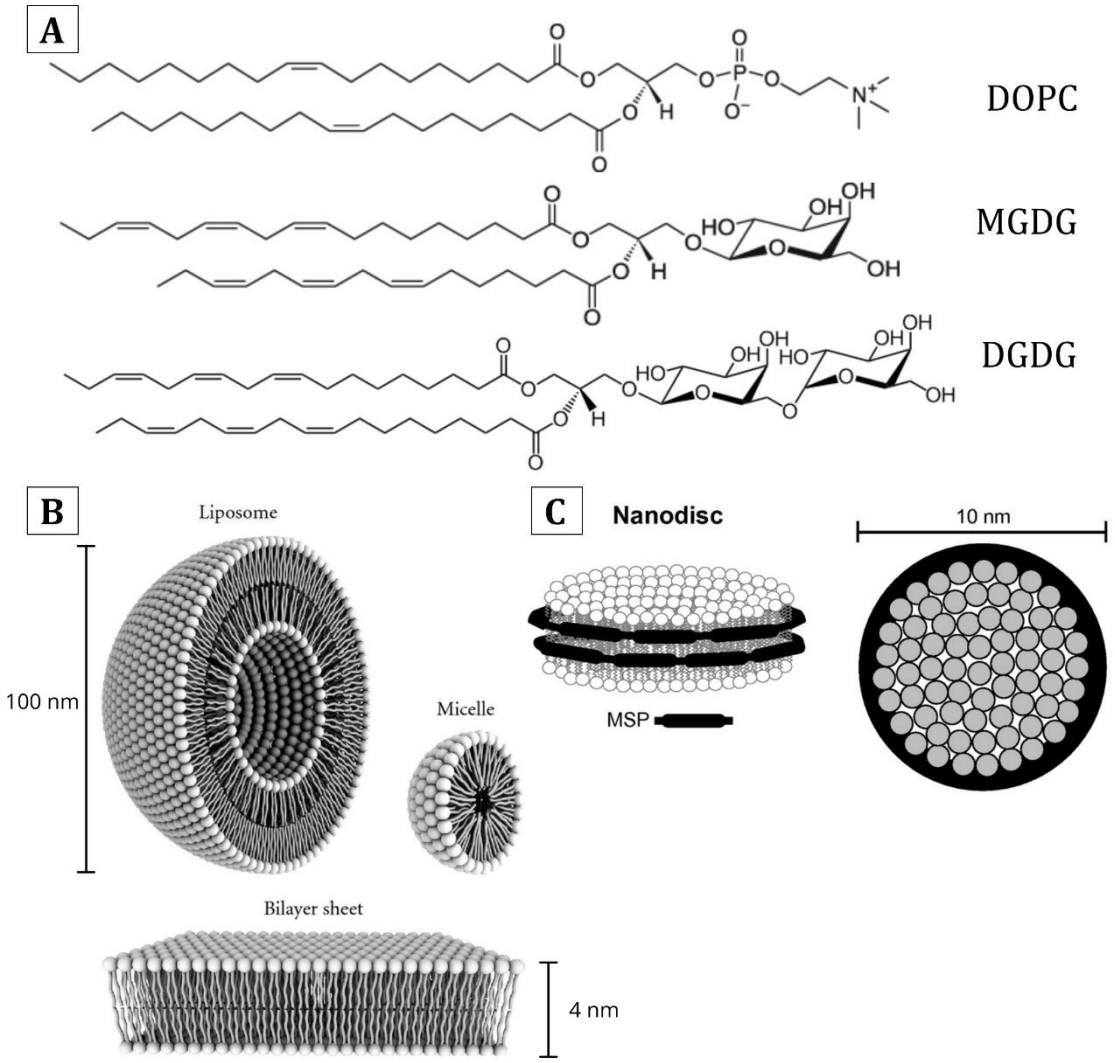

Figure 1.10: Examples of model lipid bilayers and lipid structures. **(A)** Structures of a commonly used synthetic lipid, DOPC, and two lipids found in photosynthetic thylakoid membranes, MGDG and DGDG. Structures obtained from Avanti Lipids. **(B)** Various examples of model lipid bilayers. *White, circles* represent hydrophilic lipid headgroups. *Grey* represents the hydrophobic lipid tails that bury themselves into the membrane and form hydrophobic associations to avoid contact with the aqueous buffer. Adapted from Bitounis et al (2012)[116]. **(C)** A side- and top-view schematic of a nanodisc assembled from lipids (*white*) and MSP polypeptide (*black*). Hydrophobic regions on the MSP associated with the hydrophobic lipid tails, to enclose a disk of lipids within the polymer "belt. Adapted from Malhotra et al (2014)[117].

Model lipid bilayers can also be used as a platform to study proteins and their function, by incorporating proteins into "proteoliposomes" during the self-assembly process. Membrane proteins are typically solubilised into detergent micelles during the procedures used for their isolation and purification procedure from natural membranes. Then, proteoliposomes can be formed by removal of the detergent which allows reconstitution of membrane proteins into lipid bilayers, which is often done by rapidly diluting the protein solution to lower detergent concentration or by the gradual removal of detergent by porous polystyrene beads[118]. This reduces the concentration of detergent in solution below the critical micelle concentration causing micelles to disassociate, and the membrane proteins will then reconstitute into lipid bilayers to minimise free energy by removing their hydrophobic regions from contact with the aqueous solution. These "proteoliposomes" can be studied in solution[98], tethered to a surface for microscopy measurements[105, 119] and can also be deposited onto surfaces to form supported lipid-protein bilayers[74]. Proteoliposomes can be used to study the effect of in-membrane protein aggregation[120], lipid-protein interactions[120, 121], changes in environmental conditions[122], and can even be utilised to study differences in chemical conditions on the interior versus the exterior of the liposome[123].

One potential issue with the use of proteoliposomes is the interactions that may occur between many proteins reconstituted within the bilayer, which complicate the measurement of specific features occurring the single-protein level; this can be especially challenging when studying proteins with known conformational and functionality changes related to aggregation[124]. To study individual membrane proteins independently of protein-protein interactions, lipid nanodiscs have been developed to encapsulate individual membrane proteins (**Figure 1.10c**). These nanodiscs consist of amphiphilic scaffold proteins that self-assemble to form a amphipathic "belt" of a defined radius that encapsulates a section of lipid bilayer and a single membrane protein so that measurements on truly isolated membrane proteins reconstituted into their native membrane environment are possible[125].

Numerous researchers have incorporated photosynthetic proteins into model lipid membranes, such as proteoliposomes, SLBs and nanodiscs, in order to study them in a near-native lipid environment from both bacterial[126], and plant systems[127].

LHCII and PSII have been co-reconstituted into proteoliposomes to quantify the enhancing effect of LHCII energy transfer to the activity of PSII by observing the increase in PSII oxygen evolution with the incorporation of the antenna protein[128]. PSII and ATP synthase have also been co-reconstituted into proteoliposomes in order to create an 'artificial chloroplast' where the cross-membrane proton gradient produced by PSII in the water splitting reaction is used to drive ATP synthase in an in vitro system[129]. The deposition of proteoliposomes onto solid surfaces as supported lipid bilayers allows the effect of different lipid compositions on the stacking of membranes containing photosynthetic protein to be studied[74]. It also allows physical measurements such as single molecule force spectroscopy to be performed on proteins and reveal the stabilising effects of different lipids. LHCII aggregation is thought to be a driving force in the process of non-photochemical quenching, and LHCII reconstitution into proteoliposomes is an established method of studying both the effect of different lipids and of protein aggregation on the photophysical properties of the protein[119]. The likelihood of LHCII-LHCII interactions within the membrane can be mediated by altering the lipid:protein ratio in proteoliposomes, which reveals a gradual change of the system towards an energy dissipative state LHCII-LHCII interactions are increased[79, 120] Lipid nanodiscs are able to provide a membrane environment with minimal LHCII-LHCII interactions, resulting in a significant reduction in the quenching of LHCII fluorescence and further enforcing the idea that the dissipative state is strongly related to aggregation[79, 120]. The minimised dissipative pathways of LHCII reconstituted into nanodiscs also allow the focused study of interchromophore energy transfers that occur within a single non-quenched LHCII complex using ultrafast spectroscopy techniques[62].

A challenge associated with lipid bilayers is the lengthy process of biochemical purification required to prepare purified proteins (which often includes the removal of native thylakoid lipids[74, 129-131]) and the complex procedures required to reconstitute proteins into proteoliposomes. For these reasons, such model systems are often limited to one or two types of protein, which simplifies the numerous interactions that are present in thylakoids, and may poorly represent the composition of the native membrane. In addition, there has been little success in reconstituting photosynthetic membrane proteins into lipid bilayers at biologically

relevant concentrations (previous models have achieved a protein occupation of a maximum of ~25 % of the membrane area[74, 98] compared to 60-70% *in vivo*). Therefore, the effects observed in model lipid membranes must be carefully interpreted when compared to processes that may occur in native thylakoid membranes.

1.3.4 Array-patterning of supported lipid bilayers

Patterned lipid membranes are commonly used to restrict the movement and diffusion of lipids/proteins to prevent the mixing of lipids between corralled membranes or to prevent the diffusion of lipids/proteins into certain parts of the sample[132-135]. In addition, membrane patterning can provide discrete and easily recognisable micro arrays that can increase the throughput or accuracy of analysis[135-137]. A widely used approach to generate patterned lipid bilayers is to use "microcontact printing", in which a lipid "ink" is deposited onto a surface using a micropatterned stamp (typically PDMS), which can generate features as small as a few micrometers[136, 138, 139]. However microcontact printing has the potential for surface fouling, non-specific binding or "overspill" from the stamp, and risks denaturation of the associated molecules if the "ink" dries. Other approaches include direct patterning of the bilayer using UV photolithography[140], dip-pen nanolithography (i.e. "writing" a lipid ink using an AFM probe)[141], or incubating liposomes onto a chemically (i.e. alternating regions of hydrophobic/hydrophilic areas) or physically (i.e. an empty template) patterned substrate such that lipids associate with hydrophilic or hydrophobic regions of the pattern to form discrete lipid membranes[134, 142].

1.3.5 In-membrane electrophoresis of supported lipid bilayers

One application of micropatterned membranes is a method known as "in-membrane electrophoresis" (**Figure 1.11a-c**), which utilises electric fields applied parallel to patterned lipid membranes to control the movement and concentration of charged molecules that are associated with the membrane[143-145]. Here, researchers have typically used lipids with a fluorophore attached to them (as a probe for fluorescence microscopy) or membrane-associated proteins (e.g., streptavidin). When charged molecules (or any particle) are placed in an electric field, they experience a Lorentz force equal to:

$$\overline{\boldsymbol{F}} = q\overline{\boldsymbol{E}} \qquad \text{Eq. 1.6}$$

where q is the charge of the molecule, $\boldsymbol{E}$ is a vector representing the direction and magnitude of the electric field, and $\boldsymbol{F}$ is a vector representing the direction and magnitude of the force[146]. The Lorentz force causes charged particles molecules to accelerate in the direction of the force, ultimately reaching a "terminal drift velocity" that describes their velocity when the Lorentz force is balanced with frictional forces that may occur in the system (e.g. bilayer viscosity, or friction between the molecules and the buffer). Fluorescence microscopy can be used to track the motion of lipid-tagged fluorophores and measure the E-field induced migration velocity (or the usual random 2-D diffusion). The terminal drift velocity is proportional to the magnitude of the electric field that is applied to the membrane, such that:

$$\boldsymbol{V_{drift}} = \mu_{EP} q\overline{\boldsymbol{E}} \qquad \text{Eq. 1.7}$$

Where $\boldsymbol{V_{drift}}$ is the terminal drift velocity and μ is the electrophoretic mobility (i.e. the strength of the response of a molecule to the Lorentz force). The electrophoretic mobility is related to the Einstein mobility (i.e., the tendency of a molecule to randomly diffuse) by:

$$\mu_{EP} = \alpha\mu_{FRAP} = \alpha \frac{D}{k_B T} \qquad \text{Eq. 1.8}$$

where D is the diffusion constant (in $\mu m^2 s^{-1}$) of the molecule measured via fluorescence recovery after photobleaching experiments, k_B is Boltzmann's constant and T is the temperature[146]. The difference between μ_{EP} and μ_{FRAP}, denoted by the ratio α, is due to frictional forces experienced by the molecule during electrophoresis. Specifically, ions in the buffer can accumulate close to the lipid bilayer, due to electrostatic interactions between the charged fluorophores and the buffer, and will migrate in the opposite direction to the fluorophores when an electric field is applied to the system. The resulting friction between the fluorophores and the buffer is known as "electroosmotic drag". Different molecules will experience differing amounts of electroosmotic drag, due to their relative charges and the amount that the molecule protrudes into the aqueous buffer[143, 145], and previous researchers have taken advantage of this effect to selectively separate specific fluorophores from a mixture of molecules (see example in **Figure 1.11d**)[143, 144].

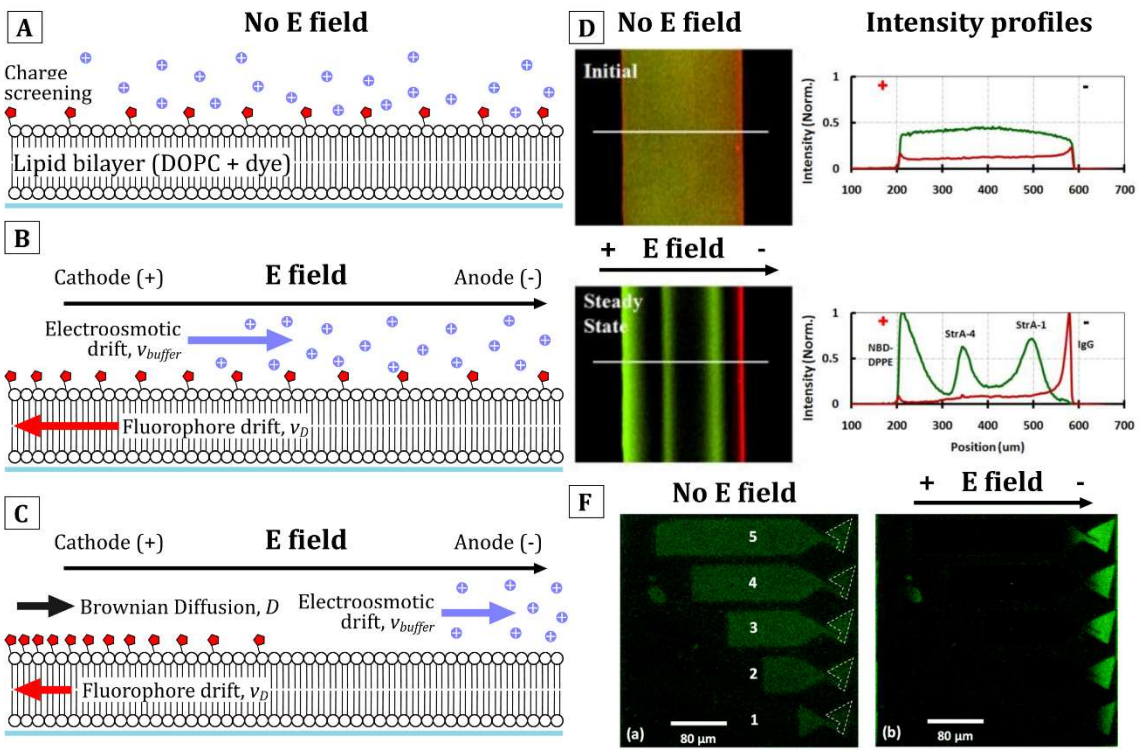

Figure 1.11: Cartoon schematic of an in-membrane electrophoresis experiment and various examples from literature. **(A)** Prior to the application of the electric field, charged fluorophores (*red*) are uniformly distributed throughout the membrane due to random diffusion. Oppositely charged ions (*blue*) accumulate close to the membrane surface to screen electrostatic interactions. **(B)** Immediately after the application of an E-field. Charged fluorophores begin to drift at the terminal drift velocity due to the applied Lorentz force. The oppositely charged ions also experience a Lorentz force in the opposite direction to the fluorophores. Friction between the fluorophores and the buffer creates "electroosmotic drag". **(C)** A long time after the E-field is turned on. The system reaches an equilibrium where electrophoretic forces are balanced by the random diffusion of molecules. **(D)** Separation of a mixture of fluorescent proteins (membrane bound and fluorescently labelled streptavidin) and lipids using in-membrane electrophoresis. Different electrophoretic and electroosmotic properties drive the separation of molecules when the electric field is applied. Adapted from Liu et al (2011)[147]. **(E)** An electrophoresis trap with complex geometry (series of rachets/hooks) is used to concentrate fluorophores in a spiral pattern using alternating current fields. (i) The starting distribution of fluorophores (ii) After the application of the field for 10 minutes. Adapted from Bao et al (2012)[145]. **(F)** In-membrane electrophoresis being used to increase the concentration of fluorescently labelled transmembrane protein, proteorhodopsin (pR). By varying the trap geometry (length) it was possible to modulate the final pR concentration at the end of the trap by up to 7× its initial concentration in the membrane. Adapted from Bao et al (2017)[148].

During in-membrane electrophoresis, the patterned membrane acts as an impermeable barrier, such that when fluorophores migrate through the membrane they will eventually reach the pattern edge and begin to accumulate at that location. Eventually, the system reaches a dynamic equilibrium, wherein the electrophoretic Lorentz force is balanced by the random diffusion of fluorophores, and the concentration of fluorophores, *C*, at a distance, *r*, away from the pattern edge is given by

$$C(r) = C_0 e^{-\frac{V_{drift}}{D}r} \qquad \text{Eq. 1.9}$$

Where C_0 is the concentration of fluorophores at r = zero[143, 146]. This methodology can be used to increase the concentration of charged fluorophores. Changing the length and shape of the patterned membrane changes the maximum concentration reached during in-membrane electrophoresis, by focusing more fluorophores into a smaller area. Many researchers have worked on the synthetic lipid-tagged fluorophore Texas Red to design electrophoresis traps which use complex geometries or alternating currents that are capable of increasing the fluorophore concentration by up to 25× its initial concentration[144, 145, 149]. To date, there is only one published report where in-membrane electrophoresis was applied to increase the concentration of trans-membrane (i.e., membrane spanning) proteins. In this report, the concentration of fluorescently-labelled proteorhodopsin proteins (a membrane-spanning proton pump) could be increased by up to 7× its initial concentration (see example in **Figure 1.11f**[148]). This study was a convincing demonstration of the ability to manipulated and generate SLBs containing high concentrations of transmembrane proteins, however, the characterisation relied upon fluorescence intensity and AFM measurements alone (i.e. no fluorescence lifetime data) and no attempt was made to assess the effect of protein concentration on its fluorescent properties or its light-mediated functionality. An exciting potential application of in-membrane electrophoresis would be to increase the concentration of photosynthetic membrane proteins (e.g. LHCII, PSII) in lipid bilayers to biologically relevant concentrations and to use fluorescence lifetime or structural measurements to determine the effect of protein organisation on the photophysical properties of these proteins. In-membrane electrophoresis has the advantage that patterned SLBs are highly adaptable and modular. It would theoretically be possible to screen a variety of membrane compositions and physiochemical conditions with

the aim of delineating the complex mechanisms involved in photosynthetic photoprotection.

1.4 Aims of this thesis

This introduction has provided an overview of the basics of photosynthesis and has discussed the current frontiers of photosynthetic research. In particular, this chapter has highlighted the challenges involved in delineating the numerous interactions that occur in photosynthetic membranes, and the large scale structural and photophysical changes that result in the non-photochemical quenching (NPQ) of chlorophyll fluorescence and the photoprotective capabilities of land plants. A large suite of model systems are available to researchers to interrogate the effects of different proteins, lipids or physiochemical conditions on photosynthetic processes, however, none of these systems are able to provide a complete understanding of photosynthesis and each platform has its own associated benefits and flaws. Therefore, photosynthetic research must rely on a multi-disciplinary approach, combining multiple experimental and theoretical platforms, and a careful interpretation of results in order to address the current unknowns in the field.

With this context, the aims of this thesis can be briefly summarised into the following: (i) to develop and characterise a range of experimental platforms which may be used to investigate energy transfer and dissipation that occurs between synthetic fluorophores and photosynthetic proteins in lipid membranes, (ii) to employ these platforms to investigate the manner in which the organization and concentration of fluorophores in lipid membranes may alter energy transfer and energy dissipation between synthetic fluorophores and photosynthetic proteins, (iii) to exploit the energy transfer between synthetic fluorophores and photosynthetic proteins to increase the light-harvesting or electron transfer capabilities of photosynthetic model membranes as bio-hybrid nanomaterials and (iv) to interpret our results, in context with existing literature, to delineate the mechanism of photoprotective non-photochemical quenching in thylakoid membranes.

The remainder of this thesis as follows. Chapter 2 provides the theoretical background of experimental techniques used throughout this thesis. Chapter 3 details the experimental protocols used in the preparation and characterisation of samples. Chapter 4 describes the characterisation of a new type of model membrane that is surface-supported and micro-patterned and the use of this model membrane for the interrogation of a mixture of thylakoid proteins. Chapter 5 details the development of two types of model membranes designed to interface the synthetic chromophore Texas Red (TR) to chlorophyll(Chl)-containing proteins. We demonstrate the ability to incorporate a range of concentrations of both TR and proteins into the membranes and to enhance the overall absorption cross-section of the system. Chapter 6 describes the use of electric fields to control the organisation of charged organic fluorophores within surface-supported model membranes and FLIM measurements as a means to investigate the self-quenching that occurs between small-molecule fluorophores. Three commonly used synthetic fluorophores were investigated and found to undergo fluorescence quenching as a function of their concentration within the membrane. Finally, chapter 7 documents the application of electric fields and FLIM to quantify the self-quenching that occurs between photosynthetic proteins, in order to provide insight into the mechanism of photoprotective non-photochemical quenching in plants.

2 Theory of experimental techniques

This chapter provides a theoretical basis for experimental techniques used throughout this thesis.

2.1 Optical spectroscopy

2.1.1 Steady state fluorescence spectroscopy

Steady-state fluorescence spectroscopy is a technique used to determine the level of fluorescence emission from a sample at a particular wavelength after excitation at another wavelength. Typically, there are two kinds of steady-state fluorescence measurements that can be made with a standard fluorescence spectrometer. (i) Fluorescence emission spectroscopy, in which samples are excited at a defined constant wavelength whilst the intensity is measured as the different emission wavelengths are scanned. This produces an "emission spectrum". (ii) Fluorescence excitation spectroscopy, in which emission intensity is measured at a defined wavelength whilst the excitation wavelength range is scanned. This produces an "excitation spectrum".

In a fluorescence spectrometer (schematic in **Figure 2.1**) a white light lamp with a wide wavelength range is used to create an initial beam of light. This beam is then passed through an adjustable monochromator which produces a beam of light centred at a specific wavelength to excite the sample. This excitation beam will have a 'slit width' with defines the range wavelengths in the beam that exits the slit. This light will be directed towards the sample, often though an iris which can open or close to mediate beam intensity, where it will interact with the sample. Fluorescence emission from the sample is then collected at 90° from the excitation beam. The emission beam passes through a second adjustable monochromator which will allow a defined wavelength range, again with a defined emission 'slit width', to reach a detector that records the fluorescence intensity of the sample for those specific excitation and emission wavelengths.

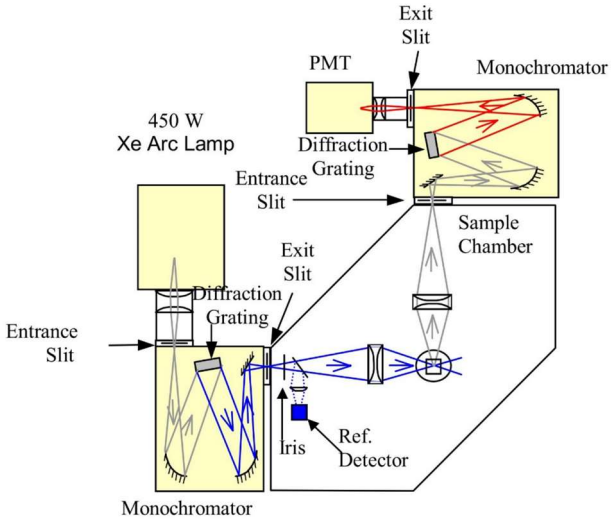

Figure 2.1: Fluorescence spectrometer schematic. Adapted from Edinburgh Instruments FLS980 fluorescence spectrophotometer manual.

2.1.2 Absorption spectroscopy

Absorption spectroscopy is a steady-state technique which measures how much light is absorbed by a sample at a particular wavelength. Chromophores and systems made up of many chromophores, such as light-harvesting proteins, often have complex absorption spectra due to different absorption efficiencies at different wavelengths. Changes in a chromophore local environment, such as charge, solvent or interactions with other chromophores, often manifest as changes in the absorption spectra that can be measured with absorption spectroscopy. The absorbance of a sample, A, is proportional to the concentration in accordance with the Beer-Lambert law:

$$A = \varepsilon l c \qquad \text{Eq. 2.1}$$

where ε is the molar extinction coefficient of relevant component ($M^{-1}cm^{-1}$), l is optical path length of absorption spectroscopy measurement (cm), and c is the molar concentration of relevant component (M). An absorption spectrometer uses a white light lamp with a wide wavelength range to create an initial beam of light. This then passes through an adjustable monochromator which utilises concave mirrors and a diffraction grating to produce light centred at a specific wavelength; this beam will have a controllable 'slit width' which defines the wavelength range of light produced. The beam will pass through the sample and toward a detector to quantify the intensity of light transmitted to the detector, and therefore the light absorbed by the sample at each wavelength. To take into account the absorption of

the cuvette and any solution used a 'blank' measurement must be taken of the solution and cuvette without the sample. This can be done with a parallel cuvette and beam-splitter or a 'matched' cuvette as used for the sample measurement. This measurement of 'blank' absorption is subtracted from the sample measurement to provide a spectra of the sample absorption only.

2.2 Epifluorescence Microscopy

Epifluorescence microscopy is a form of microscopy where excitation light illuminates a sample at an angle of 90° from the surface and emission is collected along the same path as the excitation. Fluorescence microscopes can be used to image different fluorophores by having selective excitation and emission filters which control the wavelength range of excitation light that reaches the sample and the wavelength range of emission light collected, respectively (**Figure 2.2**). The excitation and emission filters are paired with a dichroic mirror, which will reflect shorter wavelengths and transmit longer ones with a defined cut off, to form a 'filter cube' that is matched to the spectral properties of the desired fluorophores. The dichroic cut off is typically designed to separate excitation and emission wavelength.

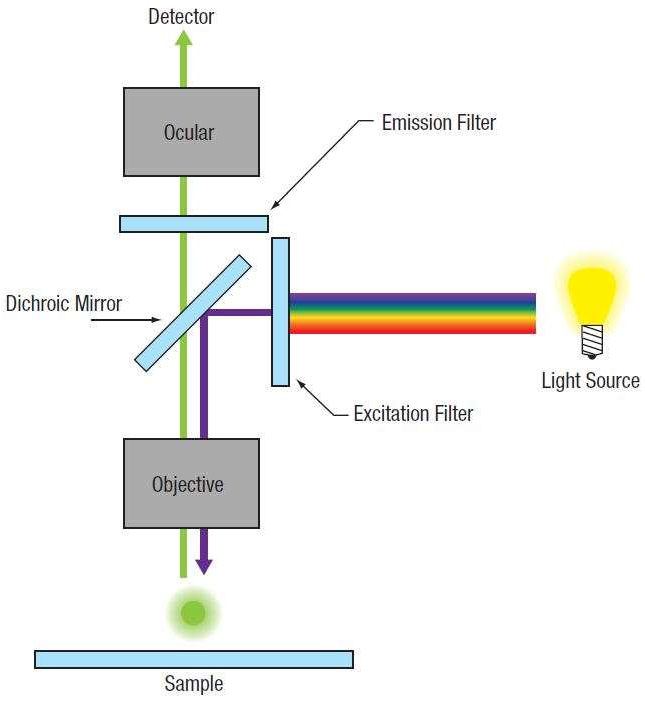

Figure 2.2: Schematic of the optics within an epifluorescence microscope. Adapted from ThorLabs user manual.

In a typical epifluorescence microscopy system, a white light lamp with a wide wavelength range provides a beam of light. This beam initially passes through a mechanical aperture which can open and close to block the beam or mediate its width. The white light is directed towards the excitation filter, allowing the desired excitation wavelengths to pass through. This excitation beam is then reflected 90° towards to the sample by the dichroic mirror, through a magnifying objective lens, and onto the sample stage. The excitation light will cause chromophores in the sample to fluoresce and the emitted light will travel back through the objective lens. Due to the Stokes' shift, the emitted light is red-shifted by approximately ~50 nm relative to the excitation light. The emitted light is then transmitted though the dichroic mirror, though a final emission filter and onto the CCD detector where an image is recorded.

2.3 Fluorescence lifetime imaging microscopy

2.3.1 Overview

An important characteristic of fluorescent molecules is their distinctive fluorescence lifetime; measured as the characteristic time it takes for an excited fluorophore to relax from an excited state to a ground state, and release the excitation energy as a photon[150]. For most biological molecules, or artificial dyes (commonly used as fluorescence bio-markers), the fluorescence lifetime is of the order of a few nanoseconds[151], but will change predictably as a result of interactions between the fluorophore and its local environment. As such, fluorescence lifetime measurements provide a quantitiative method to probe the pH, [152, 153] viscosity, [154] [155] ion concentration and other conditions using a range of commonly used "lifetime-based sensors" [156-159].

Fluorescence lifetime imaging microscopy (FLIM), is a microscopy technique that has gained popularity because of its high sensitivity to the molecular environment. FLIM typically encompasses a scanning laser which passes through a confocal pinhole (or two photon-excitation) to eliminate out-of-focus light and provide high-resolution intensity maps. The application of multiple lasers, often used in Pulsed Interleave Excitation (PIE) mode makes multi-spectral detection relatively easy,

such that FRET donors and acceptors can be probed simultaneously[160, 161]. In addition to fluorescence intensity measurements, FLIM can be used to generate fluorescence decay curves at each location, providing an average lifetime measurement (as can be produced with ensemble spectroscopy), as well as information about the colocalisation of fluorophores[98], and allowing for the correlation of fluorescence lifetimes and microscale structures within a sample. FLIM can also be combined with other surface-based microscopies, such as atomic force microscopy, to directly probe the relationship between fluorophore arrangement, sample structure and interactions that may alter the photophysical state.

2.3.2 Principle of Time Correlated Single Photon Counting

Time-correlated single photon counting (TCSPC) is a spectroscopic technique used to the determine the average fluorescence lifetime of chromophores. The method is based on the excitation of fluorophores with a narrow pulse of light, followed by the precisely timed registration of the arrival of single photons that are emitted from these fluorophores. The time difference between the excitation and emission is accurately measured by a combination of timing electronics and highly sensitive single-photon detectors that act like a stopwatch. This cycle is repeated many times, and then stopwatch readings are sorted into a histogram consisting of a range of time bins, typically with a temporal resolution of <50 picoseconds. The result is a fluorescence decay curve where the amplitude of the curve at each point represents the probability of recording photon emission at that time after the initial excitation. The fluorescence lifetime can be calculated by fitting an exponential function to the decay curve.

Fluorescence lifetime imaging microscopy (FLIM) combines TCSPC measurements with sample scanning, such that a TCSPC decay curve is obtained for each pixel in an image. To achieve this, a coarse time-tag is recorded for each photon, in addition to the “stopwatch” time, called the Time-Tagged Time-Resolved (TTTR) data stream. This TTTR records the macroscopic time of arrival for each photon, and is then synchronised with the position of the scanner at that time, as illustrated in **Figure 2.3a**.

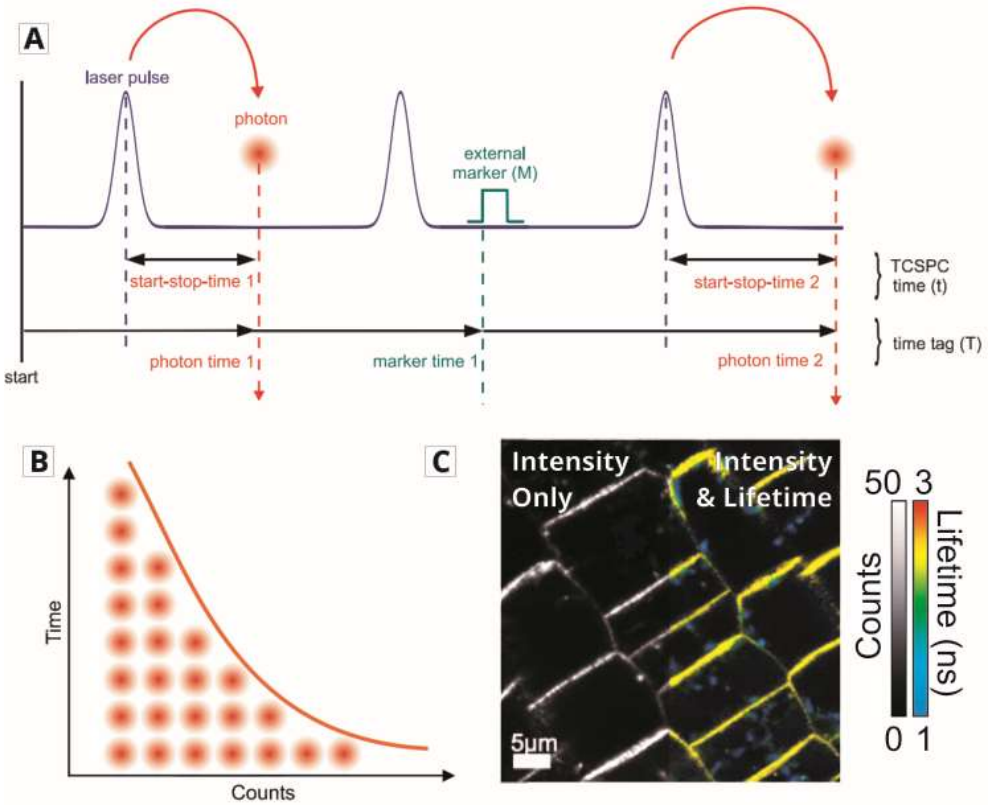

Figure 2.3: Instrument schematic for the generation of FLIM images using Time-Correlated Single Photon Counting **(A)** TCSPC and TTTR data streams. In the TCSPC data, the start-stop-time for each photon is measured as the time period between the peak of the laser pulse (*blue* line), and the registration of the photon by a detector. In the TTTR data, the time of arrival for each photon is measured from the start of the experiment, and synchronised with external markers, to correlate the photon arrival with the location of individual pixels. **(B)** A representation of the TCSPC data after it is "binned" into a histogram to generate a fluorescence decay curve. **(C)** An example FLIM-image, showing the intensity only data (*left*), and intensity data overlaid with false-colour lifetime data (*right*). Adapted from technical documentation from FLIM manufacturer Picoquant (GmbH).

This enables the electronics to reconstruct 2D, or even 3D, images, consisting of both intensity (the number of detected photons) and fluorescence decay curves (the histogram of "stopwatch" times) for each pixel (**Figure 2.3b**). The combination of spatial, and temporal information, is a particularly powerful tool to interrogate systems where the structural arrangement of fluorophores may result in changes to their photophysical properties. To display this information, FLIM data is typically represented as 2D images, where the "brightness" represents the fluorescence intensity at each location, and a false-colour scale is used to represent the average

fluorescence lifetime (an example is shown in **Figure 2.3c**). For consistency and ease of interpretation, in all FLIM-images shown throughout this thesis, lifetimes are represented by a false-colour scale which is *blue-green-yellow-orange-red* from short lifetime to long lifetime.

2.3.3 Typical FLIM instrumentation

In FLIM measurements, an optical microscope is used as a sample stage with the ability the couple light to the FLIM Main Optical Unit (MOU) containing confocal optics. Briefly, the MOU consists of the following components: 1) An excitation segment, 2) A basic confocal unit, 3) Beam diagnostics, 4) Detection channels. A complete schematic of the Main Optical Unit (MOU) is shown in **Figure 2.4**. Prior to the excitation beam segment (**Figure 2.4**, *yellow*), the emission from up to three Laser Diode Head (LDH) sources are aligned and coupled into a single-mode fibre optic leading to the MOU. The laser intensity can be adjusted by the placement of neutral density filters and a "razor-blade" that blocks a portion of the beam.

To maintain the shortest possible laser pulse width and provides the best temporal resolution, the voltage supplied to each laser is always set at the minimum required to allow lasing and kept constant for all measurements. The correct laser is chosen to match the absorption of the sample fluorophore. For imaging samples consisting of multiple fluorophores, multiple LDHs can be operated in Pulsed Interleaved Excitation (PIE) mode, such that two, or more, wavelengths of laser light are pulsed in an alternating sequence with precisely defined intervals (which should be sufficient to allow exciton decay before the next pulse). This allows for dual channel measurements that are both spectrally (selected through excitation and emission wavelengths) and temporally resolved and results in multiple FLIM channels with high specificity and minimal cross talk (typically <1%) between channels. The pulsed excitation is directed to the sample using a "FLIMBee" mirror-based galvanometer scanner (PicoQuant) that is attached to the basic confocal unit. The rapid raster speed and precision of the galvanometer allows for both FLIM images, and rapid video-speed measurements over large areas.

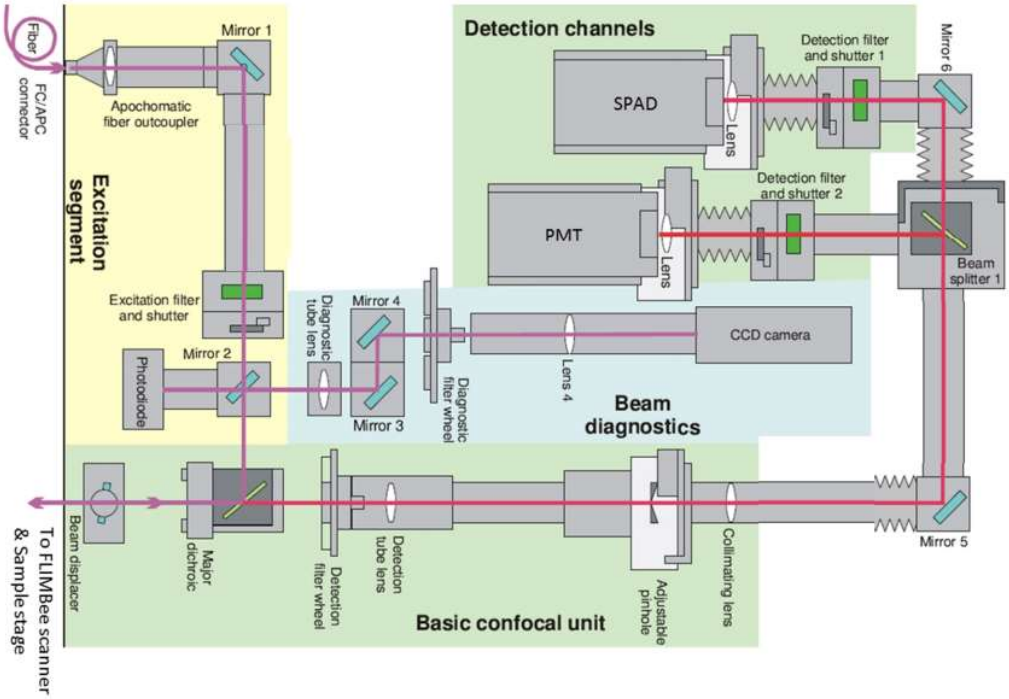

Figure 2.4: Instrumental schematic for the FLIM system at the University of Leeds with sections coloured corresponding to the different segments. Adapted from the Picoquant (GmbH) user manual.

Light returning from the sample to the dichroic consists of two components; i) light that has been scattered by the sample-substrate interface and ii) light that has been absorbed and re-emitted by fluorescence molecules on the substrate. The scattered light has the same wavelength as the excitation light, and is therefore reflected by the dichroic mirror to the beam diagnostic segment (**Figure 2.4**, *blue*) of the MOU where the symmetry of the laser beam and quantity of scattered light can be monitored. The re-emitted light has a longer wavelength than the excitation beam (due to a Stokes shift of ~50 nm for most common fluorophores) and transmits through the dichroic to other components of the confocal unit (optical filters) and towards the detection segment (**Figure 2.4**, *green upper*). Within the detection segment, the emitted signal can be directed towards two detectors (**Figure 2.4**, *upper green*), a Photon Multiplier Tube (PMT) or a SPAD (Single Photon Avalanche Detector). With this arrangement of detectors, multiple fluorophores can be probed independently by placing different emission filters in front of each detector. Typical experimental parameters for FLIM measurements are given in Chapter 3 (and where required per experiment).

2.3.4 Common FLIM artefacts: Pile-up and wrap-around effects

After registering a photon, the detectors require some time to reset and be ready for the detection of the next photon. This so-called "dead time" is typically in the range of 25 to 90 ns for high-quality detectors. If multiple photons arrive within a single cycle, the first photon to arrive at the detector will be registered, but the second photon is "lost". Therefore, this effect, termed the "pile-up effect" (**Figure 2.5a**), manifests itself as an over representation of photons with shorter lifetimes, a shortened average measured lifetime, and the addition of a more rapid decay component – a mono-exponential decay, will become a bi-exponential decay. To avoid these lifetime artefacts, only one photon must reach the detector per cycle. This requirement is met by ensuring that the probability of detecting a single photon per cycle is low (in fact, many cycles will not result in a detected photon at all) by attenuating the excitation laser power at the sample in order to limit the number of excited fluorophores generated by each pulse. In order to maintain single-photon statistics, on average only 1 in 100 excitation pulses should generate a count at the detector. This parameter is monitored during TCPSC experiments, ensuring that the average count rate at the detector does not exceed at most ~1% of the laser pulse rate. For example, for a pulsed laser source running with a repetition rate of 20 MHz, the average detector count rate should not exceed 0.2 MHz (200,000 counts per second).

A second form of TCSPC artefact, called "wrap-around artefacts" (**Figure 2.5b**), occurs when the excitation pulse rate is large enough that multiple pulses occur within the lifetime of a single excited state. In this scenario, the emission of an excited state generated by one laser pulse is likely to be registered as the response to a later laser pulse. This leads to distortions in the fluorescence decay curve, where excited states with a long lifetime are under-represented or registered as short-lifetime components, and the baseline (i.e. background level) of the fluorescence decay curve increases in response to overlapping portions of the fluorescence decay curve. To prevent these artefacts in the fluorescence decay curve, the laser pulse rate used for single (or dual) channel measurements is selected such that the excited state of the fluorophore had sufficient time to decay before a subsequent laser pulse. The ideal pulse rate for any given fluorophore can be found experimentally (by

visually inspecting the decay curve to ensure complete decay before the next pulse), or mathematically using the exponential decay function

$$I(t) = Ae^{-t/\tau} \qquad \text{Eq. 2.2}$$

Where I(t) is the time-resolved intensity, A is the amplitude, t is the time after a laser pulse, and τ is the lifetime of the fluorophore. Substituting, the fluorescence lifetime of LHCII (~4 ns) into this equation, shows that the fluorescence intensity has almost completely decayed (to less than 1% of the initial amplitude) after ~20 ns. A pulse rate of 20 MHz (i.e. one pulse every 50 ns) is therefore more-than-sufficient for measurements of photosynthetic proteins.

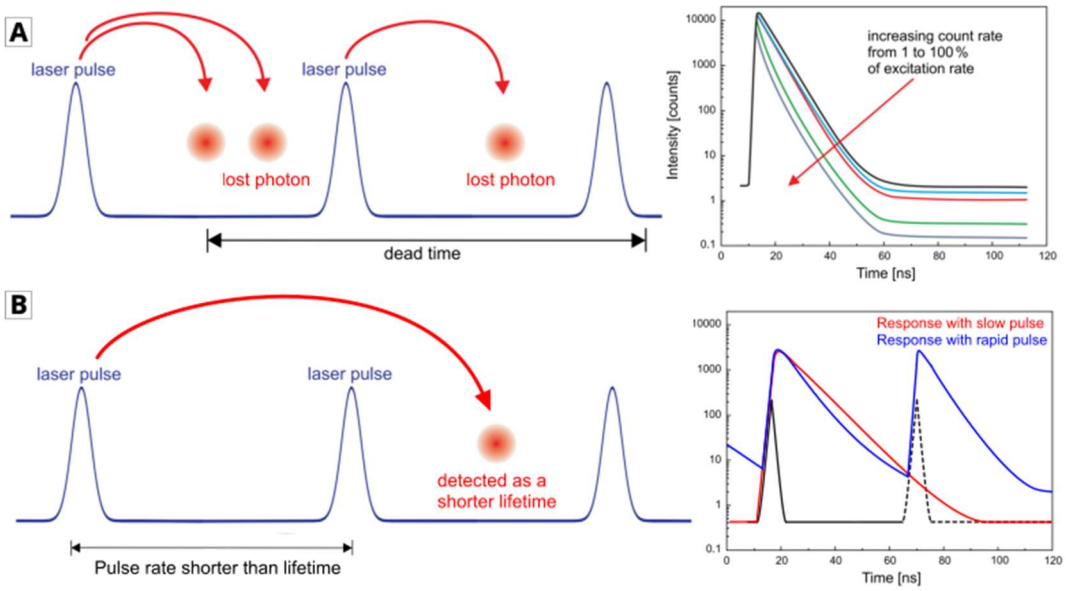

Figure 2.5: Examples of common TCSPC artefacts. **(A)** Photon pile-up effect. **(B)** Wrap around effect. The fluorescence decay curves (*right*) show an curve unaffected by wrap-around effects due to the slow pulse rate (*red*), compared to a decay curve where the second pulse (*black, dashed*) occurs before the curve has fully decayed (*blue*). The result is a higher baseline, and a shortened fluorescence lifetime. Adapted from the Picoquant (GmbH) technical documentation.

2.3.5 Interpretation and analysis of fluorescence decay curves

The characteristic of a TCSPC system that summarizes the overall time precision is the instrument response function (IRF). The IRF represents the sum of all the temporal inaccuracies of the system including the detector resolution, the laser pulse width and the timing jitter of the electronic components. The most significant

component of the IRF is often the uncertainty of the detector, due to the time taken to convert a photon into an electrical signal. For most TCSPC detectors, this may introduce uncertainties of 200 to 400 ps. The second most contribution to IRF broadening is the pulse width of the excitation source, which, including the time taken to obtain a reference signal, can be as large as 100 ps.

Overall, an estimate of the overall IRF width, can be obtained from the geometric sum of individual components, or the propagated error of each component

$$FWHM_{IRF} \gg \sqrt{\sum FWHM_{component}^2} \qquad \text{Eq. 2.3}$$

The IRF for our system was found experimentally by calculating the full width at half-maximum (FWHM) of the temporal response of the FLIM to scattered light. In this case, the time-dependence of the detected signal is only the result of instrument uncertainty (since light is scattered instantaneously), and provides an approximate estimate for the resolution of the system. As a rule of thumb, and in favourable experimental conditions, reconvolution analysis can be used to recover lifetimes down to ~1/10th of the IRF width.

To accurately calculate the lifetimes from fluorescence decay curves, IRF measurements were made for each detector (using a particular laser and repetition rate), prior to each series of measurements. Measured IRFs were used as part of a reconvolution fit, in the SymPhoTime software. Initially, data was fit to a monoexponentially model and the number of parameters was increased until an acceptable fit was achieved. An acceptable fit is characterized by the following criteria: (i) the fitted curve overlays well with the decay curve, (ii) the residuals are minimized and randomized around zero, (iii) the χ^2 value approaches 1, and (iv) the calculated fitted values are reasonable (positive amplitudes and lifetimes). The fitted decay curve can be described by a sum of exponential components, where each exponential curve represents a population of fluorophores following a particular decay mechanism. The time-resolved intensity, I(t), of an ensemble of fluorescent molecules at given time, t, after an excitation pulse, is given by

$$I(t) = \sum A_i \exp\left(-\frac{t}{\tau_i}\right) \qquad \text{Eq. 2.4}$$

Where A_i is the amplitude (normalised such that the sum of A_i equals 1) and τ_i is the time constant of each decay component. The average lifetime of a fluorophore is typically quoted as the mean amplitude-weighted lifetime, $<\tau>$ and is calculated from average of the time-constants, weighted by their respective amplitudes.

$$< \tau > = \sum A_i \tau_i \qquad \text{Eq. 2.5}$$

2.4 Atomic force microscopy

2.4.1 Overview

The atomic force microscope (AFM) was developed out of the scanning probe microscope (SPM) classification of microscopes used for studying surface properties of materials from the atomic to the micron level. The AFM measures forces between a solid probe and the sample whilst scanning in a raster fashion across the surface to give a surface topography. The AFM can measure: forces at the pN scale, lateral distances at the nm scale and vertical distances at the sub-angstrom scale. Coupled with the ability to operate under physiologically relevant, liquid environments this makes the AFM a great tool for high-resolution structural and mechanical investigations of biological samples in a non-destructive manner. Developments in each component have, and continue to allow advances in resolution, speed and function which will be discussed further in the following sections.

2.4.2 Typical instrumentation

A common instrumental set up of an AFM is shown schematically in **Figure 2.6**. Two vital components of an AFM are the probe and the scanner. The probe consists of a cantilever and a sharp tip (with tip radius of ~2 nm or greater), whereby forces between the sharp tip and sample cause a deflection in the typically ~100 μm long, flexible cantilever to which it is bound. This deflection causes a change in angle of the cantilever which can be detected by a laser beam reflecting off the back of the cantilever end, onto a photodiode split into 4 quadrants. The SPM scanner is made from piezoelectric materials in such a configuration that provides precise positioning control. Piezoelectric materials contract or expand when a voltage is applied with a mechanical movement that is proportional to the voltage applied. The scanner has a combination of independently operated piezo electrodes for X, Y, and

Z in a single tube, making a scanner that can manipulate samples and probes with high precision in three dimensions. AC voltages applied to the different electrodes of the piezoelectric scanner produce a scanning raster motion in the x and y directions. The AFM probe can be mounted on piezoelectric device, also. This combination allows the probe to be scanned over the sample, or the sample scanned under the probe, whilst measuring cantilever deflections which can then be interpreted by a computer to generate a map of surface topography (X, Y and Z positions).

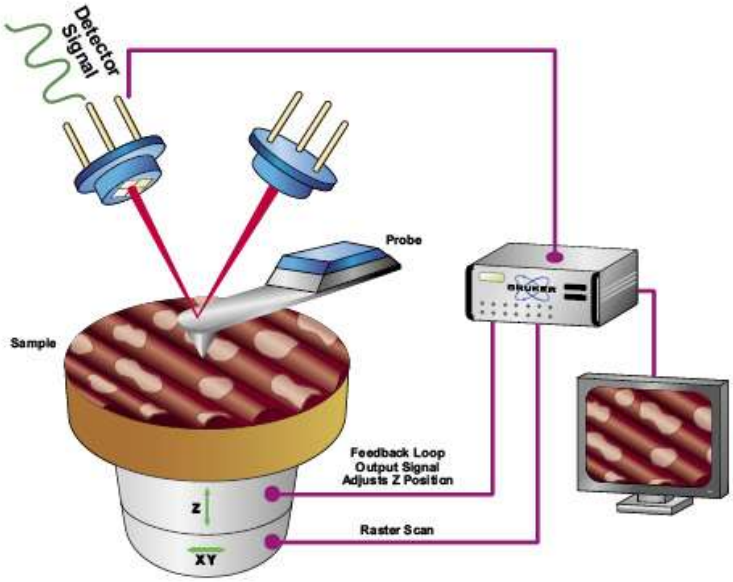

Figure 2.6: Schematic diagram showing the basic components of contact mode atomic force microscopy. Here, the piezo-scanner is mounted under the sample stage. Alternatively (or additionally) the piezo-scanner can be mounted on the AFM probe. Adapted from Bruker.

To control the force applied by the tip to the sample a feedback loop is used to ensure the tip tracks the surface. The feedback circuit uses the real-time cantilever deflection signal (measured in voltage by the photodiode) as an input and attempts to keep the cantilever deflection to a user-defined value by changing the voltage applied to the Z-direction piezo-scanner thus changing the tip-sample separation distance. This regulates the applied force generated by the AFM probe on the sample and allows this force to be minimized, which is useful in preventing damage to soft biological samples (and the tip). In addition, this feedback in the relative change in height of the sample is used as the signal for generating an AFM height image (topography map). The sensitivity of the feedback loop can be controlled by user-

defined settings known as the integral and proportional gain, correcting for either the errors or proportional difference in cumulative height, respectively.

2.4.3 Modes of operation

The original mode of AFM operation is Contact Mode (CM), in which the tip stays in physical contact with the sample whilst scanning. The two different methods of operating in CM are either by holding the probe at constant force or at constant height. During constant force mode the feedback loop maintains constant tip-sample interaction force by controlling the z-piezo. In this mode, the position of the z-piezo replicates the topography. In constant height mode no feedback loop is used and the cantilever is held at a constant level in relation to the surface. An image is then created from the cantilever deflection giving greater vertical sensitivity but at the expense of potentially large applied forces to any sample which is not very flat. In CM of AFM, the tip is always in contact with the surface which can create high shear (torsional) forces that could damage and deform the surface and, in some cases, sweep the sample off the surface. The relatively large shear forces applied on the surface can make CM unsuitable to image some sensitive, soft biological samples such as dispersed proteins. However, CM can be useful for imaging supported lipid bilayers which are often relatively flat (~1 nm) and laterally stabilised by hydrophobic forces.

In Tapping Mode (TM) of AFM the tip is oscillated in the Z-direction whilst still being raster scanned in the XY-directions across the surface (**Figure 2.7**); this greatly reduces shear forces and sample damage relative to CM. A sinusoidal voltage is applied to the piezo causing the tip to oscillate at its resonant frequency. When the tip is far from the surface, the piezo motion causes the cantilever to oscillate with a high amplitude (~ 20 nm). As the tip is moved towards the surface it begins to lightly touch or “tap” the surface and the cantilever oscillation is reduced due to energy loss. The reduction in oscillation amplitude is used to identify and measure the surface features. The feedback loop attempts to maintain a constant cantilever amplitude by moving the cantilever further from or closer to the surface so that the TM imaging force is maintained at a user-defined level.

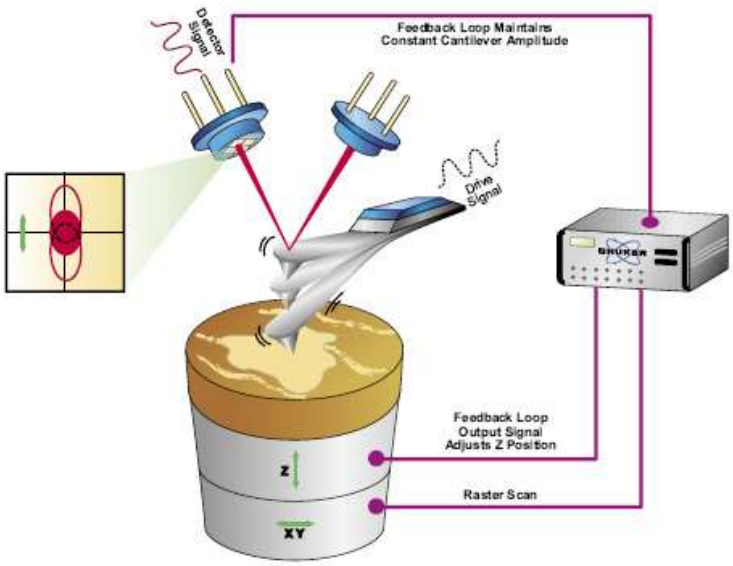

Figure 2.7: Schematic diagram showing the basic components of tapping mode atomic force microscopy. Adapted from Bruker.

A more-recently developed imaging AFM mode is Peak Force Tapping (PFT) mode (**Figure 2.8**), where the cantilever is sinusoidally oscillated close to the sample but well below the resonance frequency. Interactions between the probe and the sample (i.e. Van der Waal forces, or adhesion) result in changes to the tip deflection and the measured signal, which is measured as a force-distance curve as the probe approaches and withdraws from the surface. One major advantage of PFT as compared to TM is the direct force control over every approach-retract cycle, with feedback over the real-time force applied. Additionally, a multitude of material properties can be extracted and quantified from the force-distance curve at each pixel within an image, such as modulus, adhesion force, and deformation depth. In PFT, the oscillation of the probe is significantly slower compared to standard TM and results in more gentle tapping forces and less damage to the sample, at the cost of a slower imaging technique compared to TM/CM.

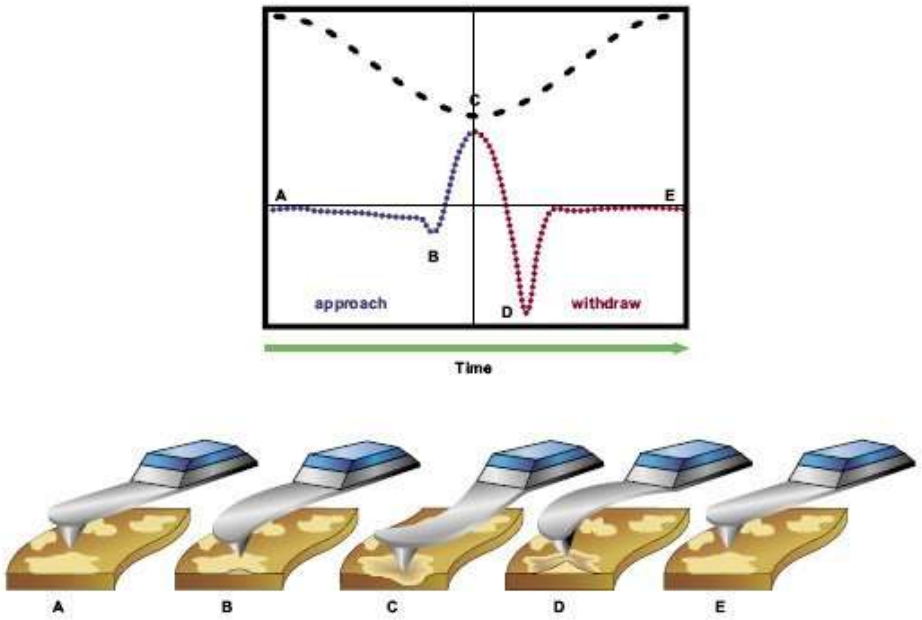

Figure 2.8: Schematic diagram showing the trajectory of the probe (*black dashed line*) during peak force tapping measurements. Each tip approach and withdrawal generates a force distance curve (*blue/red, dashed line*) that can provide mechanical information about the sample alongside topography measurements. Adapted from Bruker.

3 Experimental protocols

This chapter documents the experimental procedures used and developed within the thesis and gives details of the samples and substrate preparation used. Protocols throughout the rest of the thesis are as described here, unless specifically stated in subsequent chapters.

3.1 General protocols

3.1.1 Materials

All solvents and chemical solids were purchased from Sigma-Aldrich, unless otherwise stated. Solvents were Bio-Ultra analytical grade or higher, and chemical solids were HPLC grade or higher, unless otherwise stated.

3.1.2 Standard Buffers

All water used was deionized and filtered by a milli-Q water purification system (Millipore). All buffers were initially prepared as concentrated stock solutions, typically a 50 mL volume at 1 mole/litre (M), by weighing solids to a 1 mg precision and dissolving in ultrapure water to be within <1 % difference of the intended concentration. Stock solutions were stored at 4 °C for up to 3 months. For each experiment, buffers were prepared by diluting the concentrated stocks in with milliQ water to achieve the desired concentration. Buffers were purified through 0.22 µm filters using syringes before use and typically stored at 4 °C for up to a week. pH-fixed buffers were prepared to be within 0.1 of the intended final pH by the dropwise addition of 1-10 M hydrochloric acid or sodium hydroxide.

3.1.3 Preparation of hydrophilic substrates

Hydrophilic glass was prepared by incubating glass coverslips (#1.5 thickness) in “piranha solution” of 3:7 sulphuric acid (H_2SO_4) hydrogen peroxide (H_2O_2) for 30 minutes, followed by copious rinsing with milliQ water. Glass coverslips were used within 5 days of cleaning by removing the substrate from the water with clean tweezers, and drying with nitrogen gas flow.

3.2 Protein biochemistry

3.2.1 LHCII isolation and purification

Trimeric LHCII complexes were biochemically purified directly from spinach leaves using a previously established procedure by Hancock et al.[98], adapted from the procedures of the Johnson group[56]. Briefly: leaves were macerated using a blender, chloroplasts were osmotically lyzed and then thylakoid membranes solubilized with 0.5 % n-dodecyl α-D-maltoside (α-DDM ≥99 % purity, Generon). Thylakoid membrane proteins were isolated using continuous sucrose density gradients in 20 mM HEPES pH 7.5, 0.03 % α-DDM (8-13 % w/w sucrose) and ultracentrifuged at 100,000 g for 36 hr, 4 °C. The dense green band of LHCII trimers was collected and concentrated using a 30 kDa Amicon Ultra centrifugal filters (Merck Millipore, UK). LHCII trimers were further purified using high-resolution size exclusion chromatography using a 16/600 Superdex 200 prep grade column and an AKTA Prime FPLC system (GE Healthcare Life Sciences, PA, USA) in the buffer 150 mM NaCl, 0.03 % α-DDM, 20 mM HEPES (pH 7.5). Appropriate eluted fractions were pooled and concentrated. Finally, LHCII trimers were at a concentration of approx. 100 nM, corresponding to an absorbance of ~20 at 675 nm estimated by absorption spectroscopy, in a final buffer of 20 mM HEPES (pH 7.5) and estimated 0.3 % α-DDM. SDS-PAGE and Native-PAGE confirmed protein purity and oligermisation state. **Note on contributions:** All LHCII isolation and purification was performed and characterised by A. M. Hancock.

3.2.2 Preparation of extracted thylakoids

Thylakoid membranes were isolated from spinach (*Spinacia oleracea*) as described by Morigaki and co-workers.[162] Briefly, this involved macerating leaves at 4°C, disruption of the chloroplasts by passing them through a high-pressure vessel and recovery of thylakoid membranes in an aqueous buffer (50 mM KH_2PO_4, 10 mM NaCl, 2 mM $MgCl_2$, 330 mM sorbitol, pH 7.5). Absorption specstropy confirmed that the membranes contained the expected optically-active proteins (LHCII, PSII, PSI, see section 4.2.2). These “extracted thylakoids” were used to form hybrid membranes within a few days or were flash-frozen with liquid nitrogen and stored

at -80°C. **Note on contributions:** Thylakoid extracts were prepared in Kobe by members of the Morigaki group and shipped to Leeds.

3.3 Formation of model lipid membranes

3.3.1 Lipid preparation and storage

Plant thylakoid lipids monogalactosyldiacylglycerol (MGDG), digalactosyldiacylglycerol (DGDG), sulphoquinovosyldiacylglycerol (SQDG) and the synthetic lipid 1,2-dioleoyl-sn-glycero-3- phosphocholine (DOPC) were purchased from Avanti Polar Lipids as lyophilized solids (received as ampules sealed under dry nitrogen). The fluorescently-tagged lipids Texas Red 1,2-dihexadecanoyl-sn-glycero-3-phosphoethanolamine (TR-DHPE), 1,2-dipalmitoyl-sn-glycero-3-phosphoethanolamine-N-(7-nitro-2-1,3-benzoxadiazol-4-yl) (NBD-DHPE) and N-(4,4-Difluoro-5,7-Dimethyl-4-Bora-3a,4a-Diaza-s-Indacene-3-Propionyl)-1,2-Dihexadecanoyl-sn-Glycero-3-phosphoethanolamine (BOD-DHPE) were purchased as a solid from Life Technologies (Invitrogen), Avanti Polar Lipids and Thermo Fischer Scientific, respectively (received as ampules and sealed under dry nitrogen). Lipid mixtures was prepared by solubilising dry lipids in chloroform to a known concentration, and mixing the required volumes of the lipid-chloroform solutions to obtain the desired ratios and mass for sample formation. Fluorescently-tagged lipids were dissolved in chloroform and added as required to aliquots of lipid mixtures before drying. Solubilised lipids were then subsequently dried under dry nitrogen gas flow for 40 min and then placed in vacuum desiccator for 3-12 hrs to remove any residual traces of solvents (room temperature, in the dark). Lipid aliquots were then either used immediately or stored under argon gas at -80 °C until use. Single-use glass vials were used throughout when working with lipids in organic solvents.

3.3.2 Liposome formation

Aliquots of dry lipid mixture were solubilised in a buffer solution of 20 mM HEPES (pH 7.5), 40 mM NaCl to reach a final lipid concentration of 1 mg/mL. Vortex mixing was applied to fully solubilise the solution until there is no visible lipid film in the vial and the solution is turbid. The lipid solution was then loaded into a temperature-controlled glass sample holder (pre-cooled to 4 °C) and tip sonicated for 20 minutes at 20 % power (Sonifier 250, Branson, USA) to form small unilamellar vesicles. To

remove titanium residue from the sonicator tip, samples are centrifuged at 10,000 g for 3 min before the supernatant (liposome solution above the precipitated solid) was transferred into fresh vials and used for further characterisation.

3.3.3 Proteoliposome formation

Proteoliposome samples were formed containing either DOPC lipids or a thylakoid lipid mixture that was comprised of 35 % MGDG, 20 % DGDG, 12 % SQDG, 8 % Soy-PG and 25 % DOPC (% wt/wt), adapted from Grab et al[163], as specified in subsequent chapters. Aliquots of dry thylakoid lipid mixture ("Grab mix" as prepared above) or DOPC lipids where specified were solubilised with 0.5 % α-DDM, 20 mM HEPES (pH 7.5) at room temperature for approximately 12-16 hours with agitation via a pinwheel rotator to generate a mixed micellar lipid-DDM solution (approx. 9:1 molar ratio of detergent-to-lipid). For example, typically 0.4 mL of this buffer would be added to 1 mg DOPC to give approx. 2.5 mM DOPC and 22 mM DDM in final volume of 0.4 mL (lower masses of thylakoid lipids were often used due to their cost and a lower final volume). The starting protein-lipid-detergent suspension was prepared in plastic microfuge tubes by mixing calculated volumes of the following: the pre-solubilized lipid-DDM suspension, aqueous buffers, and purified LHCII trimers to a final concentration of: 1 mM total lipid, 0.2 % α-DDM, 20 mM HEPES (pH 7.5), 40 mM NaCl and the desired LHCII concentration. The desired LHCII concentration was achieved by calculating the volume of isolated LHCII trimers required to reach a defined lipid-to-protein (mol/mol) ratio for each sample (with molar concentration of lipids calculated from known masses and molecular weights and LHCII protein concentration determined from absorption as stated above). The lipid-DDM-protein mixture was then incubated with Bio-Beads SM-2 Adsorbents (Bio-Rad) to gradually remove the detergent and allow proteoliposome formation via self-assembly, as follows: four incubation cycles with increasing quantities of fresh Bio-Beads (8 mg/mL, 20 mg/mL and 40 mg/mL and 100 mg/mL) for 90 min, 90 min, 90 min, and ~16 hours, respectively. Proteoliposome samples were prepared in parallel, typically in sets of 5 to 7 samples, stored in the dark at 4 °C when not in use, and diluted samples from these immediately were characterised by ensemble spectroscopies (within 16 hours) and by microscopies (within 24-72 hours). Sample volumes were varied based on the required quantity of material needed (generally governed by the characterisation to be performed), typically

volumes of 300-500 µL were used to allow good mixing of BioBeads in the detergent removal stage and provide enough volume to be diluted for both cuvette based spectroscopy and microscopy. Samples were diluted by the desired factor for the characterization method, typically using a buffer solution of 20 mM HEPES (pH 7.5) 40 mM NaCl, unless any other additives were required.

3.3.4 Formation of supported lipid bilayers

Supported bilayers were formed on hydrophilic glass by pipetting a droplet of liposome solution onto the surface at a desired lipid concentration (typically within the range of 0.2 to 0.5 mg/mL). An "open-droplet" sample geometry was maintained by using either "multi-well" ultrathin adhesive spacers (Grace Bio-Labs) or a custom-built flow chamber or an OEM sample holder. After 20 minutes, samples were then washed into milliQ-water with at least 10 changes of the sample buffer to remove any loosely adsorbed liposomes (pure water has previously been reported to help rupture liposomes through a process of osmotically stressing the liposomes) before being washing into the imaging buffer to maintain a consistent pH and to keep characterisation conditions consistent between different measurements.

3.3.5 Preparation of polymerised lipid templates and hybrid membranes

The polymerized lipid templates were prepared by collaborators at the University of Kobe, as described in several previous publications.[134, 164] Briefly, lipid bilayers of 1,2-bis(10,12-tricosadiynoyl)-*sn*-glycero-3-phosphocholine (Diyne-PC) were deposited onto substrates by vesicle spreading and then polymerization was conducted by UV irradiation using a mercury lamp, using very careful control over power delivered, process temperature and presence of oxygen. Substrates patterned with polymerized Diyne-PC could be stored in water for weeks at room temperature. Immediately before use, patterned substrates were dried with nitrogen and placed into a microscopy sample holder as desired (as above, either adhesive imaging spacers or the AFM OEM coverslip holders). **Note on contributions:** Polymerized Diyne-PC templates were prepared in Kobe by members of the Morigaki group and shipped to Leeds.

3.3.6 Formation of hybrid or patterned membranes in polymerised lipid templates

Hybrid membranes were formed by incubating a mixture of extracted thyalkoids and DOPC liposomes on polymerized Diyne-PC templates. First, extracted thylakoids and DOPC vesicle suspensions were combined in a lipid ratio of 1:1 (w/w) unless otherwise stated. DOPC (0.5 mM) is 0.393 mg/mL (MW = 0.786 g/mol). 1 mg Chl/mL is equal to 3.524 mg lipid/mL,[165] therefore 0.165 mg Chl/mL is 0.68 mM. The thylakoid/DOPC suspension was added to the substrate at a final concentration of 0.68 mM DOPC. After 30 min incubation, samples were rinsed with copious buffer solution and were ready for microscopy. Patterned lipid-only membranes were formed by incubating a solution of DOPC liposomes, containing a small percentage (typically 0.5 % (w/w)) of lipid-tagged fluorophores, on polymerized Diyne-PC templates. The liposome solution was diluted to a final concentration of 0.5 mg/mL, using an open droplet, a 20 minute incubation, and rinsed with milliQ followed by copious amounts of buffer solution.

3.4 Experimental protocols for sample characterisation

3.4.1 Fluorescence spectroscopy

All cuvette-based steady-state fluorescence spectroscopy on proteoliposomes was performed using an Edinburgh Instruments FLS980 fluorescence spectrophotometer equipped with dual excitation monochromators and dual emission monochromators. Samples were maintained at 20 °C and gently stirred at 500-1000 rpm during all measurements using a thermoelectrically-cooled cuvette-holder with magnetic stirring capabilities (Quantum Northwest TC 1 Temperature Controller). A 450W Xenon arc lamp was used for excitation and a red-sensitive-PMT for detection (Hamamatsu R928 PMT). Emission scans with selective excitation of LHCII were acquired with excitation at 473 nm, collecting emission between 500-800 nm (2 nm and 1 nm bandwidth excitation and emission slits, respectively). Emission scans with selective excitation of Texas Red were acquired with excitation at 540 nm, collecting emission between 550- 800 nm (1 nm bandwidth for both excitation and emission slits). Data acquisition parameters were 0.5 nm steps, integrating 0.1 s/ step and five scans averaged for all samples. All ensemble

spectroscopy data were further analysed in Origin Pro (v.9) graphing software. **Note on contributions:** All cuvette-based fluorescence spectroscopy data was collected and analysed by A. M. Hancock

All cuvette-based time-resolved fluorescence spectroscopy (TCSPC) measurements of LHCII in detergent and LHCII proteoliposomes were made using the Edinburgh Instruments FLS980 fluorescence spectrophotometer, described above. Samples were maintained at 20 °C and gently stirred, as above. A 473 nm pulsed diode laser (EPL-475, pulse width of ~100 ps) was used for selective excitation of LHCII, collecting emission at 681 nm with 10 nm bandwidth emission slits. A laser repetition rate of 0.5 MHz was always used. A dedicated high-speed red-sensitive PMT was used for detection (Hamamatsu H10720-20 PMT). A built-in ND filter wheel was applied to the pulsed laser for LHCII lifetime measurements to set excitation power as desired, an average power of approximately 1.5 μW for LHCII (pulse energy of 3.0 pJ). Control measurements for excitation power versus fluorescence lifetime showed that singlet-singlet annihilation effects are likely to be avoided using these settings. Decay curves from the Edinburgh FLS980 system were fitting using the manufacturer's supplied software. The instrument response function (IRF) was determined by measuring scattered excitation light using a dilute solution of colloidal silica (Ludox, MilliporeSigma) and has a FWHM of ~270 ps.

All cuvette-based TCSPC measurements of lipid tagged fluorophores in solvents, detergent and proteoliposomes were made using a Horiba PTI Quantamaster 8000 fluorescence spectrometer equipped with a higher power supercontinuum 75 W excitation laser (pulse width of ~100 ps). This was because the 560 nm laser available for the Edinburgh system was an LED (not a "true" laser source) which had relatively low power and relatively broader pulse; we found that the Quantamaster instrument produced higher quality data. Samples were maintained at 20 °C and gently stirred. The acquisition parameters were: 0.5 MHz laser repetition rate, excitation set to 540 nm (1 nm slit) and emission collected at 610 nm (5 nm slit) with a dedicated PPD-900 PMT detector. Decay curves from the Quantamaster system were fitted using open source DecayFit TCSPC analysis software. The IRF was determined, as above, to have a FWHM of ~225 ps. **Note on contributions:** All

cuvette-based fluorescence TCSPC data was collected and analysed by A. M. Hancock (all FLIM TCSPC data was collected S. A. Meredith).

3.4.2 Absorption spectroscopy

All cuvette-based absorption spectroscopy for proteoliposome samples were performed using an Agilent Technologies Cary 5000 UV-Vis-NIR absorption spectrophotometer equipped with an "integrating sphere" (also called a Diffuse Reflectance Accessory, Agilent) to remove any minor scattering effects. Absorbance scans were taken with a wavelength range of 380-800 nm, 0.5 nm step size, 0.5 s dwell time. 'Blank' measurements of the absorbance of buffer-only samples to be automatically subtracted from sample absorption spectra were made before each set of measurements were taken. **Note on contributions:** All absorption spectroscopy data was collected and analysed by A. M. Hancock.

3.4.3 Epifluorescence microscopy

Epifluorescence microscopy was performed using a Nikon E600 microscope equipped with a Andor Zyla 4.2 sCMOS detector and appropriate filter cubes (LHCII cube: excitation 450-475 nm, dichroic 500 nm, emission 650-800 nm; Texas Red cube: excitation 540-580 nm, dichroic 595, emission 600-660 nm). Images were taken using a ×40 air objective (NA 0.6), 500 ms exposure and with appropriate ND filters inserted to maintain the maximum number of counts at a level for good detector signal-to-noise and linearity (10-75 % of detector saturation). Two-channel imaging (Texas Red + LHCII) of a field of view was performed sequentially by switching between cubes and ND filters as appropriate.

3.4.4 Fluorescence lifetime imaging microscopy

FLIM was performed using a Microtime 200 time-resolved fluorescence microscope (PicoQuant GmbH). This system used an Olympus IX73 inverted optical microscope as a sample holder with light passing into and exiting various filter units for laser scanning, emission detection, and timing electronics. Excitation lasers were driven in pulsed interleaved excitation mode by a PDL 828 Sepia II burst generator module. The pulse width for the LDH 485 nm, LDH 561 nm, and LDH 640 nm lasers were 90, 70, and 90 ps, respectively. Detector 1 was a single-photon avalanche diode and detector 2 was a hybrid photomultiplier tube. The instrumentation is described in

detail in section 2.3. Specific dichroic mirrors and emission filters, as described in each chapter, were used to define the emission channel wavelength range. Analysis of all FLIM data was performed with SymPhoTime software (PicoQuant). The mean amplitude-weighted lifetime of images or specific objects, 〈τ〉, was calculated by generating fluorescence decay curves from accumulated photons, and then modelling the curve as a multiexponential decay function (excellent fits were achieved for all data, with chi-squared values <1.1 and low residuals).

3.4.5 Fluorescence recovery after photobleaching measurements

Fluorescence recovery after photobleaching (FRAP) experiments were performed using the epifluorescence microscopy described in section 3.4.1 or FLIM microscope described in section 3.4.2. Images were taken of the sample area immediately (e.g., 30 s) prior to photobleaching, before an aperture was inserted between the sample and the excitation source to expose an approx. 30 μm diameter region of the sample. This region was then exposed to bright excitation (typically white light) for a continuous period of 30 s to photodamage the fluorophores in that region. Immediately after photobleaching, full-field (aperture removed) images were acquired over a series of sequential timepoints to visualize the effect of fluorescence recovery of the bleached area. Analysis of FRAP data is described in the relevant chapters.

3.4.6 Atomic force microscopy

Standalone AFM was performed under aqueous buffers using a Bruker Dimension FastScan and PEAKFORCE-HIRS-SSB probes (Bruker AFM Probes) in Peak Force Tapping mode. Parameters were optimized while imaging to minimize applied forces of <0.2 nN, typically scanning at 2–4 Hz and 1024 × 1024 pixels. Topographs were processed and analyzed using Nanoscope Analysis Software (v1.9).

3.4.7 Combined FLIM and AFM

For combined FLIM+AFM, the AFM imaging used a JPK NanoWizard 4 driven by a Vortis Advanced control station. The FLIM lasers and optics were as described in section 3.4.2. The FLIM laser and AFM probe were initially coarsely aligned by observing the laser position and AFM probe in the eyepiece of an overhead Olympus IX73 inverted optical microscope. To improve the alignment the AFM probe was

scanned through the FLIM laser volume, such that light scattered from the AFM was detected by the FLIM optics to generate an image of the AFM probe “as seen by” the FLIM. Using this image, the position of the AFM probe was selected such that the FLIM laser and apex of the probe were within <1 μm. With the two systems aligned, the sample was placed on a JPK Tip-Assisted Optics stage which was used in a sample-scanning configuration, so that the FLIM laser and AFM probe remain in a fixed position and that the sample moved relative to both. This ensured that once the FLIM laser spot and AFM probe were aligned they remained in a fixed position to ensure consistent correlation between the two systems and minimal noise. Any misalignment (due to imaging forces or thermal drift) was monitored and corrected by repositioning the AFM probe in between measurements.

4 Hybrid membranes as a model platform to interrogate the photophysics of light-harvesting proteins

4.1 Introduction

The interaction between the photosynthetic machinery relies heavily on protein arrangement and the surrounding superstructure of the thylakoid lipid membrane.[166] In the native system, LHCII and PSII proteins are organized into "supercomplexes" which are located within stacked membranes, called "grana" (see **Figure 1.1**).[52] The overall stacked membrane arrangement provides a large surface area for incorporating many hundreds of pigments, creating a wide spatial and optical cross-section (>100 nm) for the absorption of sunlight. These grana are not static structures and dark-to-light transitions have been shown to profoundly alter the thylakoid membrane architecture (the grana diameter and number of layers is reduced in high light) and the macromolecular organization of photosynthetic complexes[17]. This structural reorganization is believed to modulate the efficiency of light-harvesting and energy transfer to the photosynthetic reaction centre, thereby protecting the reaction centre from long-term damage (photoinhibition) caused by a build up of harmful excitation energy. [39, 55, 56, 61, 66, 79, 106]

After decades of intense debate, it is now widely accepted that energy migration and photoprotective quenching (the harmless, non-radiative dissipation of energy) is modulated by the light-harvesting antenna, LHCII.[39-41] In intact chloroplasts, extracted thylakoid membranes and in model systems (e.g. LHCII aggregates and proteoliposomes), LHCII has been shown to undergo concentration-dependent quenching, manifesting as a reduced fluorescence emission and lifetime, apparently based on the extent of LHCII-LHCII associations[54, 55]. Despite this, there is still no consensus about the intra/inter protein interactions that lead to LHCII aggregation or relaxation in high or low light, respectively. Various studies have suggested that excess light results in an accumulation of a transmembrane pH gradient generated by photosynthetic electron generation[40-42] which activates interactions between

LHCII/carotenoids[41, 43-45]. The pH gradient may also trigger the protonation of the PbsS protein and leading to their dissasociation from PSII and aggregation within the membrane[46-49]. In addition to these pH driven changes, there is speculation around the exact mechanism that forms the LHCII quenched state and how these quenched states may operate within a complex network of LHCII and PSII super-complexes. A combination of some, or all, of these factors, and the resulting organisation of LHCII and PSII may be responsible for the modulation of energy migration and electron transfer across membranes.[75, 167, 168]

A particular challenge of photosynthetic research is to isolate each of these effects whilst still providing biological insight. Electron microscopy is a powerful tool that has been used to study the high-resolution structure of photosynthetic membranes *in situ*[8, 11, 53, 169]; however, it cannot usually be performed on hydrated samples at room temperature or used to investigate dynamic processes. Alternatively, AFM allows the visualisation of LH and PS protein complexes at relatively high resolution (~1 nm laterally and ~0.1 nm vertically) and can measure membrane samples under close-to-native conditions (i.e. ambient temperature and aqueous environment).[17, 72, 73, 170] AFM and fluorescence spectroscopy performed on thylakoid membranes, which have been extracted from chloroplasts onto a flat, solid surface such as mica or glass, has been used to increase our understanding of the interactions within the native system.[17, 72] However, isolated or fragmented natural membranes are not always an ideal platform to test system functionality because of their unstable nature, lack of control over membrane composition and the challenges associated in interpreting specific effects in a heterogeneous system.

Simplified model systems have also been used as an alternative to investigate photosynthetic behaviour. Interactions between LH proteins have been studied utilizing nanoscale array patterns of proteins on solid surfaces[80, 171, 172] and LH proteins incorporated into model membranes (proteoliposomes).[74, 79, 98, 119, 121, 173, 174] These model systems offer several advantages as platforms to study the inherent physicochemical properties of the proteins, such as providing precise control over protein arrangement, known membrane composition and the incorporation of specific lipids to help maintain protein stability.[120, 121] In addition, many of these platforms are accesible to fluorescence lifetime measurements that provide

information on the photophysical properties (i.e. energy dissipation and transfer) of the proteins. However, many of these models require extensive biochemical purification, chemical alteration of the protein or the support surface, and, or, removal of the native lipids, any of which may affect the stability and photophysical state of LH and PS proteins.[74, 129-131] Furthermore, these models are often limited to one or two types of protein which simplifies the complex interactions that are present in the native system, because of the procedural challenge of reconsituting multiple types of purified protein into a single artificial lipid membrane.

Therefore, there is a compelling need for a thylakoid membrane model that has an intermediate level of complexity: consisting of the full range of proteins found in the native thylakoid membrane, but with a greater control over membrane composition and amenability to fluorescence and structural microscopy. An ideal model system for the study of photosynthetic membranes would consist of a stable membrane on a solid support which contains the complete network of photosynthetic proteins embedded within a bilayer comprised of a native-like mixture of lipids. Very recently, our collaborators in the Morigaki group presented a solution through a new type of "hybrid membranes" by incorporating thylakoid components (see **Figure 4.1.a**) into supported lipid bilayers (SLBs) within an array-patterned template.[162] The empty templates were formed from photo-polymerized diacetylene-phosphocholine (Diyne-PC) lipids (**Figure 4.1b**), and have exposed lipid bilayer edges (see **Figure 4.1c-d**), which promote the formation of hybrid membranes from the combination of synthetic lipid vesicles and natural thylakoid membrane.[134, 164, 175, 176] The result is an array of discrete, high-quality SLBs that are patterned into easily recognizable micro arrays to allow for more accurate analysis.[135-137] These hybrid membranes could provide a model system to understand the photophysical and biochemical processes of photosynthesis and to inspire the design of new nanotechnologies.[177-179] However, the previously published characterization of this model[162] used simple epifluorescence microscopy to visualize the membranes at microscale resolution and did not resolve information about the nanoscale membrane structure or photophysical state of the system. To be able to use this platform as a testbed for further investigations, a crucial next step is to understand the structural arrangement and interactions between proteins

within the membrane and how this relates to their photophysical properities (manifested as a change to the fluorescent lifetime).

This chapter presents a quantitative characterisation of the nanoscale structure and photophysical properties of photosynthetic hybrid membranes using fluorescence lifetime imaging microscopy and atomic force microscopy. To test the efficacy of this platform, the following questions were addressed: (i) What is the nanoscale structure of the hybrid membranes compared to natural thylakoid membranes? (ii) How does the fluorescence lifetime of the hybrid membranes compare to the natural thylakoid membranes? (iii) What is the protein concentration of the hybrid membranes relative to the native system? (iv) How do thylakoid proteins diffuse and reorganize within the membrane? (v) Can the platform be used for more effective functionality assays of the photosynthetic activity (electron transport)? In addition to characterizing the final form of the hybrid membranes, we visualize the membrane formation to measure the migration of lipids and proteins in real-time.

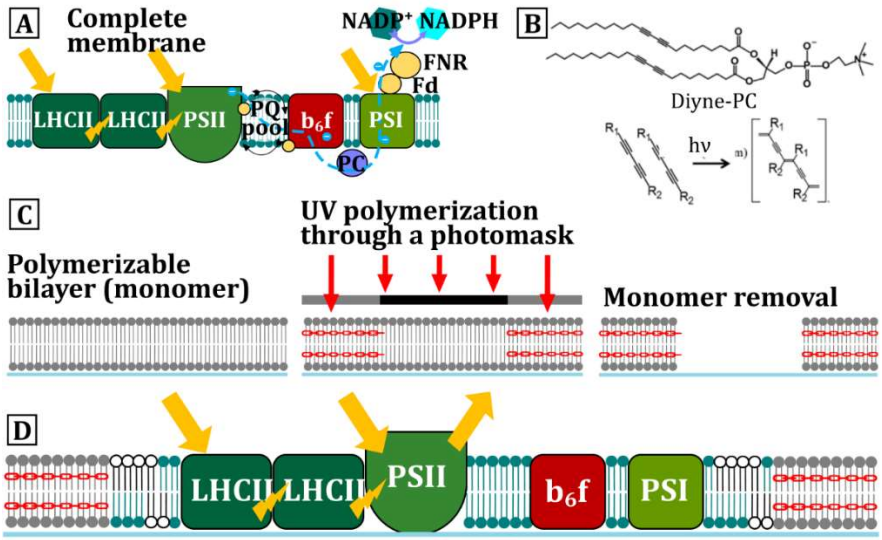

Figure 4.1. Concepts for designing model LH membranes, as reported recently.[162] **(A)** Schematic of the natural thylakoid membranes and the energy transfer processes occurring. *Yellow arrows* represent absorption of light, *yellow bolts* represent inter-protein excitation energy transfer and *blue dashed lines* represent the electron transfer chain (simplified). **(B)** Chemical structure of the Diyne-PC and the photo-polymerization reaction. **(C)** Schematic of the how photo-polymerization is carried out through a photomask to generate array patterns, where only the regions of Diyne-PC exposed to UV become crosslinked (*red linkers* indicate polymerized lipids). **(D)** Schematic of the "hybrid membranes" within the polymer-lipid template.

4.2 Characterisation of extracted thylakoids

4.2.1 The excitation fluence of FLIM measurements is optimised to prevent lifetime artefacts

Prior to any characterisation of photosynthetic samples, it was necessary to ensure that the parameters selected for FLIM measurements did not introduce lifetime artefacts into our analysis of photosynthetic samples. Singlet-singlet annihilation (SSA) is a mechanism of fluorescence quenching induced by Förster-type energy transfer between two fluorophores while they are both in their first excited singlet state (S1S1), and may result in the unintentional truncation of the fluorescence lifetime, and misinterpretation of the photophysical properties of photosynthetic systems, or a sub-optimal fluorescence signal. SSA is very likely to occur in photosynthetic light harvesting complexes,[180] due to the high density of pigments within photosynthetic proteins, and the probability of SSA is increased by increasing the concentration of excitons (or exciton flux) within the system, e.g. by increasing the intensity of exciting light.[26, 181] Therefore, it was necessary to de-couple effects of SSA or to limit experimental parameters to a regime where SSA is unlikely to occur.

Experiments were performed to select an appropriate excitation fluence for future protein measurements, and to characterise the extent of annihilation at a range of other fluences. To quantify SSA in photosynthetic systems, multiple FLIM measurements of LHCII trimers in a variety of aggregated states were obtained using a wide range of excitation fluences above and below the level where SSA was expected to occur (0.001 mJ/cm^2 to 0.373 mJ/cm^2). Since SSA within LHCII trimers is not the focus of this thesis, this series of experiments is described in full in **Appendix 1**. We find that the fitted fluorescence lifetime of LHCII remained approximately constant (<10% variation) at fluences below 0.0026 mJ/cm^2, before rapidly decreasing at fluences above 0.0026 mJ/cm^2. The results show annihilation effects can occur within LHCII complexes, and may significantly alter lifetime measurements above a laser fluence threshold. After this series of experiments, a fluence of 0.0026 mJ/cm^2 was used for all subsequent FLIM measurements of the photosynthetic systems. This medium-low fluence was chosen to allow for the

collection of data with moderate speed and high signal, whilst also minimising the effect of SSA on the fitted fluorescent lifetimes. In subsequent sections, this series of measurements gives us a high confidence in the analysis of the fluorescence lifetimes, and subsequent interpretation of the photophysical state of LH and PS proteins in a variety of conditions.

4.2.2 Ensemble absorption and fluorescence spectroscopy of extracted thylakoids show that photosynthetic proteins were not denatured

Hybrid membranes are self-assembled from a mixture of synthetic lipids and thylakoid membranes that had been extracted from spinach (see methods section 3.3.6). Prior to using extracted thylakoid membranes to form our hybrid membranes, it was necessary to confirm that proteins within the thylakoid membranes were not denatured (i.e., in transit from our collaborators) and that the structure of these membranes was as expected (multi-layered membranes containing proteins in a native-like state). In addition, the characterisation of thylakoid extracts can then act as a baseline to compare to the photophysical and structural properties of the hybrid membrane system to those of a native-like system. This allows us to comment on the photophysical and topological differences, as well as experimental considerations such as sample stability and accessibility to microscopic techniques.

Spectral shifts in the absorption and emission of the thylakoid membranes could indicate damage/denaturation of the proteins, so a basic spectroscopy characterization was used to confirm that these samples contained the expected proteins (LHCII, PSII, PSI) and that there were no significant changes to the observed spectra. First, the absorption spectrum from biochemically-purified LHCII was measured to confirm the locations of characteristic absorption peaks as measured by our system and to provide a direct comparison to the absorption spectrum of extracted thylakoids. The LHCII absorption spectrum (**Figure 4.2**, *green dashed line*) shows a clear peak at precisely 675 nm and a lower intensity peak at precisely 650 nm, representing Chl *a* and Chl *b* Q_y transitions, respectively. The ratio of peak heights between Chl *a* and Chl *b* was as expected for LHCII and the subtle shoulder

at 475 nm is indicative of the trimeric form of LHCII. These peak wavelengths and intensities are in excellent agreement with previous reports of the optical properties of spinach LHCII[55, 56, 98, 182]. Gel electrophoresis of the purified protein showed the expected bands, as previously reported by our group.[56, 98]

By comparison, the extracted thylakoids absorption spectrum (**Figure 4.2**, *solid green*) is more complex, with contributions from LHCII, PSII and PSI. There is a peak centred at ~680 nm which is significantly broader than for LHCII and there is only a shoulder at ~650 nm, rather than a distinct peak. In summary, this spectrum is very similar to published reports for extracted thylakoids.[183] In detail, the well-established features of plant thylakoids, are explained by the following: (i) PSI and its antenna has maximal Chl *a* absorption at ~682 nm as compared to the PSII at a maximum of ~677 nm, explaining why this peak is found at longer wavelength compared to isolated LHCII alone, (ii) the PSI peak is known to extend further into the red due to its more numerous low-energy chlorophylls, explaining the observed broadening of the peak towards the red end of the spectrum, (iii) furthermore, PSII has much lesser Chl *b* than LHCII, and PSI has even less again, explaining the reduced peak at ~650 nm. This is in good agreement with reports by Caffarri and co-workers[183] and others. The extracted thylakoids fluorescence emission spectrum (**Figure 4.2**, *solid red*) has one major peak at ~682 nm and broad "red tail" between 700-750 nm represents emission from low energy Chl *a* (and its extended vibrionic manifold)[102, 184] indicating that the highly connected chlorophyll network across photosynthetic proteins has been maintained in the preparation of the "extracted thylakoids" sample, again, as we would have expected.

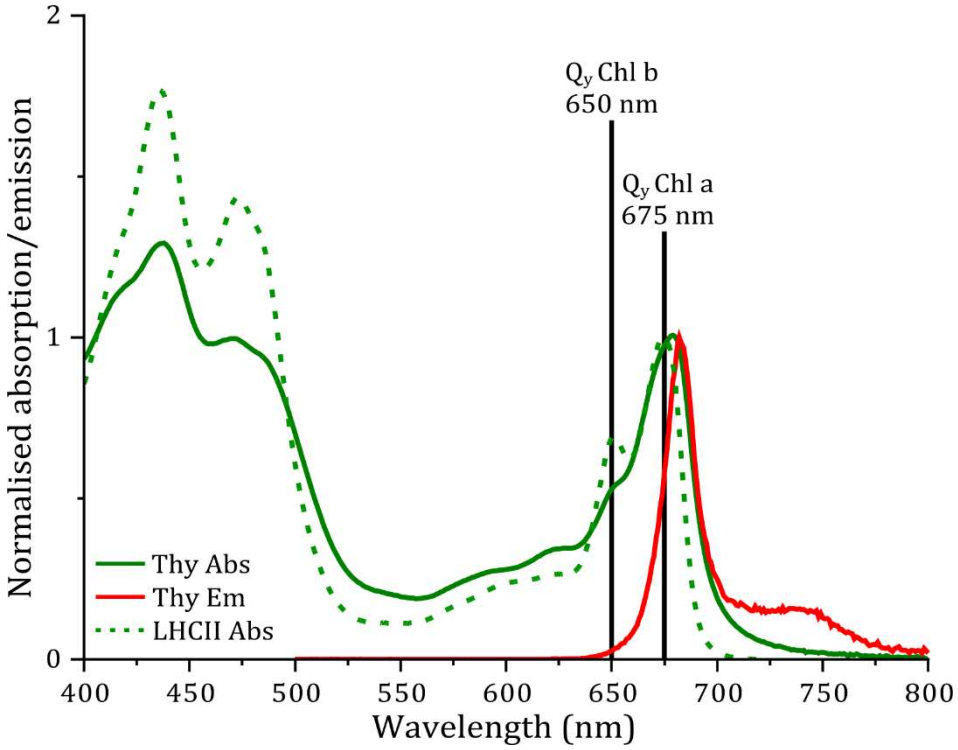

Figure 4.2: Emission (solid red) and absorption (solid green) data for extracted thylakoids and absorption data for LHCII (dashed green), normalised at 675 nm for clarity. Cuvette-based absorption spectroscopy was performed using an Agilent Technologies Cary 5000 UV-Vis-NIR absorption spectrophotometer. Cuvette-based fluorescence spectroscopy was performed using an Edinburgh Instruments FLS980 system, using excitation at 473 nm and collecting emission from 500-800 nm (2 nm and 1 nm bandwidth excitation and emission slits, respectively). The absorption spectra from both samples share some features, with similar peaks but at subtly different maximum wavelengths and with varying peak intensities. As expected, the overlapping peaks due to carotenoids and the chlorophyll Soret bands are found between 400-500 nm and the known Q_y bands for chlorophylls at 650-700 nm. Data collected by A. M. Hancock.

4.2.3 Extracted thylakoid membranes have short fluorescence lifetimes likely due to the presence of protein-protein interactions

To assess the photophysical state of proteins within the thylakoid extract, fluorescence lifetime measurements were used to quantify the degree of quenching from the excited state decay rate. The fluorescence lifetime of an excited state is shorterned as a result of energy dissipation and transfer,[185] and can therefore be used to infer the "photophysics state" (i.e. energetic processes) of the proteins and the energy pathways throughout the membrane. Tightly-packed LH proteins are known to have relatively short fluorescence lifetimes (~0.4 ns), likely due to protein-protein interactions, compared to non-interacting proteins that are known to have long fluorescence lifetimes (~4 ns).[56, 79] So changes to fluorescence lifetime may also provide information about the organisation of proteins within the membrane and interactions between proteins that occur at length-scales below the optical resolution of the FLIM. Fluorescence lifetime measurements, in combination with high resolution AFM topographs, were employed throughout the study to observe the structural arrangement of our membrane samples correlated to their photophysical properties. Specifically, a laser-scanning fluorescence microscope was used to acquire images (at ~300 nm resolution) where each pixel has both fluorescence intensity and a time-resolved fluorescence spectrum, termed "Fluorescence Lifetime Imaging Microscopy" (FLIM).[56, 80]

To make the extracted thylakoids accessible to imaging via FLIM and AFM, and to assess their initial structure and organisation, the extracted thylakoids were adhered to a hydrophilic glass coverslip by incubating a solution of extracted thylakoids in an open droplet on a hydrophilic glass substrate. **Figure 4.3a-b** shows representative FLIM images obtained from the chlorophyll (Chl) fluorescence of extracted thylakoids, revealing many distinct objects which all appear to have similar, quite short fluorescence lifetimes of ~0.5 ns. Note, all FLIM images have a colour scale with fluorescence lifetime represented from blue (short lifetime) to red (long lifetime) and an intensity scale representing the total counts in each pixel. Control measurements of "blank" buffer samples showed that there is minimal nonspecific fluorescence from any other sources or impurities, giving confidence in the detection of chlorophyll fluorescence even where the signal is low.

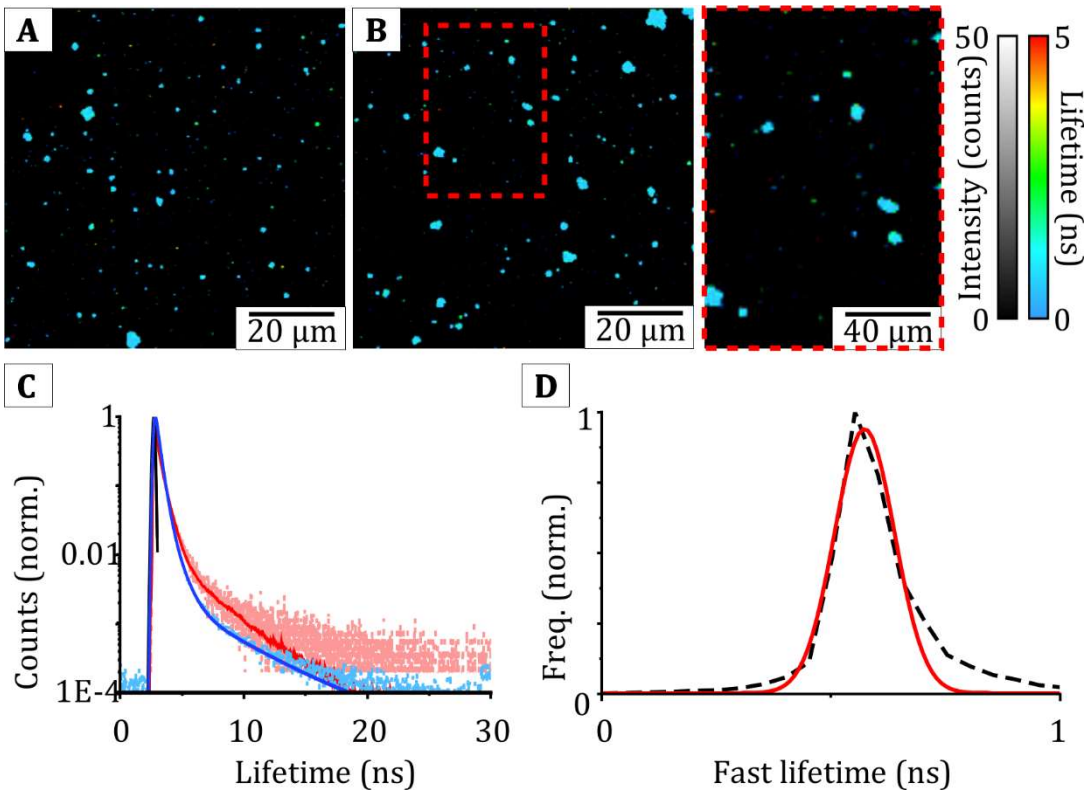

Figure 4.3: (A) + **(B)** Representative FLIM images of thylakoid extracts adsorbed onto hydrophilic glass. Small, disordered particles appear to be randomly adsorbed onto the surface, showing a short (*blue*) fluorescence lifetime. The *red, dashed* region in (B) shows an area of the sample at higher magnification. **(C)** Fluorescence decay curve obtained from extracted thylakoids. The *blue* curve shows the calculated decay curve fitted over raw, *light-blue, dashed*, data. $\langle\tau\rangle$ = 0.40 ± 0.01 ns from image (A) of extracted thylakoids adsorbed onto hydrophilic glass. The *red* curve shows the calculated decay curve fitted over raw, *light-red, dashed*, data. $\langle\tau\rangle$ = 0.5 ± 0.1 ns from time resolved fluorescence spectroscopy data of extracted thylakoids in solution. **(D)** The fastFLIM distribution (showing the average time between excitation and photon detection) for extracted thylakoids from image (A). The distribution is narrow and centred around 0.6 ns. To estimate the width of the fastFLIM distribution, a Gaussian curve (*red*) is fitted to the raw data (*black dashed*).

To analyse the Chl signal of thylakoid extracts quantitatively, a fluorescence decay curve was generated by accumulating the photons collected from the whole image (**Figure 4.3c**, *blue curve*): this reveals a mean fluorescence lifetime $<\tau> = 0.40 \pm 0.01$ ns (N = 5 images, 1000s of membranes "spots" per image). This lifetime is in good agreement with previous reports of LHCII and PSII within intact chloroplasts and leaves[186-188], and in approximate agreement with our ensemble spectroscopy data of the extracted thylakoids in solution, $<\tau> \sim 0.5 \pm 0.1$ ns, (**Figure 4.3c***, red curve*). This difference may be the result of quenching due to interactions between extracted thylakoids and the substrate, or some rearrangement of the membranes when they adhere to the surface. The fluorescence lifetime of proteins in thylakoids is much shorter than the lifetime known for isolated LH and PS proteins in detergent ($\sim$ 4 ns), as expected, and suggests the presence of protein-protein interactions, which are known to cause fluorescence quenching, within the membrane. In addition to the fitted fluorescence lifetime, the fast-FLIM histrogram (representing the distribution of the average delay between excitation and detection for each pixel in an image), shows a narrow distribution centred close to the fitted lifetime (**Figure 4.3d**, *black curve*). Fitting a Gaussian curve to this distribution (**Figure 4.3d**, *red curve*) yields a distribution centre at 0.6 ± 0.1 ns, with a FWHM of 0.10 ± 0.02 ns, showing that the lifetime of the extracted thylakoids is highly consitent within a field of view. This suggest that the protein concentration/interactions are consistent across all regions of the sample (variations in protein concentration/interactions would result in a broad range of photophysical states), and that thylakoid membranes are not disrupted when they adhere to the substrate. Overall, our FLIM data on thylakoids membrane samples agrees nicely with standard spectroscopy and shows that the "starting material" from which hybrid membranes are formed is of the expected quality.

4.2.4 Extracted thylakoids are topologically complex and difficult to characterise

Topographical maps of the thylakoids adhered to glass, measured by AFM, reveal that these objects have a heterogeneous size distribution. In a large field of view (**Figure 4.4a**), a variety of structures are observed, from relatively compact assemblies (100-200 nm laterally and 10-100 nm in height, *ringed green*) to large microscale structures (3-4 μm laterally and up to 750 nm high, *ringed blue*) which contain distinct multilayers. **Figure 4.4b** shows a multilayered structure, where height profiles (**Figure 4.4c**, *blue* and *red dashed*) has been drawn to show the increase in height over consecutive multilayers, up to ~300 nm above the underlying substrate. AFM topographs of areas that appears to contain only one membrane layer (**Figure 4.4d**) reveal a mottled surface topography containing multiple tightly packed globular particles that are ~10-20 nm in diameter. These dimensions are in reasonable agreement to the crystallographic dimensions of photosynthetic complexes[72], and suggesting that these particles are tightly packed photosynthetic proteins within the membrane, however, the precise dimensions of these particles were challenging to measure due to the instability of the adsorbed thylakoid extracts (multiple scans of the same area resulted in membrane damage), and the possibility that the particles may be oscillating within the membrane. Height profiles drawn across this single membrane layer (**Figure 4.4d**, *blue* and *red solid lines*), show a stepwise increase of ~30 nm from the substrate to the top of the membrane. PSII has a crystallographic height of ~10 nm,[72] so it is likely that even the smallest objects observed via AFM must consist of a few stacked protein-rich membranes, increasing up to tens of stacked membranes for the largest objects. The structures detected by AFM are consistent with the tightly stacked thylakoid grana membranes observed *in vivo*[47, 72], and the short fluorescence lifetime is also in agreement with that typically measured for native thylakoid membranes[186, 187]. The fact that such a heterogeneous and disordered distribution of randomly adhered membranes are observed, highlights the requirement for a method to promote the formation of large, homogeneous membrane structures that are suitable for quantitative studies and light-harvesting nanotechnologies.

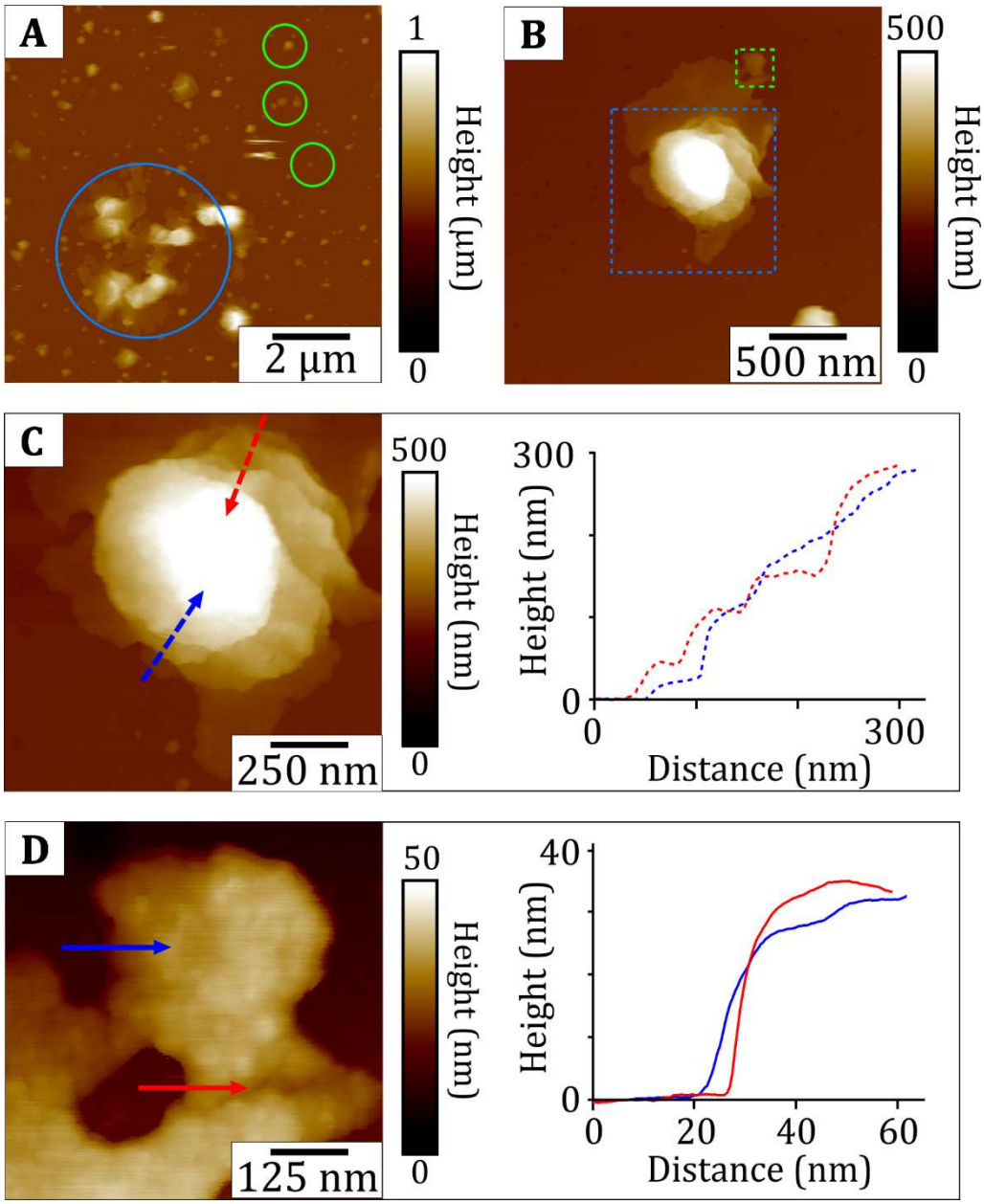

Figure 4.4: Multiple AFM images showing the distribution of extracted thylakoids and different structures within them. **(A)** AFM image of a similar sample as in **Figure 4.3a-b**. The topograph shows small, adhered membrane patches (*ringed green*) and larger multilayered structures (*ringed blue*). **(B)** A zoomed in topograph of a large multilayered thylakoid extract. **(C)** A zoomed in topograph of the *blue dashed* area in (c). Height profiles (*blue* and *red dashed*) are drawn across the multilayers, and shown in the adjacent graph. **(D)** A zoomed in topograph of the *green dashed* area in (b). Height profiles (*blue* and *red solid*) are drawn across the multilayers, and shown in the adjacent graph.

4.3 Characterisation of hybrid membranes

4.3.1 Extracted thylakoids and artificial lipids backfill patterned templates to form hybrid membranes with a long fluorescence lifetime

Hybrid membranes were prepared in a two-stage process. In stage 1, templates of polymerized Diyne-PC on glass coverslips were generated by photolithography by the Morigaki group, as previously published[162] and shown schematically in **Figure 4.1c**. The photolithogaphy generates a pattern based on the design of the photomask used; here, we chose a square-array grid pattern expected to produce an array of lipid bilayers with exposed edges providing large 20 × 20 μm corral regions of empty glass. In stage 2, natural and synthetic membranes were combined to fill the empty regions of the template and fuse with the exposed edges to form a corraled SLB. Specifically, Diyne-PC templates were incubated with an aqueous suspension of extracted thylakoids and synthetic lipid vesicles (DOPC), in a 1:3 weight/weight ratio, and the sample was washed with clean buffer solution.

To confirm that the patterned templates perfomed as expected, and resulted in well-defined hybrid membranes, FLIM measurements were performed on these samples before, and after, the templates were backfilled with hybrid membranes. The spectral and temporal selectivity of the FLIM instrument allowed for two separate FLIM channels: (i) the "Chlorophyll channel" defined as the combination of selective Chl excitation and a detector optimized for Chl detection, (ii) the "Template channel" optimized for the excitation and emission of the intrinsic fluorescence of the polymerized lipid template. Prior to hybrid membrane formation, FLIM measurements show the Diyne-PC template to be well-defined, with clear 20 × 20 μm corrals (containing no fluorescence emission) embedded as an periodic array within the surrounding polymerised bilayer (**Figure 4.5a**). There are few (negligible) counts in the Chl channel (**Figure 4.5b**) giving us confidence that the signal was due to the template alone and proving that the all-important chlorophyll fluorescence channel is not influenced by the template's fluorescence. Indeed, calculations with control samples confirmed that there was minimal spectral overlap between these channels. The percentage spectral overlap was calculated by

imaging a sample containing the template-only, and by dividing the number of counts detected in the Chl channel (**Figure 4.5b**) by the number of counts in the detected in the Template channel (**Figure 4.5a**). The Template-to-Chl overlap was found to be 0.12 ± 0.01%. By measuring a sample containing Chl fluorescence only and repeating the previous calculation the Chl-to-Template overlap was found to be 2.8 ± 0.4 %. Following hybrid membrane formation, FLIM images show clear array patterns (**Figure 4.5c-d**) where the vast majority of Chl fluorescence is localized within the square corrals regions defined by the templates. These patterned hybrid membranes were highly reproducible, with similar dimensions and fluorescence intensity across multiple preparations (~50 counts per pixel).

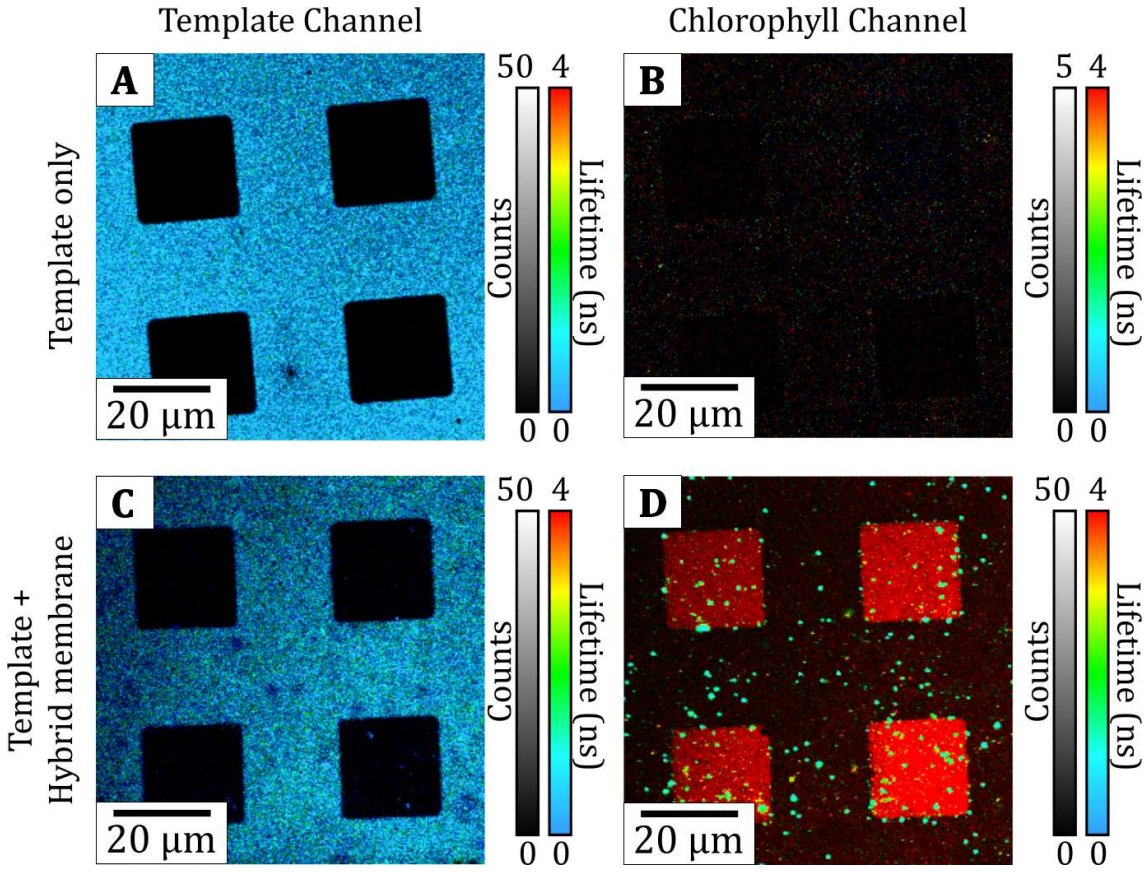

Figure 4.5: Multiple FLIM images of polymerised template before and after backfilling with hybrid membranes. **(A)** A Diyne-PC template with no hybrid membrane as imaged in the Template Channel. **(B)** The same area as in (a) as imaged in the Chl channel. Note that even displaying this panel with a compressed intensity scale compared to (a), (c) and (d) there is negligible signal due to noise or spectral overlap. **(C)** A Diyne-PC template after backfilling with a hybrid membrane, as imaged in the Template Channel. **(D)** The same area as in (a) as imaged in the Chl channel.

To confirm that the areas of Chl fluorescence were correlated to a membrane structure, combined FLIM and AFM measurements were made to record nanoscale topography maps spatially correlated to multi-channel fluorescence data. These two fluorescence channels were probed simultaneously using a pulse-interleaved excitation mode, with AFM topographs acquired on the same region immediately after. Images of an "empty" lipid template are shown in **Figure 4.6a**. The AFM height profile in **Figure 4.6c** (*red* line) revealed a 4.81 ± 0.07 nm height from the polymerized lipids to the base of the empty corral, in excellent alignment with the fluorescence intensity profile which drops from ~75 counts to ~0 counts over the same region (**Figure 4.6c**, *green* line). For the "empty" lipid template, the background signal in the chlorophyll FLIM channel was approximately zero across the entire image, as expected (**Figure 4.6c**, *blue* line). After the formation of the hybrid membranes, there was largely homogeneous Chl fluorescence within the square corral regions with no resolvable defects at this scale (**Figure 4.6b**). The increase in the Chl fluorescence intensity (**Figure 4.6d**, *blue* line) corresponded with a step change in the AFM height to a mere 0.19 ± 0.08 nm (**Figure 4.6d**, *red* line). Thus, the average measured thickness of the hybrid membrane was inferred to be 4.6 ± 0.2 nm. The precise spatial correlation between Chl fluorescence and the topography of the deposited membrane, demonstrates that the photosynthetic proteins present specifically within the corral regions and are excluded from the template grid.

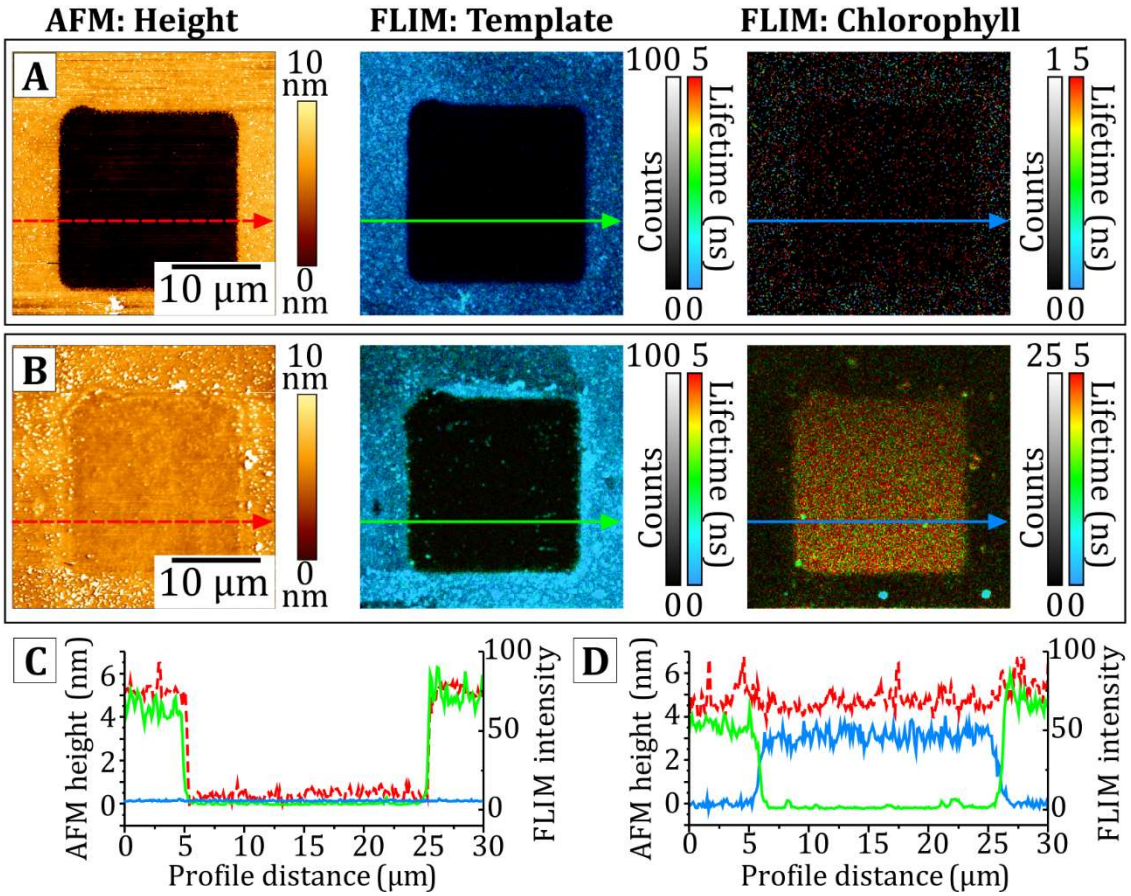

Figure 4.6: Analysis of hybrid membranes by correlated FLIM and AFM measurements of hybrid membranes. For (a) and (b) the *left panel* is an AFM topograph, the *center panel* is the "Diyne-PC FLIM channel" (i.e., optimized to detect the polymerized lipid by using excitation at 485 nm and collection of emission between 505-535 nm), the *right panel* is the "Chl FLIM channel" (i.e., optimized to detect the chlorophyll fluorescence from LH and PS proteins by using excitation at 640 nm and collection of emission between 672-696 nm). **(A)** Correlated FLIM+AFM data showing a single square of the polymerized lipid "empty" template. The minimal signal in the Chl FLIM channel is statistically indistinguishable from detector noise. **(B)** Correlated FLIM+AFM data showing a similar region as in (a), but after the corrals were "backfilled" with the extracted thylakoids and DOPC liposomes to form the hybrid membrane. **(C)** and **(D)** show profiles drawn across the region in (a) or (b), respectively: showing the AFM height (*red, dashed*), FLIM intensity from Diyne-PC (*green*) and FLIM intensity from Chl (*blue*). The Chl intensity is displayed after multiplication by a factor of 3, for comparison purposes.

4.3.2 Hybrid membranes have a longer fluorescence lifetime than extracted thylakoids

The Chl fluorescence lifetime, as determined from analysis of the time-resolved aspect of the FLIM data, was much longer for these hybrid membranes compared to extracted thylakoids. The fluorescence decay curve generated from analyzing the photons accumulated from the corral regions of the hybrid membrane (**Figure 4.7b**, *white box* regions) samples confirmed a slow decay process for hybrid membranes with $<\tau>$= 4.1 ± 0.1 ns (*red curve* in **Figure 4.7c**). This value represents entirely "non-quenched" proteins (isolated LHCII in detergent has $<\tau>$ ~4 ns),[189] in stark contrast to the short lifetime of extracted thylakoids (*blue curve*, **Figure 4.7c**). The long average lifetime suggests that the protein density in hybrid membranes must be sufficicently low that the protein-protein interactions found in the natural thylakoids (which reduce the fluorescence lifetime as discussed above) are relatively rare. Note, this long fluorescence lifetime was mainly observed inside of the corral region, with a minor sub-population of small particles with shorter lifetimes (occasional *blue/green* specks) observed on the surrounding framework. These short-lifetime particles are likely to be extracted thylakoids that have adhered to the top of the template and not merged with the synthetic lipid bilayers.

It is informative to assess the distribution of lifetimes within each sample, because this allows us to comment on the range of photophysical states, and therefore possible protein interactions, within each membrane, rather than merely the average. To do this, a frequency distribution plot of fluorescence lifetime was generated for both hybrid membranes and extracted thylakoids by binning photons into appropriate time ranges, shown in **Figure 4.7d**. These distributions can be fit to Gaussian functions centred around 0.57 ns and 4.58 ns for the extracted thylakoid sample and the hybrid membrane sample, respectively. The width of the distribution was significantly narrower for extracted thylakoids than hybrid membranes ($FWHM_{thylakoid}$ = 0.15 ns versus $FWHM_{hybrid}$ = 2.31 ns). The narrow distribution of lifetimes in thylakoid extracts, suggests that there is little variation in the local protein concentration or quenching interactions. In contrast, the broad distribution of lifetimes in hybrid membranes could suggest local density fluctuations (due to protein diffusion) or stable but heterogeneous interactions.

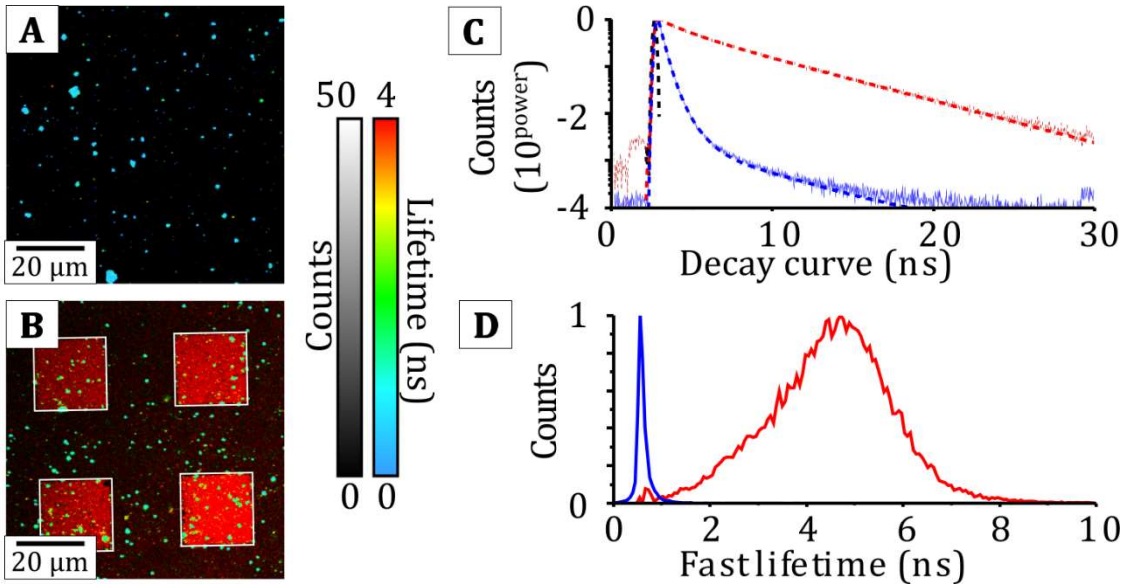

Figure 4.7: Lifetime analysis of hybrid membranes compared to extracted thylakoids. **(A)** FLIM image of extracted thylakoids adhered onto glass (repeated from **Figure 4.3a**). The photons from the whole image are accumulated to generate the fluorescence decay curve and frequency distributions shown in *blue* in (c) and (d). **(B)** FLIM image of hybrid membranes (repeated from **Figure 4.5d**). The photons from the *white, box* regions are accumulated to generate the fluorescence decay curve and frequency distributions shown in *red* in (c) and (d). **(C)** Normalized fluorescence decay curves showing raw data (*pale lines*) and fits (*dashed lines*) on log/linear axes (y/x) for extracted thylakoids (*blue*) and hybrid membranes (*red*). **(D)** Frequency distribution of the "FastFLIM" fluorescence lifetime (binned over 25 ps), samples colored as in (c), normalized to a peak of 1. Extracted thylakoids (*blue*) have a significantly narrower distribution than hybrid membranes (*red*).

The dramatic increase in Chl fluorescence lifetime observed in both the fitted lifetime <τ> and frequency distributions, leads us to conclude that large-scale protein and lipid reorganisations occur during the hybrid membrane assembly. It seems likely that the photosynthetic proteins become diluted significantly when thylakoid membranes merge with DOPC lipid bilayers, resulting in a significantly slower rate of energy dissipation and a higher proportion of absorbed energy being re-emitted as fluorescence, leading to longer fluorescence lifetimes.

Finally, we note that the formation of hybrid membranes was reproducible and consistent across numerous samples (multiple preparations are shown in **Figure 4.8a**). The fitted fluorescence lifetime of each corral was found to be extremely similar (see **Figure 4.8b** the the distribution of <τ> for 40 such corrals) with a narrow distribution of Chl lifetimes (FWHM = 0.12 ns). This suggests there is little variation in the mechanism of membrane formation across multiple preparations, and that hybrid membranes as a platform are robust against small variations that may occur between experiments.

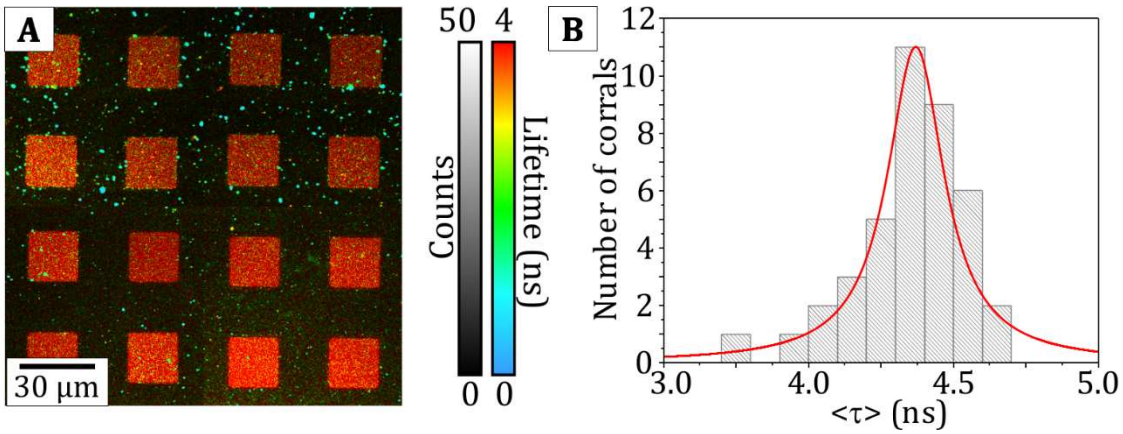

Figure 4.8: Lifetime analysis of hybrid membranes showing reproducibility across multiple preparations. **(A)** A gallery of FLIM images acquired of hybrid membranes across multiple preparations. **(B)** A histogram of fitted fluorescence lifetimes accumulated from 40 individual corrals. The fluorescence lifetime is very similar between hybrid membrane samples with a narrow distribution of Chl lifetimes (FWHM = 0.12 ns). This suggests the protein-protein interactions within the membrane are similar across multiple preparations.

4.3.3 Hybrid membranes have a significantly lower protein density than native light-harvesting membranes

To test the hypothesis that the elongated fluorescence lifetime of hybrid membranes, relative to thylakoid membranes, was due to a lower density of proteins, the protein density was estimated using a careful analysis of the absolute magnitude of fluorescence emission. The fluorescence intensity of hybrid membranes was compared to the fluorescence intensity of a known amount of LHCII, whilst taking into account changes in the level of quenching and keeping consistent acquisition parameters for FLIM measurements. The density of proteins in hybrid membranes was then calculated in terms of "LHCII-trimer equivalents" in a three-stage calculation process.

In the first stage, fluorescence emission in a sample containing a known amount of LHCII was measured. LHCII proteoliposomes were prepared from a defined quantity of purified LHCII (2.8 μM LHCII trimers) and natural thylakoid lipids, as previously described.[98] Note that proteoliposomes are analyzed in detail in other parts of this thesis (see Chapter 5) but are merely used as a "control" sample here. These proteolipsomes were adhered to piranha-cleaned glass, and imaged using the same acquisition settings and laser fluence used for the hybrid membranes, giving a direct comparison of the fluorescence intensity (**Figure 4.9a**). The average intensity per proteoliposome, $F_{vesicle}$, (N>100 proteoliposomes) was measured, and corrected for the background number of counts from detector, to be 75 ± 8 counts for a 500-frame acquisition. This equates to an average $F_{vesicle}$ of 0.149 counts per frame. **Table 4.1** shows the average intensity for 10 example LHCII proteoliposomes (*circled*) in the image shown in **Figure 4.9b**.

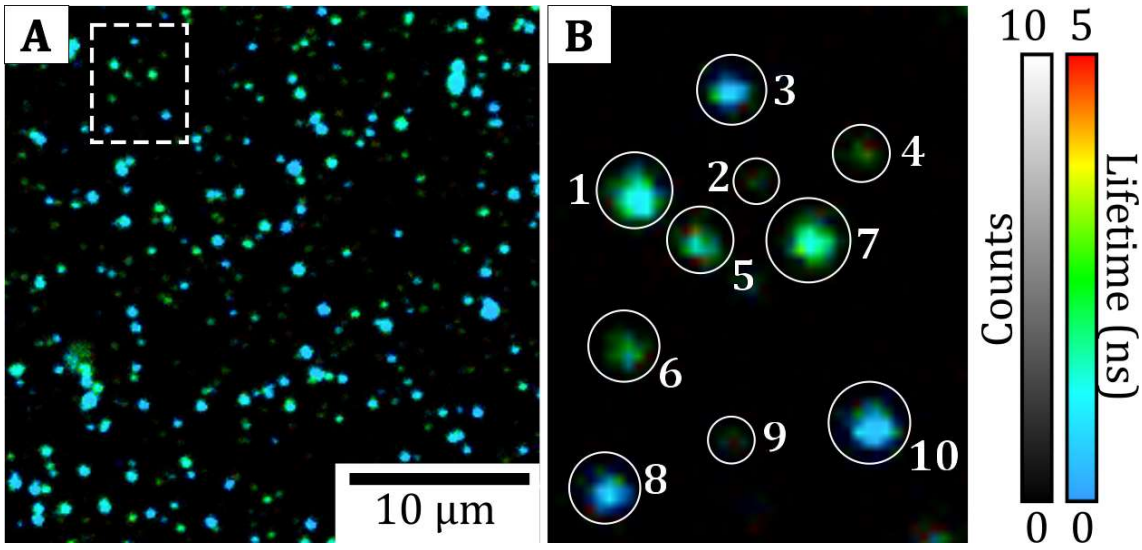

Figure 4.9: Example images of LHCII + DOPC proteoliposomes used as a comparison to calculate the protein concentration in hybrid membranes. **(A)** A representative image of LHCII proteoliposomes (containing approximately 2.8 µM LHCII and 1 mM thylakoid lipids) adhered onto cleaned glass. The samples were imaged in a buffer containing 40 mM NaCl, 20 mM, HEPES, pH 7.5 using the same acquisition settings and laser fluence used for the hybrid membranes, giving a direct comparison of the fluorescence intensity of a known amount of LHCII. (**B)** A zoomed in area from the white, dashed box from (a), showing 10 example proteoliposomes corresponding to the examples given in **Table 4.1**.

Number	**Frames**	**Noise per pixel per frame** (counts)	**Number of selected pixels** (pix)	**Total counts** (counts)	**Detector noise in the selected area** (counts)	**Corrected $F_{vesicle}$** (counts)
1	500	3.68×10^{-4}	42	155	7.73	147.27
2	500	3.68×10^{-4}	32	17	5.89	11.11
3	500	3.68×10^{-4}	21	71	3.86	67.14
4	500	3.68×10^{-4}	39	30	7.18	22.82
5	500	3.68×10^{-4}	30	47	5.52	41.48
6	500	3.68×10^{-4}	20	71	3.68	67.32
7	500	3.68×10^{-4}	23	126	4.23	121.77
8	500	3.68×10^{-4}	34	182	6.26	175.74
9	500	3.68×10^{-4}	63	18	11.59	6.41
10	500	3.68×10^{-4}	57	152	10.49	141.51

Table 4.1: Calculation of the fluorescence intensity signal for 10 example LHCII proteoliposomes (from images as shown in **Figure 4.9b**) used to estimate the fluorescence signal per LHCII trimer. This "corrected" signal represents the number of counts (photons emitted) per proteoliposome after subtracting the detector noise. For a population of N=100 proteoliposomes, the average fluorescence intensity was found to be 74.58 ± 7.66 counts for a 500-frame acquisition. This equates to an average $F_{vesicle}$ of 0.149 counts per frame.

In the second stage, the approximate fluorescence emission from a single trimer was calculated, by using a molecular packing model to estimate the number of LHCII trimers per proteoliposome. Here, the area per DOPC lipid headgroup was assumed to be between 0.65 to 0.70 nm^2 (using 0.67 nm^2 as a best estimated[190]) and the radius of an LHCII trimer to be 3 to 5 nm (using 4 nm as a best estimate[22]) based upon space-filling models from published protein crystallographic structures[22, 190]. The surface area of a proteoliposome, $A_{vesicle}$, is then estimated to be the sum of the areas of all of the component molecules, such that:

$$A_{vesicle} = n[A_{LHCII} + 0.5(L/P)A_{lipid}] \qquad \text{Eq. 4.1}$$

Where A_{LHCII} is the area of an LHCII trimer, calculated from $A_{LHCII} = \pi R_{LHCII}^2$, and A_{lipid} is the area of a lipid headgroup (note, the factor 0.5 is due to 2 lipids one from each two monolayer together to form one bilayer and thus occuping an area of A_{lipid}) and L/P is the lipid-to-protein ratio. Due to the uncertainty associated in space filling models, we calculated a minimum, a maximum, and a best estimate for the number of LHCII trimers per liposome, as shown in **Table 4.2**, yeilding a range of 17 to 81 trimers per liposome (best estimate = 36 trimers per liposome). In the final stage, the number of LHCII trimers per corral was estimated by comparing the fluorescence emission inside a corral to the estimated fluorescence emission per trimer, as is shown in **Table 4.3**. To account for the the relative quenching of the LHCII proteoliposomes ($<\tau_{vesicle}>$ = 0.64 ± 0.01 ns) and hybrid membranes ($<\tau_{hybrid}>$= 4.1 ± 0.1 ns), the assumption was made that the fluorescence quantum yeild was proportional to the relative fluorescence lifetime, $\frac{\tau_{vesicle}}{\tau_{DDM}}$ (τ_{DDM} is the lifetime of LHCII in detergent) and the intensity per LHCII is "corrected" by this factor. Our best estimate for the protein content is 44,300 ± 5,500 LHCII-trimer-equivalents per corral (1,860,000 chlorophylls). The possible range for the protein density is estimated to be 69 – 326 trimers/μm^2 corresponding to 0.27 – 2.56 % of the total membrane area being occupied by photosynthetic proteins (best estimates of 111 trimers/μm^2 and 0.56%). Given that natural photosynthetic membranes are comprised of 60-70% protein by weight,[52] these estimates are in agreement with the hypothesis that the hybrid membranes contain a relatively low concentration of proteins. Later sections assess if the change in the photophysical state and reduced density affects the functionality and energy transfer within the system.

Scenario	D (nm)	L/P (mol/mol)	$A_{vesicle}$ (nm^2)	A_{lipid} (nm^2)	A_{LHCII} (nm^2)	n (LHCII /vesicle)	density (LHCII /μm^2)
best estimate	60	1071	11310	0.67	50.3	28	2444
min. estimate	50	1071	31416	0.70	38.5	17	2205
max. estimate	100	1071	7854	0.65	78.5	81	2586

Table 4.2: Calculations for the number of LHCII proteins found on average per proteoliposome, given the estimated dimensions for the protein, lipids and the vesicle. This is for the proteoliposome sample shown in **Figure 4.9** and **Table 4.1** (which has 2.8 μM LHCII and 1 mM thylakoid lipids).

D, average diameter measured via dynamic light scatterting measurements (DLS), 60 nm is the average but given the accuracy of DLS the low and high values shown represent reasonable low and high estimates;

L/P, the average lipid-to-LHCII trimer ratio, as determinated from ensemble absorption spectroscopy measurements and spectral decomposition analysis using published methodology[98];

$A_{vesicle}$, calculated from $4\pi r^2$ (where, r= D/2);

A_{lipid}, published value for DOPC headgroup area, given the uncertainty we use 0.65 and 0.70 as the low and high estimates;

A_{LHCII}, estimation of the membrane area occupied by one LHCII, from the consideration of space-filling models of published protein structures and then approximation of LHCII as a circular area (πr^2) where r = 3.5, 4.0 or 5.0 for the low, medium and high estimates (range due to uncertain protein packing);

Area per vesicle approximates to the following equation (note, the factor 0.5 is due to 2 lipids one from each two monolayer togethe to form one bilayer and thus occuping an area of A_{lipid}):

$$A_{vesicle} = n[A_{LHCII} + 0.5(L/P)A_{lipid}] \quad \text{Eq. 4.1}$$

This expression was solved to calculate **n** using the values for **L/P**, **$A_{vesicle}$**, **A_{lipid}** and **A_{LHCII}**.

Density = n / $A_{vesicle}$.

The minimum, maximum and best estimates are made using the different possible values shown for each term, as shown.

Est.	N_{LHCII} per vesicle (#)	$F_{vesicle}$ (cnts/ frame)	$\tau_{vesicle}$ (ns)	F_{LHCII} (cnts /frame)	F_{corral} (cnts /frame)	N_{LHCII} per corral (#)	Density (/μm²)	A_{LHCII} (nm²)	$A_{\%}$ (%)
best	28	0.149	0.637	0.0263	1503	44300	111	50.3	0.56
min.	17	0.149	0.637	0.0446	1503	27800	69	38.5	0.27
max.	81	0.149	0.637	0.0083	1503	130000	326	78.5	2.56

Table 4.3: Calculations for the number of proteins per corral for hybrid membranes, in terms of "LHCII-equivalents". This uses the average fluorescence counts measured by FLIM for an LHCII proteoliposome and converts to counts per LHCII protein, given the measured number of proteins within a typical proteoliposome (from **Table 4.2**). Consistent acquisition parameters were used to record FLIM images of both LHCII proteoliposomes and hybrid membranes.

$N_{LHCII/vesicle}$, estimated number of LHCII-equivalents per proteoliposome (**n** from **Table 4.2**). This range from the minimum to the maximum considering our combined uncertainties;

$F_{vesicle}$, estimated fluorescence intensity measured per proteoliposome per frame ("average $F_{vesicle}$" as stated in the caption of **Table 4.2**);

$\tau_{vesicle}$, the measured mean fluorescence lifetime of a typical LHCII proteoliposme (mean of N=100 measured particles from images similar to **Figure 4.9**);

F_{LHCII}, the FLIM counts expected per LHCII trimer per frame calculated for each possible **$N_{LHCII/vesicle}$,** as follows. LHCII within proteoliposomes is known to self-quench, shortening the fluorescence lifetime due to the self-association of neighbouring LHCII.[56] The measured $\tau_{vesicle}$ of proteoliposomes of 0.637 ns (SD = 0.015 ns) implies significant quenching relative to isolated LHCII in detergent ($\tau_{DDM} \approx 4$ns), so to crudely take this into account we can multiply by the ratio of the lifetimes (4/0.637). Thus, the intensity of the proteins in the unquenched state is estimated as:

$$\mathbf{F_{LHCII}} = \frac{\mathbf{F_{vesicle}}}{\mathbf{N}_{\left(\frac{\mathbf{LHCII}}{\mathbf{vesicle}}\right)}} \times \left(\frac{\tau_{DDM}}{\tau_{vesicle}}\right) = \frac{0.149}{\mathbf{N}_{\left(\frac{\mathbf{LHCII}}{\mathbf{vesicle}}\right)}} \times \left(\frac{4}{0.637}\right) = \frac{0.94}{\mathbf{N}_{\left(\frac{\mathbf{LHCII}}{\mathbf{vesicle}}\right)}} \qquad \text{Eq. 4.2}$$

F_{corral}, average fluorescence intensity measured in FLIM of hybrid membranes, as total counts within one corral per frame. This vale is found from careful analysis of the corrals from many images of hybrid membranes similar to those shown in **Figure 4.9** (N = 16 corrals);

$N_{LHCII/corral}$, is the estimated number of LHCII trimers per corral, $N = F_{corral} / F_{LHCII}$;

Density (LHCII/corral) = $\mathbf{N_{LHCII/corral}} / A_{corral}$ (where each corral has area $A_{corral} = 400$ μm²);

A_{LHCII}, is the area occupied by a single trimeric LHCII protein complex, as estimated in **Table 4.2**;

$A_{protein}$(%), estimated surface area fraction of the corral occupied by LHC and PS proteins:

$$A_{protein}(\%) = Density(\mu m^2) \times A_{LHCII}(nm^2)/10^6 \qquad \text{Eq. 4.3}$$

4.3.4 Chl-containing proteins within hybrid membranes appear to be highly mobile as shown by fluorescence recovery after photobleaching

In an ideal model system, photosynthetic proteins would be able to freely diffuse or interact with each other in ways that mimic the dynamics of the natural system. To assess the ability of the proteins to diffuse within the hybrid membranes, we attempted to quantify the mobility of LH and PS proteins (detected via Chl fluorescence), and, by extension, determine if the sample substrate is hindering protein interactions.

Fluorescence recovery after photobleaching (FRAP) measurements are a common method to determine the mobility of fluorophores within supported lipid bilayers (SLBs),[191, 192] and typically involve the deliberate photobleaching of a small circular region within an "infinitely" large membrane (i.e., significantly larger than the bleached spot), and followed by monitoring the recovery of fluorescence within the bleached spot over time. If the fluorophores are mobile, the intensity of the bleached spot will increase, as bleached fluorophores diffuse out of, and bright (non-bleached) fluorophores diffuse into, the bleached area. The rate of fluorescence recovery, and the proportional increase of the fluorescence intensity, can then be used to estimate the diffusivity and mobile fraction of the fluorophores. Due to the finite and small area of the hybrid membranes, the assumptions used in commonly used FRAP experiments were no longer accurate. Firstly, the size of the hybrid membranes is not "infinite" and there is a limited number of non-bleached fluorophores that can diffuse into the bleached area. Secondly, the bleached region was bound by a solid square edge (the Diyne-PC template), meaning that the mathematical models for the rate of recovery and calculations of the diffusion constant derived for circular bleached spots could not be applied.

Therefore, to semi-qualitatively estimate the diffusivity of the photosynthetic proteins, FRAP measurements of Chl fluorescence were compared to FRAP measurements of a fluorophore with a known diffusion constant (DOPC lipids, labelled with 0.5% Texas Red (TR) mol/mol) deposited into the Diyne-PC template. The epifluorescence instrument was a Nikon E600 microscope equipped set up with

a filter cube optimized for either the labelled lipid fluorescence (excitation 540-580 nm, dichroic 595 nm, emission 600-660 nm) or the Chl fluorescence (excitation 450-475 nm, dichroic 500 nm, emission 650-800 nm). Images were acquired using an 100× oil objective, 0.5 s exposure and appropriate neutral density (ND) filters. For deliberate photo-bleaching, an aperture was inserted to expose a circular region (~15 μm diameter) of the sample for a continuous period of 30 s at full power (i.e. no ND filters). Immediately following bleaching, full-field images were acquired sequentially over a period of 120 s, and the fluorescence recovery plotted over time.

Figure 4.10a shows a FRAP experiment performed on a DOPC lipid bilayer that was formed with the template pattern (i.e., only lipids, no proteins). The aperture was positioned over the corner of a corral to deliberately photo-bleach fluorophores within the *blue, dashed* area. The intensity of bleached area is seen to recover over subsequent time points (t = 10 s, 20 s etc) as fluorophores that were not bleached diffuse into that region. To account for photo-bleaching that occurs during the period after FRAP, the intensity of a neighbouring reference area (*red, dashed*) is also monitored. A similar experiment was performed for a typical hybrid membrane sample (i.e., containing thylakoid proteins), and can be seen in **Figure 4.10b**. The results of each experiment are shown graphically in **Figures 4.10c** and **4.10d** for TR-lipid and Chl-protein fluorescence, respectively. In each graph, the intensity of the bleached area (*black*) is corrected for (divided by) the amount of photo-bleaching in the reference area (*red*) to provide an estimate for the rate of recovery (*blue*). Note that Chl pigments become significantly more bleached than the TR fluorophore over the image acquisition, so this correction was essential to avoid underestimating the rate of fluorescence recovery. A mono-exponential fit, $F = F_0(1 - e^{-kt})$, was used to obtain the "doubling time", $\tau = \ln(2)/k$, for both (TR) lipid and (Chl) protein fluorescence, this was found to be 21.5 ± 1.6 s and 44.7 ± 10.3 s, respectively (fit ± standard error,). From the relative fluorescence doubling time, we approximate the diffusion constant of LH and PS proteins to be ~48 % of the diffusion constant of DOPC lipids ($D_{Chl}/D_{DOPC} = \tau_{Chl}/\tau_{DOPC}$).

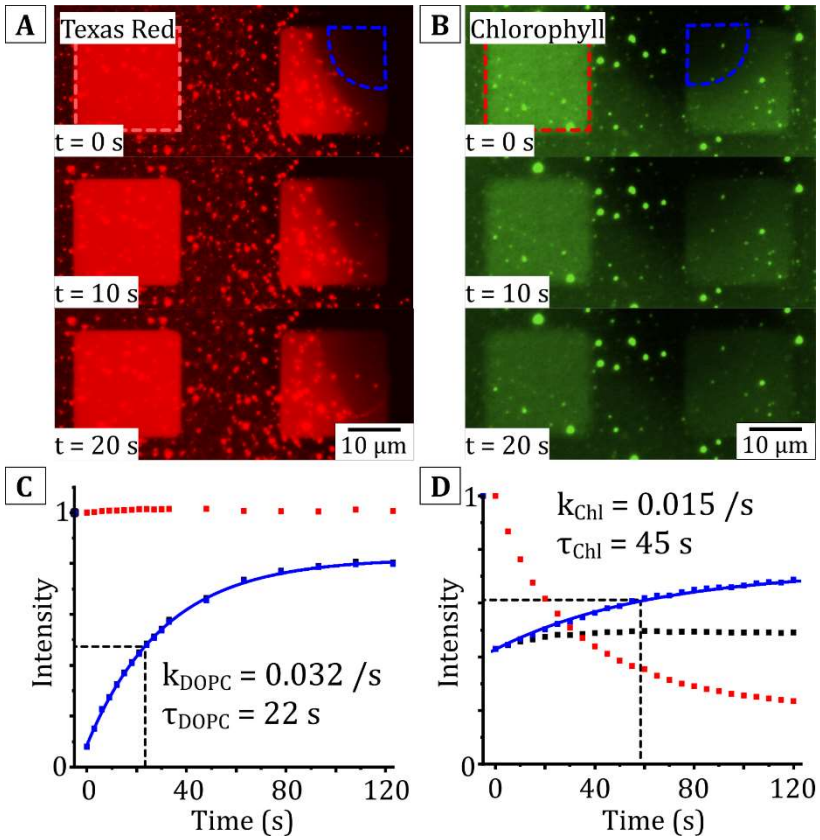

Figure 4.10: Epifluorescence microscopy with photobleaching (FRAP) experiments to assess the lateral mobility of proteins and lipids within hybrid membranes. Images were acquired at the time-points as labelled on panels. **(A)** An epifluorescence time-lapse image series of a patterned DOPC lipid membrane which contained 1% Texas Red (TR) DHPE fluorescently-labelled lipids (mol/mol). The TR fluorophores were bleached within the blue dashed region at t = 0 s. The fluorescence can be seen to recover in subsequent images. **(B)** An epifluorescence time-lapse image series of a hybrid membrane. LH and PS proteins were bleached within the blue dashed region at t = 0 s, and non-bleached proteins can be seen to diffuse into the bleached region over the subsequent images. **(C)** Analysis of the recovery of fluorescence from (A) representing the lipid diffusion rate. The red line shows the fluorescence intensity tracked in a reference corral to correct for any photobleaching that occurs during image acquisition. The blue line shows the fluorescence intensity in the bleached area, corrected for photobleaching, as it increases over 120 s. As there is minimal bleaching during imaging the raw data (black) and the corrected (blue) datapoints overlap. A mono-exponential growth function was fitted to the recovery data (blue line), $F(t) = F_0\ e^{kt}$, where t=time, k= rate constant, $F(t)$ is the intensity at time t, F_0 is the initial intensity. This yields a fluorescence doubling-time τ = 22 s ($\tau = ln2/\ k$). **(D)** Analysis of the recovery of fluorescence from (B) representing the photosynthetic protein diffusion rate. This analysis was performed as described for (C) and yielded a doubling-time τ = 45 s.

In addition to the diffusion constant, we attempted to calculate the mobile fraction of the PS and LH proteins by devising a simple analysis procedure. This uses the logic that the "bleached" region must recover to an intensity equal to the "non-bleached" regions if the mobile fraction is 100%. Therefore, the mobile fraction is calculated by:

$$M = \frac{F_R}{F_D} \qquad \text{Eq. 4.4}$$

where F_R is the fluorescence intensity of the bleached area, and F_D is the fluorescence of an area within the corral that was not bleached, after the system has been allowed to reach an equilibrium. As F_R increases, the intensity of F_D decreases, as bright fluorophores migrate into the bleached area, and vice versa. In the scenario where there is 100% mobility, $F_R/F_D = 1$ as the fluorescence of the two areas will tend to the same intensity over time.

To account for fluorophores that are not completely bleached after 30 s, equation 4.4 takes the form:

$$M = \frac{F_{R\infty} - F_{R0}}{F_{D\infty} - F_{R0}} \qquad \text{Eq. 4.5}$$

where F_{R0} and $F_{R\infty}$ is the intensity of the bleached area at t = 0s and at t = ∞, respectively. In our analysis, we approximate $t = \infty \sim 120\ s$. Both F_R and F_D are corrected for any photobleaching that has occurred by tracking the intensity of an adjacent reference corral.

To verify this method of calculating the mobile fraction, we first calculated the mobile fraction for lipids (labelled with 0.5% Texas Red DHPE). The mobile fraction for lipids is expected close to 100% (multiple authors report high mobile fractions for DOPC supported lipid bilayers[193-195] and using the calculations shown in **Table 4.4,** the mobile fraction of DOPC was found to be 96.9 ± 0.7 % (mean ± standard error, N = 6). By contrast, the mobile fraction of Chl fluorescence was found to be much lower (76.8 ± 3.1 %, **Table 4.5**). This finding suggests that there is some interaction between the substrate and the proteins that hinders the free diffusion of LHCII and PSII, however the large majority of proteins are able to migrate throughout the membrane. The high mobile fraction could indicate that the method of membrane self-assembly favours the incorporation of mobile proteins; this possibility is interrogated in later sections of this chapter.

Ref. area (t = 0s)	**Ref. area (t = 120s)**	**Photo-bleach**	**Bleach area (t = 0s)**	**Non-bleach area (t = 0s)**	**Bleach area (t = 120s)**	**Corr. for photo-bleach**	**Non-bleach area (t = 120s)**	**Corr. for photo-bleach**	**Mobile %**
I_{Ref0}	$I_{Ref\infty}$	(P)	F_{R0}	F_{D0}	$F_{R\infty}$	$F_{R\infty}/P$	$F_{D\infty}$	$F_{D\infty}/P$	M
414.5	405.6	0.98	67.86	482.4	223.9	228.8	228.4	233.4	97
414.5	405.6	0.98	89.77	507.7	262.1	267.9	265.9	271.7	98
426.9	426.8	1.00	26.53	428.8	175.9	176.0	183.6	183.6	95
426.9	426.8	1.00	17.56	334.2	112.7	112.7	119.0	119.0	94
426.9	426.8	1.00	76.02	437.4	327.7	327.8	332.7	332.8	98
426.9	426.8	1.00	59.81	422.4	282.3	282.4	283.8	283.9	99

Table 4.4: Calculations for mobile fraction of lipid-only membranes (DOPC/ TR-DHPE) backfilled into Diyne-PC templates.

$\mathbf{I_{Ref0}}$ and $\mathbf{I_{Ref\infty}}$, the fluorescence intensity of a reference corral, measured at time t = 0 s and t = 120 s, respectively. This is used to calculate the extent of photobleaching, **P**, that occurs during the FRAP acquisition as: $\mathbf{P = 1 - (I_{Ref\infty}/I_{Ref0})}$

$\mathbf{F_{R0}}$ and $\mathbf{F_{R\infty}}$, the fluorescence intensity of the bleached area, measured at t = 0 s and t = 120 s, respectively.

$\mathbf{F_{D0}}$ and $\mathbf{F_{D\infty}}$, the fluorescence intensity of a non-bleached area in the same corral as the bleached area, measured at t = 0 s and t = 120 s, respectively.

M, the mobile fraction calculated from

$$M = \frac{F_{R\infty} - F_{R0}}{F_{D\infty} - F_{R0}} \qquad \text{Eq. 4.5}$$

where $\mathbf{F_{R0}}$ and $\mathbf{F_{R\infty}}$ is the intensity of the bleached area at t = 0s and at t = ∞, respectively. In our analysis, we approximate $t = \infty \sim 120\ s$.

The average mobile fraction was found to be 96.9 ± 0.7 % (mean ± standard error, N = 6).

Ref. area (t = 0s)	**Ref. area (t = 120s)**	**Photo-bleach**	**Bleach area (t = 0s)**	**Non-bleach area (t = 0s)**	**Bleach area (t = 120s)**	**Corr. for photo-bleach**	**Non-bleach area (t = 120s)**	**Corr. for photo-bleach**	**Mobile %**
I_{Ref0}	$I_{Ref\infty}$	(P)	F_{R0}	F_{D0}	$F_{R\infty}$	$F_{R\infty}/P$	$F_{D\infty}$	$F_{D\infty}/P$	M
458.3	132.0	0.29	60.52	327.5	90.72	315.1	110.2	382.6	79
332.8	81.45	0.24	38.16	127.2	56.22	229.7	78.22	319.6	68
383.2	89.63	0.23	35.30	169.8	64.69	276.6	74.72	319.5	85
381.1	89.64	0.24	47.01	193.2	70.66	300.4	86.67	368.4	79
286.3	84.90	0.30	34.12	132.3	52.62	177.4	75.02	253.0	65
286.3	84.90	0.30	37.51	125.4	49.48	166.9	56.51	190.6	85

Table 4.5: Calculations for mobile fraction of LH and PS proteins in hybrid membranes.

I_{Ref0} and **$I_{Ref\infty}$**, the fluorescence intensity of a reference corral, measured at time t = 0 s and t = 120 s, respectively. This is used to calculate the extent of photobleaching, **P**, that occurs during the FRAP acquisition as: **$P = 1 - I_{Ref\infty}/I_{Ref0}$**.

F_{R0} and **$F_{R\infty}$,** the fluorescence intensity of the bleached area, measured at t = 0 s and t = 120 s, respectively.

F_{D0} and **$F_{D\infty}$,** the fluorescence intensity of a non-bleached area in the same corral as the bleached area, measured at t = 0 s and t = 120 s, respectively.

M, the mobile fraction calculated from

$$M = \frac{F_{R\infty} - F_{R0}}{F_{D\infty} - F_{R0}} \qquad \text{Eq. 4.5}$$

where **F_{R0}** and **$F_{R\infty}$** is the intensity of the bleached area at t = 0s and at t = ∞, respectively. In our analysis, we approximate $t = \infty \sim 120\ s$.

The average mobile fraction across multiple measurements was calculated to be 76.8 ± 3.1 % (mean ± standard error, N = 6).

4.3.5 Hybrid membranes are topologically flatter and larger than thylakoid extracts but contain nanoscale imperfections

In addition to correlated FLIM and AFM measurements, a standalone AFM was used to obtain higher resolution topographical data to assess the nanoscale structure of the hybrid membranes. To identify structural features that are specific to presence of material from the thylakoid membranes, the topography of DOPC-only lipid membranes formed with the template was compared to the topography of hybrid membranes. Firstly, the thickness of the hybrid membrane was confirmed to be ~4.5 nm by direct comparison of the step height at the edge of a corral before and after backfilling (**Figure 4.11a**), in agreement with other measurements. Note that DOPC-only lipid membranes and hybrid membranes had a similar thickness (*green* and *red lines* in **Figure 4.11a(iv)**).

Further AFM measurements were performed at the centre of the corrals, to avoid any pattern-related imperfections at the corral edge that could adversely affect the membrane structure (multiple Diyne-PC patches can be observed in **Figure 4.11a(i)**, *ringed green*, as a result of the resolution limit of the UV patterning). AFM topographs (**Figure 4.11b** and **4.11c**) taken at the center of the hybrid membrane reveal the structure to be mostly flat and homogeneous across widespread areas (tens of micrometers). Multiple small pores were present in the membrane and occupy ~10% of measured area. These pores typically have a lateral scale of ~100 nm and an average depth of 4.45 ± 0.62 nm (n = 10 profiles). The depth of these pores is in agreement (**Figure 4.11d**, *height profile*) with the published values for a DOPC bilayer (~4.5 nm), and show that the hybrid membranes have a similar thickness.[196] Note that these pores were not present in membranes formed solely from DOPC and AFM measurements of DOPC-only lipid membranes showed a contiguous and defect-free DOPC-only membrane (**Figure 4.11a(ii)** and **4.12a-b**) confirming the quality of our synthetic lipid vesicles and suggesting that the small breaks within the hybrid membranes are due some interaction between the extracted thylakoids and synthetic lipids and/or the template.

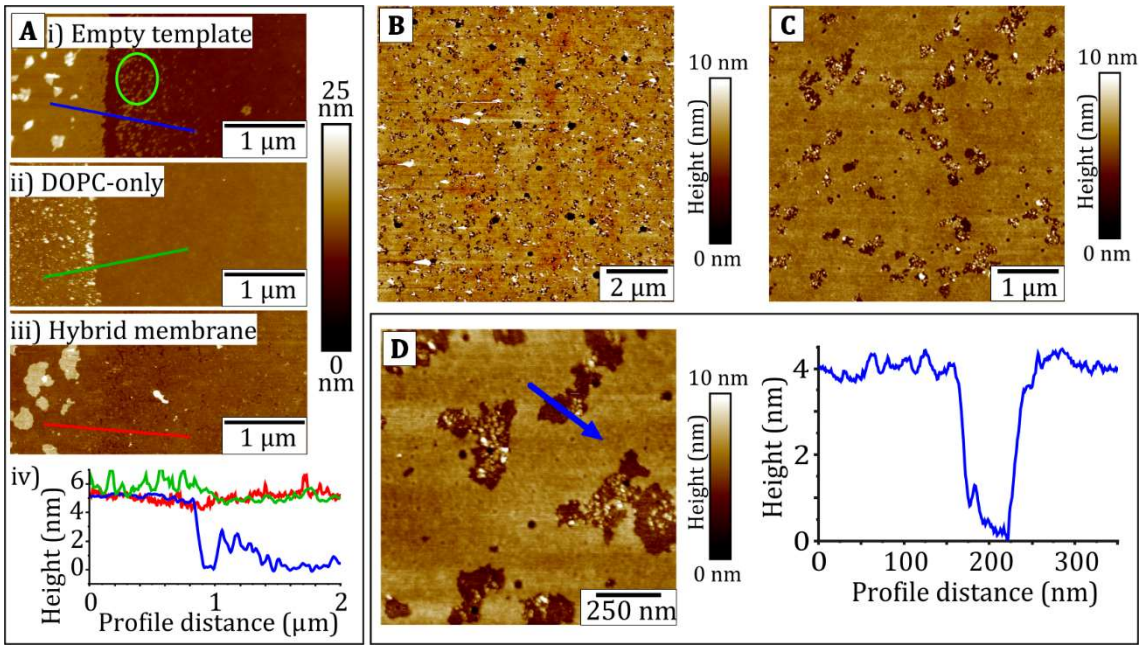

Figure 4.11: High resolution AFM analysis of "empty" templates versus hybrid membranes vs DOPC membranes. **(A)** AFM image centered on the step from the Diyne-PC template to the middle the corral for **(i)** an empty template (the *green ringed area* shows possible effects photolithography pattern blurring), **(ii)** a DOPC-only lipid membrane and **(iii)** a hybrid membrane. **(B)** and **(C)** AFM topographic images of a similar sample as in (a)(iii), taken in the centre of a corral where there are no pattern-related imperfections. **(D)** A zoomed in topograph of the hybrid membrane, with a height profile (*blue arrow*) showing the step height across a pore in the hybrid membrane.

4.3.6 AFM measurements of protein density are in agreement with FLIM estimations

To confirm the protein density estimated from FLIM measurements, a manual analysis of particles observed in the high-resolution AFM topographs was performed. Firstly, to estimate the percentage of these particles that represent thylakoid membrane proteins (and not impurities from other sources), the particle density in hybrid membranes was compared to the particle density in lipid-only membranes. Qualitatively, significantly fewer particles can be seen in the DOPC-only membranes (**Figure 4.12a-b**) than in hybrid membranes (**Figure 4.12c-d**), suggesting that the vast majority of the particles in hybrid membranes are likely to be photosynthetic proteins. To show this more precisely, a careful manual analysis was performed across multiple topographs for hundreds of "protein-candidate" particles. Specifically, particles that are between 5-10 nm in height and ~10-20 nm in diameter, as expected for the thylakoid membrane proteins.[72] Our analysis showed that the particle density was significantly higher for hybrid membranes (77.0 particles/μm^2) than for the control sample of DOPC-only (9.7 particles/μm^2). This suggests that ~80% of the particles observed in hybrid membranes by AFM can be confidently identified as LH or PS proteins, leading to an estimated protein density of ~60 proteins/μm^2. This approximated protein density from AFM measurements was on the same order, but lower, than our previous estimates of protein density calculated via fluorescence intensity (AFM estimations of ~60 proteins/μm^2 from **Figure 4.12**, compared to FLIM estimate of 80-450 proteins/μm^2 from **Table 4.3**). This difference can be explained by considering that only static proteins can be observed by AFM, and that any highly mobile molecules would be "invisible" to the slow raster speed of the AFM probe (in **Figure 4.12d** the tip velocity was ~0.25 μm/s, whereas protein diffusivity is predicted to be >0.5 $\mu m^2/s$). From our FRAP calculations of mobile fraction, **Table 4.5**, we hypothesize that the protein density observed by AFM only represents a small minority (~20%) of the total population. After taking the "invisible" mobile population into account, the approximated protein density from AFM comes into good agreement to the approximated protein density calculated via fluorescence (AFM estimate of ~300 proteins/μm^2, FLIM estimate of between 80-450 proteins/μm^2).

To determine which of the proteins present in thylakoid membranes (e.g. LHCII, PSII etc) may have incorporated into the hybrid membranes, we attempted to classify proteins based on the height of their protrusion from the lipid membrane, with knowledge that AFM instruments have much higher (~0.1 nm) z-axis resolution than lateral resolution (~1.0 nm). Height profiles were drawn across hundreds of proteins (N = 250) to measure the protrusion (i.e., the maximum height) of each protein from the surrounding lipid bilayer. A frequency histogram of these protrusions shows three distinct populations (see **Figure 4.12e-f**) that may represent different species of proteins. Note that there is some overlap between these populations, possibly due to an uncertainty in the measured particle protrusion caused by vibrational noise, particle oscillation, or other experimental factors. These populations can be fitted to a Gaussian distribution ($R^2 > 0.99$), and were found to protrude from the bilayer by 0.75 ± 0.03 nm (assigned P1), 1.91 ± 0.04 nm (assigned P2) and 3.19 ± 0.06 nm (assigned P3), respectively. Our results are in moderate agreement with the known crystal structures of LHCII, PSII and cytochrome b_6f, and with previous AFM studies that have used the same approach.[72] The P1 peak is consistent with the predicted height for LHCII, and the P2 and P3 peaks show the same relative heights for PSII and Cyt b_6f, respectively. From this we conclude that hybrid membranes contain many of the relevant photosynthetic membrane proteins.

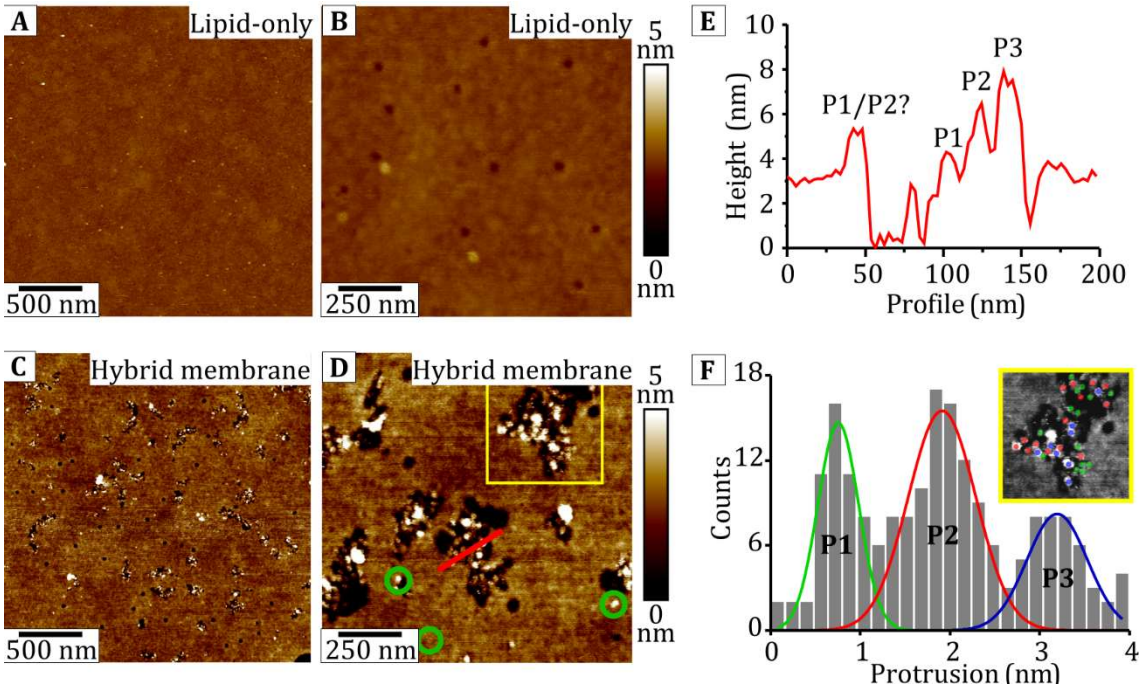

Figure 4.12: High resolution AFM analysis of lipid-only (DOPC) membranes versus hybrid membranes. **(A)** AFM image of an area at the center of a corral backfilled with a DOPC lipid bilayer. **(B)** AFM image of (a) at higher magnification. **(C)** An area at the center of the corral backfilled with hybrid membrane. Pores are visible with this resolution. **(D)** AFM image of (c) at higher magnification where particles are observed within the pores and lipid bilayers (ringed *green*). **(E)** Height profile from the *red* line shown in panel (d), showing three possible types of immobilized proteins found within pores (denoted P1, P2 and P3). **(F)** A particle height histogram obtained from profile analysis across N=250 particles. Height traces were drawn across individual particles, as in (A), and the difference in particle height from the surrounding bilayer (protrusion) across many particles was accumulated as a histogram. Within this population, three peaks are observed with corresponding particle protrusions of 0.753 ± 0.027 nm (assigned P1), 1.911 ± 0.035 nm (assigned P2) and 3.194 ± 0.062 nm (assigned P3), respectively. The inset shows an example region (*yellow box,* panel (d)), where particles have been color coded (P1 = *green*, P2 = *red*, P3 = *blue*) corresponding to their particle classification.

4.4 Investigating the dynamics of hybrid membrane formation

Understanding the mechanism of hybrid membrane self-assembly is useful for explaining the changes in photophysics of the incorporated proteins and the occurrence of micro/nanoscale topographical features. We hoped to montinor changes to the membrane during self-assembly, as well as identifying the exact role of each component in the self-assembly process, to suggest reasons for the photophysical and structural features that are observed. In a biophysical context, one may also wish to understand more about the processes of self-assembly in a more general context, so that hybrid membranes may be developed and formed from other highly-curved natural membranes.

4.4.1 The diyne-PC template and a nascent lipid bilayer play an essential role in hybrid membrane formation

To investigate the specific role of the various components in the hybrid membrane formation, a series of experiments was devised to interrogate each component independently. *Firstly*, to test if the hybrid membrane would form in the absence of DOPC lipids, a diyne-PC template was incubated in a solution containing only extracted thylakoids (no DOPC). *Secondly*, to test if the hybrid membrane would form in the absence of the template, a hydrophilic glass substrate was incubated in a solution containing both DOPC liposomes and thylakoids (no template). *Finally*, to test if the hybrid membranes could form via protein insertion into a pre-formed DOPC membrane, a lipid-only membrane was assembled into the diyne-PC template, before being incubated in a solution of extracted thylakoids. Following a 30 minute incubation, all three samples were washed copiously with buffer, to remove any loosely adsorbed material. In all three scenarios, the hybrid membrane did not form. The data is presented below.

Firstly, in the absence of DOPC, the thylakoids membranes adhere to the hydrophilic glass surfaces and remain as distinct particles (*right panel,* **Figure 4.13**). The FLIM data bears resemblance to extracted thylakoids deposited on to hydrophilic glass (no template) suggesting that the thylakoids remain in the same state (multilayered membranes with tightly packed proteins). Note that there is no fluorescence signal in the TR channel (*left panel*, **Figure 4.13**), as expected, because no synthetic lipids or lipid dyes were present in this sample.

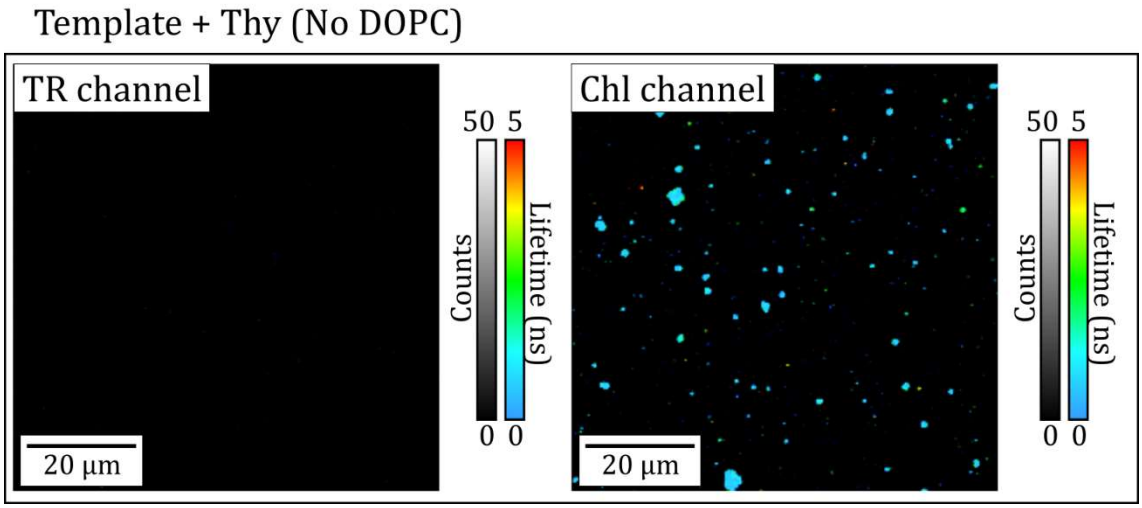

Figure 4.13: The deposition of thylakoid extracts onto patterned glass substrates in the absence of lipids to investigate what determines the formation of high-quality hybrid membranes. FLIM image of thylakoid extracts deposited on a patterned surface. The sample was prepared by incubating the standard concentration of thylakoid extracts (0.18 mg/mL) with a patterned glass coverslip for 30 min. The sample was washed with copious buffer solution before imaging. Left column: fluorescence due to lipids (Texas Red DHPE). Right: Fluorescence due to the thylakoid proteins (chlorophyll).

In the absence of a template, the DOPC lipids appear to form an imperfect lipid bilayer (*left panel,* **Figure 4.14**), with multiple holes and bright patches surrounded by an otherwise homogeneous distribution of intensity. Inspecting the Chl channel (*right panel,* **Figure 4.14a**), it seems that the thylakoid membranes did not merge with the DOPC membrane and remained as distinct particles. A FRAP (photobleaching) experiment was performed to test whether the thylakoid membranes were connected to the DOPC bilayer; if the thylakoid fluorescence could even partially recovered after photobleaching this would suggest that some proteins can diffuse between the DOPC membrane and the thylakoid extracts. After photobleaching, there was no recovery of the bleached thylakoid extracts (**Figure 4.14c**), whereas the lipids within the synthetic membrane showed significant lateral diffusion (**Figure 4.14b**) within the DOPC bilayer. This is evidence that the Diyne-PC template is absolutely required in order for thylakoid membranes to merge with DOPC lipid membrane during the formation process of hybrid membranes.

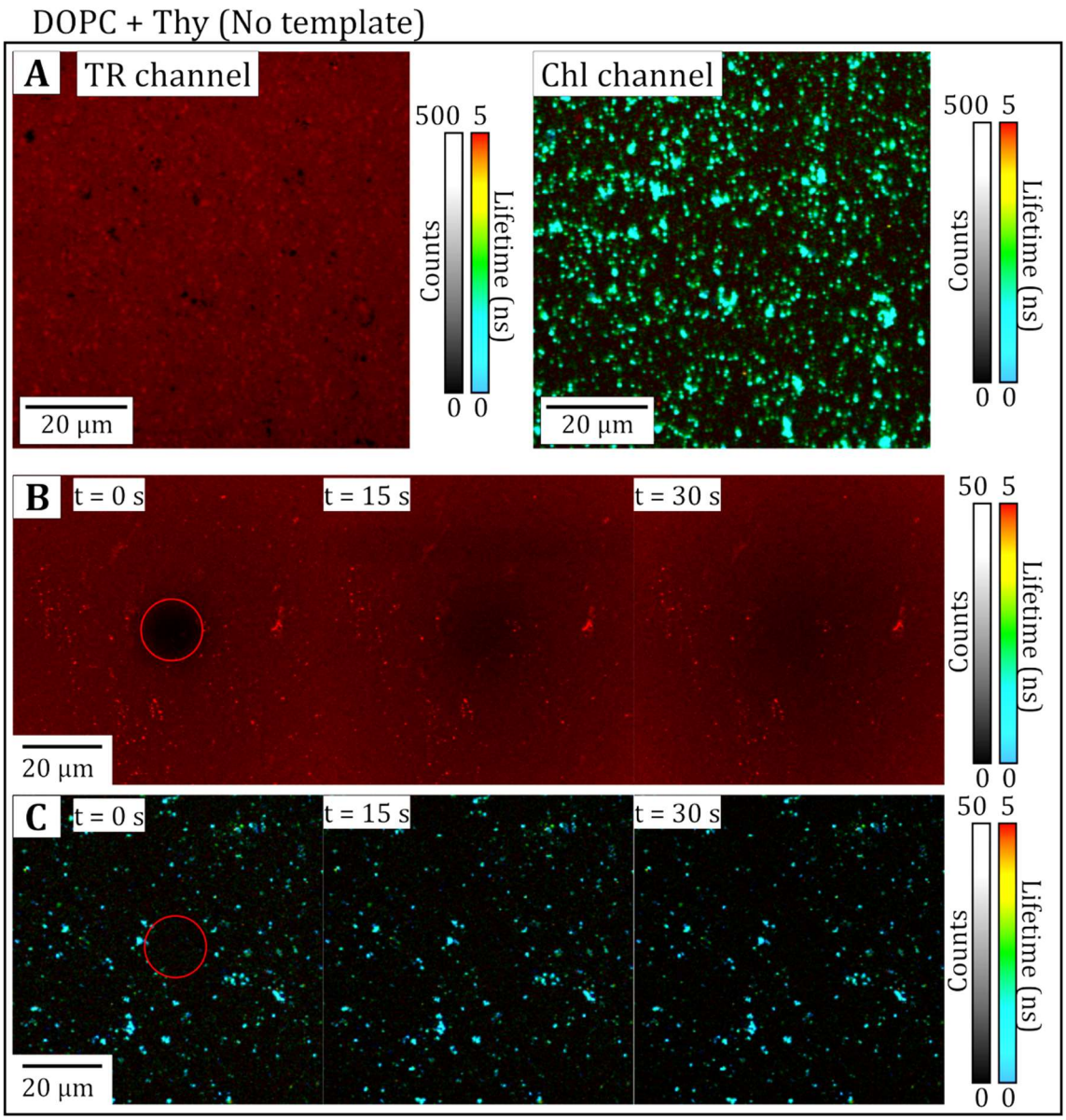

Figure 4.14: The deposition of thylakoid extracts and DOPC lipids without a template to investigate what determines the formation of high-quality hybrid membranes. **(A)** FLIM image of a mixed assembly of thylakoid membranes and DOPC SLBs on glass. The sample was prepared by mixing the standard 1:3 ratio (weight/weight) of extracted thylakoid membranes with DOPC vesicles as an aqueous suspension (total concentration 0.5 mg/mL), and then depositing these onto a hydrophilic glass coverslip for 30 minutes. The sample was washed with copious buffer solution before imaging. Here, the DOPC liposomes were labelled with 0.5% (mol/mol) Texas Red-DHPE. **(B)** and **(C)** Photobleaching measurements to test the lateral diffusion of the lipids and proteins shown in the *top* panel. Left column: fluorescence due to lipids (Texas Red DHPE). Right: Fluorescence due to the thylakoid proteins (chlorophyll).

Finally, a DOPC membrane was pre-formed within a template and thylakoid membrane added afterwards, then the surface was washed with buffer flow to remove any loosely attached particles. This sample was imaged in a two-stage process, recording the location of thylakoid extracts immediately after incubation but prior to washing the sample and after the sample has been washed with copious amounts of buffer. Before washing, thylakoid particles can be observed across the surface with no particular pattern of preferential adherence to either the template grid or DOPC box region (**Figure 4.15a**) (although this could be obscured by the many out-of-focus particles which are in solution above the surface). This suggested that there were only loose interactions between thylakoids and a complete lipid bilayer. This was confirmed by the subsequent images acquired after washing the surface with fresh buffer solution, where thylakoid extracts have been completely removed from the sample surface (**Figure 4.15b**).

The fluorescence lifetimes of the Chl fluorescence in all four scenarios were very short (~0.5 ns) and similar to the lifetime of thylakoid extracts. This suggests that the density of proteins was still very high, and that proteins had not been able to diffuse outward from the thylakoids into a hybrid membrane resulting in a lower protein density and a longer fluorescence lifetime (~4 ns). All together, this series of experiements demonstrate that it is not merely the presence of DOPC or the template that triggers the insertion of LH and PS proteins into the bilayer, but the combination of the exposed edge of the diyne-PC template together with a developing DOPC bilayer. More specifically, the lack of protein incorporation when thylakoids are deposited on top of a pre-formed lipid bilayer shows that it is unlikely the proteins are able to transfer vertically between the thylakoid and the DOPC membranes (this would expose hydrophobic portions of the protein to the polar solvent which would be thermodynamically unfavourable[197]).

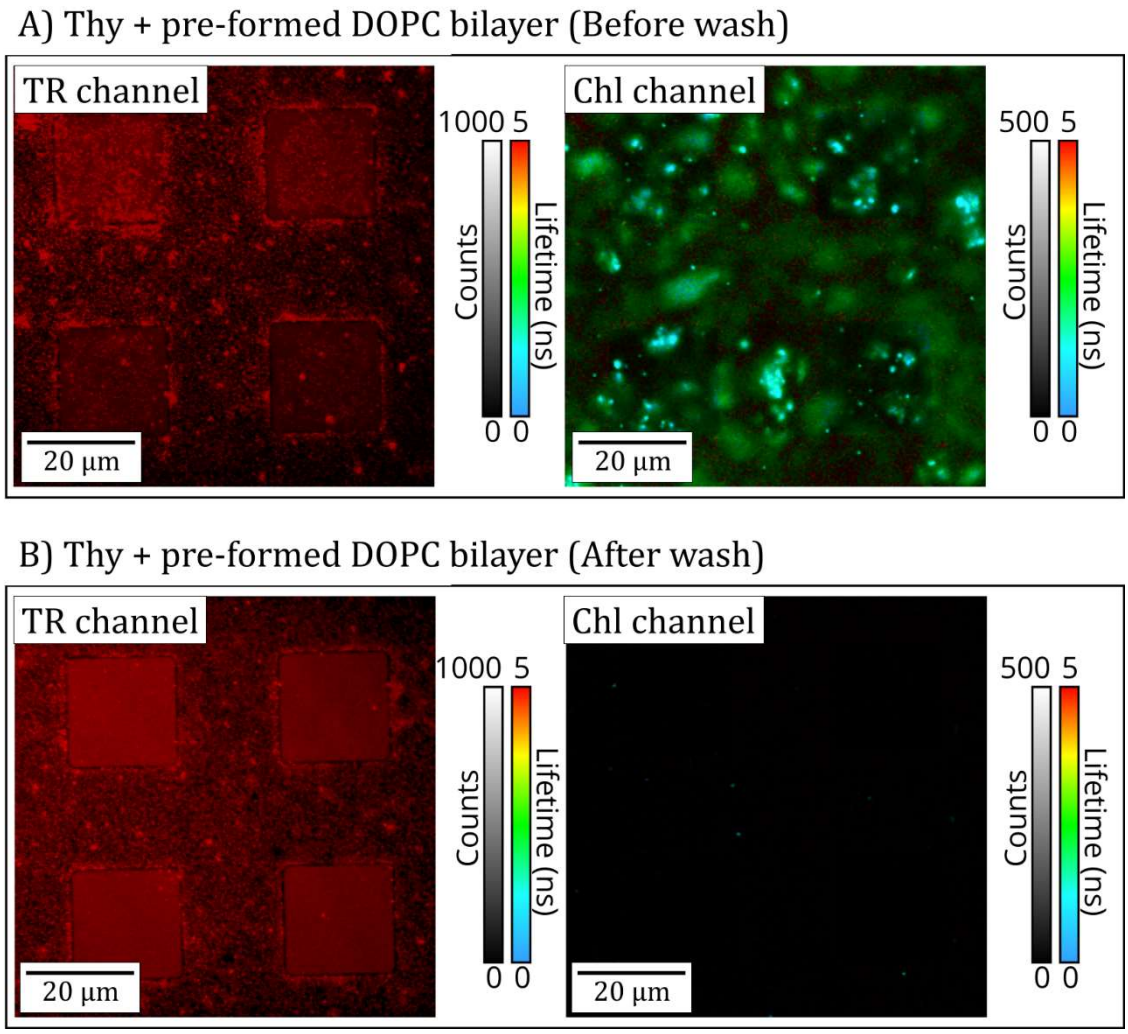

Figure 4.15: The deposition of thylakoid extracts onto performed lipid membranes to investigate what determines the formation of high-quality hybrid membranes. **(a)** FLIM image after thylakoid extracts were incubated with "pre-formed" lipid membranes within the standard Diyne-PC template pattern, before any washing procedures. This sample was prepared in a two-stage process: (i) a template pattern was incubated with 1 mg/mL lipid vesicles comprised of 99.5% (mol/mol) DOPC and 0.5% Texas Red-DHPE for 30 min and then washed with buffer solution, (ii) this surface was then incubated with the standard concentration of thylakoid extracts (0.121 mg/mL). Microscopy was performed on this sample immediately. **(B)** FLIM image after washing the sample from (A) with copious buffer. As can be observed, no thylakoid membranes remained. Left column: fluorescence due to lipids (Texas Red DHPE). Right: Fluorescence due to the thylakoid proteins (chlorophyll). The buffer used was 50 mM KH_2PO_4, 10 mM NaCl, 2 mM $MgCl_2$, 330 mM sorbitol, pH 7.5 throughout.

4.4.2 Time-lapse FLIM reveals that the lipid membrane forms before the protein incorporation into the membrane has reached its maximum

To directly observe the process of the hybrid membrane formation, time-lapse FLIM measurements were taken over the duration of the hybrid membrane self-assembly, and the intensity and lifetime of Chl fluorescence was monitored during this time. Each image (**Figure 4.16a**) represents the cumulative sum of all photons detected in a 20 s period, the minimum time required to provide sufficient signal for analysis. Over the 30-minute duration of the experiment, the time-lapse FLIM data shows an increasing Chl intensity. There appeared to be two types of membranes, distiniguished by their size and photophysical features: (i) a fluorescence signal with a relatively long fluorescent lifetime, ~4 ns, that predominantly occupied the square corral regions of the diyne-PC template (*red square* features in **Figure 4.16a**); (ii) a signal with a short fluorescent lifetime, ~0.4 ns, that appeared as small globular particles across the whole image and became more numerous over time (large *blue/green* spots in **Figure 4.16a**). These two sub-populations had very similar fluorescent lifetimes to the "washed" hybrid membranes and extracted thylakoids previously calculated (see **Figure 4.16c,** repeated from **Figure 4.7**) and were therefore presumed to be developing hybrid membranes and extracted thylakoids that had not merged with the synthetic lipid bilayers for (i) and (ii), respectively. At later time points (after 300 s), the intensity due to extracted thylakoids continued to increase, ultimately obscuring the long-lifetime signal underneath. In several instances, Chl fluorescence appeared to diffuse radially outward from an extracted thylakoid that had adhered on top of a developing corraled membrane (**Figure 4.16b**), suggesting some level of connectivity between the two.

To be able to suggest different mechaisms for the membrane self-assembly, we wished to quantify the rate of deposition for different membrane components. To achieve this, the FLIM was set up to detect either Chl fluorescence or fluorescence specific to the synthetic tipids (DOPC), and timelapse FLIM measurements were obtained during incubation of the patterned template in the thylakoid/DOPC solution to directly observe the membrane self-assembly.

First, to monitor the deposition of photosynthetic components, frequency distribution plots of the fluorescence lifetimes were generated for each 20 s timepoint (**Figure 4.16d**). As anticipated from the FLIM images, we observed a bimodal lifetime distribution, consisting of a long lifetime peak and a short lifetime peak, consistent with the frequency distribution plots from the steady-state samples of hybrid membranes and extracted thylakoids, respectively. The lifetime distribution for each timepoint was deconvoluted into two Gaussian populations, as shown in **Figure 4.16e** (acceptable fits were achieved for all time-points, with $R^2 > 0.9$). The peak amplitude of each Gaussian, representing the size of the sub-population, was plotted against time in order to determine the rate of deposition for each type of membrane, see **Figure 4.16f**. The amplitude for extracted thylakoids increased with time in a roughly linear manner suggesting a progressively increasing surface coverage (*blue line* in **Figure 4.16f**). This signal may be expected to saturate after a sufficiently long time as the surface becomes completely covered by extracted thylakoids, but the deposition process was stopped before this point was reached. For hybrid membranes, the amplitude increased at a much faster rate reaching a maximum value at ~500 s (*green line* in **Figure 4.16f**).

Next, to monitor the rate of the assembly of synthetic lipids, a small amount of fluorescently-tagged lipids were incorporated into DOPC vesicles (0.5 % weight/weight Texas Red lipids), before mixing with extracted thylakoids. Time-lapse FLIM was performed on this sample (**Figure 4.17a**) to track the fluorescence specific to lipids during hybrid membrane formation, and images were analyzed as above (**Figure 4.17b** and *red data points* in **Figure 4.17c**). This was compared to the accumulation of Chl fluoresence into hybrid membranes into hybrid membranes (*green data points* in **Figure 4.17c**). Analysis of this comparison shows that the lipid component saturates much earlier than the protein component ($t_{max} \sim 100$ s for TR-lipids, $t_{max} \sim 600$ s for Chl-proteins) and **Figure 4.17a** shows the lipid fluorescence was homogeneous across the corral at t = 100 s, suggesting a close to, or completely, fluid DOPC bilayer at this time.

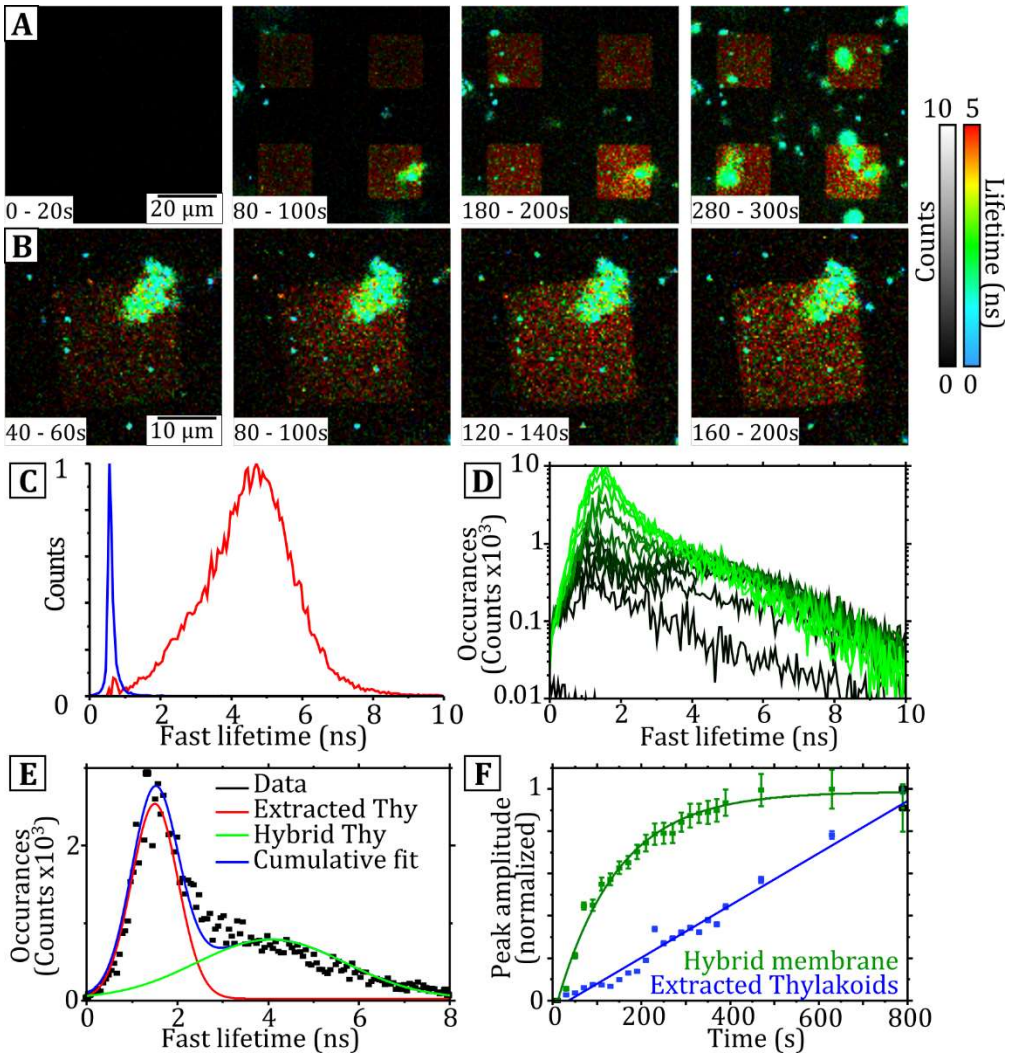

Figure 4.16: Analysis of the dynamic assembly processes occurring during hybrid membrane formation. **(A)** Time-lapse series of FLIM images during hybrid membrane formation. Each panel shows a 20-second acquisition. **(B)** Time-lapse series of FLIM images during the formation of hybrid membranes showing an example of a large extracted thylakoid adhered to a nascent membrane. **(C)** Frequency distribution of fluorescence lifetimes from extracted thylakoids (blue) and hybrid membranes (red). This panel is repeated from **Figure 4.8** to allow a side-by-side comparison with subsequent panels. **(D)** Evolution of the frequency distribution of fluorescence lifetimes during the time series shown in (a). *Dark green* to *light green* coloured curves represent increasing time-points **(E)** An example frequency distribution from a 20s snapshot (t = 220-240s), deconvoluted into two peaks (long-lifetime and short-lifetime). **(F)** The growth of components of the hybrid membrane over time (normalized to its maximum value for display purposes). *Green*: photosynthetic proteins in the hybrid membrane, tracked through the long-lifetime peak amplitude from (e). *Blue*: extracted thylakoids signal, tracked through the short-lifetime peak amplitude from (e).

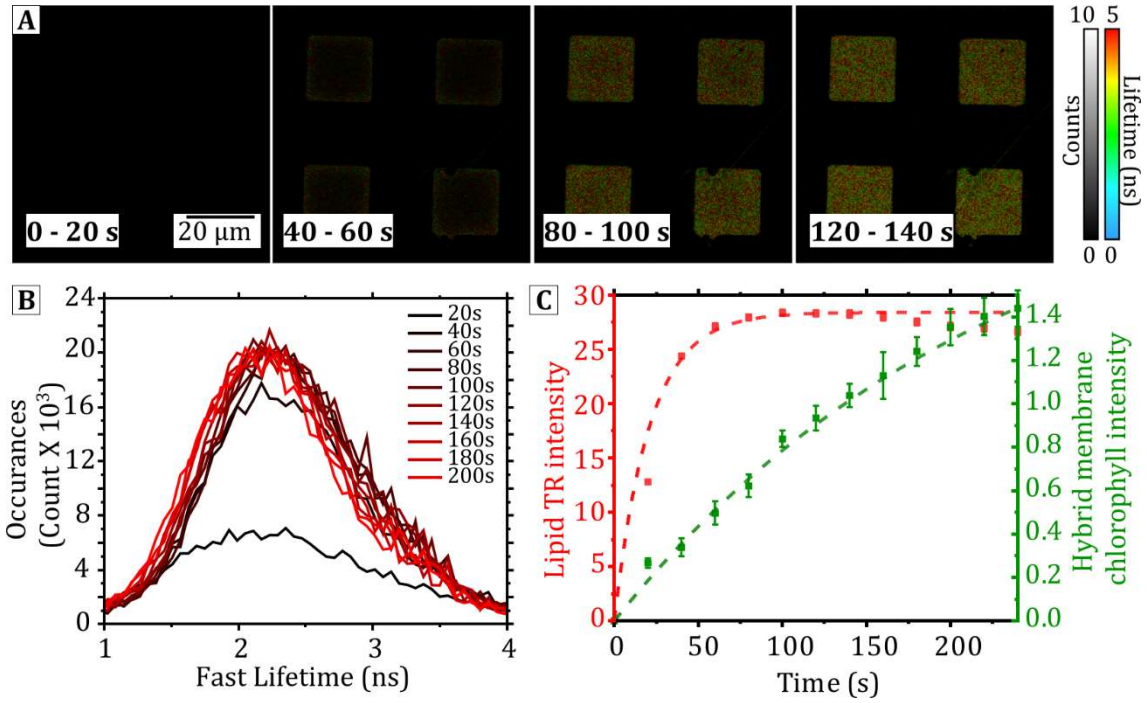

Figure 4.17: Analysis of the dynamic process of hybrid membrane formation monitoring the formation of the lipid component. **(A)** A series of FLIM images showing the deposition of a hybrid membrane containing both photosynthetic proteins and fluorescently tagged (TR-DHPE) lipids. The FLIM channel shown here is optimized for the detection of Texas Red, in order to compare the rate of lipid deposition to the deposition of photosynthetic proteins (excitation at 561 nm and emission collected between 590-650 nm). **(B)** Evolution of the frequency distribution of lifetimes during the deposition. Dark red to light red represents the cumulative frequency distribution at increasing time points of 20-40s, 40-60s, 60-80s, 80-100s, 100-120s, 120-140s, 140-160s, 160-180s, 180-200s. Each distribution is fitted to a Gaussian curve, in order to calculate the Peak amplitude at each point. **(C)** Analysis of the growth over time of the TR intensity (from the peak amplitude data from panel (b), compared to the hybrid membrane Chl intensity (from the long-lifetime Chl peak amplitude data from main text Figure 3). The time at which the lipid signal reaches a maximum value, t_{max}, is a lot sooner (~60s) than that for the hybrid membrane Chl intensity (~500s).

For both lipid and protein accumulation, it is possible that the saturation behaviour arises from the effect of filling the finite area within the corral regions. This is consistent with the established model for a Langmuir isotherm,[198] where the rate of material adsorption onto a substrate is proportional to the remaining free space on the substrate. In the early stages of this model, there is a large amount of free space remaining and the rate of deposition is almost linear. At later stages, the surface become increasingly occupied, and the rate of deposition then starts to slow down, eventually saturating. The Langmuir model is expressed mathematically as $n = N - e^{(-\frac{R}{N}t+C)}$, where n is the number of absorbed molecules, R is a rate constant, N is the number of empty sites, t is the elapsed time, and C is some constant. To compare the two processes, the peak amplitude curve for both the protein and lipid deposition was fit to the Langmuir model, and the rate of lipid deposition was found to be 5.5 times greater than the rate of protein deposition ($R_{lipids} = 0.039$, $R_{proteins} = 0.007$). Both the faster depositon rate and the time-lapse images suggest that a bilayer of synthetic lipids is largely assembled inside the corral, before the majority of photosynthetic proteins have been incorporated into the membrane: in fact, the amplitude representing proteins assembling in hybrid membranes increases another two- to three-fold after the lipid signal has saturated (compare *green* vs *red* curve at t=100 s in **Figure 4.17c**).

4.4.3 Discussion of the mechanism of hybrid membrane assembly into the Diyne-PC templates

The findings of this section can be briefly summarised into a several points that broadly describe the process of hybrid membrane formation: (i) Both the diyne-PC template, and a developing lipid membrane are required for hybrid membrane formation. (ii) Proteins are unlikely to move vertically between stacked membranes. (iii) Thylakoid extracts adhere to the top of the forming hybrid membrane, and Chl fluorescence appears to spread radially from the extracts into the hybrid membrane (iv) The lipid component of the hybrid membrane forms very rapidly, and is mostly complete before the bulk of the proteins insert into the hybrid membrane.

From the direct observations of the migration of Chl fluorescence from an extracted thylakoid into the hybrid membrane (**Figure 4.16b**) and the results suggesting that

proteins are unable to move vertically between bilayers (**Figure 4.15**), it seems probable that proteins and thylakoid lipids migrate laterally between the ruptured thylakoids and the DOPC membrane. Therefore, we hypothesize that extracted thylakoids adhere to, and form lipid bridges with, exposed edges in the developing DOPC lipid bilayer. These adhered thylakoids may act as reservoirs, from which photosynthetic proteins undergo diffusion down a concentration gradient into the spreading hybrid membrane, as proposed in the cartoon in **Figure 4.18a**. Random (Brownian) motion in 2-D is expected to lead to an overall migration of membrane proteins from a high concentration in the thylakoids to a lower concentration in the hybrid membranes.[199] This diffusion would eventually tend towards a dynamic equilibrium where a lower energy state is achieved, and result in the saturation-like behaviour observed in both the lipid and protien deposition curves.

This hypothesis may also explain some of the characteristics of hybrid membranes examined in previous sections. Firstly, the concentration driven diffusion of proteins from a high to a low concentration, would result in a reduced protein density, and the elongation of fluorescence lifetimes previously described (section 4.2.2 and section 4.3.2). It also is likely that this method of hybrid membrane formation favours the generation of a system with a large proportion of mobile proteins (as observed in FRAP measurements in section 4.3.4), since only those proteins that are able to laterally diffuse along lipid bridges could be incorporated into the membrane. By extention, this process could result in the selective sorting of proteins into one transmembrane orientation with the exclusion of proteins that have an orientation where bulky extramembraneous protrusions would come into contact with the substrate. For example, PSII protrudes asymmetrically from the lipid bilayer (~4 nm on the lumenal side, compared to ~1.7 nm on the stromal side[72]), and is likely to be immobile if the lumenal side experiences friction with the underlying substrate.

Finally, this process of membrane self-assembly may also result in the defects observed in AFM measurements (section 4.3.5). It is possible that the nanoscale pores in the membrane form when thylakoids that are loosely associated or have partially fused with the SLB are stripped away from the surface, pulling away sections of the membrane and leaving some material stuck to the substrate

(illustrated in **Figure 4.18b-c**). This interpretation is in agreement with other studies which observed lipid and cofactor diffusion between multilayers of stacked model membranes[200] and bears similarities to the dynamic protein rearrangements which occur in natural thyalkoids.[75, 166]

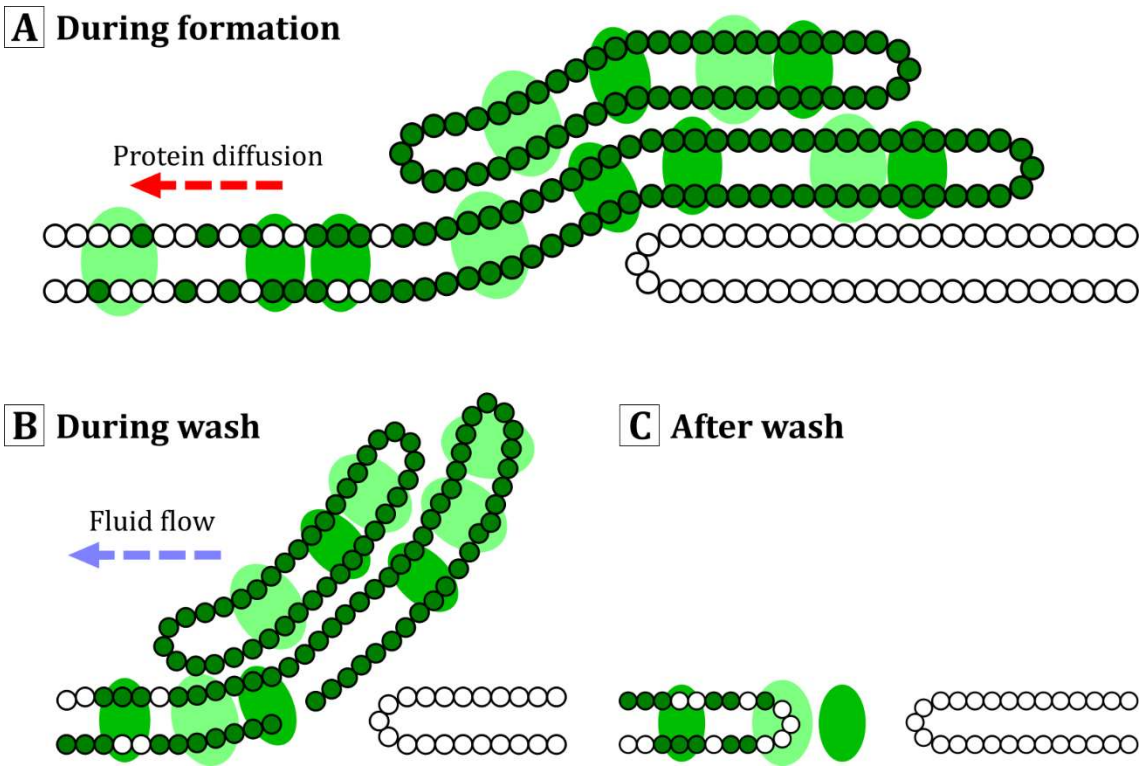

Figure 4.18: Illustration of the proposed process of hybrid membrane formation. **(A)** Extracted thylakoids adhere to the top of the membrane, and form lipid bridges with the underlying DOPC membrane (*green* and *white circles* represent thylakoid lipid and DOPC headgroups, respectively). Proteins within the thylakoid extract diffuse into the underlying hybrid membrane. **(B)** Proposed schematic of the hybrid membrane during the wash step. The loosely adsorbed thylakoid extracts are washed away in the direction of fluid flow, severing the connection with the hybrid membrane. **(C)** The hybrid membrane after the wash step. The removal of the lipid bridge between the thylakoid extract and the hybrid membrane may result in a defect where some photosynthetic proteins are immobilised.

4.5 Assessing the photosynthetic activity of hybrid membranes reveals that a commonly used functionality assay may be non-specific

Finally, we attempted to assess the photosynthetic activity of the hybrid membranes, specifically, the transduction of excitation energy into electron transport (photochemistry). If this functionality is even partly retained in hybrid membranes, then this model system could be used to investigate these fundamental processes, or, due to the ability of PSII to donate electrons to downstream inorganic systems, may have applications in future photo-electronic technologies.[201, 202]

4.5.1 Experimental concept: a photochemical assay to test electron transfer functionality from PSII

Multiple studies have proposed that, by selectively switching on or off portions of the electron transfer energy process, various photochemical inhibitors can give an indirect measure of the activity of PSII.[203-206] Therefore, we performed a "photochemical assay" on hybrid membranes by monitoring changes to the Chl fluorescence intensity (and lifetime), in response to these inhibitors. In hybrid membranes as prepared, the water-soluble proteins responsible for electron transport from PSII to other proteins are likely to be missing and therefore PSII is unable to transfer electrons (see **Figure 4.19a**). In this scenario, the PSII is saturated with electrons and absorbed energy from PSII would be primarily released as Chl fluorescence. In the first stage of the assay to test the system, an exogenous electron acceptor, DMBQ, is introduced to the membranes at a relatively high concentration, to replace the natural electron carriers (PQ) which are likely to be saturated.[203, 204, 207] If DMBQ successfully accepts electrons from PSII, the level of Chl fluorescence should be reduced in its presence compared to its absence, because excitation energy can be used to eject electrons rather than being re-emitted (**Figure 4.19b**). In the final stage of the assay, "hydroxylamine" can be added as an aqueous solution and is known to increase the Chl fluorescence again (see **Figure 4.19c**).[206, 208, 209] Hydroxylamine is a small highly reactive compound, that has been frequently used to block the electron flow of PSII.[210] It is reported to affect various cofactors within

PSII, disrupting the oxygen-evolving complex and inhibiting the electron transfer cycle.[211]

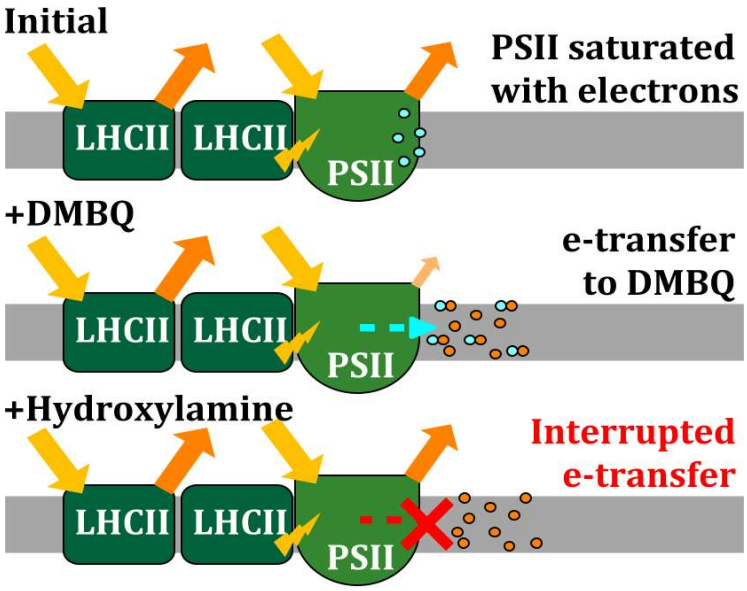

Figure 4.19: Illustration of the photochemical assay used to measure the electron transfer capabilities of hybrid membranes. **(A)** Initially, electron transport from PSII is prohibited and PSII is saturated with electrons (*blue circles*), and energy is primarily released as Chl fluorescence. **(B)** Upon the addition of DMBQ (*orange circles*), electron transfer occurs from PSII to DMBQ, and Chl fluorescence is quenched. **(C)** After the addition of hydroxylamine, electron transfer from PSII to DMBQ is interrupted, and the Chl fluorescence recovers.

4.5.2 The electron transfer assay has positive results for both PSII and LHCII (suggesting that it is inaccurate)

The photochemical assay described above was performed on hybrid membranes and control samples and characterized by FLIM. **Figures 4.19a(i)-(ii)** show that for hybrid membranes the Chl fluorescence intensity is indeed significantly quenched after the addition of DMBQ, to 55 % (± 13 %) of its original intensity. The additional decay mechanism resulted in the decreased fluorescence lifetime within the corrals of hybrid membrane (from *red* to *green* on the false-colour FLIM scale). Upon the addition of hydroxylamine, the fluorescence intensity recovered back to 97 % (± 17 %) of its initial intensity, see **Figure 4.20a(iii)**. The trends for fluorescence intensity and for fluorescence lifetime of hybrid membranes are shown as *green lines* in the graphs of **Figure 4.20c** and **4.20d**, respectively.

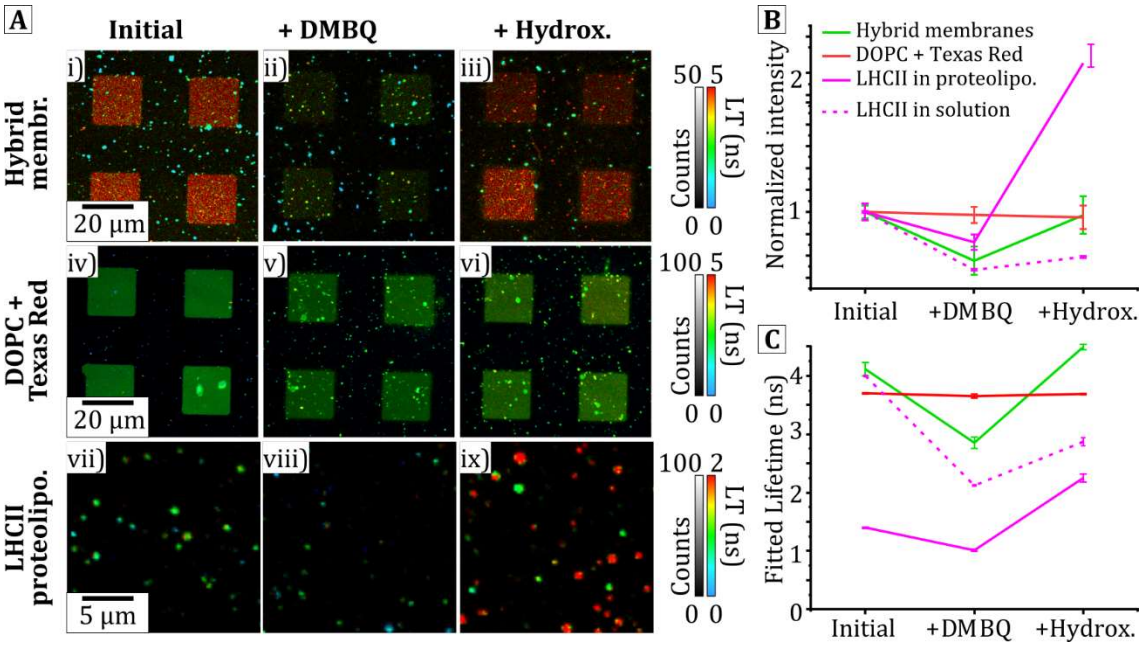

Figure 4.20: Quantification of possible photochemical activity using hybrid membranes and FLIM. **(A)** FLIM measurements of hybrid membranes, DOPC/TR lipid membranes, and LHCII proteoliposomes, before and after the addition of 0.5 mM DMBQ and after the addition of 0.5 mM hydroxylamine (as labelled). The FLIM instrument was set up to either detect Chl fluorescence for (i)-(iii) and (vii)-(ix) (with 640 nm excitation and 672-696 nm emission filters), or to detect TR fluorescence for (iv)-(vi) (with 561 nm excitation and 590-650 nm emission filters). Spectral overlap between these FLIM channels was minimal. **(B)** Graph showing the normalized fluorescence counts of each sample plotted against the different experimental conditions from (a) (averaged over 4 fields of view). **(C)** Graph showing the mean fluorescence lifetimes for each sample against the experimental conditions from (a) (averaged over 4 fields of view).

The fluorescence lifetime was reduced from 4.11 ± 0.12 ns initially to 2.85 ± 0.09 ns upon the addition of DMBQ, before recovering to 4.49 ± 0.05 ns upon the addition of the hydroxylamine. This final lifetime is longer than in the initial system and could be due to changes in the configuration of pigments within PSII after the addition of hydroxylamine.

A series of control samples were studied to assess the specificity of this assay for photosynthetic proteins and for probing electron transfer. DOPC lipid membranes containing the fluorophore Texas Red (without any proteins) showed typical images of patterned membranes (see **Figure 4.20a(iv)-(vi)**), with no significant change at any stage of the photochemical assay of either the fluorescence lifetime or the fluorescence emission intensity. This showed that DMBQ does not cause quenching of this chromophore and hydroxylamine does not affect it either (*red lines* in **Figure 4.20b-c**). Photochemical assays were then performed on control samples of both LHCII proteins within membranes that were deposited onto glass (*solid magenta lines* in Figure **4.20b-c**) and isolated LHCII proteins suspended in an aqueous solution (*dotted magenta lines* in **Figure 4.20b-c**). These were assessed as samples which contained Chl but not PSII and either represented the quenched state or non-quenched state of LHCII, respectively. Therefore, these samples are examples of photosynthetic proteins that lack the electron transfer functionality inherent in PSII that this assay is expected to probe. Surprisingly, the DMBQ caused quenching of the fluorescence intensity and lifetime in both LHCII-only samples, followed by the subsequent de-quenching by hydroxylamine. LHCII in proteoliposomes showed significantly less DMBQ-induced quenching and more hydroxylamine-induced de-quenching compared to LHCII in solution, presumably because LHCII in proteoliposomes started in an already heavily quenched state.

4.5.3 Discussion: Interpreting the results of the photochemical assays

The results of the photochemical assays suggest that the DMBQ/hydroxylamine assay is not specific for detecting electron transfers to and from PSII. Neither DMBQ or hydroxylamine induced a change in the fluorescence of Texas Red, so it is possible that the effects of this assay are specific to systems containing chlorophyll pigments. Whilst we cannot definitively rule out the possibility that the glass surface alters the structure or chemical activity of LH or PS protein complexes, we note that previous studies have concluded that LHCII and other protein complexes are not adversely affected by interactions with glass[80, 172] or mica[56] surfaces (comparisons of their fluorescence emission spectra indicate that the native protein conformation is maintained).

One possibility for DMBQ-induced quenching is a direct "collisional quenching" mechanism whereby DMBQ diffuses through the lipid bilayer or through the aqueous solution and quenches an excited state upon close contact with Chl pigments.[212] Alternatively, several authors report fluorescence quenching in LHCII via internal charge transfer mechanisms,[103, 213-215] and there are even reports that LHCII can act as a photosensitizer for biophotovoltaic devices, i.e., it can directly donate electrons to electrodes under certain conditions (e.g., applied voltage).[216, 217] Therefore, it seems feasible that DMBQ could accept electrons from both PSII and LHCII resulting in the reduction in fluorescence lifetime and intensity of Chl fluorescence.

The exact mechanism for the inhibition of PSII by hydroxylamine has been the subject of some scrutiny within the photosynthetic community. Various papers suggest that PSII inhibition by hydroxylamine consists of two-mechanisms, a reversible and non-reversible mechanism, that occur at high (>1 mM), and low (<1 mM) concentrations of hydroxylamine, respectively.[218] In the reversible process, oxygen-evolution is inhibited due to the reduction and subsequent release of manganese (an essential catalyst for O_2 conversion[210]) from the oxygen evolution complex (OEC) of PSII.[219, 220] This process seems unlikely to apply to LHCII, or other Chl containing proteins, that are not responsible for O_2 evolution. In the irreversible

process, hydroxylamine is believed to competitively bind with specific moieties within PSII as part of a chemical reaction with either water-splitting enzymes or pigments.[211, 221] It seems more likely that hydroxylamine lacks binding specificity and has the potential to react with and disrupt other Chl-containing proteins (and potentially other molecules). Indeed, hydroxylamine seems to be used as a small-molecule reducing agent for various purposes in chemistry and other industries (e.g., photography).[222] The increased Chl fluorescence lifetime of >4 ns could suggest that hydroxylamine may either cause some sort of disaggregation of Chls which increases the intra-protein Chl-Chl distance, or a chemical change to the Chls which decreases the dipole-dipole coupling.

A virtue of the use of FLIM over fluorescence intensity measurements is that one can quantify fluorescence quenching more definitively to give confidence in our interpretations (intensity measurements can be subject to distortions due to changes in pigment concentration whereas decay rate is unaffected). Despite the lack of PSII specificity of the photochemical assays, the results show that our hybrid membranes contain "active" Chl which responds to chemical modifications in a very different manner to other fluorophores, such as Texas Red. Our comparisons of LHCII in a quenched and non-quenched state, also indicate that the initial photophysical state of the proteins can significantly alter the outcomes or interpretations of functionality assays.

4.6 Section summary and discussion

Hybrid membranes have distinct advantages when compared to native thylakoids or other model systems as a platform to study the fundamentals of photosynthesis. Natural thylakoid extracts are heterogeneous, micro/nanoscale structures and are difficult to study due to their relatively instability. Alternative model membrane systems are typically formed by "bottom-up" approaches that use purified proteins and lipids to exert control over the system composition. For example, proteoliposomes can be very useful but they are formed at the expense of missing out many important components of an LH membrane and a resulting in a simplification of the complex interactions observed in natural membranes.[74, 79, 119-121, 173, 174, 177-179] Hybrid membranes offer an intermediate situation, and consist of a

stable, flat, and largely homogeneous structure (observed by FLIM and AFM) formed via self-assembly from natural membranes, such all the natural LH and PS proteins are potentially available for analysis. Our FLIM and FRAP measurements show that the proteins are highly mobile (~80% mobile fraction) and are free to interact with the surrounding lipids/proteins in a way that is unimpeded by the substrate. The protein concentration (approx. 1% of the membrane area) is significantly lower than that of native membranes, and the dilution of thylakoid proteins with synthetic lipids could disrupt natural protein-protein interactions in a way that they may not return. However, there are many possible avenues which could be pursued in future studies to increase the protein concentration or alter the structural organisation of the hybrid membranes to better represent the native system, such as altering the concentrations of the starting material,[162] or by using techniques established in the SLB community to direct the diffusion of membrane proteins.[223, 224] Another possible limitation is that protein incorporation into hybrid membranes may favour particular proteins, and the ratio of LHCII to PSII (or other proteins) in hybrid membranes may not reflect the ratio found in natural systems. To account for this, future studies should aim to precisely quantify the protein populations present in hybrid membranes. One possibility could be to use detergents to extract the proteins from hybrid membranes for separation and analysis via gel-electrophoresis or size exclusion chromatography[225, 226] (multiple samples may need to be extracted and combined to obtain sufficient material for these type of biochemical methods). Alternatively, if mobile proteins (which appear highly mobile) could be made visible to AFM this would allow for a more complete analysis of protein dimensions and species. This could be achieved by either significantly increasing the AFM raster speed (previous studies have applied "fast scanning" AFM to study protein dynamics[227, 228]), or by significantly reducing the protein mobility (by reducing the temperature[229], or by inducing lipid-phase transitions lipids to "lock" the proteins in place[230, 231]).

The combination of FLIM and AFM allowed us to observe the dynamic behaviours and interactions of individual elements of photosynthesis (i.e., LH and PS protein complexes) in a controllable platform, and opens the possibility to manipulate them. The fluorescence lifetime increased from ~0.5 ns in natural membranes to ~4 ns in the hybrid membranes, which suggests that the chlorophyll-proteins are switching

from a quenched to a light-harvesting state as the protein concentration decreases. Such changes in fluorescence lifetime have been previously suggested to relate to energy-dissipating pathways within LHCII being switched on and off and the crucial process of "photoprotection" in plants.[39, 55, 56, 61, 66, 79, 106] It seems feasible that future studies could explore the fluorescence switching of single LH and PS proteins by utilizing a hybrid membrane platform that has a very low protein concentration within the membrane (to allow single protein tracking). Another key advantage of using model membrane systems is that specific proteins of interest can be investigated, as shown in our application of our hybrid membranes and proteoliposomes to photochemical assays. This revealed new challenges in accurately determining electron transport using DMBQ and hydroxylamine, suggesting that the assays used in the photosynthesis community may have to be reassessed.[206, 208, 209, 211]

By imaging the self-assembly of lipids and photosynthetic proteins onto the solid surface in real time, we found that both the hydrophobic edge of the Diyne-PC corral and the developing DOPC bilayer are necessary for the formation of flat and contiguous membranes from highly curved natural membranes. One possibility is that hydrophobic interactions between the diyne-PC lipids and the thylakoid extracts reduces the free-energy required for bilayer formation and help to stabilise the otherwise highly-curved thylakoid membrane[133, 232] This suggests that the polymerized lipid template could be used to support the formation of supported lipid bilayers from a range of biological membranes that are otherwise difficult to study (high-curvature, protein-dense).

4.7 Concluding remarks and future outlook

In this chapter, the photophysical properties and topological structure of the hybrid membrane model system have been compared to the structure of native-like bio-membrane extracts. The hybrid membranes were characterized in detail to provide new information regarding the nanoscale structure of the membrane, the kinetics of membrane self-assembly, and their applicability to testing the function of photosynthetic functionality. Overall, the results in this chapter demonstrate the consistency and experimental accessibility of the hybrid membrane as a testbed for

photosynthetic research. Despite the significantly lower protein density than that found in natural systems (1% vs ~70%), it was possible to acquire much useful information about membrane structure and the resulting photophysical properties. The limitation of a low protein density may be overcome in future work.

In future studies, hybrid membranes could be applied to investigate the roles of specific photosynthetic components by directly controlling the membrane composition. There are several possible routes to generate a new variety of model membranes, including (i) varying the starting thylakoid-to-DOPC ratio to alter the protein concentration, (ii) incorporating natural membranes from different plant mutants to alter the distribution of protein species[233, 234], and (iii) merging thylakoids with liposomes containing photosynthetic components (thylakoid lipids, additional purified proteins[74, 163]) to exert a more precise control over the membrane composition or to introduce specific components and determine their effect. In this respect, hybrid membranes may have a particular advantage, in that "simple" changes to the experimental protocol could result in a series of samples that are both complementary (i.e., similar topography, dimensions, and experimental accessibility), yet sufficiently diverse to interrogate specific aspects of light-harvesting. In addition, it may be possible to generate desirable membrane architecture that might mimic the stacked structure of chloroplasts. Previous studies have shown that it is possible to generate self-assembling multilayered lipid membranes by exploiting electrostatic attractions between anionic lipids and cationic polymers,[200, 235] divalent cations,[236] or protein-protein interactions (including LHCII-LHCII).[74] It may be possible to modify our methodology in similar ways to generate multilayered Diyne-PC templates to address the stacked nature of bioenergetic membranes.

Finally, it may also be possible to take advantage of the self-assembly mechanism of hybrid membrane formation in order to introduce additional lipophilic components of interest (e.g., additional pigments for light-harvesting[98] or quinones[200]). In the following chapter, the potential modularity of the hybrid membrane system is investigated to generate light-harvesting membranes that are enhanced by the incorporation artificial chromophores. In later chapters, a modified version of the

hybrid membranes are used to investigate protein self-quenching, by using electric fields to directly control the protein concentration.

4.8 Chapter acknowledgements

This chapter describes results that have been published within the study:
Meredith S. A., Yoneda T., Hancock A. M., Connell S. D., Evans S. D., Morigaki K. Adams P. G. (2021), *Model Lipid Membranes Assembled from Natural Plant Thylakoids into 2D Microarray Patterns as a Platform to Assess the Organization and Photophysics of Light-Harvesting Proteins*, Small, 10.1002/smll.202006608

S. A. Meredith was responsible for the preparation of membrane samples, acquisition of FLIM, AFM and some solution-based spectroscopy data, analysis and presentation of data, and wrote the first drafts of the manuscript. T. Yoneda prepared the patterned membrane templates, and was first author in the original development of hybrid membranes (DOI: 10.1021/acs.langmuir.0c00613). A. M. Hancock performed purification of the LHCII protein, reconstitution of LHCII into proteoliposomes, acquisition and analysis of solution-based spectroscopy and epifluorescence data. K. Morigaki was the academic supervisor of T. Yoneda. S. D. A. Connell and P. G. Adams were the academic supervisors of both S. A. Meredith and A. M. Hancock. S. D. Evans provided additional academic supervision to S. A. Meredith.

5 Incorporating synthetic dyes into model membranes to generate bespoke light harvesting nanomaterials

5.1 Introduction

The biological systems characterised in this thesis are often a source of inspiration for the development of "artificial photosynthetic systems". Specifically, the enhancement of the pre-existing photosynthetic network is often the area of focus for energy research and nanotechnology, with scope to develop new bio-nanomaterials that can be used for light harvesting or the conversion of light energy into useful formats.

One promising avenue of bio-hybrid photosynthetic research is the concept of increasing the amount of light that is absorbed by the photosynthetic system. The combination of pigment arrangements and interactions in the plant LHCII gives the protein complex a high absorption efficiency across the bulk of the visible spectrum[1, 22], with two distinct peaks centred around 436 nm and 676 nm, respectively. However, there exists an area of minimal absorption between 520-620 nm, which has been marked in photosynthetic nomenclature as the 'green gap'[237]. Numerous authors have successfully filled the green gap by interfacing LHCII with complementary chromophores that absorb strongly in this spectral region, and transfer energy to the protein via Förster Resonance Energy Transfer (FRET)[237-242]. This was first demonstrated through the covalent attachment of one Rhodamine Red (absorption peak: 573 nm) dye per LHCII monomer[237] such that the dye was positioned in close proximity (<3 nm) to chlorophyll pigments in the proteins. In this system, the rhodamine acts as a FRET donor, due to the extensive overlap between the donor emission spectra and the LH (acceptor) absorption spectra. When this dye-protein system was excited within the green gap, the dye emission was almost entirely quenched, and the fluorescence emission of the LHCII was increased significantly, confirming that energy was being successfully transferred from the Rhodamine-donor to the LHCII-acceptor.

Since this initial demonstration, the list of proven donors for LHCII enhancement has evolved to include synthetic organic compounds[237-240] and quantum dots,[241, 242] and has so far relied on the direct attachment of the donor to the LHCII or the removal of LHCII from a native-like lipid environment. An obvious advantage of covalent bonding is that one may control the distance and orientation of the chromophores relative to each other, and optimise this to maximise the efficiency of energy transfer. However, the genetic and chemical protocols required to modify the protein are often expensive and time-consuming. The low throughput of protein modification for trialling lots of potential compounds is also a severe hindrance to the development, namely scalability, of these methods when considering future applications for light harvesting nanomaterials.

An alternative approach would be to introduce additional chromophores to LHCII, in a system that does not require direct covalent attachment but makes use of spontaneous self-assembly instead. Both micelles and liposomes have been used to bring FRET donor and acceptor molecules into close proximity, by relying on the self-assembly of amphiphilic molecules such as lipids.[243-245] In addition, it has already been demonstrated that LHCII can be integrated into model membranes (e.g. proteoliposomes and supported lipid bilayers[74, 119, 124]) as a platform to study its biophysical properties. Therefore, it seems feasible that a combination of LHCII and complementary chromophores could be reconstituted into a model membrane, as a means to enhance the spectral range of chlorophyll absorption. Whilst FRET between similar non-covalently coupled chromophores has been successfully demonstrated,[243] the free diffusion of tagged-lipids or proteins within the membrane, or inconsistencies with the self-assembly, may make it difficult to maintain a consistent distance between FRET components. Therefore ensuring that chromophore-chromophore coupling is sufficient for energy transfer is a potential challenge for applying this approach to photosynthetic enhancement.

Designing a modular system, in which there is control over individual components, would allow for a tuneable spectral range and energy transfer efficiency (ETE) and expanding the feasibility of this system for light harvesting materials with specific optical properties. In addition, adding the the chromophore to the lipid membrane would have several advantages compared to covalent modification of LHCII: (i)

lipids provide a more native environment for membrane proteins than detergent, (ii) membranes readily adsorb to hydrophilic solid supports so would be compatible with surface-based nanotechnologies (e.g., thin-film coatings), (iii) non-covalent systems allow greater flexibility to change the chromophore concentration (or type), (iv) membranes allow the potential to co-assemble other components to make for a modular system (e.g., other photosynthetic proteins or other small amphiphiles), and (v) the chromophore could self-assemble into a variety of model systems (e.g., proteoliposomes, SLBs, or hybrid membranes), creating a parallel series of solution- or surface-based nanomaterials with well characterised spectroscopic properties.

This chapter presents the development and quantification of two types of "enhanced" model membranes, in which the absorption of LHCII and other photosynthetic proteins is effectively increased by the introduction of synthetic pigments that self-assemble into model membranes.

5.2 Concept 1: Proteoliposomes as light harvesting nanomaterials

5.2.1 Modular reconstitution of LHCII and Texas-Red into proteoliposomes

The small organic chromophore Texas Red (TR) was selected as a suitable donor for a FRET based system to enhance the absorption of LHCII. TR is available to purchase in the form where the dye is tethered to a lipid headgroup (TR-DHPE, see **Figure 5.1c**), and has been shown to readily self-assemble into a variety of model lipid systems. In addition, the absorption of TR peaks at 591 nm fits well into the "green gap" of LHCII, and has an extensive overlap with Chl *b* Q_y band absorption in the LHCII absorption spectra (**Figure 5.1a**).

Initially, the viability of TR to act as a FRET donor to LHCII was assessed by calculating the Förster radius of the TR-LHCII pair (the distance at which energy transfer is 50% efficient, see section 1.1.4). From theory[28], the Förster radius (R_0) in Angstroms of a hypothetical donor-acceptor pair is defined as:

$$R_0^6 = 8.79 \times 10^{(-5)}\, J\, \kappa^2\, n^{-4}\, \phi \qquad \text{Eq. 5.1}$$

Where *J* is the spectral overlap integral between the donor emission and acceptor absorption, κ is the relative orientation of the donor and acceptor transition dipoles, *n* is the optical refractive index of the medium, and ϕ is the fluorescence quantum yield of the FRET donor. For a lipid-tethered-dye, such as TR, the fluorescent moiety was assumed to be randomly-orientated relative to the LHCII due to combined effect of both the lateral diffusion of both the lipid, and rotational diffusion of the tethered dye, equating to a value for κ^2 of 2/3.[29] The refractive index of the optical medium was assumed to be halfway between water (1.33) and lipid tail groups (1.55),[243] and was given a value of 1.45. A value of 0.93 was used for the fluorescence quantum yield of TR[246]. Finally, the spectral overlap integral was calculated using the measured spectra of TR emission and LHCII absorption (see *grey shaded area*, was calculated as 71.0 Å for the TR-LHCII pair. Therefore, providing that the TR and LHCII are geometrically close and in a favourable orientation, the TR may be able to act as the donor and pass an exciton to the Chl *b* chromophore in the LHCII complex (see structures in **Figure 5.1c-d**). In addition, the average distance between TR and LHCII molecules and therefore the energy transfer efficiency, can be modulated simply by changing the donor or acceptor concentrations. By varying the membrane composition it would be feasible to create membranes with desired spectroscopic properties and to maximise the energy transfer efficiency with sufficiently high concentrations of TR or LHCII. Proteoliposomes were selected as a model system to interrogate membrane proteins and lipids due to the established and straightforward methodology for their formation[247] and their accessibility to solution-based ensemble spectroscopy. In solution, the thermodynamically driven self-assembly of the lipid-LHCII membranes was expected to lead to the formation of fully enclosed liposomes such that no hydrophobic edges of the bilayer, or hydrophobic moieties on the protein are exposed to unfavourable interactions with the aqueous buffer[248]. This schematic is shown in **Figure 5.1b** where TR-DHPE and LHCII is incorporated into the membrane.

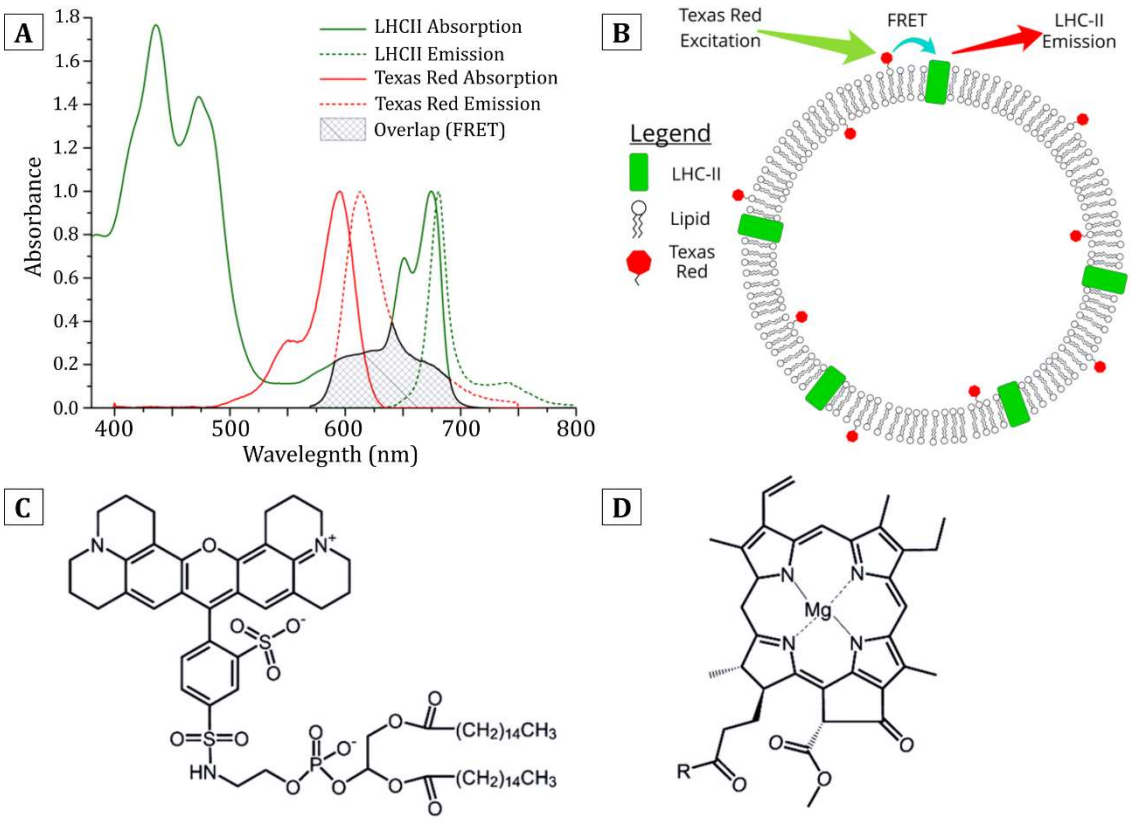

Figure 5.1: Considerations for the reconstitution of TR and LHCII into proteoliposomes capable of TR to LHCII energy transfer. **(A)** Absorption and emission spectra of TR and LHCII showing the spectral overlap integral which should allow efficient FRET. Normalised spectra of LHCII in 20 mM HEPES (pH 7.5), 40 mM NaCl and the normalised absorption and emission spectra of TR in detergent. The overlap between the donor (TR) emission and acceptor (LHCII) absorption is highlighted with a grey cross-hatch. **(B)** A schematic of a LHCII and TR proteoliposome (not to scale) highlighting the FRET relationship between a pair of chromophores. TR has the potential to pass excitation energy to the Chl *b* chromophore in the LHCII which could then be re-emitted by the LHCII complex. **(C)** Chemical structure of sulforhodamine 101 acid chloride, 1,2-dihexadecanoyl-sn-glycero-3-phosphoethanolamine, better known as Texas Red DHPE. **(D)** Chemical structure of chlorophyll *a*.

5.2.2 Spectroscopy measurements show that LHCII and TR incorporate into proteoliposomes with a high yield

LHCII protein was extracted from spinach leaves and biochemically purified using the protocols described in methods section 3.2.1. The TR-DHPE lipid was used as purchased (Life Technologies) and mixed to the desired ratios with synthetic lipids in organic solvents (see section 3.3.1). Both LHCII and TR-DHPE can be incorporated into vesicles and proteoliposomes at the desired concentrations using the procedures, previously outlined in methods, sections 3.3.2 and 3.3.3, but briefly described here. Initially LHCII, TR-DHPE and thylakoid lipids are fully solubilised with α-DDM detergent, followed by a gradual detergent removal using porous absorptive beads. This causes the thermodynamically-driven self-assembly of proteoliposomes. Other characterization by collaborators assessed the vesicle diameter as 50-100 nm (data not shown)[98].

To confirm the successful reconstitution of LHCII and TR into the proteoliposomes and assess the modularity of the system with regard to controlling both the donor and acceptor concentration, samples were prepared in two series. Proteoliposome Series 1 was designed to have a constant LHCII concentration of ~0.7 μM and a TR range from 1.4 to 14.1 μM. Proteoliposome Series 2 was designed to have a similar TR concentrations of ~6.8 μM with a LHCII range from 0.2 to 3.5 μM.

Firstly, ensemble absorption and fluorescence spectroscopy was performed on an isolated form of LHCII trimers in detergent micelles (*red dashed line,* **Figure 5.2a** and **5.2b**). This allowed for the quantification of the relative optical properties of the isolated state of LHCII and acted as a baseline for comparison to the proteoliposome system planned, where a series of LHCII-LHCII and LHCII-TR interactions are expected. These spectra can be compared to the spectra from proteoliposomes (*solid black-to-green lines,* **Figure 5.2a** and **5.2b**). All LHCII samples have similar absorption spectra with peaks representing chlorophyll (Chl) and carotenoids between 400-500 nm and the Q_y bands of Chl *b* and Chl *a* at 650 and 675nm, similar to the example shown in **Figure 5.1a**. Zooming in, the LHCII Q_y absorption peaks at 650 and 675nm have minimal shifts (<1-3 nm) (**Figure 5.2a**), and the single LHCII fluorescence peak is very similar across all LHCII concentrations (**Figure 5.2b**).

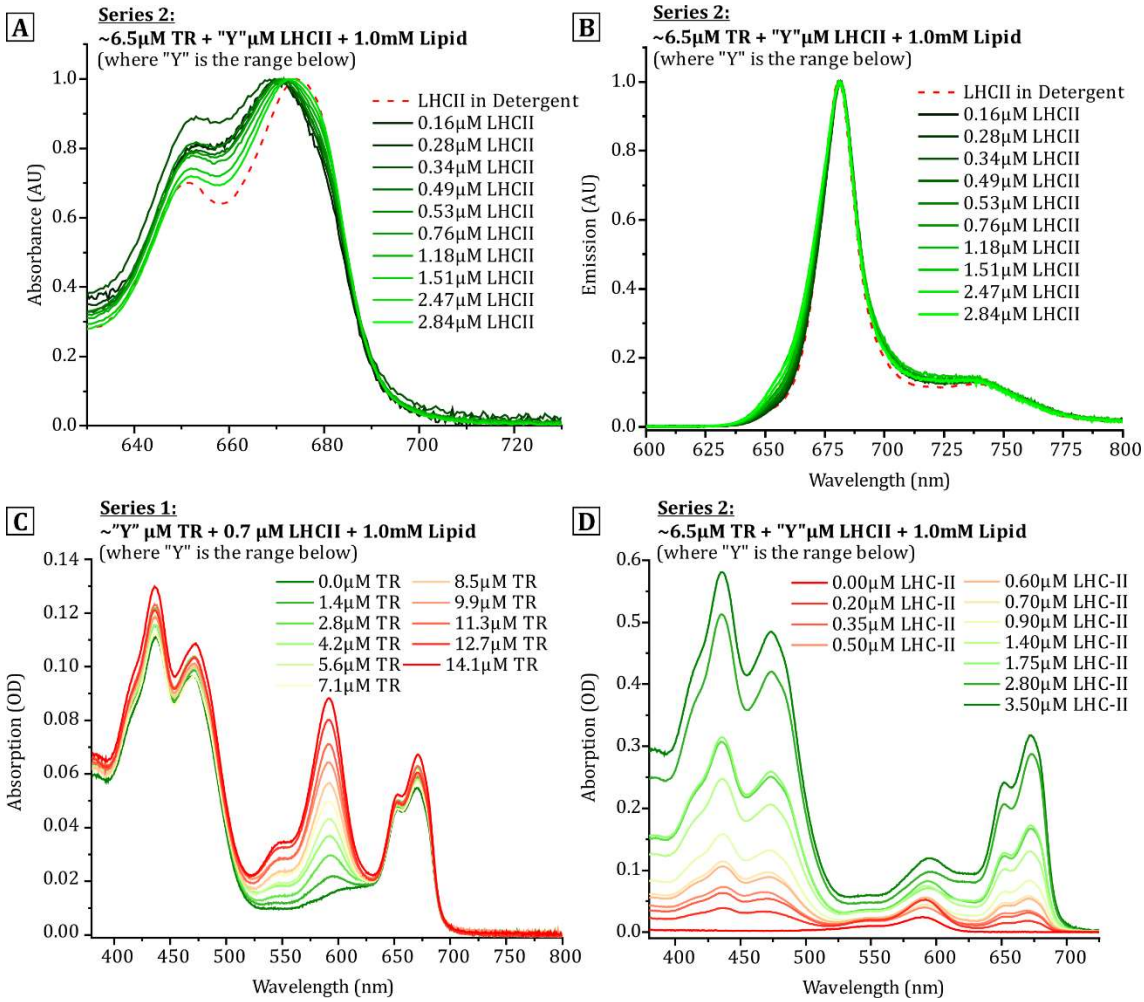

Figure 5.2: Solution-based absorption spectra demonstrating the modularity of the proteoliposome system. Proteoliposomes were prepared across two sample series. In Series 1, the LHCII concentration was held constant whilst the TR concentration was incrementally increased. In Series 2, the TR concentration was held constant whilst the LHCII concentration was incrementally increased. **(A)** Normalised absorption spectra of LHCII in detergent micelles (*red, dashed line*), compared to the absorption of LHCII in proteoliposomes (*black* to *green solid lines*). The absorption peak shifts slightly (<1-3 nm). **(B)** Normalised fluorescence emission spectra of LHCII in detergent micelles (*red, dashed line*) compared to the emission of LHCII in proteoliposomes (*black* to *green solid lines*). Decreasing LHCII concentration results in peak broadening (up to 13%) of the emission spectrum. Spectra in (A) and (B) are normalised to allow for direct comparison of spectral shape and peak width. **(C)** Absorption spectra of proteoliposome Series 1. Increasing the TR concentration results in a growing absorption peak centred at ~591 nm. **(D)** Absorption spectra of proteoliposome Series 2. Increasing the LHCII concentration results in an increasingly large contribution of the LHCII absorption spectrum. Data was collected and analysed by A. M. Hancock.

In the emission spectra (**Figure 5.2**), there is a slight broadening of the emission peak at lowest LHCII concentration (*black line*, **Figure 5.2b**) compared to isolated LHCII trimers in detergent micelles (*red, dashed line*, **Figure 5.2b**). The integrated peak area increases by up to 13 % across all samples, suggesting that a small fraction of chlorophylls may have an altered membrane environment. This is in agreement to other proteoliposomes studies where LHCII appears to be very slightly destabilised at low protein concentrations[56, 79]. Despite this, the general good agreement between the fluorescence and absorption spectra of LHCII in detergent versus LHCII in proteoliposomes suggest that the pigments within the proteins have similar energy levels and connectivity and that LHCII is structurally and functionally intact within proteoliposomes.

Next, we wished to calculate the concentration of each component that had been successfully incorporated, rather than assuming that all of the starting material had been co-assembled into the membrane. To calculate the LHCII and TR concentrations, c, the optical path length, l = 1 cm, and the measured molar extinction coefficient, ε, was used in accordance with Beer lamberts law (discussed in section 2.4.1).

$$A = \varepsilon l c \qquad \text{Eq. 2.5}$$

The absorbance of each component, A, was calculated from absorption spectra for each sample and the two absorption spectra (LHCII and TR) were mathematically deconvoluted to separate each component. **Figures 5.2c** and **5.2d** show the ensemble absorption spectra for proteoliposome Series 1 (constant LHCII concentration) and Series 2 (constant TR concentration), respectively. Qualitatively, in Series 1 (**Figure 5.2c**), the increasing intensity of a peak centred around 591 nm can be seen to be concordant with the increasing TR concentration (the green to red colour scheme represents increasing TR concentration). Samples in Series 1 were found to have very similar LHCII concentrations of 0.52–0.61 μM (8.6–9.4 % of total proteoliposome mass) with a TR range from 0.9 to 12.3 μM (0.09–1.2 % of total lipid composition) (see **Table 5.1**). Similarly, in Series 2 (**Figure 5.2d**), the same effect is observed for LHCII, where the increasing intensity of the LHCII absorption spectra is superposed with the constant TR absorption. Samples in series 2 all had similar TR concentrations calculated as 5.0–8.4 μM (0.5–0.84 % of total lipid composition) with a LHCII range from 0.16 to 2.84 μM (2.4–30.5 % of total mass) (see **Table 5.1**).

Overall, this series of samples demonstrates the ability to tune the concentration of each component with a high and reliable yield (>80% of the initial concentration) and without significant alteration of the protein from its native state. This sample series will allow the effect of donor-acceptor energy transfer to be quantified as a function of component concentration.

Initial concentration		Measured Absorbance		Calculated Concentration		Component yield	
LHCII (μM)	TR (μM)	LHCII (Area: 635-800nm)	TR (OD at 591nm)	LHCII (μM)	TR (μM)	LHCII (%)	TR (%)
0.70	0	34.91	0.000	0.52	0.0	74.3	N/A
0.70	1.4	35.45	0.079	0.53	0.9	75.7	64.3
0.70	2.8	38.35	0.186	0.57	2.2	81.4	78.6
0.70	4.2	36.97	0.313	0.55	3.7	78.6	88.1
0.70	5.6	37.53	0.399	0.56	4.7	80.0	83.9
0.70	7.1	36.34	0.514	0.54	6.0	77.1	84.5
0.70	8.5	37.48	0.599	0.56	7.0	80.0	82.4
0.70	9.9	38.5	0.721	0.57	8.5	81.4	85.9
0.70	11.3	37.98	0.807	0.56	9.5	80.0	84.1
0.70	12.7	36.68	0.954	0.54	11.2	77.1	88.2
0.70	14.1	40.99	1.047	0.61	12.3	87.1	87.2
0	6.8	0	0.364	0.00	4.3	N/A	63.2
0.20	6.8	10.93	0.710	0.16	8.4	80.0	123.5
0.35	6.8	19.19	0.656	0.28	7.7	80.0	113.2
0.50	6.8	23.1	0.453	0.34	5.3	68.0	77.9
0.60	6.8	33.09	0.618	0.49	7.3	81.7	107.4
0.70	6.8	35.5	0.424	0.53	5.0	75.7	73.5
0.90	6.8	50.94	0.429	0.76	5.0	84.4	73.5
1.40	6.8	79.74	0.672	1.18	7.9	84.3	116.2
2.75	6.8	102.01	0.466	1.51	5.5	54.9	80.9
2.80	6.8	166.12	0.448	2.47	5.3	88.2	77.9
3.50	6.8	191.46	0.682	2.84	8.0	81.1	117.6

Table 5.1: Quantity of LHCII and Texas Red incorporated into proteoliposomes (black) and the calculated concentration and yeild measured in samples (red). To calculate the concentration of each component, spectral decomposition analysis was used to isolate the LHCII and TR components and the concentration calculated from the optical density and extinction coefficient (analysis performed by collaborator Ashley Hancock).

5.2.3 Single-particle microscopy measurements confirm the colocalization of LHCII and TR in the majority of proteoliposomes

In addition to ensemble measurements, which only provide information about the population mean, we wished to assess the distribution of proteoliposomes across the population and confirm that both components (TR and LHCII) had incorporated into the majority of proteoliposomes during the self-assembly process. Fluorescence Lifetime Imaging Microscopy (FLIM) was used to confirm successful incorporation of both components into individual proteoliposomes using high resolution intensity and lifetime data. For this, two representative samples were prepared, termed as "low-LHCII" proteoliposomes (1.2 μM LHCII + 12 μM TR-DHPE + 1 mM DOPC) and "high-LHCII" proteoliposomes (2.8 μM LHCII + 12 μM TR+ 1 mM DOPC). Two FLIM channels were defined: (i) an LHCII channel, excited at 485 nm and detected in the range of 655 to 725 nm, and (ii) a TR channel, excited at 561 nm and detected in the range of 590 to 650 nm. In addition to their spectral separation, the two channels were temporally separated by the Pulsed Interleaved Excitation (PIE) mode, such that the 485 nm laser was pulsed at t ~ 0 ns (pulse width ~90 ps) and the 561 nm laser was pulsed at t ~ 50 ns (pulse width ~90 ps), with an overall periodicity of 100 ns. A dilute solution of proteoliposomes was deposited onto glass coverslips, with incubation time and concentration optimized to give a number of small bright objects observed on the surface at a low density, such that the majority of particles are distinct and well separated from other particles. **Figure 5.3a** and **5.3b** shows representative FLIM data obtained for the high- and low-LHCII samples, respectively. The majority of the observed proteoliposomes are diffraction limited, and have intensity profiles with a FWHM of approximately 300 nm (close to the optical resolution of the microscope). This is in agreement with the expected membrane diameter of 50 - 100 nm, and also shows that within each sample there are few/negligible amounts of large membrane aggregates that may significantly skew ensemble statistics.

To determine the presence of both the LHCII protein and the TR in a single proteoliposome it was necessary to determine the "true" portion of the fluorescence signal per particle, i.e., the number of counts that remain after all other sources of noise or spectral overlap have been subtracted. The spectral overlap between the

two imaging channels is relatively low: measured to be a 0.89% spill-over from TR into the LHCII channel and 4.2% spill-over from LHCII into the TR channel (quantified as in section 4.3.1). However, this must be carefully taken into account if we are to make an accurate assessment of the samples' content of TR/LHCII.

Firstly, the number of counts in each channel was measured per proteoliposome by selecting a region of interest that encompassed all of the pixels containing a fluorescence signal. Each proteoliposome was ascribed a "Particle number" to allow to accurate labelling across a large field of view (10 example particles are shown in **Figure 5.3c**). At this stage in the analysis, proteoliposomes that were poorly resolved (e.g., cropped by the image border, or "touching" other proteoliposomes) were excluded to avoid over or underestimating the number of counts (examples are *red, circled* in **Figure 5.3c**). Secondly, the fluorescence spillover (from the TR channel to the LHCII channel, and vice versa) was calculated for each proteoliposome and subtracted from the measured number of counts. Generally, the LHCII signal was 10-100 times lower than the TR signal, due to the comparatively lower quantum yield and rapid bleaching (low photo-stability) of the protein, therefore, the LHCII overlap typically contributes <1% of the detected photons in the TR channel and can be largely ignored. In contrast, the TR fluorescence is much more intense and it was found that a large proportion (up to 50%) of the counts in the LHCII channel for any given particle could be attributed to the fluorescence spill over of colocalised TR. To subtract the TR-to-LHCII fluorescence spillover, the number of counts detected in the TR channel, was multiplied by the amount of spectral overlap (0.89% and 4.2% for TR-to-LHCII and LHCII-to-TR overlap, respectively), and subtracted from the number of counts detected in the LHCII channel. The background noise (i.e., the number of dark counts per pixel per frame) of each detector was also subtracted. The remaining number of counts, after accounting for all other sources, is determined to be the "true" signal representing only the molecule of interest, and is shown in **Table 5.2** for 10 example particles. To ensure that the result of this analysis accurately represents the whole population, this process was repeated for >250 proteoliposomes per sample. This rigorous quantitative analysis is a fair way to estimate the intensity of fluorescence in multi-component samples and was validated by and correlated to later results which also assess co-localization.

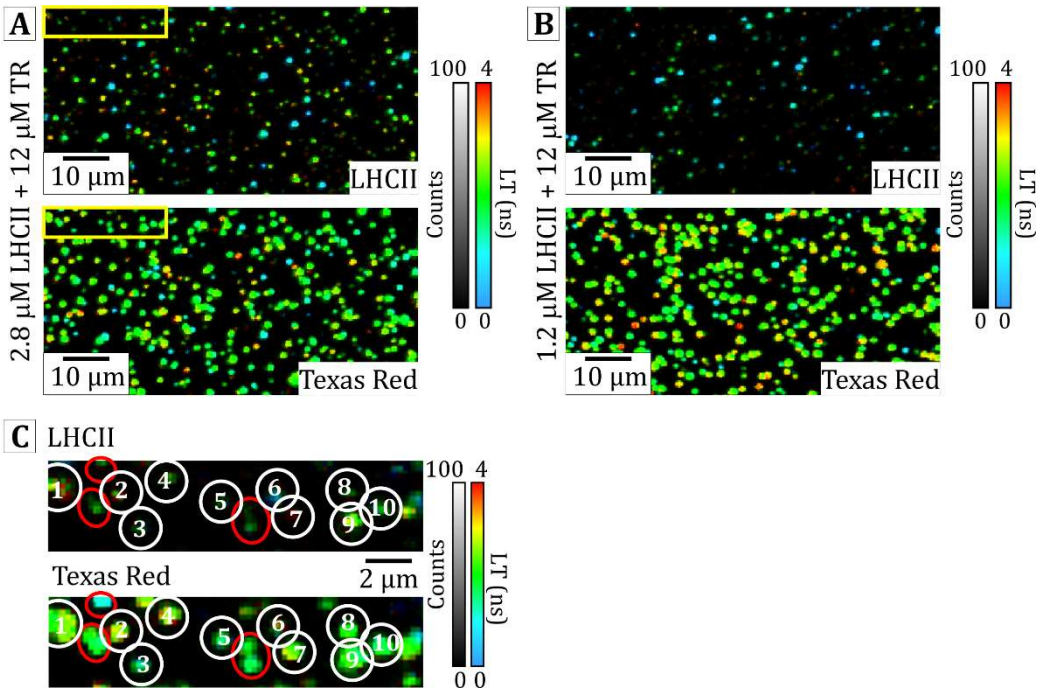

Figure 5.3 - Example FLIM images of proteoliposomes adhered to hydrophilic glass. **(A)** The "high-LHCII" sample containing 2.8 µM LHCII + 12 µM TR-DHPE + 1mM DOPC. *Upper:* LHCII channel, *Lower:* TR channel. **(B)** The "low-LHCII" sample containing 1.2 µM LHCII + 12 µM TR-DHPE + 1mM DOPC. *Upper:* LHCII channel, *Lower:* TR channel. **(C)** A zoomed in image of the *yellow* area in (a), showing 10 example proteoliposomes (*white, circled*). These proteoliposomes were used for the analysis in **Table 5.2.** Proteoliposomes that were poorly resolved (*red, circled*) were excluded from the analysis.

Particle number	Pixels in particle	LHCII Raw signal	Spill over from TR (TR× 0.89%)	LHCII corrected signal	TR Raw Signal	Spill over from LHCII (LHCII×4.2%)	TR corrected signal
#	#	Counts	Counts	Counts	Counts	Counts	Counts
1	42	204	94	110	10572	9	10563
2	32	88	35	53	3903	4	3899
3	21	284	21	263	2364	12	2352
4	39	40	42	-2	4760	2	4758
5	30	111	27	84	3047	5	3042
6	20	115	12	103	1287	5	1282
7	23	67	20	47	2255	3	2252
8	34	40	18	12	2053	2	2051
9	63	563	121	442	13605	24	13581
10	57	1557	63	1494	7054	65	6990

Table 5.2: Single particle analysis for proteoliposome colocalization. Each particle is assigned an index, and the intensity measured in both the LHCII and TR channel. The number of spillover counts is calculated for each channel and then subtracted from the raw signal to give the corrected "true" signal. The row highlighted in *red* is a liposome where no LHCII is believed to be present whereas all others appear to contain both TR and LHCII.

To reduce the likelihood that a noise variation or contaminant within the buffer is wrongly identified as a proteoliposome, images were taken of an "empty" sample (a droplet of buffer on similar glass substrates) in both the LHCII and TR channels. Statistical analysis of these images (shown in **Figure 5.4**) shows that a negligible number of contaminants are present in the buffer or on the substrates, and that the small number of fluorescent spots that were detected had an extremely low intensity (99.9% of possible "particles" in the buffer had an intensity <5 counts per pixel). Therefore, proteoliposomes can be distinguished from the background fluorescence with extremely high confidence.

From this analysis, a particle is considered colocalised if it has a >99.5% likelihood of being distinguishable from background noise/contaminants, and if there is sufficient signal in both the LHCII and TR channels at the same location once fluorescence spill over has been subtracted. Based upon this stringent criteria, it was found that a minimum of 83% and 80% of individual proteoliposomes detected in the "low-LHCII" (1.2 μM LHCII) and "high-LHCII" (2.8 μM LHCII) samples contained both LHCII and TR. Measurements later in this chapter show that this is a conservative estimate. This gives high confidence that both components have been successfully incorporated into the artificial membrane, with only a small population of proteoliposomes where one component may not be present.

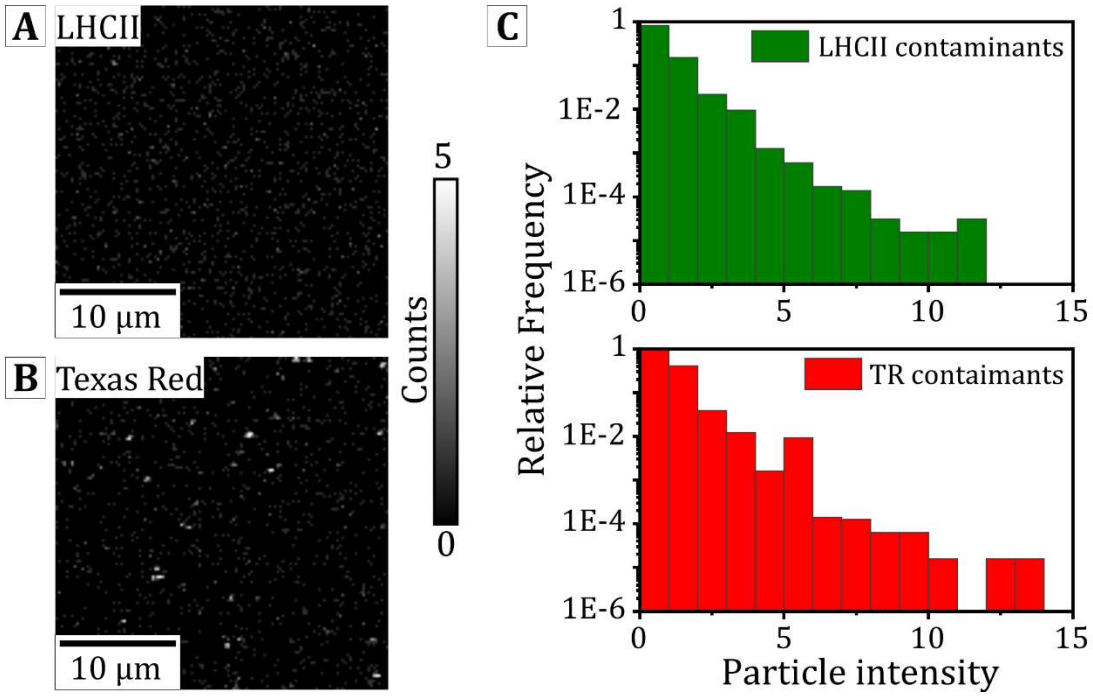

Figure 5.4: Example FLIM images of a "blank" buffer-only sample to ensure that background contaminants are not misidentified as proteoliposomes. Note that whilst some spots of fluorescence signal are apparent these are only visible due to an enhanced contrast: the greyscale of 0-5 counts represents a very low number of photons. **(A)** FLIM image of a "blank" sample as imaged in the LHCII channel. **(B)** FLIM image of a "blank" sample as imaged in the TR channel. **(C)** Frequency distribution histograms of the intensity of contaminants or noise within the blank samples (shown on a semi-logarithmic scale). The vast majority of potential particles (~99.9%) have an intensity of <5 counts per pixel.

	LHCII channel			**TR Channel**		
Bin centre Counts	Number of pixels #	Relative Frequency	Cumulative percent %	Number of pixels #	Relative Frequency	Cumulative percent %
1.5	9636	0.971	97.1	59834	0.931	93.1
2.5	1405	0.022	99.3	3977	0.062	99.3
3.5	298	0.005	99.8	299	0.005	99.8
4.5	82	0.001	99.9	72	0.001	99.9
5.5	39	0.000	100	35	0.000	99.9
6.5	11	0.000	100	16	0.001	100
7.5	9	0.000	100	9	0.000	100
8.5	2	0.000	100	8	0.000	100
9.5	1	0.000	100	4	0.000	100

Table 5.3: Intensity histogram data for the number of background contaminants for a buffer-only "blank" sample in both the acceptor (LHCII) and donor (TR) channels. The cumulative percent describes how many pixels (%) have an intensity that less than or equal to the bin centre.

5.2.4 Ensemble spectroscopy shows that LHCII fluorescence emission is enhanced by energy transfer from Texas Red

When isolated LHCII is excited within the "green gap" a minimal level of LHCII fluorescence should be observed. However, if additional energy is being transferred to LHCII from TR in proteoliposomes, the LHCII fluorescence emission intensity is expected to be "enhanced". Enhancement of LHCII fluorescence due to energy transfer from TR was quantified by calculating the relative LHCII "fluorescence per mole" when excited at 540 nm (selective excitation for TR). This was assessed for proteoliposomes Series 1 which consist of a fixed LHCII concentration and a range of increasing TR concentrations (from Section 5.2.2). The absorption spectra of this series of samples (**Figure 5.5a**) shows an incrementally increasing peak centred at 540 nm, as the TR concentration is increased in each sample, whilst the LHCII Chl *a* and Chl *b* peaks at 650-675 nm remain largely consistent between samples.

To determine the amount of LHCII enhancement when excited in the green gap, sample-to-sample differences were accounted for by determining the LHCII concentration (as in **Table 5.1**) and then calculating the relative LHCII enhancement in terms of the fluorescence emission per mole. **Figure 5.5b** shows the LHCII emission increasing as a function of increasing TR concentration (*dark green* to *light green*). The TR emission has been deconvoluted and removed from these spectra for clarity. It was observed that the relative emission of LHCII excited at 540 nm increases 3-fold from $\sim 1 \times 10^{14}$ counts/mol to $\sim 3 \times 10^{14}$ counts/mol over the range of TR concentrations in this series (0 – 12.4 μM TR). An alternative visualisation of this data is shown in **Figure 5.5c** where the relative emission of LHCII within this proteoliposome series is plotted against the molar TR concentration. In this format, 100% represents the initial intensity of 0.55 μM LHCII (the average LHCII concentration for this sample series) reconstituted into proteoliposomes in the absence of TR. Within this range of TR concentrations, the enhancement of LHCII emission when excited at 540 nm was found to linearly increase with TR concentration, up to a maximum of 314% compared to LHCII-only proteoliposomes. This ensemble spectroscopy was performed by my colleague and acts as a baseline for my own FLIM analysis (section 5.2.6 onwards).

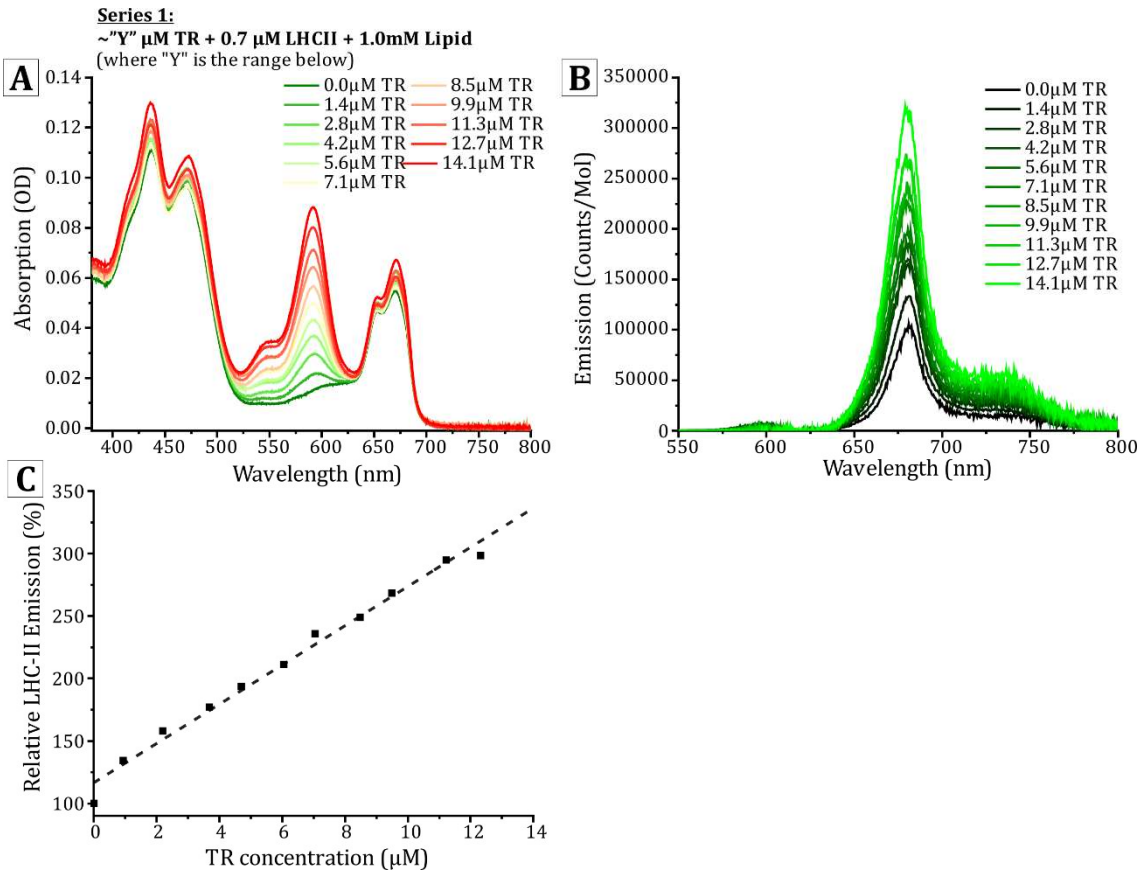

Figure 5.5: Steady-state absorption and emission spectra of Texas Red reconstituted into Texas Red-LHCII proteoliposomes with varying TR concentration. **(A)** Ensemble absorption spectroscopy of proteoliposome Series 1 (constant TR concentration and increasing LHCII concentration). Repeated from **Figure 5.2** to allow side-by-side comparison with the data in panels B and C. **(B)** Steady state fluorescence emission spectra of the same sample series as in (A). TR emission has been removed via deconvolution for visual clarity. **(C)** Relative LHCII emission (calculated from area under curve) versus TR concentration, calculated from the same sample series as (A). Here 100% is defined as the baseline intensity of LHCII emission observed for proteoliposomes containing 0.55 µM LHCII and 1 mM total lipid (as this is the average LHCII content for this sample series). Data collection and analysis by A. M. Hancock.

5.2.5 Ensemble spectroscopy shows that Texas Red fluorescence is quenched by the presence of LHCII

As previously stated, the energy transfer from the donor (TR) to the acceptor (LHCII) can be directly observed by the enhanced fluorescence intensity of the LHCII and the corresponding diminished fluorescence intensity of the TR. However, this method of observation is dependent on factors such as variation in excitation intensity, individual proteoliposome concentration, and is also susceptible to changes in pH or impurities that are present in the solution. A more robust method to confirm the presence of FRET, is to consolidate information obtained through intensity measurements with fluorescence lifetime data. As well as the decrease in fluorescence intensity, FRET has also been shown to cause the reduction in the fluorescence lifetime of the donor fluorophore[28]. The energy transfer to the acceptor provides an additional decay mechanism for the excited electrons, and as a result, the donor remains in the excited state for a shorter average time.

Ensemble absorption spectra of proteoliposome series 2 shows an increasing LHCII contribution (broad peaks from 400-500 nm and 600-650 nm) centred around a constant TR peak centred at ~590 nm (**Figure 5.6a**, repeated from **Figure 5.2d**). Initial intensity measurements were made using ensemble spectroscopy to demonstrate the diminishing relative TR emission intensity in the presence of increasingly higher concentrations of LHCII. **Figure 5.6b** shows the steady state TR emission of proteoliposome Series 2 (from Section 5.2.2), which have a fixed TR concentration. For clarity, these spectra have been de-convoluted to subtract the LHCII component, revealing only the TR peak at 610 nm. It was observed that as the LHCII content was increased from 0.00 μM to 3.50 μM, the relative TR emission intensity was reduced to as low as 2% (compared to its level in the absence of LHCII) as the absorbed energy was transferred non-radiatively to the FRET acceptor. Time-resolved fluorescence measurements were performed in ensemble, as a secondary technique, to complement the steady-state data. The proteoliposome samples were selectively excited using a pulsed 540 nm laser, and the fluorescence decay curves for samples in proteoliposome Series 2 (fixed TR concentration) were collected and displayed in **Figure 5.6c**. The fluorescence decay curves reveal the faster decay of the TR fluorescence as LHCII concentration was increased, representing quenching

in correlation with the steady-state intensity data. Fitting of the decay curves showed that the TR lifetime decreases from 4.4 ns in the absence of LHCII to a minimum of 0.7 ns at the maximum LHCII concentration.

Graphical analysis of fluorescence intensity and fluorescence lifetime data allowed the observed trends to be quantified. Energy transfer efficiency was calculated from both steady-state (ETE_{SS}) and time-resolved (ETE_{TR}) data by comparison of samples with and without acceptors (LHCII), as given by the equations:

$$ETE_{SS} = 1 - \frac{F_D}{F_0} \quad \text{Eq. 5.2}$$

$$ETE_{TR} = 1 - \frac{\tau_D}{\tau_0} \quad \text{Eq. 5.3}$$

where F_D and F_0 are the donor fluorescence intensity per mole in the presence and absence of the acceptor, respectively, and τ_D and τ_0 are the donor fluorescence lifetime in the presence and absence of the acceptor. **Figure 5.6d** shows that the ETE increased non-linearly with LHCII concentration and is fitted to an exponential growth function, as efficiency is expected to saturate at high acceptor concentration. Steady-state and time-resolved data show good agreement of the trend and estimate a maximal ETE of ~94% and ~77%, respectively (*black* vs *red datapoints* in **Figure 5.6d**). We expect that the exact maximal ETE is between these two values (different spectroscopic techniques often differ in absolute efficiency values and a definitive calculation of ETE will be studied in future work). This trend of ETE is attributed simply to the reduction in average distance between TR and LHCII as the concentration of LHCII is increased.

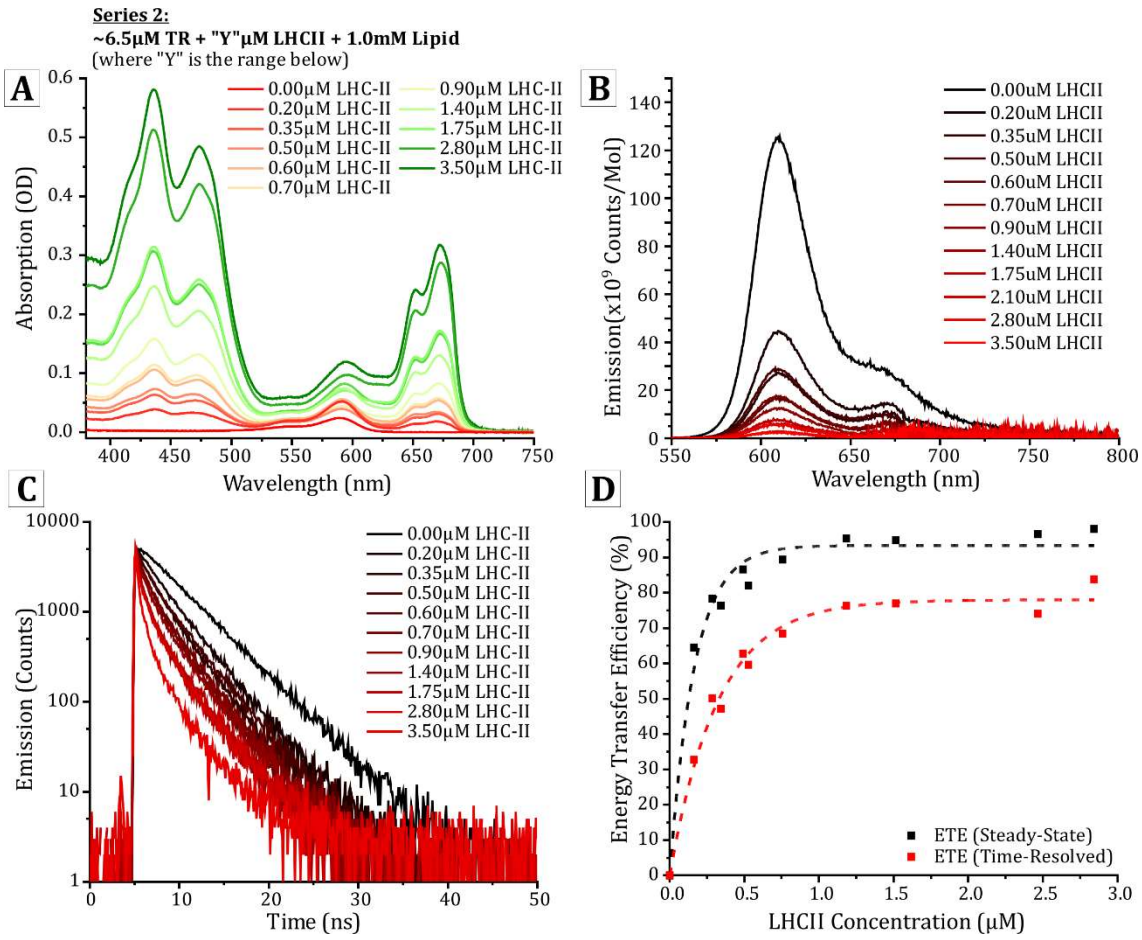

Figure 5.6: Steady-state and time-resolved fluorescence of Texas Red reconstituted into Texas Red-LHCII proteoliposomes with varying LHCII concentration. **(A)** Ensemble absorption spectroscopy of proteoliposome Series 2 (constant TR concentration and increasing LHCII concentration). Repeated from **Figure 5.2** to allow side-by-side comparison with the data in panels B - D. **(B)** Steady state fluorescence emission spectra of the same sample series as in (A). Texas Red emission is displayed as Counts per mole to show relative quenching at different LHCII concentrations. LHCII emission has been removed via deconvolution for visual clarity. **(C)** Time-resolved fluorescence data of the same sample series as in (A). **(D)** Energy transfer efficiency versus LHCII concentration, calculated from the same sample series as in (A). ETE is calcualted using the conventional FRET relationship as described in Equations 5.2 and 5.3. *Dashed lines* are to guide the eye. Data collection and analysis by A. M. Hancock.

5.2.6 Single-proteoliposome analysis shows a homogeneous distribution of lifetimes and energy transfer efficiencies

Complementary to the ensemble spectroscopy, FLIM measurements of individual proteoliposomes were performed to determine how the presence of LHCII changed the distribution of TR lifetimes across the population of membranes. As described in section 5.2.3, FLIM data was collected for proteoliposomes deposited onto glass at a low surface density for representative samples containing "low-LHCII" (1.2 μM LHCII + 12 μM TR-DHPE + 1 mM DOPC) and "high-LHCII" (2.8 μM LHCII + 12 μM TR-DHPE + 1 mM DOPC), as well as a TR-only (12 μM TR-DHPE + 1 mM DOPC) sample to represent TR in the absence of the LHCII-acceptor. Due to the significant spill-over of TR fluorescence into the LHCII channel (**Table 5.2**), it is likely that fluorescence decay curves generated in the LHCII channel will be skewed by an unknown amount for each proteoliposome (dependent on both LHCII concentration and the TR concentration in each proteoliposome). As such, it is difficult to deconvolute these effects and provide accurate quantification of the LHCII lifetimes within these samples. However, since the LHCII intensity typically contributes <1% of the counts in the TR channel, the TR fluorescence lifetime can be confidently assessed allowing energy transfer between the TR and LHCII to be identified.

In the absence of LHCII, the TR/DOPC liposomes (**Figure 5.7a**) have long fluorescence lifetimes and are visualised as a number of distinct particles that appear orange/red in the FLIM false-colour scale (*red*-to-*blue* represents long-to-short lifetimes). In the LHCII channel a low signal is observed, due to the small amount of spectral overlap from the TR channel to the LHCII channel (0.89%), as previously discussed. **Figures 5.7b** and **5.7c** show representative fields of view for the "low-LHCII" and "high-LHCII" proteoliposome samples, respectively. In both the samples that contain LHCII, the proteoliposomes appear "bluer" in the TR channel, corresponding to a shorter lifetime and indicating the presence of TR quenching due to energy transfer to the LHCII. Fluorescence decay curves were generated for all three samples by accumulating all of the photons within a field of view and compared. It was observed that the TR fluorescence decayed more rapidly in proteoliposomes with increasing LHCII concentrations (*green lines*, **Figure 5.7d**) versus the TR-only sample (*red* line, **Figure 5.7d**).

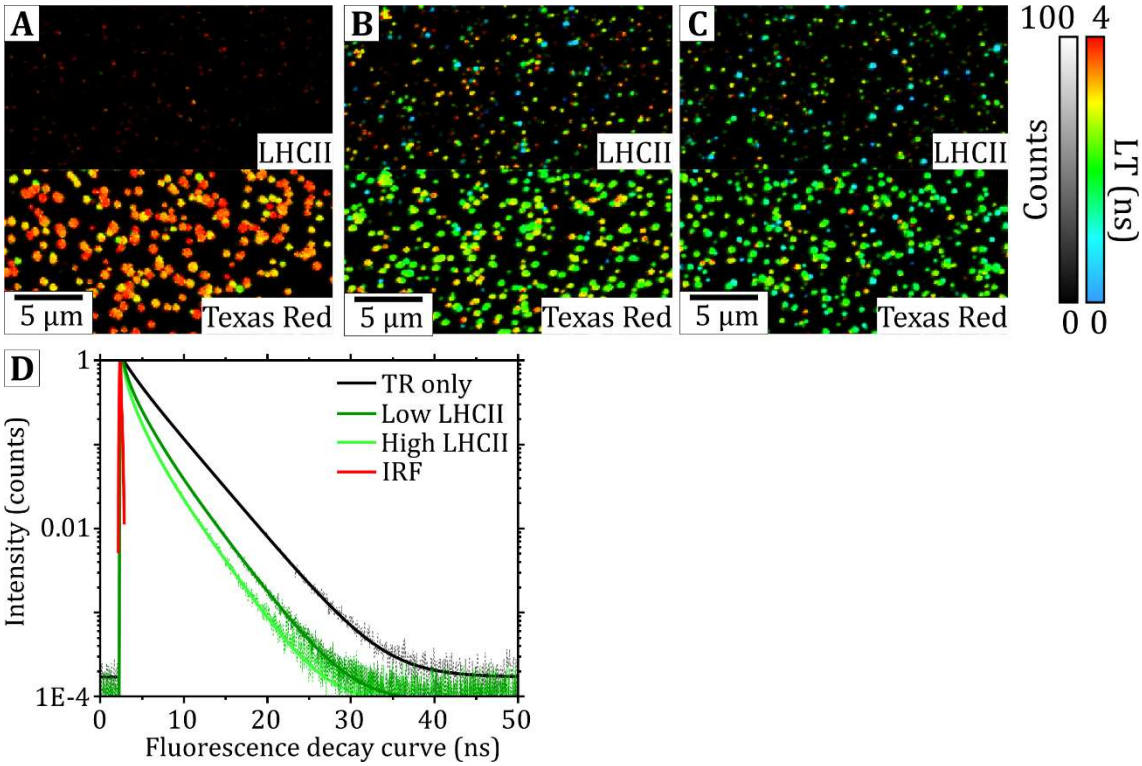

Figure 5.7: FLIM measurements of TR- and LHCII-containing proteoliposomes in comparison to liposomes containing only TR (and normal DOPC lipids). In all FLIM data, the *top row* is the FLIM channel optimised for the detection of LHCII and the *bottom row* is the FLIM channel optimised for the detection of TR. Particles are generally below the diffraction limit (<300 nm) and appear homogeneous in size and intensity. All vesicles contain 1 mM mixed thylakoid lipids in addition to the stated µM-concentrations of TR and LHCII. **(A)** FLIM data of 12 µM TR reconstituted into liposomes adhered onto hydrophillic glass at a low concentration. **(B)** FLIM data of 12 µM TR and 1.2 µM LHCII reconstituted into proteoliposomes. **(C)** FLIM data of 12 µM TR and 2.8 µM LHCII reconstituted into proteoliposomes. **(D)** Fitted fluorescence decay curves for the TR lifetime of (proteo)liposomes containing zero LHCII (TR-only), a low concentration of LHCII (1.2 µM) and a high concentration of LHCII (2.8 µM). *Dashed lines* show the raw data, *solid lines* show the fitted decay curves.

Amplitude-weighted lifetimes calculated from these decay curves show this trend more clearly, where the TR fluorescence lifetime reduces from 3.36 ± 0.01 ns in the TR-only liposomes to 1.87 ± 0.01 ns and 1.50 ± 0.01 ns in the low- and high-LHCII proteoliposomes, respectively. This trend is in strong agreement with those observed in ensemble spectroscopy measurements in Section 5.2.4 and is a clear indication of the concentration-dependent energy transfer that is occurring in this system.

To observe this behaviour in individual proteoliposomes and to develop an understanding of the distribution of lifetimes and proteoliposome variation within each sample, a more quantitative analysis was performed by calculating the lifetimes for individual proteoliposomes. Single proteoliposomes were selected and identified as described in Section 5.2.3 (five example proteoliposomes are *circled, red* in **Figure 5.8a**) and "per proteoliposome" fluorescence decay curves were generated from all the photons accumulated in the selected region in the TR channel (**Figure 5.8b**). Only well-resolved proteoliposomes with sufficient signal to produce a good fit (greater than 500 counts and with a fit quality of $chi^2 < 1.2$) were used to fit an amplitude weighted lifetime, $\langle\tau\rangle$, for each proteoliposome. The author accepts that this is likely to skew the results towards larger/brighter proteoliposomes, however, the overall trend of these data matches the results seen in ensemble spectroscopy, and this type of population analysis is not possible using ensemble spectroscopy only. This process was repeated for multiple proteoliposomes (N>200) for each sample, to generate a frequency histogram showing the "per proteoliposome lifetime" distribution for the TR-only (*red*, **Figure 5.8c**), low-LHCII (*blue*, **Figure 5.8c**) and high-LHCII samples (*green*, **Figure 5.8c**).

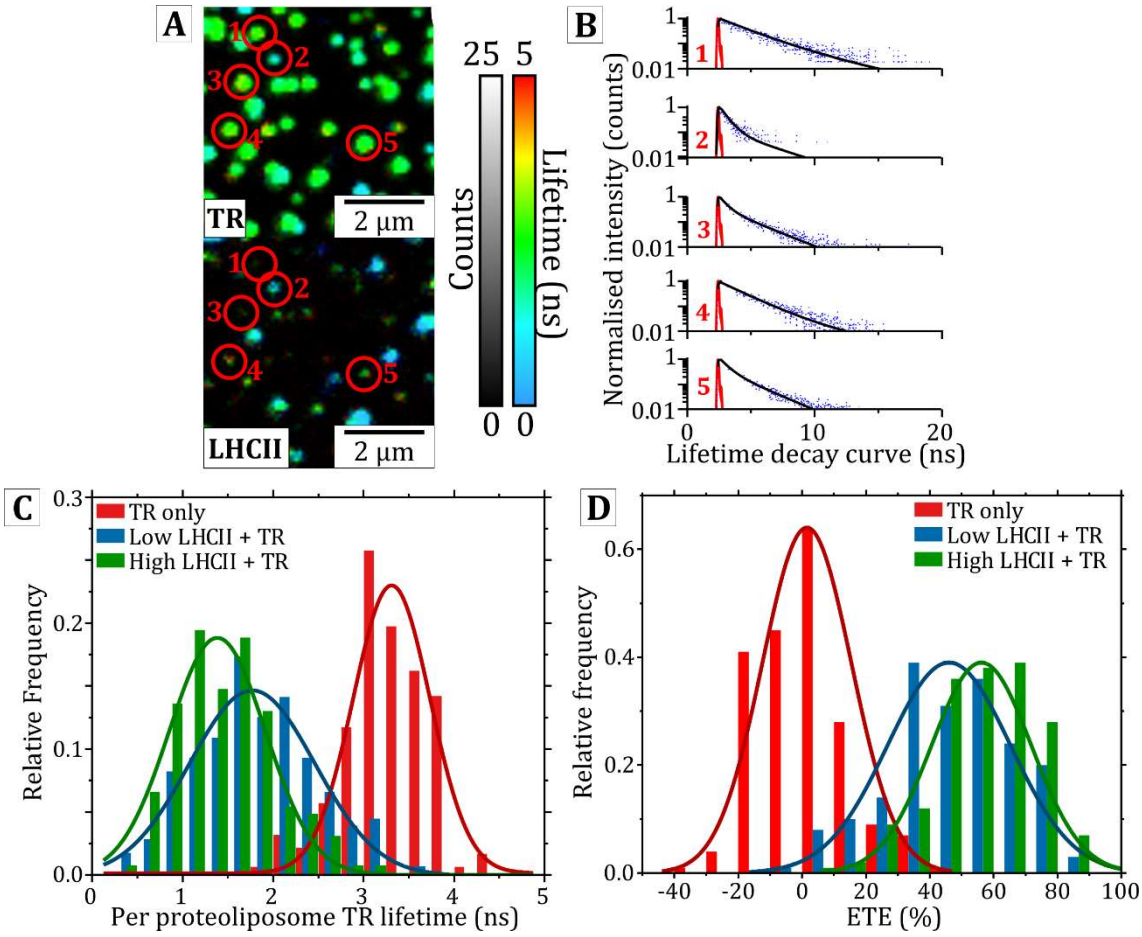

Figure 5.8: Per proteoliposome lifetime distributions of TR and LHCII reconstituted into proteoliposomes. **(A)** An example FLIM image (acquired over 500 frames) of proteoliposomes containing TR and a high concentration of LHCII (12 µM TR + 2.8 µM LHCII + 1 mM DOPC). Five example proteoliposomes are circled (*red*) and photons detected in that area in the TR channel are accumulated to generate fluoresence decay curves. **(B)** TR fluorescence decay curves for the five proteoliposomes shown in (a). Each decay curve is fitted by reconvoluting the IRF (*solid, red*) from the raw data (*dashed, blue*) to calculate the fitted fluorescence decay curve (*solid*, *blue*). **(C)** Per proteoliposome lifetime distribution for each sample. **(D)** Per proteoliposome energy transfer efficiency (ETE) distribution for each sample. For each proteoliposome the ETE is calculated using **Equation 5.5** and the per proteolipsome fitted lifetime. Guassian distributions are fitted to each histogram in (c) and (d) to find the population centre and FWHM.

For each sample there is a mono-disperse population of lifetimes, with a central peak that shifts towards shorter lifetimes with the increasing concentration of LHCII. From this it is possible to make several conclusions. Firstly, it can generally be said that there are no sub-populations of proteoliposomes and all proteoliposomes can be described as a single distribution (at least for the proteoliposomes highlighted with this method of analysis). This is a good indication that proteoliposomes formed using this procedure are largely homogeneous and there are no large aggregates of TR and LHCII. Secondly, the shortening of the TR lifetimes increases as more LHCII is incorporated into the proteoliposomes, in direct agreement with the ensemble time-resolved fluorescence measurements and clearly demonstrating the non-radiative energy transfer from the TR to the LHCII within a controllable system. To find the centre and FWHM of each population, a Gaussian relationship is fit to each histogram (*solid lines*, **Figure 5.8c**). From these fits, it is observed that the mean TR fluorescence lifetime decreases from 3.31 ± 0.85 ns (centre ± FWHM) in TR liposomes without LHCII to 1.77 ± 1.38 ns and 1.38 ± 1.06 ns for "low-LHCII" and "high-LHCII" proteoliposomes, respectively. The fact that proteoliposomes containing LHCII have a larger FWHM of the fluorescence lifetime (for both low- and high- LHCII concentrations) could suggest that the inclusion of proteins causes more variation in the proteoliposome self-assembly, however, across whole populations and within this sample series the relationship between LHCII concentration and the extent of TR quenching is clear.

Finally, the per liposome ETE was calculated using the conventional FRET equations (as in Equation 5.2 and 5.3), this time taking the form:

$$ETE_{PL} = 1 - \frac{< \tau_i >}{\overline{< \tau_0 >}} \qquad \text{Eq. 5.4}$$

where $< \tau_i >$ is the per proteoliposome lifetime and $\overline{< \tau_0 >}$ is the mean per proteoliposome lifetime for the TR-only sample. The result is a per proteoliposome ETE distribution for each sample as shown in **Figure 5.8d.** As expected, the per proteoliposome ETE distribution shifts to higher percentages for samples containing higher concentrations of LHCII, from 0% for the TR-only sample (by definition from Equation 5.4) up to 44% for the Low-LHCII sample and 60% for the High-LHCII sample. These values are significantly lower than the time-resolved ETE calculated from ensemble spectroscopy for the same LHCII concentrations (76.3%

and 83.7%, respectively). The reason for this discrepancy is discussed in the following section. Despite this, the results show that within a population, the ETE varies between individual proteoliposomes, likely a result of variation of proteoliposome size and the LHCII/TR content in the self-assembly process.

5.2.7 Photobleaching of fluorophores results in disruption of FRET and alters the interpretation of lifetime measurements

One possible reason for the discrepancy between FLIM measurements and ensemble spectroscopy is the amount of photobleaching that occurs in each type of measurement. Photobleaching is the result of reactions between excited singlet states and reactive oxygen which reduces covalent bonds in the fluorescent molecules and causes permanent damage. During ensemble spectroscopy measurements proteoliposomes are suspended in solution and continuously stirred. The result is that proteoliposomes diffuse in and out of the excitation volume and each proteoliposome only experiences a small fraction of the total excitation energy per measurement. In contrast, in FLIM measurements, proteoliposomes are adhered to glass at a fixed location within the field of view and experience a greater amount of excitation energy, and therefore photodamage, per measurement. To quantify the amount of photobleaching per FLIM measurement and to determine how this may affect the measured lifetimes, a series of timelapse FLIM measurements was used to monitor changes to proteoliposome samples as a result of FLIM excitation.

First, to quantify the level of photobleaching of each component independently from the influence of FRET, three control samples were prepared: (i) TR-only (12 μM TR + 1 mM DOPC, no LHCII), (ii) Low-LHCII-only (1.2 μM LHCII + 1 mM DOPC, no TR), (iii) High-LHCII-only (2.8 μM LHCI + 1 mM DOPC I, no TR). These samples were designed to be consistent with the concentrations of TR and LHCII reconstituted into previous samples (sections 5.2.3 and 5.2.6) but, instead, only containing one fluorescent component. FLIM measurements of these control proteoliposomes obtained using the same parameters as proteoliposomes in section 5.2.3 and 5.2.6 (500 frames per image) and then separated digitally into a time-lapse series of FLIM images (where each timepoint contains 50 frames), in order to monitor the amount

of photobleaching that occurs over time. These analyses found that LHCII reconstituted into proteoliposomes became photo-damaged significantly faster than TR, as described below. Across multiple frames, LHCII reconstituted into proteoliposomes at both low- and high-concentrations can be seen to rapidly decrease in fluorescence intensity (**Figure 5.9a-b**), whereas the fluorescence intensity of TR appears to remain largely consistent (**Figure 5.9c**). After 500 frames (the full FLIM acquisition), the LHCII intensity had decreased by ~75% of its initial intensity in both LHCII-only samples (*dark* and *light, green*, **Figure 5.9d**), whereas the TR had decreased by only ~30% (*red*, **Figure 5.9d**).

These results have several implications that must be considered in order to ensure the accuracy of data analysis when using FLIM to quantify FRET in proteoliposomes containing both LHCII and TR. Firstly, the "optically-active" concentration of LHCII and TR is changing as a direct result of FLIM excitation, and fluorescence measurements may no longer reflect the true concentration of either component that has been reconstituted into the membrane. Secondly, LHCII and TR within proteoliposomes photobleach at uneven rates, therefore significantly complicating the interpretation of intensity measurements and spill-over calculations when considering different time-points in the acquisition. Finally, TR or LHCII that becomes photodamaged will be unable to donate or accept energy from other fluorophores, therefore the TR-to-LHCII energy transfer efficiency will change over time. Since energy transfer is manifested as a reduced fluorescence TR lifetime, the lifetimes observed via FLIM are likely to change during the process of acquiring FLIM images and may be subject to misinterpretation. It seems likely that photobleaching could explain the discrepancy between the FLIM measurements and cuvette spectroscopy measurements and suggests that lifetimes measured by FLIM may be overestimated. All together, this means that either photobleaching must be prevented or somehow taken into account (corrected for) during the analysis.

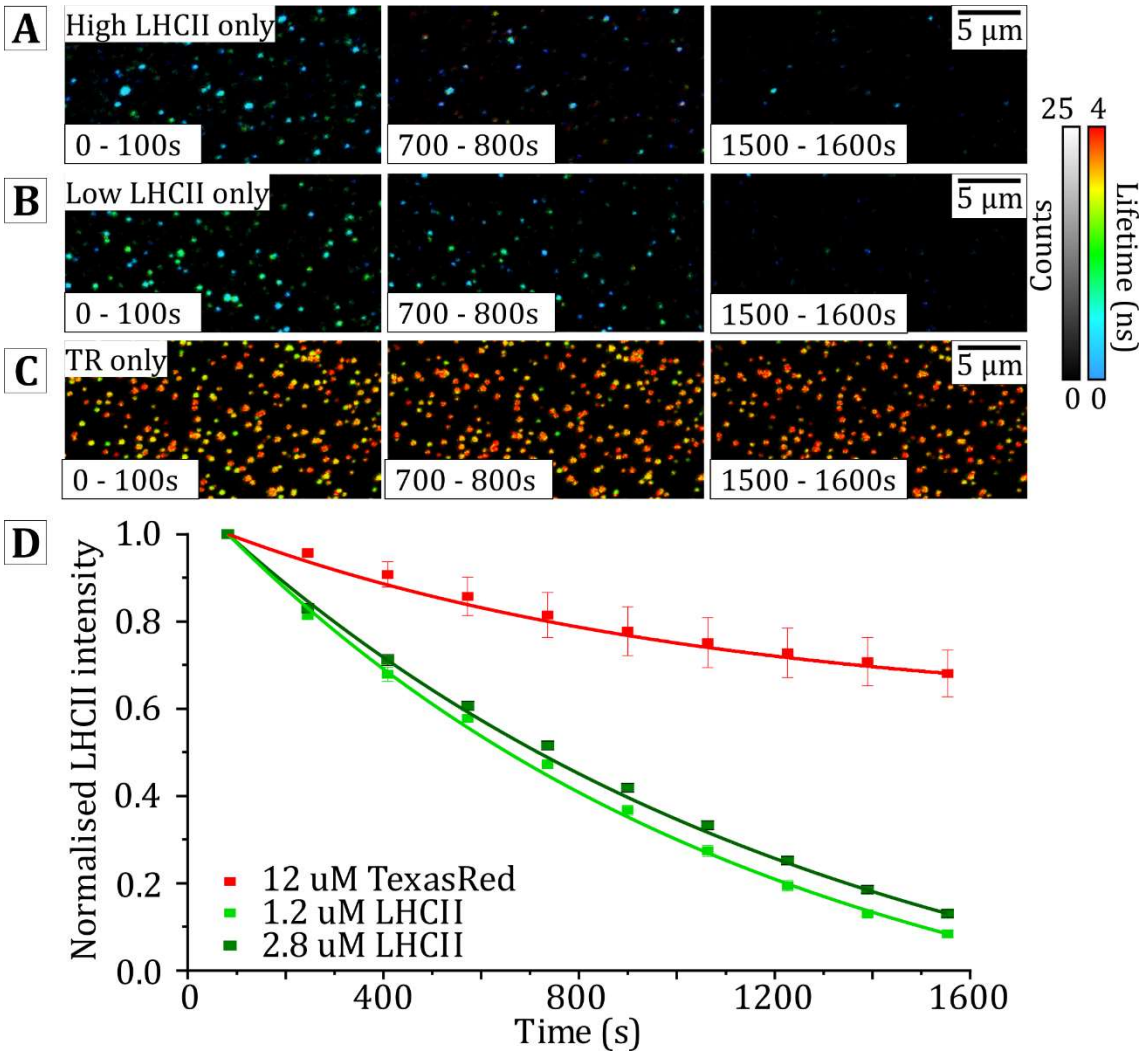

Figure 5.9: FLIM measurements of TR-only and LHCII-only proteoliposomes, to determine the extent of photobleaching occuring during FLIM acquisitions. The images displayed (A-C) and each datapoint (D) are computed from the sum of the photons collected within a specific time period within an acquisition, i.e., 100s (frames 1-50), 200s (frames 51-100), 300s (frames 101-150) and so on. **(A)** FLIM timelapse showing the photobleaching of proteolipsoomes containing a high concentration of LHCII only (2.8 µM LHCII + 1 mM DOPC). **(B)** FLIM timelapse showing the photobleaching of proteolipsoomes containing a low concentration of LHCII only (1.2 µM LHCII + 1 mM DOPC). **(C)** FLIM timelapse showing the photobleaching of proteolipsoomes containing TR only (12 µM TR + 1 mM DOPC). **(D)** Photobleaching curves for proteoliposomes containing TR or LHCII only. Each data point represents the total intensity accumulated at each 50-frame (100 s) timepoint and for clarity, the intensity for each timepoint is normalised to a starting intensity set as 1.0. The datapoints are fit with an exponential decay function (*solid lines*) to guide the eye.

To quantify and correct for these effects in our proteoliposome system, a series of time-resolved FLIM images were obtained for proteoliposomes containing both LHCII and TR. **Figure 5.10a** shows a series of images, analyzed as above, for proteoliposomes containing TR and a low-concentration of LHCII (12 μM TR + 1.2 μM LHCII + 1 mM DOPC). Initially (t = 0–100s), proteolipsomes in the LHCII channel appear relatively bright before decreasing in intensity over the subsequent timepoints as a result of photobleaching. Correlated to this decreasing LHCII intensity, proteoliposomes in the TR channel *increase* in intensity, and show a significant shift from mostly green/blue particles (representing short lifetimes, <1 ns) to almost entirely red particles (representing longer lifetimes, >4 ns) by the end of the acquisition. The amplitude-weighted lifetime, obtained by fitting the fluorescence decay curve for each timepoint, shows that the TR lifetime increases over 2-fold from 0.97 ± 0.02 ns at t = 0-100 s to 2.18 ± 0.01 ns at t = 1500-1600 s (**Figure 5.10b**). This is correlated to an exponential decay in the LHCII intensity. We note that LHCII-photobleaching occurs more rapidly in samples containing both LHCII and TR (~100% reduction after 1600 s), compared to LHCII-only (~80% reduction after 1600 s, **Figure 5.9b,d**), suggesting that the additional excitation provided by TR-to-LHCII energy transfer results in additional photodamage of the protein. Correlated to the increasing fluorescence lifetime, the fluorescence intensity of TR also increases over time, as a result of the photobleaching of LHCII. Over the duration of the acquisition, the TR intensity increases over 3-fold (3.5× the starting intensity at t = 900 s), before starting to decrease. It seems likely that this is the combined effect of rapid "unquenching" of TR at the start of the acquisition, followed by TR photobleaching becoming more dominant once the TR is mostly unquenched.

This time-resolved "FRET uncoupling" was consistent for both samples of LHCII and TR reconsituted into proteoliposomes (see full summary of results in **Table 5.4**). The resulting increase in Texas Red fluorescence intensity is from 1.0 to 4.72 ± 0.14 (370% increase) and from 1.0 to 3.08 ± 0.25 (210% increase) for 'high-LHCII' and 'low-LHCII' proteoliposomes, respectively, concomitant with an increasing TR fluorescence lifetime from 0.73 ± 0.02 ns to 1.77 ± 0.02 ns (140% increase) for 'high-LHCII' and from 0.975 ± 0.02 ns to 2.18 ± 0.01 ns (120% increase) for 'low-LHCII'.

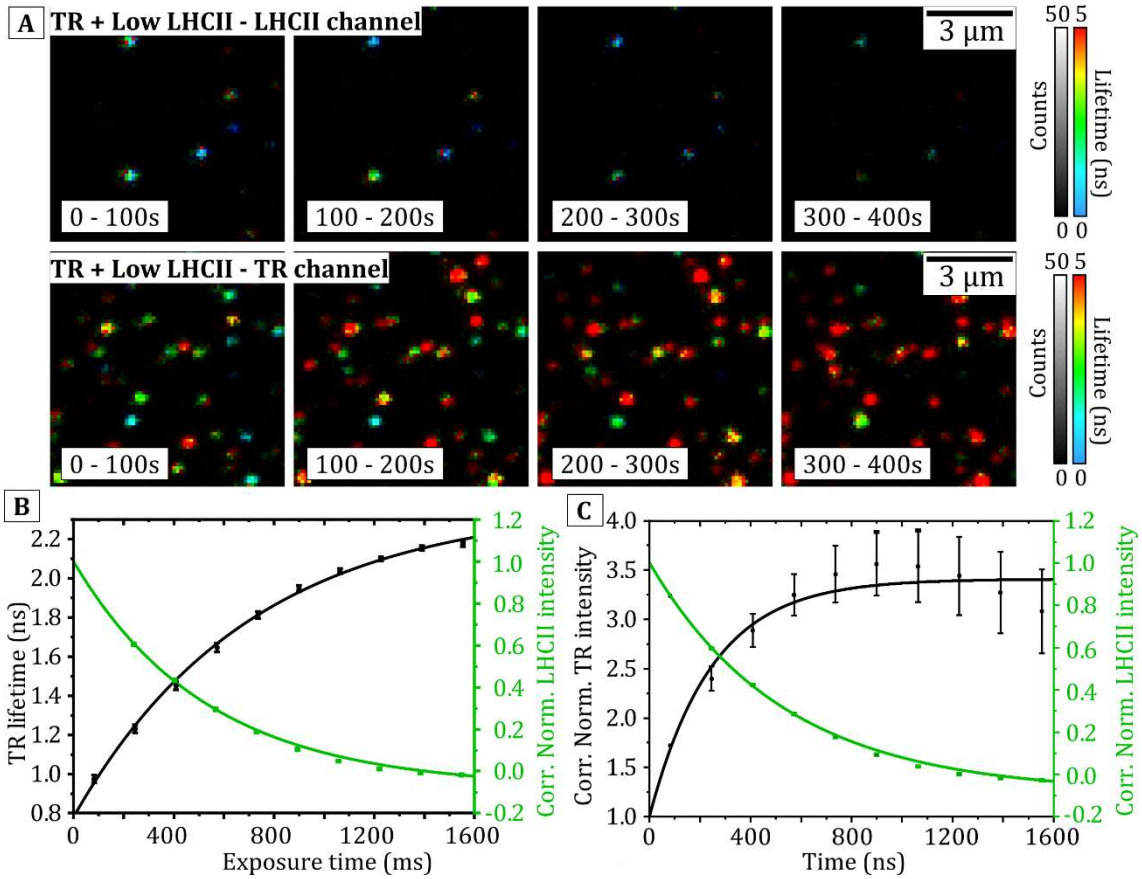

Figure 5.10: Time-lapse series of FLIM measurements of proteoliposomes containing TR and a low concentration of LHCII showing the effects of photobleaching on a FRET-coupled system. **(A)** FLIM data of proteoliposomes containing LHCII and TR during photobleaching. **(B)** The fitted TR fluorescence lifetime (*black*) and the LHCII intensity (*green*, normalised to a starting intensity of 1.0 at t = 0 s) plotted against each timepoint. **(C)** The TR (*black*) and LHCII intensity (*green*), both normalised to a starting intensity of 1.0 and plotted against each timepoint. The *black, solid* lines are mono-expontential fits to guide the eye.

Frames	Time	TR only (12 µM TR)		Low-LHCII + TR (1.2µM LHCII +12µM TR)		High-LHCII + TR (2.8µM LHCII +12µM TR)	
	(s)	Norm. intensity	Fitted lifetime (ns)	Norm. intensity	Fitted lifetime (ns)	Norm. intensity	Fitted lifetime (ns)
1-50	81.8	0.98 ± 0.01	3.02 ± 0.01	1.72 ± 0.01	0.97 ± 0.02	1.40 ± 0.02	0.73 ± 0.01
50-100	245	0.96 ± 0.03	3.08 ± 0.02	2.40 ± 0.07	1.23 ± 0.02	2.10 ± 0.07	0.87± 0.01
100-150	409	0.91 ± 0.09	3.11 ± 0.01	2.89 ± 0.10	1.45 ± 0.02	2.63 ± 0.08	1.02 ± 0.01
150-200	572	0.86 ± 0.14	3.17 ± 0.02	3.25 ± 0.12	1.65 ± 0.02	3.11 ± 0.10	1.19 ± 0.02
200-250	736	0.81 ± 0.16	3.19 ± 0.01	3.46 ± 0.17	1.81 ± 0.02	3.44 ± 0.14	1.31 ± 0.01
250-300	899	0.78 ± 0.18	3.24 ± 0.01	3.56 ± 0.19	1.95 ± 0.02	3.86 ± 0.15	1.44 ± 0.02
300-350	1060	0.75 ± 0.18	3.29 ± 0.02	3.54 ± 0.21	2.04 ± 0.01	4.21 ± 0.15	1.53 ± 0.02
350-400	1230	0.73 ± 0.18	3.33 ± 0.02	3.44 ± 0.23	2.10 ± 0.01	4.48 ± 0.15	1.62 ± 0.02
400-450	1390	0.71 ± 0.17	3.33 ± 0.02	3.27 ± 0.24	2.16 ± 0.01	4.63 ± 0.15	1.71 ± 0.02
450-500	1550	0.68 ± 0.17	3.36 ± 0.01	3.08 ± 0.25	2.18 ± 0.01	4.72 ± 0.14	1.77 ± 0.02
% Difference		**- 32%**	**11%**	**208%**	**175%**	**372%**	**142%**

Table 5.4: Summary of numerical data from proteoliposome quenching experiments for (proteo)liposomes. The fluorescence data shown here is for the TR channel.

We hypothesise that LHCII becomes photodamaged when exposed to the FLIM laser, and is no longer able to accept energy from TR. This results in "de-quenching" (i.e., fluorescence recovery) of TR fluorescence as this pathway for de-excitation has been removed. This effect is larger for samples with a higher initial concentration of LHCII, since there is a larger potential for de-quenching.

A signifcantly smaller de-quenching effect was also observed in proteoliposomes containing TR-only (see **Table 5.4**), where the TR fluorescence lifetime was found to increase from 3.02 ± 0.01 ns to 3.36 ± 0.01 ns (11% increase) despite the overall decrease in TR intensity (to 68% of the initial intensity). The results suggest some level of "self-quenching" between TR fluorophores reconstituted into proteoliposomes that is uncoupled as the TR becomes increasingly photodamaged. Indeed, monochromatic dyes, including TR, have been previously shown to self-quench at moderate to high concentrations[145] (this phenomenon is investigated thoroughly in Chapter 6).

These images (**Figure 5.10a**) demonstrate the striking effect of dynamic photobleaching in which we observe particles "dimming"/ "lighting-up" in correlation over time. Overall, the results of photobleaching experiments highlight the need to accurately quantify the effects of photobleaching in both single-fluorophore (TR-only) and more complicated systems (e.g., FRET between fluorophores). In both scenarios, photodamage resulted in significant changes to the fluorescence lifetime and intensity over the duration of the acquisition, which, if neglected, may result in the misinterpretation of photophysics in FLIM measurements. We address these (mis)interpretations and attempt to correct these in the following section. Specific to the development of light-harvesting nanomaterials, the results show that proteoliposomes containing LHCII and TR are still functionally active (i.e., able to transfer energy) when deposited on a surface, and that this activity can be "switched off" by selectively photodamaging the LHCII.

5.2.8 Correcting for the distortion of lifetime measurements and ETE calculations caused by photobleaching

Using single-proteoliposome lifetime FLIM measurements, the ETE for LHCII and TR reconstituted into proteoliposomes was previously estimated to be 44% and 60% for low- and high- concentrations of LHCII, respectively (see section 5.2.6), which was significantly lower than the ETE calculated from ensemble spectroscopy for the same samples (76.3% and 83.7%, respectively). In FLIM measurements, where proteoliposomes are adhered to a substrate, we now know that LHCII becomes photodamaged as a result of FLIM excitation, as shown in the last section (5.2.7). The subsequent unquenching of TR fluorescence causes the measured fluorescence lifetime of TR to be weighted towards longer values, therefore resulting in an underestimation of the ETE from TR to LHCII. Therefore to more accurately calculate the FRET efficiency within individual proteoliposomes, a correction was developed and applied to remove the effect of the TR lifetime elongation.

Firstly, to calculate the change in TR lifetime as a result of photobleaching, the TR lifetime compared at the start of a FLIM acquisition, where LHCII photobleaching was minimal, to the TR lifetime measured at the end of a FLIM acquisition, where LHCII photobleaching was prominent. First, the TR lifetime was calculated for an initial period of acquisition where LHCII bleaching was minimal and FRET was largely intact. Photons were accumulated within the first 100 s (50 frames) of a FLIM acquisition, where LHCII photodamage was <10% (see photobleaching measurements in **Figure 5.9**). Due to the low signal, it was not possible to achieve good fits for single proteoliposomes within this time period, so the average TR lifetime was calculated by combining the fluorescence decay curves of numerous proteoliposomes (N>500) in a single field of view (**Figure 5.11a** and the *red* decay curve in **Figure 5.11b**). This was compared to the average lifetime for the full period of acquisition (between 0 to 1600 s, 500 frames) where the acceptor is gradually photodamaged by the intensity of the laser (**Figure 5.11a** and the *blue* decay curve in **Figure 5.11b**).

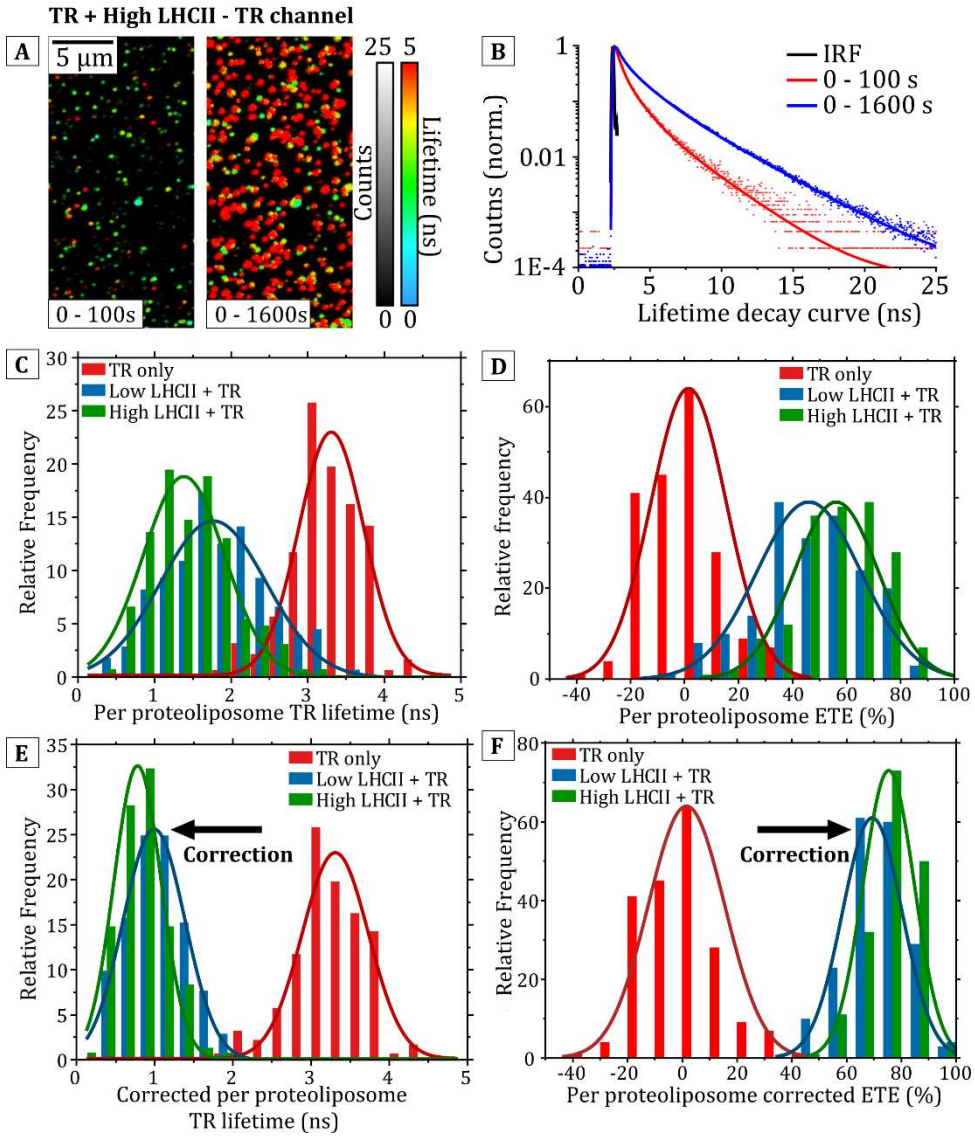

Figure 5.11: FLIM measurements of LHCII + TR proteolipsomes showing the change in TR lifetime due to LHCII photobleaching and the corrections applied to per proteoliposome distributions. **(A)** FLIM image of proteoliposomes in the TR channel accumulated from photons in the first 100s (*left panel*) versus an image aquired from photons detected during the whole acquisition (0 – 1600 s, *right panel*). **(B)** Fluoresceence decay curves generated from photons collected between 0 – 100 s (*red*) and 0 – 1600s (*blue*) during a FLIM acquisition. The IRF (*black,* solid) is reconvoluted from the raw data (*dashed*) to calculated fitted fluorescence decay curves (*solid, red and blue*). **(C),(D)** The raw data for the per proteoliposome lifetime and ETE distribution for each proteoliposome sample, repeated from Figure 5.8. **(E)** The per proteolipsoome lifetime distribution for each sample, following the correction described in Equation 5.5. **(F)** The per proteoliposome ETE distribution for each proteoliposome sample, calculated from the corrected per proteoliposome lifetimes in panel (E). The corrected lifetimes from (e) causes the ETE for each population to shift towards higher values.

From this, an estimation of the relative change in TR lifetime was calculated by:

$$\Delta\tau_{ratio} = \frac{< \tau_{0-100} >}{< \tau_{full} >} \quad \text{Eq. 5.5}$$

Where $< \tau_{full} >$ is the amplitude-weighted lifetime calculated from the full FLIM acquisition, and $< \tau_{0-100} >$ is the amplitude-weighted lifetime calculated from the first 100 s of the FLIM acquisition (where LHCII photodamage is minimal). From this $\Delta\tau_{ratio}$ was determined to be 0.53 for the high-LHCII proteoliposomes and a 0.52 for low-LHCII proteoliposomes (see **Table 5.5**).

To calculate corrected lifetimes and ETEs for single-proteoliposome FLIM measurements, each per proteoliposome lifetime (**Figure 5.11c**, repeated from section 5.2.6), <τ>, was multiplied by the average change in TR lifetime, for both the Low- and High-LHCII samples. The result is a shift to lower lifetimes for both the Low- and High-LHCII per proteoliposome distributions (see **Figure 5.11d**). With this correction applied, the average lifetime (determined from a Gaussian fit), changes from 1.77 ± 1.38 ns to 0.99 ± 0.93 ns and 1.38 ± 1.06 ns to 0.78 ± 0.71 ns for Low- and High-LHCII proteoliposomes respectively. As previously, the corrected per proteoliposome lifetimes were used to generate a per proteoliposome ETE distribution. Following the correction, the ETE distribution for each sample was shifted to higher efficiencies (**Figure 5.11e** versus **Figure 5.11f**). The average ETE increased from 44% to 71% for the Low-LHCII sample and from 60% to 77% for the High-LHCII sample, bringing the single-proteoliposome data into strong agreement with ETE's obtained from time-resolved fluorescence spectroscopy (76% and 84%, respectively). These corrected distributions contain more detailed information population statistics than can be measured through ensemble spectroscopy, and we can identify a significant fraction of vesicles that have an ETE >90%. It is not unreasonable to speculate that it may be possible to biochemically purify a sub-population of vesicles enriched for high ETE.

Frames	Time (s)	Low-LHCII + TR (1.2 µM LHCII + 12 µM TR) Fitted lifetime (ns)	High-LHCII + TR (2.8 µM LHCII + 12 µM TR) Fitted lifetime (ns)
1-50	0-100	0.71 ± 0.03	0.71 ± 0.02
1-500	0-1600	1.36 ± 0.01	1.34 ± 0.01
	$\Delta\tau_{\%}$	**0.524**	**0.534**

Table 5.5: Calculating the difference in the average TR lifetime before and after large amounts of acceptor (LHCII) photobleaching.

5.2.9 Direct observation of FRET disruption reveals a larger population of proteoliposomes with colocalised LHCII and Texas Red

An indirect measurement of the colocalisation of TR and LHCII in proteoliposomes can be made using the (somewhat destructive) method of deliberate acceptor photo-damage. This allows for the detection of the LHCII through its effect on the TR lifetime, in a way that is observable on an individual proteoliposome and provides quantitative results on the amount of photo-active LHCII in a single proteoliposome even when the number of counts is not measurable. By monitoring any increase in TR lifetime during the acquisition, the fraction of proteoliposomes in which FRET occurs can be approximated by the proxy of the TR de-quenching effect. To do this, single-proteoliposome analysis was performed for FLIM images consisting of photons collected during the first 100 s of acquisition (where LHCII is <10% photodamaged), compared to FLIM images consisting of photons collected during the final 100 s acquisition (where LHCII is almost entirely photodamaged). Single proteoliposomes were selected, as described previously, and the TR fluorescence intensity was assessed before and after LHCII had undergone significant photobleaching (see **Table 5.6**). There was inadequate signal to produce good per proteoliposome fluorescence decay curves, so the per proteoliposome "fastFLIM" was used as a metric to monitor changes to the TR lifetime (fastFLIM is a measure of the average time-of-arrival for detected photons after the excitation laser pulse).

It was observed that approximately 95% and 90% of the Low- and High-LHCII proteoliposomes displayed a significant increase in TR lifetime (where "significant" is defined as the final TR fastFLIM being at least a 25% increase (1.25×) in the initial value). Lifetime changes of this magnitude were only present in proteoliposome samples containing both LHCII and TR (in TR-only liposomes the TR lifetime increase was only 11%, **Table 5.4**), and 1.25× was deemed an appropriate threshold to avoid any noise in fastFLIM lifetimes (which typically vary by ±10%). Therefore, we conclude that the majority of proteoliposomes have successfully reconstituted both LHCII and TR components. These results show that the initial estimations for the number of colocalised proteoliposomes had underestimated this population by

~10% (intensity calculations in section 5.2.3 suggested 83% and 80% of proteoliposomes were colocalised in Low and High-LHCII samples).

Particle number	Intensity (0 – 100 s)	Intensity (1500 – 1600 s)	%ΔI	Per proteo. Fast FLIM (0 – 100 s)	Per proteo Fast FLIM (1500 – 1600 s)	%ΔfastFLIM
	Counts	Counts	(%)	(ns)	(ns)	(%)
1	51.0	28.0	-45.1	1.90	3.40	78.9
2	30.0	44.0	46.7	0.60	2.30	283
3	24.0	27.0	12.5	1.30	3.50	169
4	35.0	77.0	120	1.30	2.30	76.9
5	7.00	31.0	343	0.50	2.80	460
6	5.00	34.0	580	0.30	1.90	533
7	10.0	44.0	340	0.70	3.40	386
8	32.0	32.0	0.00	1.20	2.00	66.7
9	36.0	159	342	0.80	2.90	263
10	46.0	127	176	0.60	2.40	300

Table 5.6 Comparing the TR fluorescence intensity and lifetime (fastFLIM) for 10 example proteoliposomes before and after LHCII photodamage. An increase in the fastFLIM lifetime indicates that a proteoliposome contains LHCII, that has become photodamaged during the FLIM measurement resulting in TR de-quenching. A "significant" increase in the TR lifetime was defined as at least a 25% increase in the initial value. When N > 100 single proteoliposomes were analysed the following numbers were observed to have significant TR lifetime changes: 95 (95%) and 90 (90%) for the Low-LHCII and High-LHCII samples.

5.2.10 Summary and discussion of proteoliposomes as light harvesting nanomaterials

In this section, proteoliposomes containing LHCII and lipid-tagged Texas Red were investigated using a combination of solution spectroscopy and microscopy techniques. Ensemble absorption spectroscopy of proteoliposomes has shown that LHCII and TR can be reliably reconstituted into proteoliposomes with excellent control over the final composition of the membrane (**Figure 5.2**). Complementary single-proteoliposome fluorescence measurements suggest that the majority of proteoliposomes (>80%) contain LHCII and TR that have successfully reconstituted into the membrane, and that there is only a small population of proteoliposomes that may contain only TR *or* LHCII (**Figure 5.3**). A virtue of single proteoliposome measurements is that these proteoliposomes can be analytically separated from the

bulk population; it is not unreasonable to suggest that this population of proteoliposomes could be biochemically purified such that only proteoliposomes containing both components are present[105, 119].

The presence of TR-to-LHCII energy transfer was assessed in proteoliposomes by measuring the "effective" enhancement of the LHCII absorption range. Increasing the concentration of TR in proteoliposomes resulted in increased LHCII emission when the system was excited within the "green gap" (540 nm), where the LHCII emission per mole was found to increase linearly with the concentration of TR, suggesting that each TR molecule in the system is transferring energy to LHCII with a consistent contribution. At extremely high concentrations of TR, we would expect to reach a maximum amount of LHCII enhancement as the result of TR self-quenching that is known to occur at high concentrations[145], or by photoprotective quenching mechanisms that can occur in LHCII when there is a high density of excited singlet states[249].

Steady-state and time-resolved fluorescence measurements were used to quantify the quenching of TR due to energy transfer to LHCII. In ensemble measurements, TR-to-LHCII energy transfer was confirmed by the decrease in TR fluorescence emission concomitant to a decrease of the fluorescence lifetime in the presence of increasing concentrations of LHCII. The change in intensity and lifetime was related to an increase in the energy transfer efficiency, ultimately saturating at 95% at high concentrations of LHCII. This saturation effect is likely due to the increasing LHCII concentration resulting in a decrease in the average TR-LHCII separation below the Förster radius of ~7 nm for a TR/LHCII donor/acceptor pair, and is consistent with randomly distributed chromophores undergoing FRET in a 2D bilayer system[250].

FLIM measurements showed that proteoliposome populations had relatively consistent sizes (diffraction limited), free of any large microscale aggregates or other unexpected particles that can skew population statistics. Per-proteoliposome lifetime distributions showed that the population of lifetimes within a sample consisted of one distinct peak, suggesting that the proteoliposome self-assembly process results in proteoliposomes that all have a similar membrane composition, and no sub-populations that contain vastly different amounts of TR or LHCII. Per

proteoliposome lifetime measurements were also used to verify TR-to-LHCII energy transfer, showing that the TR lifetime was significantly quenched in proteoliposomes containing TR compared to proteoliposomes containing TR only, in agreement to the trends observed in time-resolved fluorescence measurements.

Measurements of the per proteoliposome TR lifetime allowed for the calculation of the TR-to-LHCII energy transfer efficiency on a per proteoliposome level. ETEs for proteoliposomes containing low and high concentrations of LHCII were found to be 44% and 60% respectively, in apparent disagreement with ETEs calculated from time-resolved fluorescence measurements of the same samples (81% for low-LHCII proteoliposomes, and 87% for high-LHCII proteoliposomes). This discrepancy was determined to be the result of significant photodamage of both fluorophores that was occurring during microscopy measurements. LHCII was found to photobleach more rapidly than TR, resulting in TR de-quenching as LHCII was no longer able to accept energy from the FRET donor. When photodamage and TR de-quenching was accounted for, the ETE calculated from per proteoliposome lifetimes (71% and 77% for Low- and High-LHCII proteoliposomes respectively) and ensemble time-resolved fluorescence were found to be in good agreement. Our results highlight the need to account for photobleaching when performing FLIM measurements to avoid the misinterpretation of photophysical properties. In photosynthetic systems, the majority of photodamage that occurs is believed to be caused by direct damage to the chlorophyll molecules by singlet oxygen (either for in vitro experiments or under natural conditions). Triplet excited states of chlorophylls can react with molecular oxygen to form highly reactive singlet oxygen states which, once formed, can reduce any covalent bond in its immediate vicinity causing irreparable structural damage.[35] Removal of oxygen from the protein's local environment (aqueous buffer), using O_2-scavenging enzymes, has already been demonstrated to be an effective measure in limiting the photodamage of photosynthetic systems and preserving photophysical interactions.[56, 80]

Through direct observation of TR de-quenching we were able to determine the presence of LHCII and TR in ~90% of proteoliposomes, even when the number of counts is low, as well as demonstrating that the LHCII had retained its activity in proteoliposomes that are adsorbed onto a surface. Retaining the optical

functionality of LHCII on a surface is crucial for any applications of this concept in bio-hybrid devices. Numerous studies have already used photosynthetic machinery to make photovoltaic devices by adsorbing bacterial reaction centres on nanowires,[251] graphine,[252] and gold electrodes,[253] and model membranes containing electron transferring proteins can also be deposited onto electrodes with efficient electron transfer.[200] A logical next step for the enhancement of light-harvesting with lipid-tagged chromophores is to apply this approach to a photosynthetic membrane that is capable of electron transfer (i.e., contains active PSII), such that the additional absorbed light can be converted to a useful format for nanotechnologies.

5.3 Concept 2: Enhancing "hybrid membranes" through self-assembly of thylakoid extracts with synthetic pigments

In Section 5.2 the enhancement of LHCII was demonstrated in lipid bilayers by interfacing the protein complex with lipid-tagged chromophores that were spectrally complementary (TR-DHPE lipids). Here, we exploited the spontaneous self-assembly of lipids and proteins to generate proteoliposomes and, by modulating the concentrations of either component, it was possible to exert control over the amount of LHCII enhancement and the TR-to-LHCII energy transfer efficiency. Light-harvesting nanomaterials, such as these proteoliposomes, have potential applications in bio-hybrid photovoltaic devices with bespoke photophysical properties[254, 255], however, any potential application will rely on the efficient conversion of energy into a chemical format (i.e., energy trapping). Therefore, it would be useful to develop model membranes including complexes capable of photochemistry, such as PSII, which can also transfer electrons to other electron acceptors[256], including conductive electrodes to generate simple bio-photovoltaic solar cells[257]. Photosynthetic electron transport is most efficient in membranes containing PSII in conjunction with large areas of antenna proteins, which can transfer absorbed energy to a central photosystem at an optimal rate to allow regular photochemistry to take place[1]. Therefore, an ideal light-harvesting membrane would contain a combination of LHCII and PSII proteins, optimised to maximise the rate of electron generation.

In Chapter 4, a model membrane system assembled from synthetic lipids and natural thylakoid membranes was characterised. AFM and FLIM analysis suggested that these "hybrid membranes" contain a mixture of LHCII and PSII proteins that are able to freely diffuse and interact unhindered by the underlying substrate. In addition, hybrid membranes were found to show some level of photochemical activity when an electron acceptor, DMBQ, is introduced to the membrane, suggesting that the system is capable of electron transfer to electro-active compounds in close proximity to the membrane. At the end of that study, we hypothesised that it would be possible to introduce other components (amphipathic molecules, quinones, or proteins) into hybrid membranes by taking advantage of their self-assembly formation mechanism. In particular, we wished to test if it was possible to enhance hybrid membranes by incorporating complementary chromophores into the membrane, to form a light-harvesting nanomaterial that was capable of generating electrons. The following section details our efforts to enhance hybrid membranes using the strategy described for LHCII-TR proteoliposomes

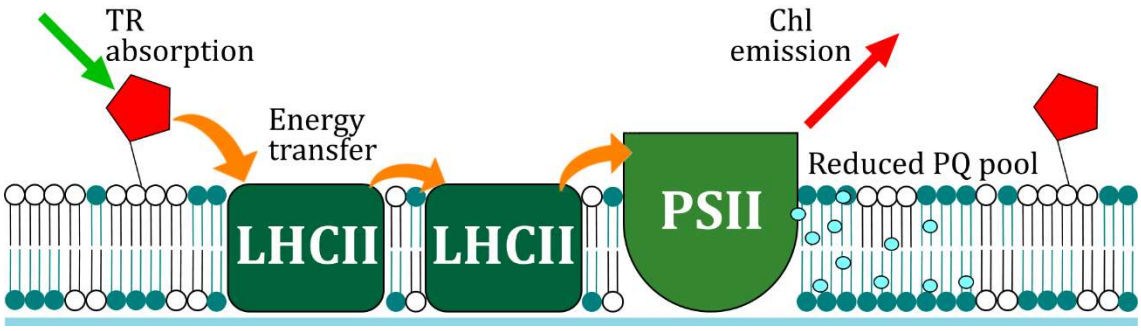

Figure 5.12: Potential schematic for energy transfer occurring in enhanced hybrid membranes. Light is absorbed by TR and transferred via FRET to Chl pigments in LHCII/PSII or other photosynthetic pigments, and is funnelled towards the photosynthetic reaction centre. In the absence of soluble proteins (such as ferredoxin) or other electron acceptors, all plastoquinones are likely to become reduced within the membrane, so energy will be primarily emitted as Chl fluorescence.

5.3.1 Texas Red fluorescence is quenched and Chl fluorescence is enhanced in hybrid membranes containing TR

As in section 5.2, Texas Red (TR) was selected as an ideal candidate to enhance hybrid membranes because it can be easily incorporated into the workflow for sample preparation. As shown in section 4.3.4, TR-DHPE lipids can be incorporated into hybrid membranes by introducing a small percentage (0.5 % (w/w)) of TR-DHPE into the DOPC liposomes before they were mixed with the extracted thylakoid membranes so that they merge and form hybrid membranes including TR. When these TR-DOPC liposomes were used to form hybrid membranes, it was observed that the TR was able to diffuse laterally throughout the membrane, with a high mobile fraction (96.9 ± 0.7 %) and relatively fast rate of diffusion (approximately twice as fast as PS proteins incorporated into the membrane, **Figure 4.11**). It is therefore feasible that the TR fluorophores would be able to interact with the proteins within the membrane and transfer energy via FRET to the photosynthetic proteins in this model system (see **Figure 5.12** for schematic).

Successful TR to Chlorophyll energy transfer would be manifested as a shortening of the TR fluorescence lifetime and an enhancement of Chl emission when excited in the “green gap” of low Chl absorption. Therefore, the presence of excitation energy transfer in TR-enhanced hybrid membranes was assessed in two ways. *Firstly*, by comparing the fluorescence properties of TR in the absense of Chl to TR incorporated into an enhanced hybrid membrane. *Secondly*, by comparing the Chl fluorescence of hybrid membranes with and without TR when excited in the aforementioned ”green gap”. Measurements were performed with the FLIM instrument set up to selectively excite *either* LHCII *or* TR and collect fluorescence optimised for *one* or *other*. Spectral and temporal selectivity allowed us to define 3 separate FLIM channels: (i) the “TR channel” defined as the combination of the selective TR excitation (561 nm) and a detector optimised for TR emission (590-650 nm); (ii) the “standard Chlorophyll (Chl) channel” defined as the combination of the selective Chl excitation (640 nm) and a detector optimised for Chl emission (655 – 725 nm); (iii) the “Chl Enhancement channel” defined as the combination of selective TR excitation and the detection of Chl emission. As a result, the Chl

enhancement channel was sensitive to the Chl fluorescence which occurs due to energy transfer from TR to the Chl pigments of LHCII, PSII or other proteins.

Lipid-only membranes were formed in the corrals of a diyne-PC template by incubating the substrate with liposomes containing DOPC and 0.5% (w/w) TR-DHPE. The lipid-tagged dye appeared to spread homogeneously and a well-defined square array of 20 × 20 um boxes was observed, with ~800 counts per pixel visible in corrals in the TR channel (**Figure 5.13ai**). Spillover into the Chl channel was negligible as shown by minimal fluorescence detected in the Chl channel (**Figure 5.13aii**) and was quantified as (0.23 ± 0.05)% of counts (mean ± SD, N = 16 corrals). Spillover into the Chl enhancement channel was quantified as (3.1 ± 1.0) % of the counts detected in the TR channel (**Figure 5.13aiii**); this percentage is small but leads to significant counts due to the fact that the TR signal is consistently ten times larger than signals in the Chl and Chl enhancement channels. Therefore, this relatively minor spectral overlap contributes a significant number of counts to the enhancement signal and must be accounted for during later analysis (~25 counts per pixel). In the absence of Chl-containing proteins, the TR fluorescence has a long-lived excited state with $\langle\tau\rangle$ = 3.69 ± 0.03 ns.

In the "enhanced hybrid membrane" (i.e., containing Chl + TR), the TR fluorescence appeared significantly quenched, indicative of FRET. In the TR channel (**Figure 5.13ci**), the intensity is somewhat lower (~500 counts/pix), although this could be explained either as FRET-related quenching or alternatively due to a lower concentration of TR (this cannot be ruled out as it is conceivable TR could be "diluted" by the presence of the thylakoid lipids and proteins). Fluorescence lifetime measurements are generally independent of fluorophore concentration, so can be used reliably to determine the extent of quenching and thus energy transfer. Qualitatively, the TR fluorescence decay was altered from a relatively long lifetime (*orange*) in the lipid membrane sample (**Figure 5.13ai**) to a moderate lifetime (*green*) for the sample containing both TR and thylakoids (**Figure 5.13ci**). This is a strong indication of TR-to-Chl energy transfer. Indeed, the fitted fluorescence decay curve for TR becomes significantly steeper, with a calculated mean lifetime of $\langle\tau\rangle$ = 3.69 ± 0.00 ns for TR-only membranes (**Figure 5.13d**, *red curve*) compared to $\langle\tau\rangle$ = 1.86 ± 0.01 ns for TR in enhanced hybrid membranes (**Figure 5.13d**, *blue curve*).

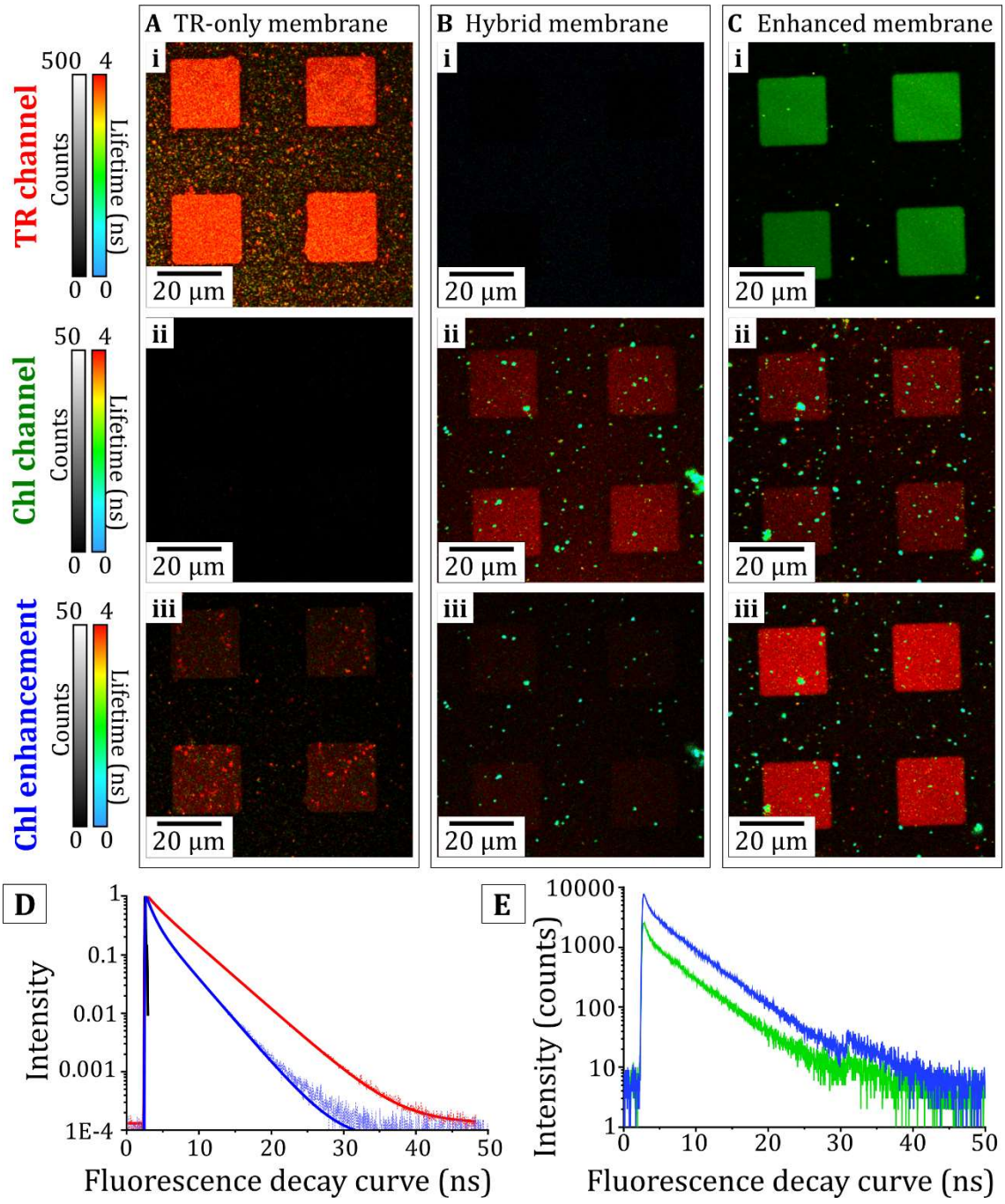

Figure 5.13: Analysis of the potential for excitation energy transfer from Texas Red to Chl for three types of patterned membranes formed within polymerised diyne-PC corrals. **(A)** FLIM of lipid-only membranes (DOPC+TR) **(B)**, hybrid membranes (thylakoids+DOPC) **(C)**, and enhanced hybrid membranes (thylakoids+DOPC+TR) **(D)** Normalized, fitted fluorescence decay curves for the TR channel, comparing the samples where thylakoid proteins were absent (red) and present (blue). Data from images (a)(i) and (c)(i), respectively. **(E)** Raw fluorescence decay curves for from hybrid membranes the Chl enhancement channel in the absence (green) and presence (blue) of TR. Data from images (b)(iii) and (c)(iii), respectively.

The energy transfer efficiency (ETE) of the system can be calculated from the equation, $ETE = 1 - \tau_{DA}/\tau_D$, where τ_{DA} is the donor lifetime in the presence of the acceptor and τ_D is the donor lifetime in the absence of the acceptor. Thus, FRET efficiency for TR-to-(LHC or PS) proteins in these hybrid membranes was calculated to be 49.6%.

To calculate the enhancement of Chl fluorescence when using excitation in the "green gap" of Chl absorption, normal hybrid membranes were compared with those containing TR. For standard hybrid membranes, the fluorescence properties were consistent with those described in Chapter 4 showing clear square regions of Chl fluorescence with a long, *red* fluoresence lifetime ($<\tau>$ = 4 ns) (**Figure 5.13bii**). There is a relatively high level of spillover and a significant portion of the fluorescence detected in the Chl channel is also registered in the Chl enhancement channel, observed as a faint array pattern with ~15-20 counts/pix (**Figure 5.13biii**). The proportion of Chl fluorescence that overlaps with the enhancement channel was calculated to be (34.6 ± 5.6)% (mean ± S.D., N = 16 corrals). This was taken into account in later calculations quantifying the extent of Chl enhancement. Spillover of Chl signal into the TR channel was negligible, leading to an extremely low number of counts (**Figure 5.13bi**).

TR-to-Chl energy transfer was evident from the significant increase in fluorescence intensity detected in the Chl enhancement channel in the hybrid membranes containing TR (**Figure 5.13ciii**) compared to those without TR (**Figure 5.13biii**). Note that the intensity observed in the standard Chl channel was similar for both samples with ~30 counts/pix (**Figure 5.13** panels **bii** vs **cii**) whilst the intensity in the Chl enhancement channel significantly increased from 15 to ~40 counts/pix (panels **biii** vs **ciii**) showing that only selective excitation of TR reveals the enhancement effect. Fluorescence decay curves accumulated in the Chl enhancement channel from all photons detected in four corrals show the difference in intensity clearly, where the total number of photons per decay curve increases from ~35,000 counts for standard hybrid membranes to ~60,000 counts for TR+hybrid membranes (integrated area under *green curve* versus *blue curve* in **Figure 5.13c**). The extent of Chl enhancement was calculated, taking into account the established fluorescence spillover between channels, with a careful numerical

analysis performed on many corrals, as shown in **Table 5.7**. The Chl enhancement (i.e. the increase in counts in the Chl enhancement channel) due to TR in hybrid membranes was found to be (108 ± 15) % given this particular concentration of TR incorporated in these samples (0.5% TR w/w). Across all FLIM channels (from both the 485 nm and 560 nm excitation), the total number of Chl counts was increased by (27.7±3.7) % due to TR. Undoubtedly, this level of enhancement could be significantly increased in future studies by using higher concentrations of TR, as demonstrated for TR-LHCII-proteoliposomes with a range of TR content.

Chl counts	**TR Counts**	**Enhancement Counts**	**Enhancement counts minus TR spillover**	**% increase in enhancement channel**	**% increase in all Chl channels**
I_{Chl} (Counts × 10^5)	I_{TR} (Counts × 10^5)	I_{En} (Counts × 10^5)	$I_{En} - I_{TR}S_{TR}$ (Counts × 10^5)	Eq. 5.6 (%)	Eq 5.7 (%)
6.51	35.32	5.35	4.28	89.68	23.06
8.56	37.81	6.92	5.76	94.50	24.30
11.10	45.35	9.52	8.14	111.93	28.78
10.21	56.54	9.715	7.99	126.09	32.42
9.09 ± 1.01	**43.8 ± 4.8**	**7.90 ± 1.06**	**6.54 ± 0.44**	**108 ± 15**	**27.7 ± 3.7**

Table 5.7: Calculations for the chlorophyll enhancement by Texas Red in enhanced hybrid membranes. Each row represents the signal accumulated from the 4 corrals that are observed in a typical field-of-view. The four rows are from different samples. The **bottom row** shows the mean values and standard deviation across all 4 samples (16 corrals total).

I_{Chl}, I_{TR}, I_{En} are the measured number of counts for four corrals in the Chl, TR and Enhancement channels respectively. S_{TR}, S_{Chl} is the proportion of signal that spills over from the TR and Chl channels into the Enhancement channel. $S_{TR} = 0.03$ and $S_{Chl} = 0.35$ calculated from control samples (see Section 4.3.1 for method);

The increase in the number of counts in the enhancement channel (excited at 561 nm) is given by:

$$\%\Delta_{En} = \left[\frac{I_{En} - I_{TR}\,S_{TR}}{I_{Chl}\,S_{Chl}} - 1\right] \times 100\% \qquad \text{Eq. 5.6}$$

The overall increase in the amount of Chl fluorescence (excited at all wavelengths) is given by:

$$\%\Delta_{Chl} = \left[\frac{I_{Chl} + I_{En} - I_{TR}\,S_{TR}}{I_{Chl} + I_{Chl}\,S_{Chl}} - 1\right] \times 100\% \qquad \text{Eq. 5.7}$$

5.3.2 Energy transfer in enhanced hybrid membranes can be "switched-off" by photobleaching

The FRET relationship between chromophores is highly dynamic, and we found that the extent of excitation energy transfer could be modified post-formation of the membranes. This was demonstrated with photobleaching experiments using epifluorescence microscopy. A hybrid membrane sample including TR is shown in **Figure 5.14a**, displaying the Chl fluorescence from three adjacent membranes, where the aperture was deliberately positioned to give different levels of exposure to the ~480 nm excitation light that selectively photobleaches chlorophyll. The left corral was completely covered and acts as a control with no photobleaching. The central membrane was partially covered, so a proportion of the proteins becomes photo-damaged by this exposure (expected to be equal to the uncovered area divided by the total corral area). The right membrane was completely exposed to the high-intensity excitation, resulting in extensive photobleaching of all proteins in that membrane. After this initial image was taken, the sample was exposed to Chl-selective light for an extended period with the aperture still in this position. The aperture was then removed, and epifluorescence images were taken using TR-specific excitation and emission filters. The intensity of the TR fluorescence appeared to be linearly proportional to the percentage of the corral area that was exposed to Chl excitation, across multiple experiments (**Figure 5.14b**, different *coloured datapoints*).

In a separate epifluorescence experiment, a single corral of membranes was imaged over a long time period with sequential exposures to TR-selective excitation. For a control sample of a DOPC+TR lipid bilayer in the absence of the LHC/PS proteins the TR gradually bleaches (**Figure 5.14c**, *upper*), decreasing to 90 % of the initial intensity after ~7 s of cumulative exposure (**Figure 5.14d,** *red line*). For a sample of hybrid membranes containing TR, in contrast, the TR fluorescence intensity increased over time (**Figure 5.14c**, *lower*), so that after 7 s of cumulative exposure, the TR intensity had increased to 170 % of the initial intensity (**Figure 5.14d**, *blue line*). This result can be explained by the fact that the Chls within LH and PS proteins are more susceptible to photobleaching than TR molecules, and can become

photodamaged as a result of either direct exposure or excitation via energy transfer from TR (as previously identified in section 5.2.7).

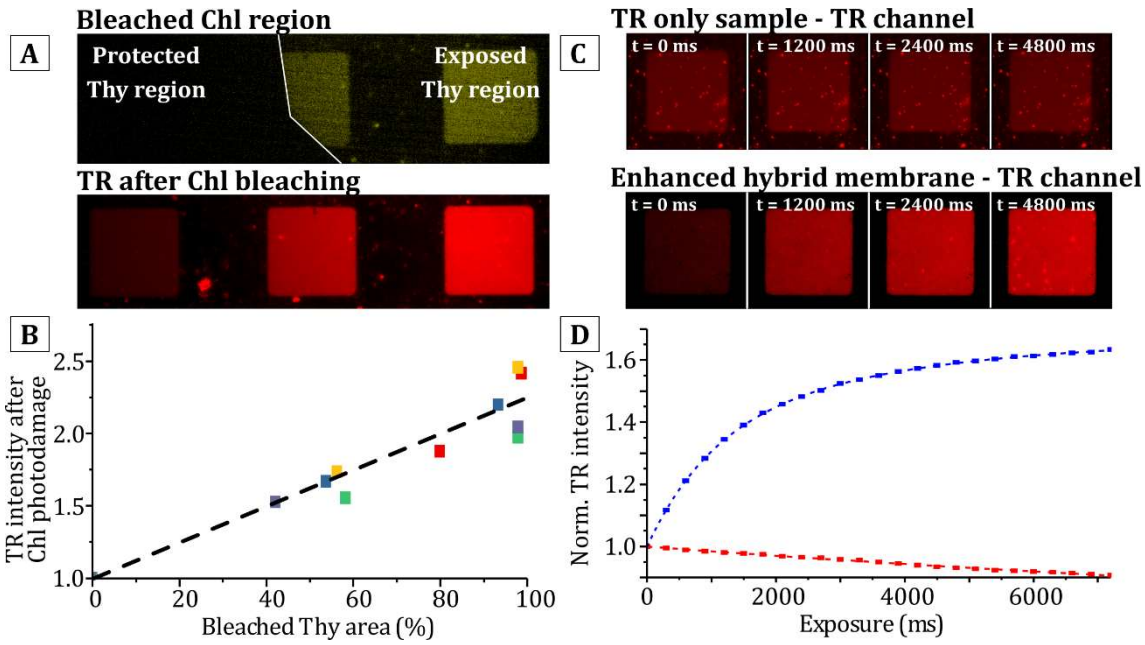

Figure 5.14: Epifluorescence microscopy experiments demonstrating control over the TR-to-Chl energy transfer occurring in enhanced hybrid membranes. **(A)** Epifluorescence images of hybrid membranes with TR, where an adjustable aperture was positioned partially over three corrals, in order control the fraction of the membrane exposed to high intensity excitation light for deliberate photobleaching. Top image: one bleaching experiment, using a filter cube optimized for selective Chl excitation and Chl emission. Bottom image: the same region after photobleaching, using a filter cube optimized for TR excitation and TR emission. **(B)** Numerical analysis of a series of photobleaching experiments similar to (a), where each data point colour represents an individual experiment (set of three corrals). Fluorescence intensity in the corral after photobleaching is plotted against the area of the square which was exposed (normalized to an intensity of 1.0 for the protected corral). **(C)** Image shows a time-lapse series of epifluorescence images of one corral of a TR only membrane versus an enhanced hybrid membrane (thylakoid/DOPC/with TR) over a long time period, using the filter cube for TR excitation/ TR emission. Over the course of the experiment, fluorescence intensity apparently increases with time. **(D)** Graph showing the TR fluorescence intensity plotted over such a time-course for the hybrid membranes shown (blue trace) and for a TR-only lipid membrane sample (red trace). The dotted lines shown are mono-exponential fits to guide the eye.

Both of these epifluorescence experiments provide indirect evidence of the excitation energy transfer from TR to the LHC and PS proteins. As the Chl-containing proteins are photo-damaged (either through direct excitation or excitation via energy transfer from TR), they become unable to accept energy from the TR donor. The visible effect of this is the dramatic "de-quenching" of the TR, evident in these images, in proportion to the amount of LHC+PS proteins that are photodamaged. This clear trend and its reproducibility shows that we have the ability to modulate the amount of energy delivered to the proteins in this system. This could be potentially interesting as a way to optically switch on or off additional energy transfer processes.

5.3.3 Summary and discussion of enhanced hybrid membranes as light harvesting nanomaterials

In this section, we have demonstrated a "proof of concept" for the enhancement of the Chl absorption in hybrid membranes by incorporating lipid-tagged Texas Red (TR) chromophores. FLIM measurements of hybrid membranes containing TR in comparison to control samples assessed the extent of Chl fluorescence enhancement and the energy transfer efficiency from TR pigments to photosynthetic proteins. When thylakoid extracts were incubated with DOPC liposomes containing 0.5% TR-DHPE, the resulting membrane was found to have a Chl emission that was increased to 208 % of its level in hybrid membranes containing no TR, when excited with green light (560 nm). Energy transfer from TR-to-Chl was identified by a decrease in the TR fluorescence lifetime from 3.69 ns when it is within DOPC membranes to 1.86 ns within hybrid membranes. The energy transfer efficiency from TR-to-Chl was calculated to be 50 % suggesting that, on average, each TR is separated from a Chl pigment by ~7 nm, given that the Förster radius is ~7 nm (section 5.2.1). The ability to "switch off" and control the energy transfer between TR and Chl was demonstrated through the deliberate photobleaching of Chl pigments, resulting in the dramatic de-quenching of the TR fluorescence intensity and lifetime. It was shown that the amount of TR recovery is linearly proportional to the fraction of the Chl that was (effectively) removed from the FRET system via photodamage, suggesting that each LH/PS protein quenches neighbouring TR by a similar amount. This is all in line with expectations from Förster theory and demonstrates that hybrid membranes behave in a predictable manner.

Whilst we have only investigated hybrid membranes containing one particular concentration of thylakoid proteins and TR, we hypothesise that increasing the TR concentration will increase the Chl enhancement, and that increasing the protein concentration will result in more significant quenching of TR fluorescence (as observed in proteoliposome samples in Section 5.2). A further series of samples could investigate this trend more directly, to maximise the light-harvesting capabilities of hybrid membranes before utilising them for bio-inspired nanotechnologies or other applications.

5.4 Concluding remarks and future outlook

In this chapter, the concept of enhancing the spectral range of photosynthetic light-harvesting with non-covalently attached chromophores has been demonstrated in two model systems. Firstly, the modularity of such systems was demonstrated using a LHCII-proteoliposome-based system and incorporating a vast range of TR-DHPE concentrations. Secondly, TR was incorporated into hybrid membranes that self-assemble from a mixture of synthetic lipids and extracted thylakoid membranes. Extremely high ETE was achieved for proteoliposomes including the highest quantities of LHCII (>90%), demonstrating that energy transfer between chromophores that are not covalently attached (but still in close proximity) can compete with the high ETEs achieved through direct attachment of complementary chromophores to LHCII[237-240]. The ETE appeared to be lower for TR within hybrid membranes (~50%) but this is likely to be due to the relatively low concentration of LH/PS complexes (estimated to occupy 1-3% of the membrane area in chapter 4). The "acceptor enhancement" of the fluorescence from Chl-containing proteins due to the FRET from TR was demonstrated for both systems. The enhanced hybrid membrane system has some notable advantages over a solution based-proteoliposome system if one wished to develop surface-based nanotechnology. Firstly, hybrid membranes contain multiple types of photosynthetic proteins that are capable of electron generation and NADPH production[162]. Secondly, it is possible to change the template pattern to generate enhanced hybrid membranes with desired dimensions or features. It would therefore be feasible to generate

microscale photovoltaic membranes that are compatible with 2D micro/nanoscale electronics (nanowires, micro batteries etc) that already exist[258-260].

Future studies should aim to quantify the electron transfer capabilities of proteins within enhanced hybrid membranes and proteoliposomes. Previous studies have already shown that LH proteins deposited onto surfaces can provide directional transfer of energy[80, 171] and can be coupled with electrodes to generate a current[261, 262]. Likewise, bacterial photosynthetic reaction centres have previously been adsorbed onto nanowires[251], graphene[252], and gold[253] and shown to generate electrons in response to high light conditions. It would be particularly beneficial to determine how extrinsic pigment-to-Chl energy transfer relates to an increase in electron generation, in order to maximise the efficiency of this concept for photovoltaic devices and to optimise the system before scaling to an industrial level. In addition, it has been shown that it is possible for energy to propagate through multi-layered membranes deposited onto electrodes[200], and future light-harvesting devices could make use of a multi-layered structure to increase the total area available for light-harvesting.

The concept of using chromophores that are non-covalently incorporated into a lipid bilayer to enhance the absorption range of chlorophyll- and carotenoid- containing proteins could also be applied beyond model systems and to full photosynthetic systems. Some lipophilic dyes have been known to incorporate into pre-formed lipid bilayer systems[263] and into natural biomembranes with high efficiency[264]. There are a plethora of synthetic chromophores that cover different portions of the visible light spectrum (and UV and NIR) and a combination could be preferentially selected to maximise the spectral coverage of photosynthetic proteins. Extrinsic chromophores could potentially be incorporated into natural systems that are already being used in biotechnology to convert light-energy into useful chemical formats. Increasing the spectral range of light-harvesting could result in increased biomass production for crop yields[265], biofuel production[266] or carbon fixation[255].

Our application of hybrid membranes in this chapter have also demonstrated the potential of this model system to study energy transfer between deliberately introduced non-native chromophores and natural photosynthetic proteins in a

mixed system, which could be utilised in future as a method of understanding the biophysics of energy transfer in complex membranes. In the following results chapters, these patterned model membranes are used as an adaptable platform that can be perturbed and controlled by the application of electric fields to investigate various aspects of photophysics for a range of synthetic lipid-attached chromophores and for membranes containing an assortment of photosynthetic proteins.

5.5 Chapter acknowledgements

Section 5.2 includes results accepted for publication within the study:
Hancock A. M., Meredith S., Connell S. D. A., Jeuken L. J. C., Adams P. G. (2019), *Proteoliposomes as energy transferring nanomaterials: enhancing the spectral range of light-harvesting proteins using lipid-linked chromophores*, Nanoscale, 10.1039/C9NR04653D

In this publication S. A. Meredith was responsible for the acquisition and analysis of FLIM data and presentation of FLIM images. A. M. Hancock performed purification of the LHCII protein, co-reconstitution of LHCII alongside lipid-tethered Texas Red (TR) chromophores into proteoliposomes, acquisition and analysis of solution-based spectroscopy and wrote the first drafts of the manuscript. All authors revised the manuscript.

6 Using model membranes to investigate the self-quenching of fluorophores

6.1 Introduction

Fluorescence quenching is a general phenomenon that has been observed when fluorescent molecules are assembled at high concentrations into a lipid membrane, for example, free chlorophylls[267] and similar monochromatic fluorophores[268-270]. It is postulated that excited states may migrate through a network of proximal fluorophores within the membrane, via FRET, before being quenched by non-fluorescent traps that may formed when two, or more, molecules interact[271, 272]. The fluorescence quenching of freely diffusing fluorophores also bears similarities to both the aggregation-induced quenching and energy transfer that is known to occur between LHCII complexes at the nanoscale, and the sub-nanometre interactions between bound pigments within LHCII that may form a quenching site as a result of local conformational changes. In all scenarios, the photophysical properties of fluorophores rely heavily on their interactions with the surrounding physical and chemical environment (pH, ionic strength, temperature) and how multiple fluorophores are organised with respect to each other (pigment-pigment coupling). Therefore, investigating the photophysics of free individual pigments (i.e., not bound to/within a protein) may also provide insight into the energy transfer processes and non-radiative dissipation of energy that occurs in photosynthetic membranes. Moreover, the photophysics of monochromatic fluorophores may be used as a baseline to compare to more complicated networks, for example to assess how fluorescence quenching may differ between freely interacting pigments and pigments that are held at fixed orientations and separations in multi-chromophore complexes.

Previous models to quantify fluorescence concentration quenching (for both monochromatic fluorophores and photosynthetic systems) have so far relied on the generation of multiple discrete samples encompassing a wide range of fluorophore concentrations or photophysical states.[268, 269, 273] This process is both time-consuming and only provides information about the handful of scenarios that are

investigated. In addition, investigations of quenching are often performed in systems that poorly represent natural membranes (pigments in organic solvent solutions and/or in the absence of lipids[274]) and the quenching behaviour may be significantly altered by the local environment or absence of native-like interactions. Alternative approaches to describe concentration quenching have involved the laborious theoretical modelling of networks of fluorophores[267, 272, 275]. Such models often describe large scale networks of fluorophores in little detail (coarse-grained models),[276, 277] or may finely describe interactions between a small number of fluorophores whilst neglecting energy transfer that may occur over large distances (greater than a few nanometres)[61]. Therefore, these models are rarely suitable to represent the combination of localised quenching and long-range energy transfer that is believed to occur between numerous fluorophores and in light-harvesting membranes.

An ideal experimental system for investigating concentration quenching would provide the ability to interrogate a large and continuous range of fluorophore concentrations and would allow for the side-by-side comparison of multiple types of fluorophores whilst maintaining consistency between different samples (e.g., similar pH, solvent conditions and ionic properties). In chapters 4 and 5, we demonstrated that both fluorescent membrane proteins (e.g., LHCII and PSII) and lipid-tagged monochromatic fluorophores (TR-DHPE) can be easily incorporated into hybrid membranes in a way that mimics the native lipid-protein/lipid-lipid interactions that may contribute to fluorescence quenching. Patterned hybrid membranes, in particular, were shown to be accessible to high-resolution AFM and FLIM measurements, in a way that vesicles are not, allowing the organisation of fluorophores to be correlated to their photophysical properties. However, the self-assembly process resulted in photosynthetic proteins that were significantly diluted within the membrane to the point where the fluorescence lifetime of related to chlorophyll emission was almost entirely non-quenched (~4 ns). Therefore, if hybrid membranes or patterned lipid membranes are to be used as a platform to interrogate concentration quenching it is necessary to increase the fluorophore concentration to the point where quenching becomes significant.

"In-membrane electrophoresis" is a powerful tool for controlling the organisation of charged fluorophores[144-147, 278-280]. By applying an electric field parallel to the plane of a surface-supported patterned lipid membrane, multiple researchers have been able to manipulate charged fluorophores such that they migrate in the direction of the Lorentz (electromagnetic) force and accumulate at the edge of the confined membrane.[146] The mechanical processes of in-membrane electrophoresis have been well documented, such that the final distribution of fluorophores (after reaching equilibrium under the electric field) can be predicted and controlled by tuning various experimental conditions, such as the buffer composition, electric field strength, and temperature[146, 147, 279]. For these reasons, in-membrane electrophoresis combined with FLIM measurements could act as a reliable and versatile method to increase the concentration of membrane-based fluorophores and assess the resulting photophysical state.

This chapter describes the application of electric fields to control the organisation and concentration of lipid-tagged fluorophores in patterned lipid bilayers. To interrogate concentration quenching that occurs between freely-diffusing fluorophores, in-membrane electrophoresis is combined with fluorescence lifetime measurements with the aim of deducing the molecular mechanism of quenching and providing insight to the underlying energy transfer and quenching pathways. To assess the accuracy and viability of in-membrane electrophoresis as a method to interrogate concentration quenching, our experimental results are compared against the existing mathematical theory for concentration quenching of fluorophores. Finally, this platform is applied to delineate a complex combination of quenching mechanisms, specifically, a combination of both concentration quenching and the quenching that may occur when multiple excited states interact with (annihilate) each other.

6.2 Experimental concept: Using electric fields to control the organisation and concentration of fluorophores in model membranes

Three inorganic fluorophores were selected as suitable targets for in-membrane electrophoresis of monochromatic pigments. Texas Red (TR), Nitrobenzoaxadiazole (NBD) and Bodipy (BOD) are commonly used as fluorescent probes and available to purchase in a form where the dye is tethered to a negatively-charged lipid headgroup DHPE. In chapter 5, we identified a self-quenching behaviour in TR, and both NBD and BOD have been the focus of investigations into self-quenching in previous publications,[268, 270] therefore we predict that increasing the concentration of fluorophores will result in a quenched fluorescence intensity and lifetime. The overall charge of each fluorophore moiety (positive/negative charges are *circled, red*/*blue* in the structures in **Figure 6.1a, b** and **c** for TR, NBD and BOD, respectively) is neutral, but when tethered to the negatively charged DHPE (**Figure 6.1d**), each molecule is predicted to have a net negative charge, q = -1*e*. Therefore we predict that all three fluorophores will migrate towards the positive potential (cathode) when an electric field is applied to the membrane.

We opted to use a polymerised lipid template to generate confined, patterned lipid bilayers (corrals) for in-membrane electrophoresis due to the ability of the template to stabilise both lipid-only and hybrid membranes containing photosynthetic proteins, and the accessibility of patterned bilayers to FLIM and AFM. Prior to the application of electric field (**Figure 6.1e**), the fluorophores are expected to be homogenously distributed in lipid bilayer due to the random diffusion of molecules. During the application of the electric field, fluorophores are predicted to diffuse towards and accumulate at one end of the corralled membrane because the edge of the polymerised template acts as an impenetrable barrier (see **Figure 6.1f**). Note that one axis of the 2-D square array pattern was deliberately aligned with the direction of the electric field, to make measurements easier (i.e., 20 x 20 μm boxes roughly aligned with the E-field direction).

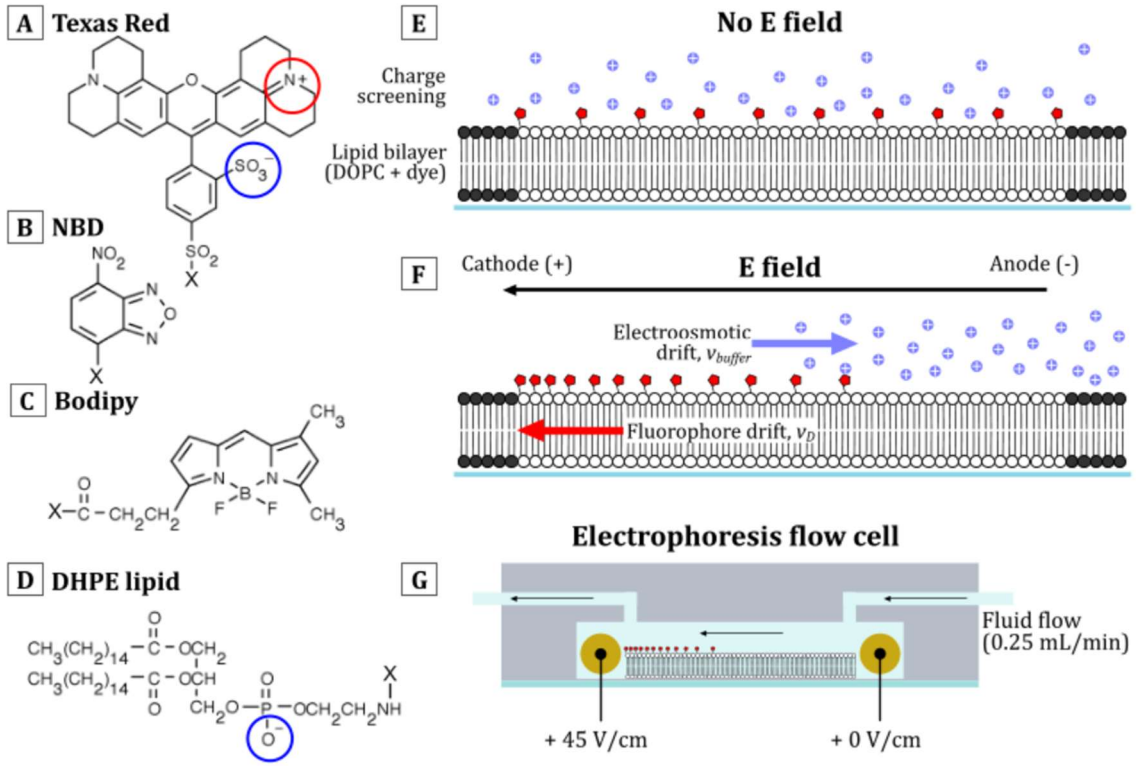

Figure 6.1: Chemical structure of the fluorophores selected for in-membrane electrophoresis, and the schematic of the electrophoresis experiment. **(A)** Chemical structure of sulforhodamine 101 acid chloride (Texas Red). **(B)** Chemical structure of N-(7-Nitrobenz-2-Oxa-1,3-Diazol-4-yl)-1 (NBD). **(C)** Chemical structure of (N-(4,4-Difluoro-5,7-Dimethyl-4-Bora-3a,4a-Diaza-s-Indacene-3-Propionyl)-1 (Bodipy). **(D)** Chemical structure of the DHPE lipid that the fluorophores in (a), (b), and (c) are tagged to (attachment point marked by X). **(E)** Schematic of a patterned lipid bilayer in a polymerised (*black*) lipid template with no applied electric field. TR fluorophores (*red*) are initially uniformly distributed in the membrane, with a screen of ions (*purple*) close to the membrane surface. **(F)** Schematic of (e) but now with an applied electric field. TR fluorophores (*red*) diffuse towards the positive electrode and accumulate at the edge of the membrane. Positive ions (*lilac*) diffuse towards the negative electrode creating osmotic friction between the buffer and the fluorophores. **(G)** Basic schematic of the electrophoresis flow cell (not to scale). *Gold* shows the position of electrodes.

After some time the system reaches an equilibrium, and the resulting concentration profile of fluorophores at the membrane edge is the result of a balance of forces that work for (e.g., Lorentz force) and against the electric field (e.g., electroosmotic drag and random diffusion, see Section 1.2.4). Increasing or decreasing the electric field strength is known to decrease or increase the width of the concentration profile, respectively.[146] Likewise, increasing the ionic strength of the buffer increases the

effect of electroosmotic drag and reduces the fluorophore drift velocity, thereby broadening the equilibrium concentration profile of fluorophores.[281] It is important to ensure that this balance of forces remains consistent across multiple electrophoresis experiments. To avoid the accumulation of positive/negative ions in the buffer due to the electrolysis of water, electrophoresis experiments were conducted under a constant flow (0.25 mL/min) of buffer (see schematic in **Figure 6.1g**). The electroosmotic drag was minimised by using an aqueous buffer containing a minimal concentration of ions (<0.1 mM HCl, pH 7.5) and the strength of the electric field (45 V/cm) was monitored using a voltmeter throughout all experiments. In later sections, we assess the electrophoretic properties of this experimental configuration and the reproducibility of fluorophore concentration profiles in different samples to confirm that these measures were sufficient to ensure experimental consistency.

6.2.1 Lipid-tagged Texas Red, NBD and Bodipy are all mobile when incorporated into patterned lipid bilayers

For a fluorophore to be a suitable target for in-membrane electrophoresis, it was first necessary to show that the lipid-tagged fluorophores can incorporate into patterned templates to form well-connected lipid membranes with high mobility. Polymerised lipid templates were prepared by UV exposure through a photomask patterned with a repeating array of 100 × 100 μm squares. This array (significantly larger scale than the 20 × 20 μm squares used in Chapter 5) was chosen to maximise the area, and therefore the number of fluorophores, in each membrane that can be concentrated by electrophoresis, whilst still ensuring that the size of the membrane did not exceed the field of view of the FLIM. After UV exposure and washing with detergent to remove areas of lipid that had not been cross-linked, the resulting template is a polymerised lipid bilayer containing square, empty regions that can be backfilled with a fluid lipid membrane. A precise concentration of fluorophores (typically 0.5 % (w/w)) was incorporated into DOPC liposomes and ruptured into the template to form pattered lipid bilayers as previously described (section 3.3.4). FLIM images were obtained in single-channel excitation mode using the photon multiplier tube (PMT) detector in order to have the highest temporal resolution for the detection and analysis of heavily quenched fluorescence lifetimes. FLIM channels were defined and optimised for the detection of NBD (excitation: 485 nm,

emission: 490 – 550 nm), TR (excitation: 561 nm, emission: 595 – 655 nm) or BOD (excitation: 485 nm, emission: 490 – 550 nm) as required. Control measurements confirmed that photobleaching during FLIM measurements was negligible.

FLIM images of lipid membranes containing 0.5 % (w/w) NBD, TR, and BOD are shown in **Figure 6.2a**. In each case, fluorescence is restricted to well-defined square patterned membranes, with minimal signal located on the surrounding template. The fluorescence within each membrane is largely homogeneous across the corral (40-50 counts/pix for all fluorophores), with a few visible bright spots that may represent non-ruptured vesicles that are loosely adsorbed onto the membrane. Overall, these membranes were highly reproducible, with minimal variation in intensity and quality across multiple preparations. To confirm that the liposomes had ruptured to form well-connected membranes containing mobile fluorophores (and not merely adsorbed into the template without rupturing), fluorescence recovery after photobleaching (FRAP) experiments were performed to monitor the diffusion of lipids over time. For each sample, a circular area (with a bleached radius, R_{bleach}, ranging from 20 – 30 μm) of membrane was deliberately photobleached using intense white light. Immediately after photobleaching, a FLIM timelapse of images (**Figure 6.2b**) was obtained to monitor the diffusion of "non-bleached" fluorophores into the bleached area. The intensity of the fluorescence recovery in the bleached spot was monitored for each timepoint (each time point is the accumulation of photons in a 16 s period) to plot a fluorescence recovery curve (**Figure 6.2c**). A mono-exponential fit, $F = F_0(1-e^{-kt})$, was used to obtain the "doubling time", $\tau = \ln(2)/k$, for each sample, from which the diffusion constant, $D = 0.22 \times R_{bleach}^2/\tau$, is calculated. To calculate the mobile fraction, images of the corral before photobleaching and after photobleaching were analysed as in Chapter 4.3.4. Briefly, the intensity of the "bleached" region is compared to the intensity of a "non-bleached" region throughout the FRAP experiment. If the mobile fraction is 100%, the two regions will have an equal intensity after the system has been allowed to reach an equilibrium. For each fluorophore, the diffusion of the lipids was compared in both patterned bilayers (lipid bilayers ruptured into a 100 μm square template) and in "infinite" bilayers (lipid bilayers ruptured onto non-patterned glass) to ensure that the polymerised lipid template did not adversely affect the lipid mobility.

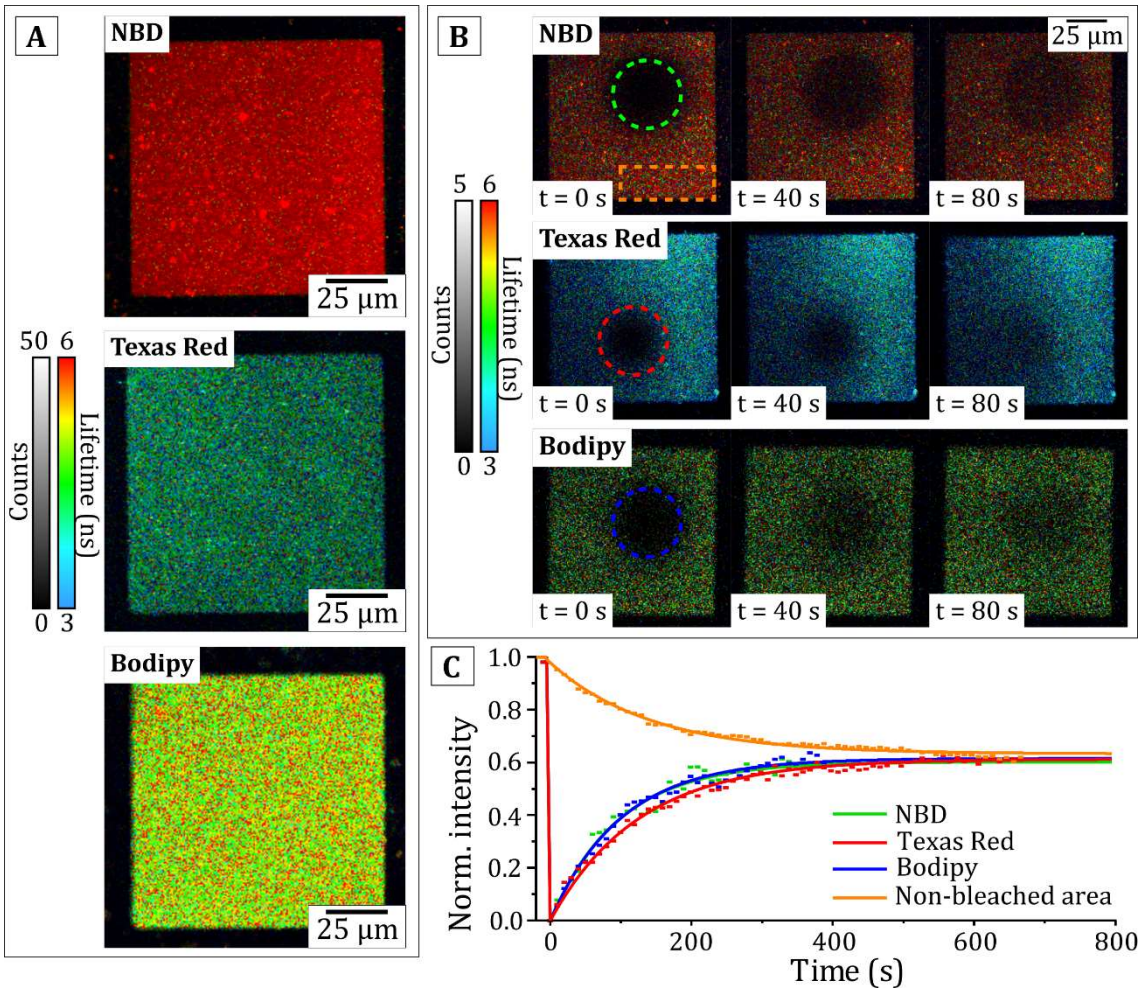

Figure 6.2: FLIM images of TR-, NBD- and BOD-containing lipid bilayers and Fluorescence Recovery After Photobleaching (FRAP) experiments confirming that the fluorophores are mobile and a suitable target for electrophoresis. **(A)** Example images of DOPC lipid bilayers containing 0.5 % (mol/mol) of either NBD (*top*), TR (*middle*) or BOD (*bottom*) formed as 100 µm wide corrals within the DiynePC polymer templates. These are all set to the same fluorescence lifetime scale of 3-6 ns to allow a visual comparison of the relative differences in lifetime. **(B)** FRAP experiments for the patterned lipid bilayers, showing the mobility of each type of fluorophore. **(C)** FRAP recovery curves showing the fluorescence intensity in the *dashed* bleached regions in (B), normalised to the intensity of the bilayer prior to photobleaching (colours as labelled on legend). The *orange* curve shows the fluorescence intensity decrease in the *orange*, *box* region in (B), showing that the intensity in the patterned membrane decreases due to there being a finite number of non-bleached fluorophores available to diffuse into the bleached region.

A summary of FRAP experiments on patterned bilayers is shown in **Table 6.1.** The calculated diffusion constant was similar for all fluorophores in both patterned and non-patterned bilayers (ranging from 1.75 to 2.27 $\mu m^2/s$) and the mobile fraction was consistently high across all samples (>94% for all fluorophores). Overall our results are consistent with the values for the diffusion constant and mobile fractions of similar lipid-tagged fluorophores reported in other studies[145, 279], and a strong indication that there is little interaction between the substrate or template and lipid-tagged fluorophores that may hinder an electrophoretic effect.

	NBD		TR		BOD	
	Patterned bilayer	Infinite bilayer	Patterned bilayer	Infinite bilayer	Patterned bilayer	Infinite bilayer
D ($\mu m^2 s^{-1}$)	2.13 ± 0.18	1.99 ± 0.20	2.27 ± 0.59	1.95 ± 0.20	2.09 ± 0.39	1.75 ± 0.17
μ_{FRAP} ($ms^{-1}N^{-1}$)	5.15 ± 0.43	4.81 ± 0.48	5.49 ± 0.14	4.71 ± 0.48	5.05 ± 0.94	4.23 ± 0.41
Mobile %	94.7 ± 2.3	97.0 ± 5.2	95.5 ± 2.5	96.6 ± 3.6	94.0 ± 1.8	95.3 ± 7.2

Table 6.1: Summary of FRAP experiments comparing patterned lipid bilayers (100 μm squares) versus non-patterened bilayers. Overall, the prescence of the polymerized lipid template has no significant effect on the mobility of lipids close to the centre of the membrane.

6.2.2 Applying an E-field parallel to the membrane causes the movement and accumulation of fluorophores at the bilayer edge

To determine if fluorophores in the membrane reorganise in response to the applied electric field, positive and negative electrodes were positioned 1 cm apart such that the applied electric field was parallel to the plane of the membrane (see **Figure 6.1g** for a schematic of the electrophoresis flow cell). The charge of each lipid tagged-fluorophore (TR-DHPE, NBD-DHPE and BOD-DHPE) was net negative (q = -1*e*), therefore the fluorophores will diffuse towards the positive electrode once the electric field is applied. **Figure 6.3a** shows a series of FLIM intensity images of a patterned lipid membrane containing 0.5 % (w/w) TR taken immediately after the electric field (45 V/cm) was switched on. Initially the fluorescence intensity in the corral is homogeneously distributed within the patterned bilayer (~6 counts/pix). At later timepoints the fluorescence intensity can be seen to move towards the positive cathode as expected, increasing up to 23 counts/pix at the left edge whilst simultaneously decreasing to 1 count/pix at the right edge of the membrane after 144 s (intensity profile plots in **Figure 6.3a**).

After a sufficiently long time, the system reaches an equilibrium, where the drift due to the Lorentz force is counterbalanced by the random 2-D Brownian diffusion of the fluorophores. To assess the final state of the membrane, FLIM images were obtained after the electric field had been applied for at least an hour and compared to the initial state of the membrane. Qualitatively, the effect of the electric field is consistent for all three fluorophores, as described below. Before electrophoresis, the fluorescence intensity is homogeneously distributed in the square patterned region (**Figure 6.3b-d** for NBD, TR and BOD), suggesting that fluorophores are randomly diffusing throughout the membrane.

After electrophoresis (labelled "45 V/cm equilibrium"), all three membranes have an asymmetric intensity profile where the fluorescence intensity is significantly brighter at the left edge (close to the cathode) than at the right edge of the membrane. This is shown more clearly in intensity profiles measured across the corrals (*right panel*, **Figure 6.3b-d**). Each intensity profile is normalised to the starting intensity of the corral, in order to compare the relative increase in intensity after electrophoresis. All three fluorophores exhibit at least a 3-fold increase in intensity relative to the intensity prior to electrophoresis, increasing to 3.01 times the initial intensity for NBD, 4.54 for Texas Red, and 3.84 for BOD. The difference in this relative increase between NBD, TR and BOD may be due to differences in the final concentration of the fluorophores (due to different electrophoretic properties) or the relative quenching strengths of each fluorophore at high concentrations. In either case, these results show that all three fluorophores are sensitive to the applied electric field, and drift towards the positive electrode resulting in an increased intensity and higher fluorophore concentration at the left edge of the membrane. In later sections, we assess the effect of concentration quenching in all three fluorophores.

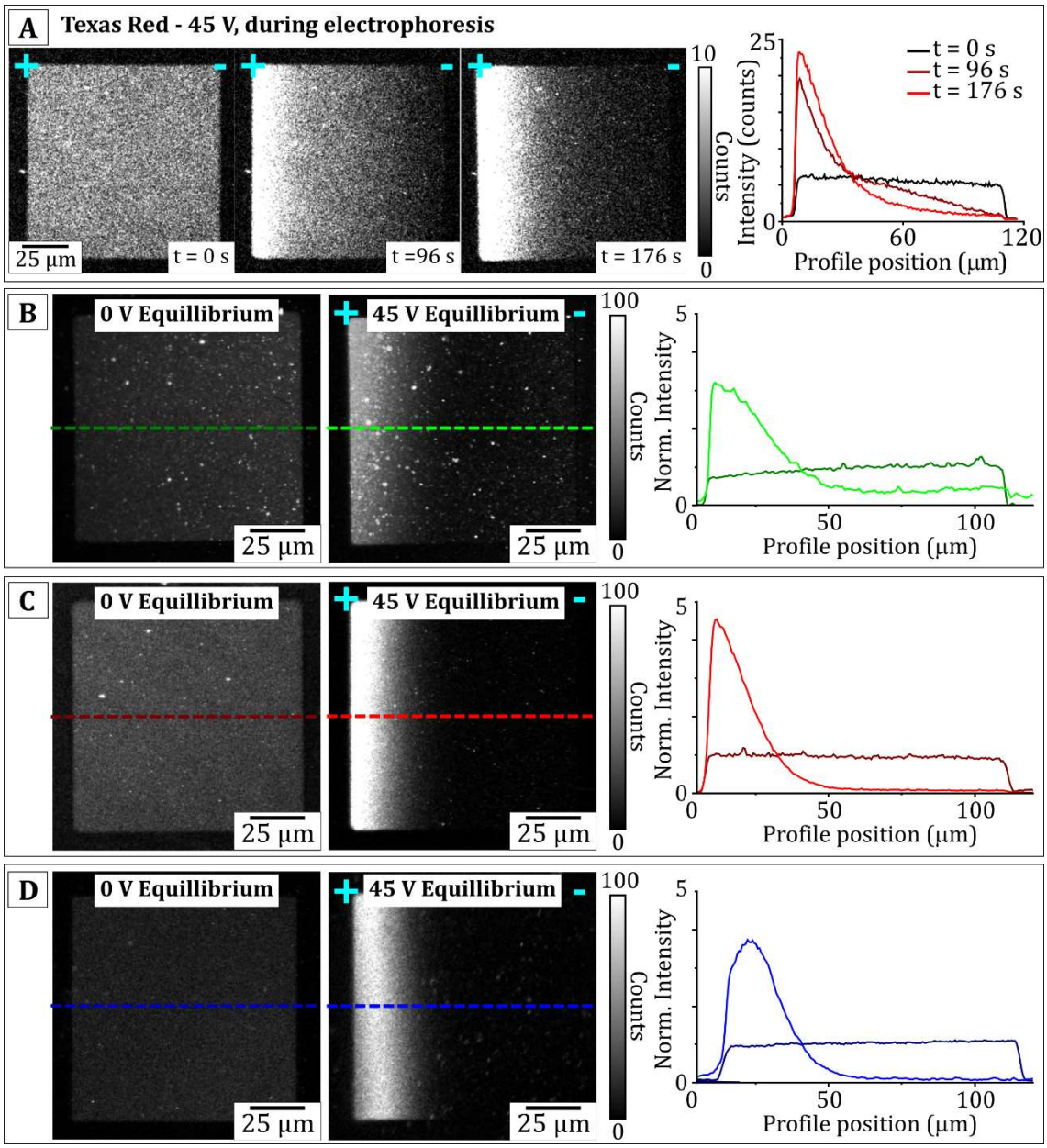

Figure 6.3: FLIM images showing the effect of electrophoresis on charged fluorophores (NBD, TR, BOD) in patterned bilayers. **(A)** FLIM timelapse of the electrophoretic mobility of TR-DHPE. TR flows in the opposite direction of the applied E-field and accumulates at the confined edge of the patterned bilayer. **(B)** Patterned bilayer containing 0.5 % (w/w) NBD-DHPE before (*left,* 0 V equilibrium) and after (*middle*, 45 V/cm equilibrium) an electric field had been applied parallel to the membrane. Intensity profiles drawn across the membrane (*right*) show that the intensity increases by a factor of 4.01 at the left edge of the bilayer. **(C)** Patterned bilayer containing 0.5 % (w/w) TR-DHPE before and after electrophoresis. Panels are labelled the same as in (B). **(D)** Patterned bilayer containing 0.5 % (w/w) Bod-DHPE before and after electrophoresis. Panels are labelled the same as in (B). In all panels, *cyan operator symbols* (+ or –) show the direction of the applied field.

6.2.3 Fluorescence is quenched as fluorophores accumulate at the end of the trap

To determine which of the fluorophores were susceptible to concentration quenching, FLIM measurements were obtained of lipid bilayers containing 0.5 % (w/w) of NBD, TR, or BOD both before and during electrophoresis experiments. After applying the E field, each sample was allowed to equilibrate for at least an hour to ensure that all subsequent measurements were consistent. For 0.5 % NBD lipid bilayers before electrophoresis (**Figure 6.4a**, labelled "0 V equilibrium") the measured fluorescence has a long lifetime that is homogenously distributed within the corral region. The fitted fluorescence lifetime was calculated from a fluorescence decay curve collected in the corral region and determined to be $<\tau_{NBD}> = 6.31 \pm 0.05$ ns (*dark green, dashed* area in **Figure 6.4a** and *dark green curve* **Figure 6.4b**). By comparison, the fluorescence lifetime of NBD during electrophoresis (**Figure 6.4a-b**, labelled "45 V equilibrium") was severely shortened, as represented by a gradient (*blue*-to-*red*) of lifetimes from left-to-right within the corral. The minimum fluorescence lifetime, measured in a region close to the end of the corral (*dark green, dashed* area, **Figure 6.4a**), was found to be 5.31 ± 0.02 ns. A similar change in the fluorescence lifetime was observed for membranes containing either 0.5 % TR (**Figure 6.4c**) or 0.5 % BOD (**Figure 6.4e**). For each sample, the fitted fluorescence lifetime before electrophoresis was compared to the minimum fluorescence lifetime during electrophoresis**.** It was found that, $<\tau_{BOD}>$ decreases from 5.01 ± 0.03 ns to 2.75 ± 0.02 ns, and $<\tau_{TR}>$ decreases from 3.92 ± 0.02 ns to 2.93 ± 0.04 ns (**Figures 6.4c-d**, and **6.4e-f** respectively). For all three fluorophores, the decreased fluorescence lifetime was correlated to the increased fluorophore intensity and strongly suggests that fluorescence is self-quenched as a function of fluorophore concentration and that at sufficiently high concentrations, molecules can interact with each other in a manner that dissipates energy non-fluorescently. The fact that quenching is observed as a broad lifetime gradient over many micrometres, suggests that the in-membrane electrophoresis results in a shallow gradient of concentrations rather than the molecular aggregation of fluorophores on the nanoscale. The latter would not be resolved optically, because a fluorophores at the same local (nanoscale) concentration would all have the same fluorescence lifetime and aggregates would likely be smaller than the diffraction limit (<250 nm).

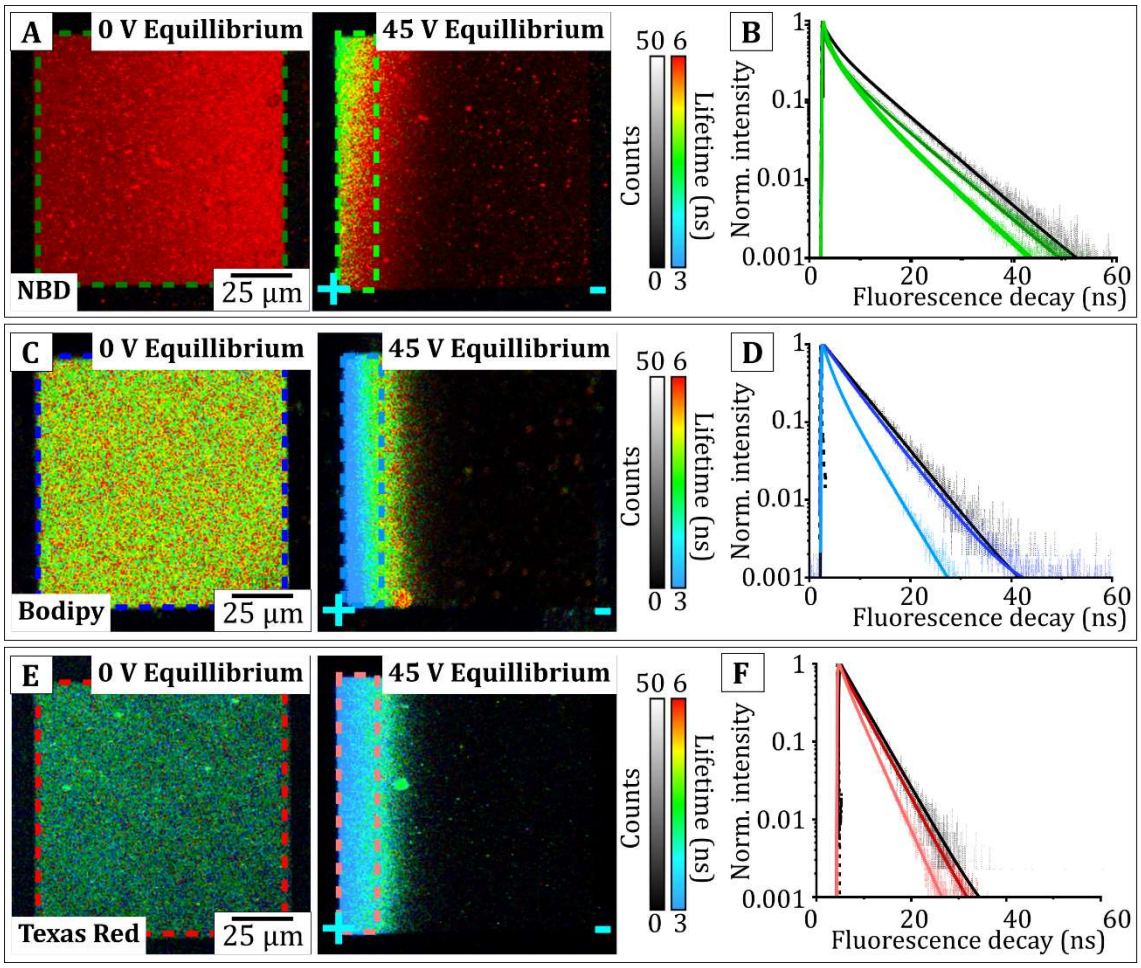

Figure 6.4: Comparison of the before- and after-electrophoresis states for all three fluorophores showing fluorescence quenching as a result of fluorophore accumulation for NBD, BOD and TR. **(A)** FLIM images of a 0.5 % NBD lipid bilayer in equilibrium in a 0 V/cm versus 45 V/cm electric field. **(B)** Fluorescence decay curves fitted to NBD in membranes prior to electrophoresis (*dark-green curve* from the *dark-green region* from (a)) and after electrophoresis (*light-green curve* from the *light-green* region from (a)). These were compared to a control sample with even lower fluorophore concentration, 0.25 % NBD, which had negligible quenching (*black curve*). **(C)-(D)** FLIM images and fluorescence decay curves of a 0.5 % BOD lipid bilayer, as labelled. **(E)-(F)** FLIM images and fluorescence decay curves of a 0.5 % TR lipid bilayer, as labelled.

To compare the self-quenching of different fluorophores (regardless of their initial fluorescence lifetime), the quenching efficiency (QE) was defined in a way that is synonymous to the energy transfer efficiency (ETE) commonly used in Förster theory as:

$$QE = 1 - \frac{< \tau_C >}{< \tau_0 >} \qquad \text{Eq. 6.1}$$

Where $<\tau_C>$ is the fitted lifetime at a concentration, C, of fluorophores, and $<\tau_0>$ is the fitted lifetime in the absence of self-quenching effects. Different polar environments can also contribute changes in the fluorescence lifetime,[282] and so to isolate lifetime effects specific to concentration quenching $<\tau_0>$ was measured in a consistent solvent environment (i.e. a lipid bilayer) and at a concentration which was sufficiently low for quenching effects to be negligible (0.25 % (mol/mol)). Values for $<\tau_0>$ for each fluorophore were calculated from fluorescence decay curves (*black, solid lines*, **Figure 6.4b,d,f**) and calculated to be 6.99 ± 0.13 ns, 5.40 ± 0.12 ns and 4.23 ± 0.17 ns for NBD, BOD and TR respectively (mean ± SD from multiple measurements obtained from at least two samples per fluorophore). These values are very similar to those reported in literature for NBD[283, 284], BOD[270, 285] and TR[98, 286] in chloroform (7-8 ns, 5-6 ns and 4-5, respectively) and so it is likely these measurements represent the fluorophores in an almost entirely non-quenched state.

Using the values determined for $<\tau_0>$ (*black* decay curves in **Figure 6.4b,d,f**) the maximum quenching efficiency during 45 V equilibrium was calculated to be 24.0 %, 30.7 %, and 49.1 % for NBD, TR and BOD, respectively. This initially suggests that BOD has the highest propensity for quenching out of the three dyes investigated (assuming that all three dyes respond similarly to the applied E-field). Overall, the results in this section show all three fluorophores experience self-quenching, and that quenching can be induced by increasing the concentration of fluorophores via in-membrane electrophoresis. This is a crucial first step towards using patterned lipid membranes to quantify quenching interactions for a wide range of membrane-based fluorophores.

6.2.4 Increasing the initial fluorophore concentration increases the amount of fluorescence quenching achieved during electrophoresis

We wished to use this experimental platform to describe the full range of quenching behaviour (QE ranging from 0 % to 100 %) for each fluorophore. In section 6.2.3, a starting concentration of 0.5% (w/w) TR resulted in a maximum QE of 30.7 % once the membrane reaches equilibrium in a 45 V/cm electric field. We predicted that increasing the concentration of fluorophores in the patterned lipid bilayer will result in a greater maximum concentration of fluorophores accumulated during electrophoresis and a greater amount of fluorescent quenching. Therefore, to measure a full range of QE, in-membrane electrophoresis and FLIM measurements were obtained for a series of patterned lipid bilayers containing different starting concentrations (%weights) of TR/DOPC (0.5 %, 1% and 1.5%). Patterned lipid bilayers did not form from DOPC liposomes containing more than 1.5 % TR, likely caused by defects that can occur when highly curved TR-DHPE lipids insert into a flat lipid bilayer and hydrophobic interactions between the aqueous environment and lipid tail groups that reduce membrane stability.[194]

As expected, increasing the concentration of fluorophores in the lipid bilayer resulted in a higher initial fluorescence intensity, despite also resulting in increased quenching (decreased lifetime). **Figure 6.5a** shows the patterned lipid membranes formed liposomes containing 0.5 % (*left*), 1 % (*middle*) and 1.5 % TR (*right*), before electrophoresis. The counts/pix generally increases as a function of concentration, as observed in intensity profiles from **Figure 6.5a** (*dashed lines,* **Figure 6.5c**), from ~50 to ~100 to ~140 counts/pix for 0.5 %, 1.0 % and 1.5 % TR, respectively. The intensity increases non-linearly due to self-quenching that occurs at even these low concentrations. Quenching is also manifested as a shortening of the initial fluorescence lifetime from 3.94 ± 0.02 ns to 3.65 ± 0.01 ns and 3.36 ± 0.02 ns for 0.5 %, 1 % and 1.5 % TR, respectively (shown in **Figure 6.5a** as a *red* to *yellow* shift on the false-colour scale). FLIM images of the same patterned membranes at equilibrium in a 45 V/cm electric field are shown in **Figure 6.5b**.

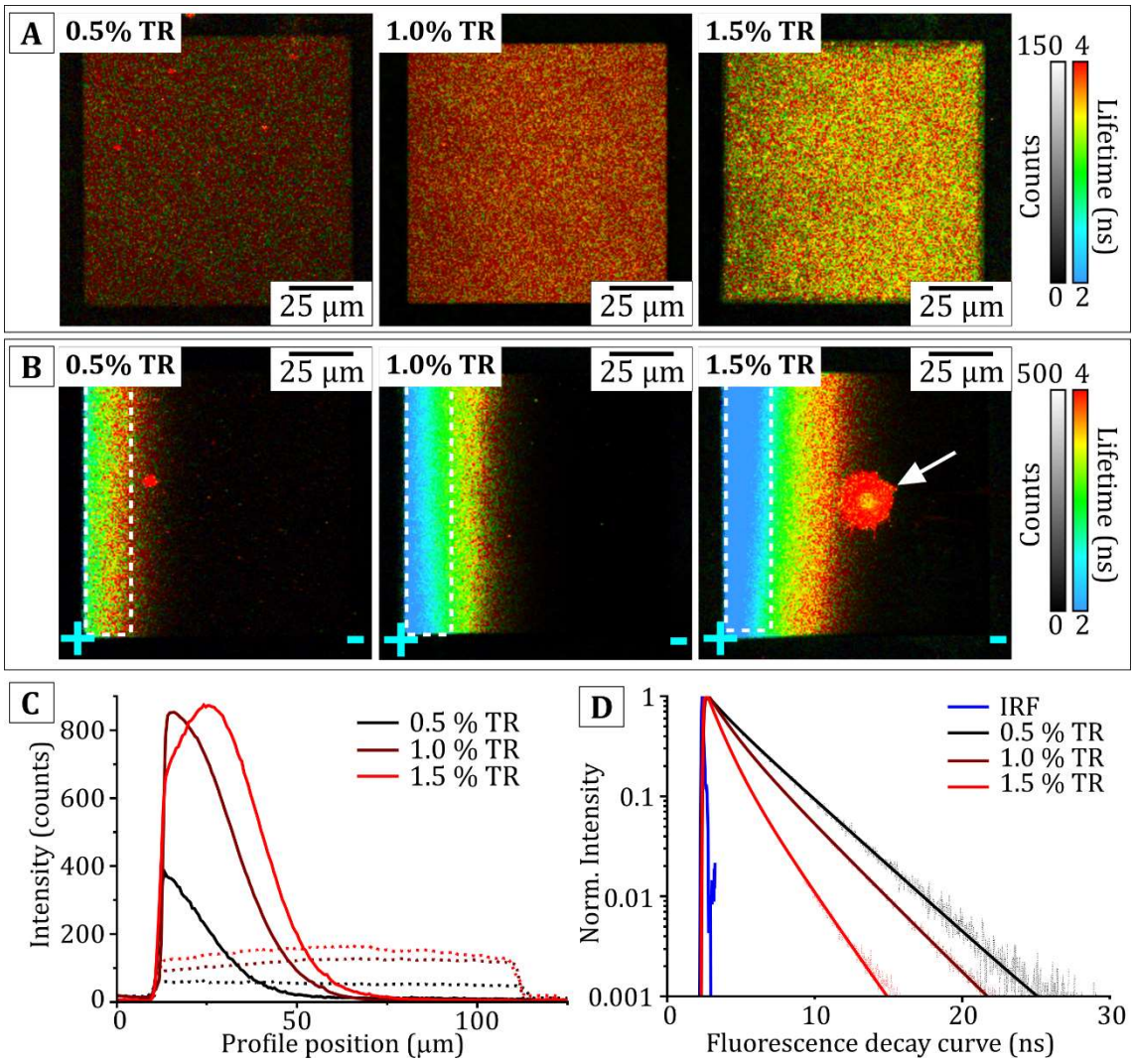

Figure 6.5: Comparison of before and after electrophoresis states for lipid bilayers containing 0.5 %, 1.0 % and 1.5% TR-DHPE. **(A)** FLIM images of patterned lipid bilayers containing 0.5 % (*left*), 1.0 % (*middle*) and 1.5 % (*right*) TR in equilibrium in a 0 V/cm electric field. **(B)** FLIM images of patterned lipid bilayers containing 0.5 % (*left*), 1.0 % (*middle*) and 1.5 % (*right*) TR in equilibrium in a 45 V/cm electric field. **(C)** Intensity profiles measured across patterned bilayers containing 0.5 % (*black)*, 1.0 % (*dark, red*) and 1.5 % (*bright, red*) TR. Intensity profiles were measured for both 0 V/cm (as in (a), *dashed lines*) and 45 V/cm (as in (b), *solid lines*). **(D)** Fitted fluorescence decay curves for membranes containing 0.5 % (*black)*, 1.0 % (*dark, red*) and 1.5 % (*bright, red*) TR, accumulated from photons in the *white, dashed* regions in (b).

Qualitatively it can be seen that increasing the initial bilayer concentration leads to an increased intensity and a wider band of fluorescence accumulating at the edge of the membrane. Some disruption to the membrane structure (*white arrow,* **Figure 6.5b**) was apparent after electrophoresis only with the highest TR-DHPE concentration samples (1.5 %, discussed later). To fairly compare the fluorescence lifetime and intensity between different membranes regions containing such defects were digitally excluded from any further analyses.

Intensity profiles (**Figure 6.5c**) taken horizontally across the corrals in **Figure 6.5b** show that the maximum intensity is greater for membrane with a higher initial concentration of charged fluorophores (~400 counts/pix compared to ~800 counts/pix for 0.5 % and 1.0 % TR respectively). In particular, in the intensity profile for 1.5 % TR after electrophoresis (*red, solid* line, **Figure 6.5c**) the intensity rapidly increases (from right to left) to a maximum intensity of ~800 counts/pix (at x ~ 30 μm) before decreasing to ~600 counts/pix at the edge of the membrane. We propose that the decline in the intensity profile at the left-hand edge of the corral, where the concentration is actually expected to be higher, suggests that at *extremely* high concentrations TR self-quenching becomes so significant that each additional fluorophore has a negative contribution to the measured intensity. Alternatively, it may be the case that different molecular structures (e.g. aggregates or clusters) form at high concentrations with significantly different fluorescent properties.

Correlated to the intensity gradient, each membrane in **Figure 6.5b** has the characteristic *blue*-to-*red* lifetime gradient (first observed in **Figure 6.5a**) from left-to-right across the membrane. The width of this gradient is visibly larger and has a lower (*bluer*) minimum lifetime for bilayers that have a higher initial concentration. The fitted lifetime at the edge of the membrane, $<\tau_{edge}>$ was obtained from fluorescence decay curves (**Figure 6.5c**) accumulated from the *white, dashed* regions in **Figure 6.5b.** For initial concentrations of 0.5 %, 1.0 % and 1.5 % (w/w) TR-DHPE, $<\tau_{edge}>$ was found to be 2.93 ± 0.04 ns to 2.12 ± 0.01 ns and 1.35 ± 0.01 ns, respectively, representing a quenching efficiency of 30.7%, 49.9% and 68.1% respectively. Overall these results show that the quenching efficiency achieved in in-membrane electrophoresis can be controlled by simple modifications to the starting

composition of the membrane, and that this platform can be used to investigate a wide range of quenching behaviours for different fluorophores.

Figure 6.5c shows an example of bilayer disruption that occurs when a 45 V/cm electric field was applied parallel to a patterned lipid bilayer containing 1.5 % TR. This bilayer disruption occurred for the majority (80%, N = 10) of membranes containing 1.5 % TR after electrophoresis. This disruption typically resulted in highly mobile strand-like features that stem from microscale regions lacking fluorescence (~5-20 μm in diameter) within the membrane. These are thought to be lipid tubules because of their similarity in appearance with previous reports[236, 287], i.e., tubes of lipid bilayer 50-100 nm diameter and many microns in length. TR-DHPE is a charged lipid with a large headgroup relative to the hydrophobic portion of the lipid (see structure in **Figure 6.1a**). It is therefore likely that high concentrations of TR induces membrane curvature and defects due to imperfect packing of a mixture of DHPE and PC lipids[288], or due to electrostatic repulsion between fluorophores that are not sufficiently screened[137, 236]. At sufficiently high concentrations of TR-DHPE, this may result in instability of the lipid bilayer, delamination of the bilayer from the underlying glass substrate, or even extreme curvature of the bilayer and lipid tubulation. It may be possible to design templates with different dimensions to better support highly curved lipid bilayers and achieve even higher concentrations of charged fluorophores. However, in the present study (using 100 μm square patterned bilayers), these membrane defects show that experimental limit for maximum concentration of fluorophores in a (quasi-)stable lipid bilayer structure has been reached.

6.3 Describing quenching behaviour as a function of concentration for monochromatic fluorophores

6.3.1 There is a high probability of exciton migration between lipid-tagged fluorophores

To identify the mechanism of fluorophore self-quenching we first considered the distances at which interactions between fluorophores may take place. FLIM measurements of bilayers containing different concentrations of TR (**Figure 6.5a**) show that fluorescence quenching occurs at concentrations as low as 1%. So to approximate the maximum distance at which two TR fluorophores may interact, the average centre-to-centre distance, *r*, for randomly dispersed fluorophores in a membrane containing 1% TR was calculated. First, the density of fluorophores was calculated using:

$$C_N = \frac{C_{\%}}{100} \times \frac{1}{A_{lipid}} \qquad \text{Eq. 6.2}$$

where C_N and $C_{\%}$ are the concentration of fluorophores in molecules per nm^2 and in %(mol/mol) respectively, and A_{lipid} is the size of a lipid headgroup (estimated to be 0.67 nm^2)[190]. Next, the average distance between molecules was calculated using:

$$\text{Effective area per molecule} = \frac{1}{C_N} = \pi r^2 \qquad \text{Eq. 6.3}$$

Thus, for a membrane containing 1 % (mol/mol) TR the average distance between molecules was calculated to be 4.69 nm. This suggests that, if quenching must involve some direct interaction between fluorophores, an excited state may travel for several nanometres before being quenched. One possibility is that an excited fluorophore may diffuse into direct contact with a nearby fluorophore whereby the fluorescence is quenched by some physical interaction of the two (collisional quenching). To test this possibility, TR was used as an example to calculate the mean displacement per exited state, <x>, using

$$< x > = \sqrt{2D\tau_0} \qquad \text{Eq. 6.4}$$

where D is the diffusion constant (D ~ 2 μm^2/s, section 4.3.4) and τ_0 is the fluorescent lifetime for TR (τ_0 = 5.4 ns, as calculated in section 6.2.3). From this calculation, the mean displacement per excited state was found to be ~0.16 nm. This

is significantly lower than the average separation of fluorophores and clearly shows that molecular collisions would occur very rarely in this system and cannot explain the magnitude of quenching observed.

Instead, numerous studies have proposed that self-quenching processes involve a combination of energy traps and exciton transfer (i.e., migration) among multiple fluorophores, with the possibility that an exciton may migrate to and be quenched at a trap site.[267, 268] These trap sites may form as a result of formal complexes of fluorophores (i.e., strongly bonded) or physical aggregates (i.e., more loosely associated) or may simply result from molecules that are in close proximity due to the random statistical distribution/diffusion of fluorophores within the membrane (i.e., without any attractive forces). These traps are inherently non-fluorescent (cannot absorb or emit photons) and may affect the intensity and lifetime in a combination of processes: (i) traps will not fluoresce in response to direct excitation (photon absorption is forbidden) and the overall fluorescence intensity is reduced by the fraction of fluorophores involved in trap sites but the fluorescence lifetime is unaffected (sometimes termed "static quenching"), (ii) fluorophores that are not part of traps can accept photons and may transfer energy to a trap site (through FRET) upon which the exciton is immediately and non-radiatively dissipated. In the second process, the trap provides an alternative route for the rapid dissipation of energy, resulting in a reduction in both the fluorescence emission and lifetime (termed "transfer-to-trap quenching"). These two processes occur simultaneously in a system such that the intensity is reduced by (i) and (ii), whereas the lifetime is only affected by (i).

In the absence of aggregation, the probability of trap formation can be described by considering a random distribution of fluorophores within a two-dimensional membrane. Through random Brownian diffusion in 2-D it possible for two fluorophores to come into close proximity and form a trap site, also known as a "statistical pair". Using the two-dimensional Perrin equation, which describes the probability of interactions between randomly distributed particles, the fraction of fluorophores, f_T, that are part of statistical pairs is given by:

$$f_T = 1 - e^{-\pi R_C^2 C} \qquad \text{Eq. 6.5}$$

where C is the concentration of fluorophores (in molecules/nm^2) and R_C is the distance at which two fluorophores have a 63% ($1 - e^{-1}$) likelihood to form a trap site, also known as the "critical radius for trap formation".[289] Due to the slow lateral and rotational diffusion of fluorophores (relative to the fluorescent lifetime) these statistical pairs can be considered as quasi-stable and immobile for the duration of an excited state. The probability that energy transfer occurs from an excited molecule to a trap site is then defined as:

$$P_{ETT} = P_{FRET} \times f_T \qquad \text{Eq. 6.6}$$

where P_{FRET} is the probability of energy transfer, as described by Förster theory[28], and f_T is the fraction of fluorophores involved in trap sites (Equation 6.5). This uses the assumption that excited molecules may only interact with a single nearest neighbour (multiple studies have shown that energy migration is dominated by nearest-neighbour interactions[272, 276]).

To assess the overall feasibility of transfer-to-trap quenching and whether it was theoretically possible for energy to migrate from an excited monomer to a trap in our samples, the probability of energy transfer between fluorophores was calculated for a range of membrane concentrations. First, the Förster radius (the distance at which resonance energy transfer is 50% efficient, see section 1.1.4) of energy transfer was calculated for NBD, TR and BOD. In this scenario, where the donor and acceptor are identical molecules[268, 270], a value for J can be calculated as the overlapping area from the measured emission and absorption spectra for each fluorophore (shown in **Figure 6.6a**) to be 0.28, 3.08 and 2.13 ×10^{15} M^{-1}cm^{-1}nm^4 for NBD, TR and BOD respectively. For a lipid-tethered-dye, the fluorescent moiety was assumed to be randomly-orientated relative to neighbouring fluorophores due to combined effect of both the lateral diffusion of both the lipid, and rotational diffusion of the tethered dye, equating to a value for κ^2 of 2/3.[29] The refractive index of the optical medium was assumed to be halfway between water (1.33) and lipid tail groups (1.55),[243] and was given a value of 1.45. The fluorescence quantum yield of NBD, TR and BOD was estimated as 0.40, 0.93, 0.99, respectively, from the literature[246, 268, 290]. The calculated values for the Förster radius was found to be 33.2, 57.3 and 54.1 Å for NBD, TR and BOD respectively. These values were found to be in good agreement with those calculated using an online calculator.[291]

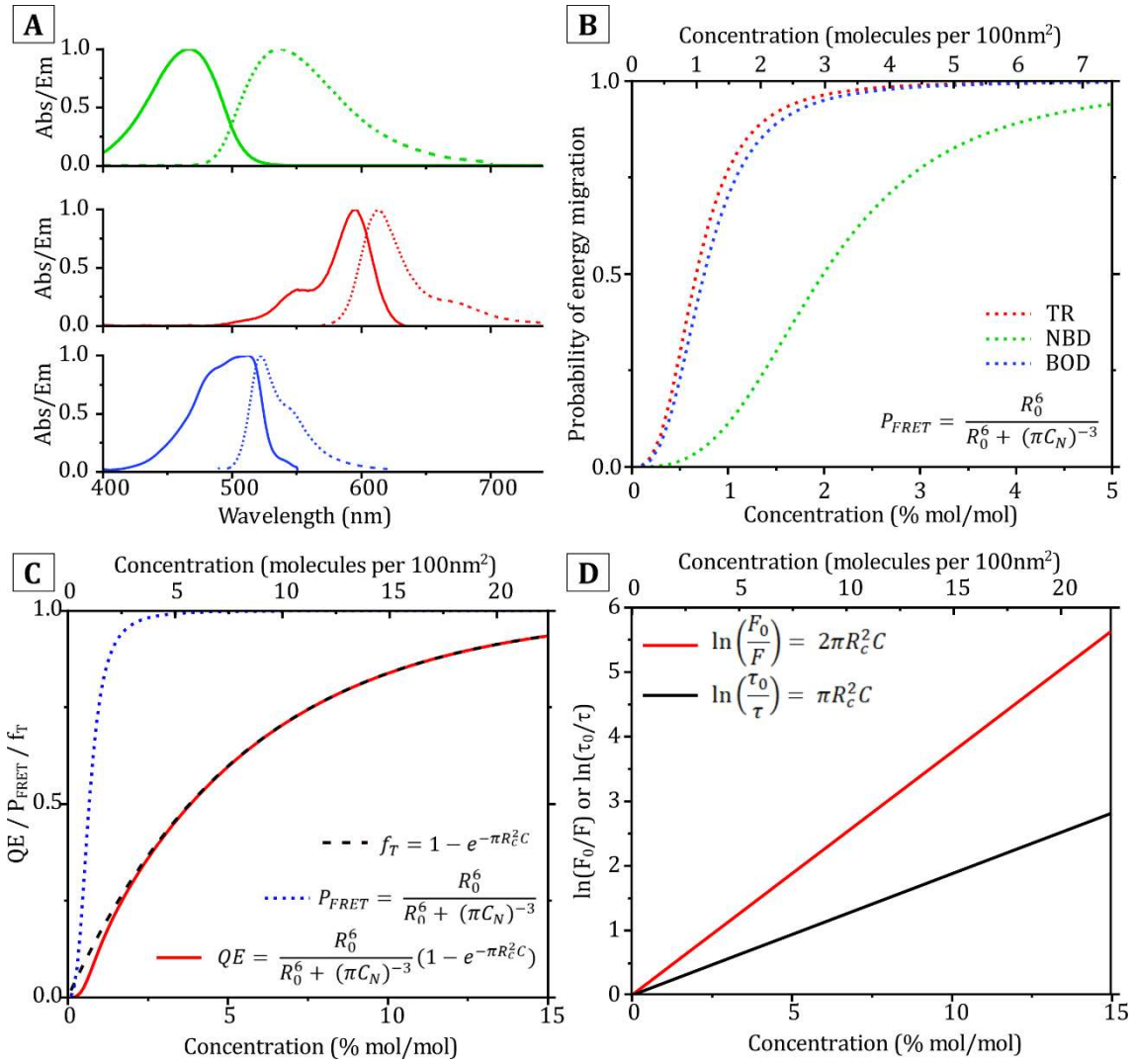

Figure 6.6: Calculation of the probability of energy migration for TR, NBD and BOD in lipid bilayers. **(A)** Absorption and emission spectra of NBD (*green*), TR (*red*) and BOD (*blue*) used to calculate the Förster radius for each fluorophore, adapted from Thermo Fisher. **(B)** Theoretical curve showing the probability of excitation energy migration as a function of fluorophore concentration in a lipid bilayer, according to the equation for FRET given as Eq. 6.8. **(C)** Theoretical curves for the probability of transfer-to-trap quenching for TR (R_0 = 57.1 Å, R_C is set to 20 Å), calculated from Eq. 6.14. P_{FRET}: *blue dashed*, f_T: *black dashed*, QE: *red, solid*. **(D)** Theoretical semi-log plots of the reciprocal relative intensity (*red*) and lifetimes (*black*) as a function of concentration as a result of quenching due to static non-fluorescent dimers and the transfer of excitons to fluorescent traps (dimers), calculated from Eq. 6.10 and Eq. 6.13.

Next, the probability of energy migration was calculated as a function of concentration for NBD, TR and BOD using the relationship for energy transfer efficiency as a function of donor-acceptor separation, described in Förster theory (see Section 1.1.4):

$$P_{FRET} = \frac{R_0^6}{R_0^6 + r^6} = \frac{R_0^6}{R_0^6 + (\pi C_N)^{-3}} \quad \text{Eq. 6.7}$$

where R_0 is the Förster radius for each fluorophore, and C_N is the fluorophore concentration. The results are shown in **Figure 6.6b** where it can be seen that for all fluorophores that the probability of energy migration increases rapidly as a function of concentration before approaching unity at ~2% (w/w) for TR and BOD and ~5 % (w/w) for NBD. This result shows that, even at relatively low concentrations of fluorophores in lipid bilayers, energy migration is extremely likely to occur throughout the membrane. More generally, these calculations suggest that excitons in lipid membranes may be considered as a "flux" of excitons that are delocalised across many fluorophores in a system, and has wider implications for study of the photophysics and energy transfer in a variety of light-harvesting membranes. Our findings in this section show that energy migration to traps (i.e. statistical pairs) is a feasible mechanism of quenching for each of the three fluorophores studied, NBD, TR and BOD, and that at sufficiently high fluorophore concentrations it is reasonable to assume $P_{ETT} \sim F_T$.

Using this assumption, it was possible to derive simplified relationships for the reduction in lifetime and intensity due to concentration quenching. Initially, considering that the fluorescence lifetime is only affected by transfer-to-trap quenching, the relative lifetime should be equal to:

$$\frac{\tau}{\tau_0} = 1 - P_{ETT} = e^{-\pi R_c^2 C} \quad \text{Eq. 6.8}$$

This can be written in a semi-logarithmic format to provide a linear relationship between fluorophore concentration and the amount of quenching:

$$\ln\left(\frac{\tau_0}{\tau}\right) = \pi R_c^2 C \quad \text{Eq. 6.9}$$

Secondly, considering that the fluorescence intensity is affected by both transfer-to-trap quenching *and* static quenching by non-fluorescent dimers, the relative intensity is expected to be equal to

$$\frac{F}{F_0} = f_T(1 - P_{ETT}) \qquad \text{Eq. 6.10}$$

Equation 6.10 can be written in terms of the fluorophore concentration by multiplying the Perrin equation (equation 6.5) with equation 6.8:

$$\frac{F}{F_0} = e^{-2\pi R_c^2 C} \qquad \text{Eq. 6.11}$$

To show the predicted quenching behaviour more clearly, theoretical quenching curves were generated for a range of TR concentrations. **Figure 6.6c** shows the theoretical Quenching Efficiency (*red*), f_T (*black*) and P_{FRET} (*blue*) versus concentration curves for TR, using the calculated value for R_0 = 57.3 Å, and an placeholder value for R_C = 20 Å. For this plot, QE was calculated in full (without the FRET simplification), by combining equations 6.7 and 6.8, as:

$$QE = \frac{R_0^6}{R_0^6 + (\pi C_N)^{-3}}(1 - e^{-\pi R_c^2 C}) \qquad \text{Eq. 6.12}$$

The theoretical plot shows that all three curves tend asymptotically towards unity, but that the rate of this approach varies drastically. Initially, P_{FRET} increases steeply with concentration before asymptotically tending towards unity at concentrations above ~2 %, whereas f_T and QE increase with a shallower gradient and only begin to tend towards unity at much higher concentrations (over 15%). Most significantly, the theoretical plot demonstrates the similarity between the QE and f_T curves, which are almost perfectly overlaid for the majority of concentrations (>2 %). This shows that transfer-to-trap quenching is dominated by the number of traps in the membrane, and that simplifying the quenching relationships, by setting P_{FRET} = 1, provides a good approximation for efficiency of transfer-to-trap quenching. **Figure 6.6d** shows the theoretical plots of $\ln(\tau_0/\tau)$ (equation 6.9, *black*) and $\ln(F_0/F)$, showing the linear relationships that are expected when quenching data is plotted on semi-logarithmic axes. In later sections, these theoretical plots will be compared to experimental results of in-membrane electrophoresis, to determine whether transfer to trap quenching is likely to be occurring in bilayers containing NBD, TR or BOD. In particular, the gradient of the semi-log plots of experimental data will be

used to determine the critical radius for trap formation to describe the relative "quenching strengths" of all three fluorophores.

6.3.2 Determining the concentration of fluorophores during electrophoresis

To quantify self-quenching over a range of concentrations and to be able to compare our results to the theory determined for the transfer-to-trap quenching mechanism (section 6.3.1), it was necessary to determine the concentration of fluorophores, correlated to the lifetime, at each location in the membrane. A methodology was devised to estimate the fluorophore concentration at each pixel in FLIM images by comparing the pixel intensity and lifetime to those measured for a known concentration of fluorophores. Supported lipid bilayers were formed on hydrophilic glass containing different chromophore concentrations, in a range from 0.25 – 1.5% (w/w), of NBD, TR or BOD. These bilayers acted as simple control samples, due to their high reproducibility, high-throughput, and the ability to accurately change the concentration of fluorophores in the membrane (protocol described in section 3.3.4). FLIM images for these samples (**Figure 6.7a,b,c**) were acquired using the same settings as described for electrophoresis measurements and the average intensity and average fitted lifetime was calculated for each image. The observed fluorescence intensity was found to increase with chromophore concentration non-linearly, as shown in **Figure 6.7d** for NBD (*green*), TR (*red*), and BOD (*blue*) respectively, due to the increasing effect of quenching that occurs at higher concentrations. The result is a complex relationship between intensity and concentration that is not trivial to delineate. In contrast, in the absence of quenching, the fluorescence intensity is expected to increase linearly with concentration and therefore provides a simple relationship from which to estimate the fluorophore concentration. The measured fluorescence lifetime (τ) was used to calculate the relative fluorescence lifetime, τ/τ_0, which was used to calculate the "non-quenched intensity" according to the expression below (a combination of Equations 6.9 and 6.11):

$$F_0 = F \times \exp\left[2 \ln\left(\frac{\tau_0}{\tau}\right)\right] \qquad \text{Eq. 6.13}$$

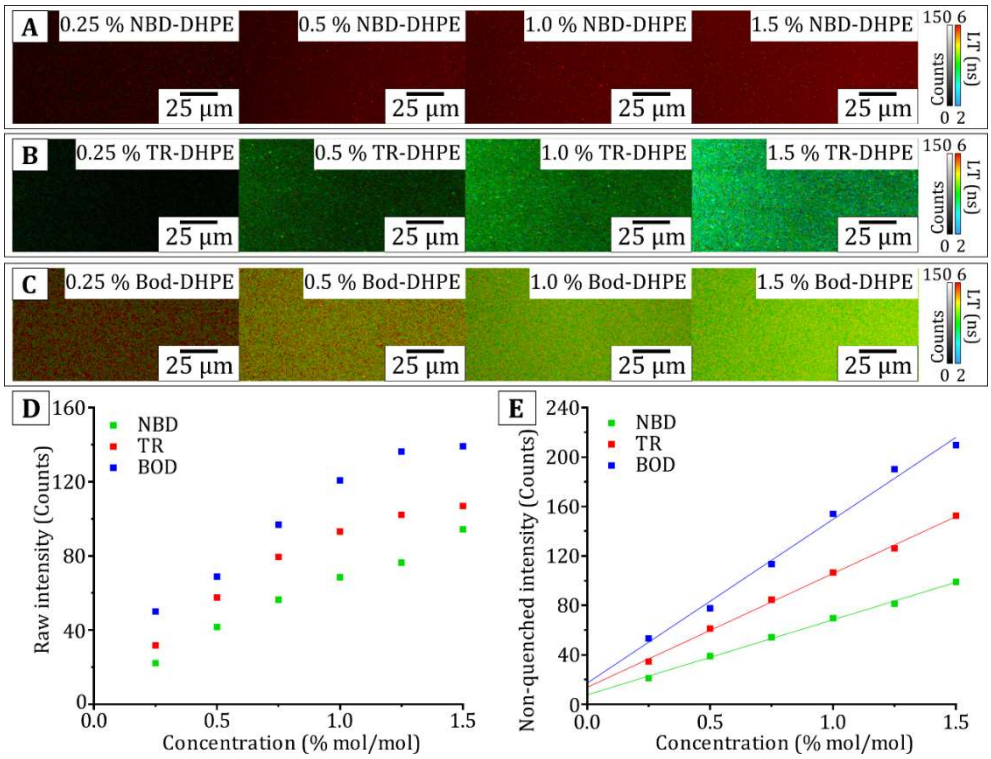

Figure 6.7: FLIM images of lipid bilayer standards containing fluorophores at a range of concentrations to generate intensity curves from which to estimate fluorophore concentrations. **(A)** FLIM images of a series of lipid bilayers containing increasing concentrations of NBD-DHPE. FLIM images were obtained using the same settings as for in-membrane electrophoresis experiments. **(B)** FLIM images of a series of lipid bilayers containing increasing concentrations of TR-DHPE **(C)** FLIM images of a series of lipid bilayers containing increasing concentrations of BOD-DHPE **(D)** Average intensity (counts/pix) versus concentration plot of the lipid bilayers in (a-c). The intensity increases non-linearly due to concentration quenching. **(E)** Non-quenched intensity versus concentration plot of lipid bilayers in (a-c). The non-quenched intensity is calculated from the average intensity and fluorescence lifetimes shown in **Table 6.2.**

	NDB				***TR***				***BOD***			
Conc % (w/w)	**F** Count s/pix	**<τ>** ns	**F₀** Count s/pix	**Conc** %(mol /mol)	**F** Count s/pix	**<τ>** ns	**F₀** Count s/pix	**Conc** %(mol /mol)	**F** Count s/pix	**<τ>** ns	**F₀** Count s/pix	**Conc** %(mol /mol)
0.25	22.1	7.17	21.0	0.21	31.7	4.13	33.3	0.14	50.0	5.23	53.3	0.18
0.50	41.6	7.13	40.0	0.41	57.5	4.07	62.1	0.28	68.8	5.09	77.4	0.37
0.75	56.3	7.13	54.2	0.61	79.4	4.07	86.1	0.42	96.8	4.99	113	0.55
1.00	68.4	6.93	69.5	0.82	93.1	3.93	108	0.57	120	4.78	153	0.73
1.25	74.0	6.67	81.3	1.02	105	3.82	128	0.71	143	4.69	190	0.91
1.5	94.3	6.82	99.0	1.22	112	3.59	155	0.85	148	4.54	209	1.09

Table 6.2: Calculation of the non-quenched intensity as a function of fluorophore concentration for NBD, TR and BOD. F and τ are measured for each image (average of all pixels in one 25-frame image). The non-quenched intensity is calculated using the non-quenched lifetime, τ_0, for each fluorophore as in Eq. 6.13.

The result of this calculation is shown in **Table 6.3** and plotted in **Figure 6.7e** for each fluorophore. As expected from equation 6.13, the non-quenched intensity increases linearly with the concentration and can be successfully fit to a straight line, $F_0 = mC + Y_0$, where m is the fitted gradient and Y_0 is the y-intercept ($R^2 > 0.99$ for all three datasets). The relationships between the non-quenched intensity and fluorophore concentration (in weight/weight) were found to be $F_0 = 60.8 \times C_{NBD} + 7.43$, $F_0 = 92.2 \times C_{TR} + 13.5$ and $F_0 = 132 \times C_{Bod} + 16.9$ for NBD, TR and BOD, respectively. Finally to convert the weight concentration to a percentage concentration and to calculate the average separation between molecules, $C_{\%}$ (mol/mol) was calculated for each fluorophore using the known molecular weights of 1382, 956 and 1067 g/mol for TR-DHPE, NBD-DHPE and BOD-DHPE, respectively. Using these relationships, the intensity and the lifetime in electrophoresis FLIM images can be used to calculate the quenching efficiency as a function of the fluorophore concentration at each location. With the known fluorophore concentration, we can now compare the quenching behaviour of multiple fluorophores to existing theory and confirm the mechanism of self-quenching for freely diffusing fluorophores

6.3.3 Quantitative analysis of fluorophore concentration and quenching efficiency

Using the relationship for the non-quenched intensity versus concentration, it was now possible to generate quenching vs concentration curves to quantify self-quenching of lipid-tagged fluorophores. A careful analysis was performed on FLIM images obtained during in-membrane electrophoresis of lipid bilayers containing increasing concentrations of either NBD-, TR-, or BOD-DHPE (such as those images in **Figure 6.4** and **6.5**). A full demonstration of this analysis is shown for lipid bilayers containing TR below and then repeated for bilayers containing NBD and BOD.

Firstly, the mean values for fluorescence intensity and lifetime were calculated for each horizontal (x) position across the membrane corral by averaging vertical columns (y) of pixels. **Figure 6.8a** shows a FLIM image of a 0.28 % mol/mol (0.5 % weight/weight) TR-DHPE membrane during equilibrium in a 45 V/cm electric field, showing the direction of the profile generated from left-to-right across the

membrane (*white dashed region*). The mean lifetime and intensity profiles are shown in **Figure 6.8b-c** (*black* and *bright red* datapoints, respectively) and from this the non-quenched intensity profile was calculated using Equation 6.13 (*dark red* datapoints in **Figure 6.8c**). The fluorophore concentration at each horizontal position was then calculated (*blue* datapoints in **Figure 6.8d**) from the non-quenched intensity and using the direct proportionality relationship previously discussed (section 6.3.2). We find that the fluorophore concentration increases exponentially towards the left edge of the membrane up to ~2.4 % (mol/mol) TR-DHPE: a 7-fold increase from the starting concentration of 0.28 % (mol/mol). This exponential increase in concentration across the confined membrane region is consistent with the relationship previously found for the steady-state of electrophoresis[146].

To fully describe the relationship between self-quenching and concentration over the full range of concentrations, ideally the full extent from 0 – 100 % fluorescence quenching should be captured. Therefore, this method of analysis was repeated for multiple FLIM images of membranes containing different initial concentrations of fluorophores. Lifetime and concentration profiles were calculated for 0.28 %, 0.56% and 0.84 % (mol/mol) TR-DHPE (**Figure 6.9,** *orange, red* and *dark red*, respectively) and indicate that membranes with a higher initial concentration result in a higher maximum concentration achieved during in-membrane electrophoresis. Notably, the relative increase in fluorophore concentration (maximum compared to initial concentration) is approximately consistent. For membranes containing 0.28, 0.56 and 0.84 % (mol/mol) TR the maximum concentration reached during electrophoresis is ~2.25, ~4.5 and ~7 %, respectively (~7-fold increase in all three cases). This demonstrates the consistency of in-membrane electrophoresis as a method to control fluorophore concentration, and shows that changing the initial membrane concentration has a predictable effect on the final state of the membrane during electrophoresis. In addition, the lifetime and concentration profiles were highly consistent for each starting concentration and across multiple corrals, as shown by the narrow range of lifetimes or calculated concentrations in each data set.

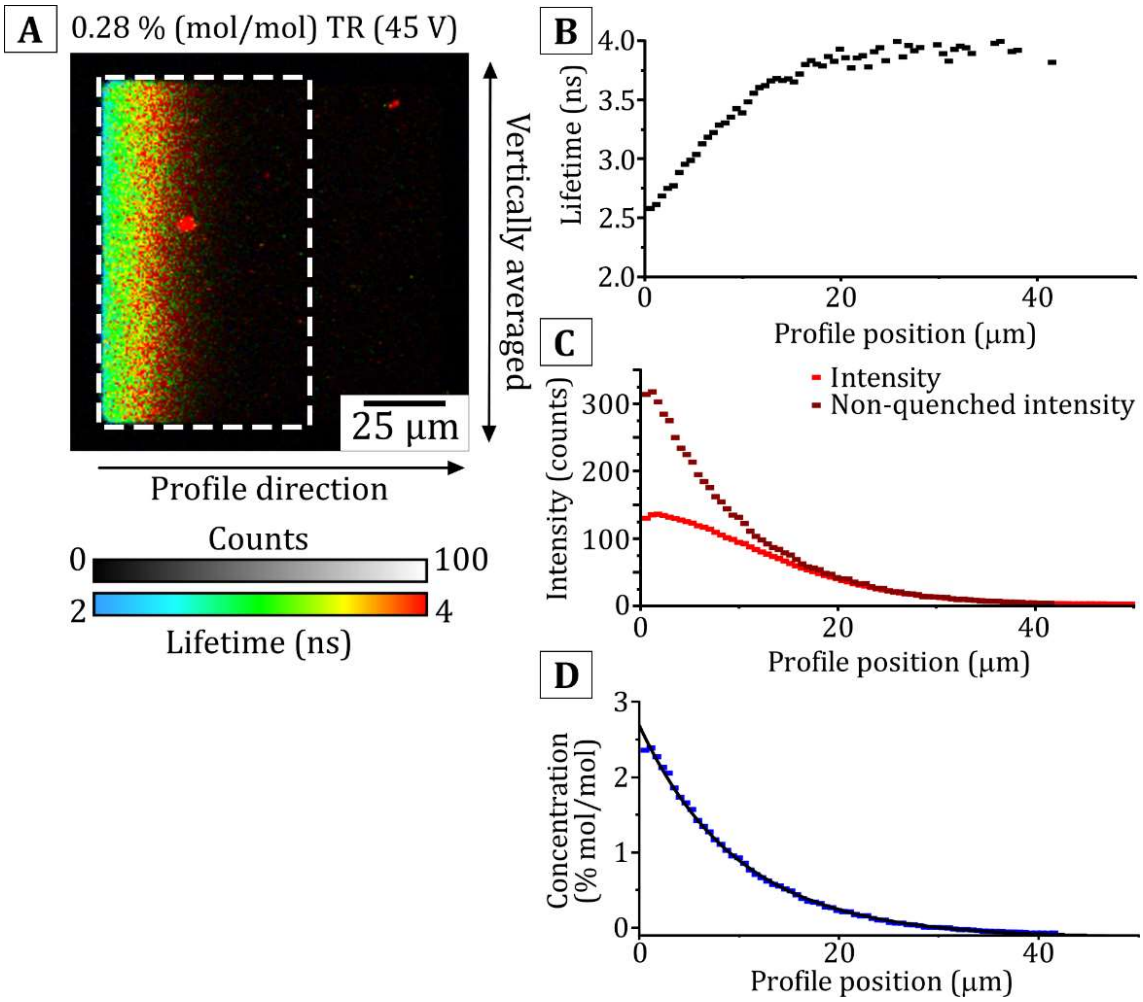

Figure 6.8: Demonstration of the method to obtaining lifetime, intensity and calculated concentration profiles from a FLIM image. **(A)** Example FLIM image of a 0.28 % (mol/mol) TR membrane during 45 V/cm equilibrium. The *white dashed* region shows the region from which lifetime and intensity profiles are obtained (representing >150 pixels accumulated vertically to minimise any fluctuations due to noise) **(B)** Mean lifetime profile obtained from the *white dashed* region in (a) showing the decrease from ~4 ns (x > 20 µm) to ~2.5 ns at x = 0 µm. **(C)** Mean intensity profile (*red*), termed *F*, obtained from the *white dashed* region in (a). The non-quenched intensity (*dark red*) is calculated from the profile for *F* and the profile for τ from (b) using the relation $F_0 = F \times exp(2 \times ln(\tau_0/\tau))$ as in Eq. 6.13. **(D)** The concentration profile in % mol/mol, calculated from the data for F_0 from (c) using the direct proportionality relationships between fluorophore concentration and non-quenched intensity $C = (F_0 - constant) / constant$ as calculated in section 6.3.2 that $C_{TR} = (F_0 - 13.5)/92.2$. The *black* line shows the result of a mono-exponential fit, $C(x) = C_0 \times e^{-Vx/D}$, used to calculate the V/D.

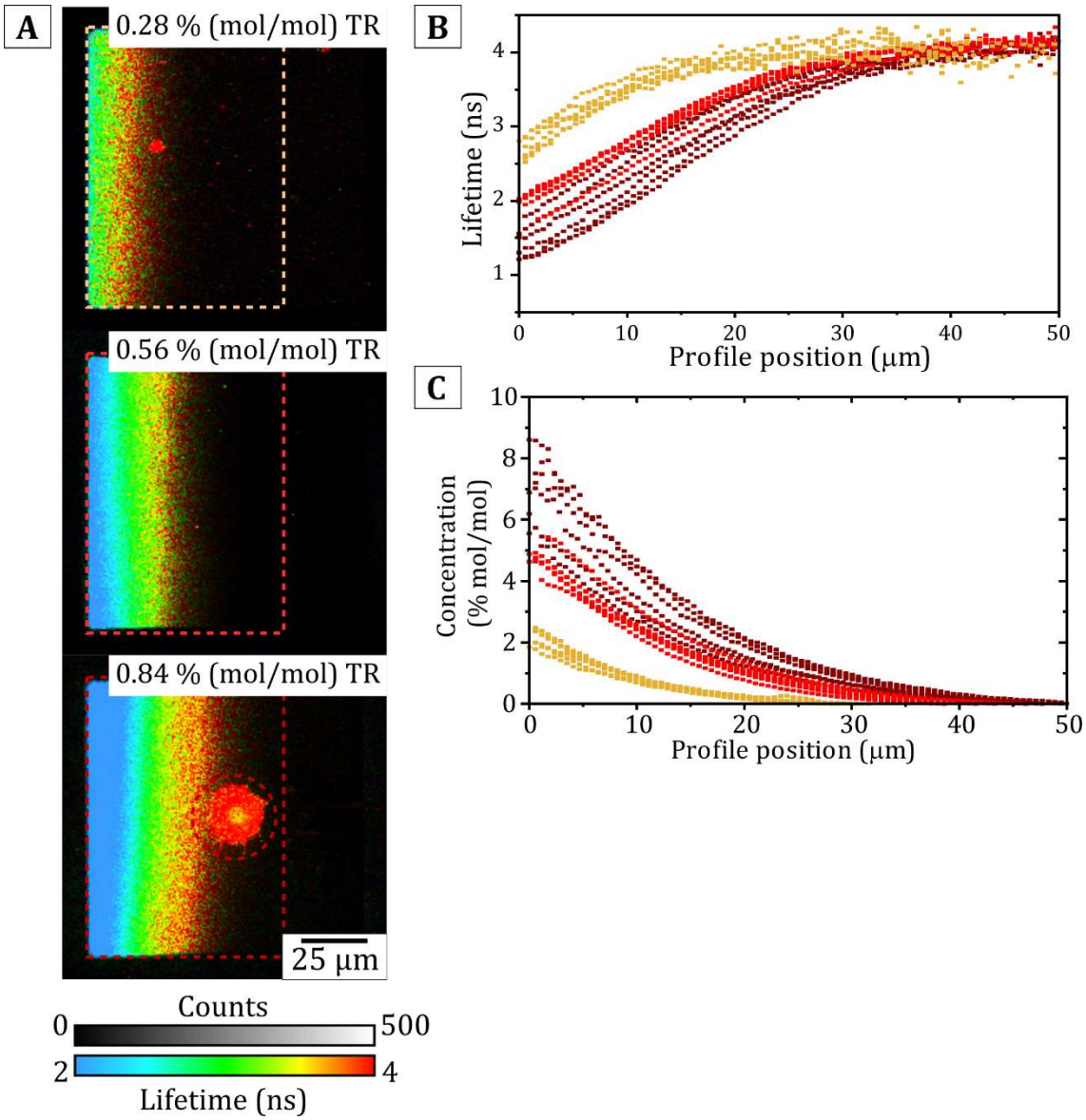

Figure 6.9: Lifetime and concentration profiles for multiple patterned corrals containing a range of concentrations of TR. **(A)** Example FLIM images of 0.28 % (*upper*), 0.56 % (*middle*), and 0.84 % (*lower*) (mol/mol) TR membranes during 45 V/cm equilibrium. The *coloured dashed box* show the regions from which lifetime and concentration profiles are obtained (vertically averaged, as previously). Different colours correspond to the different coloured scatter plots in panels (B) and (C). **(B)** Multiple lifetime profiles obtained from many different corrals, analysing regions as shown in the *coloured dashed box* areas in panel (A). *Orange, red,* and *dark red* data points shows all lifetime profiles obtained from membranes containing 0.28 %, 0.56 % and 0.84 % (mol/mol) TR respectively. **(C)** Multiple calculated concentration profiles obtained from the *coloured*, *dashed box* areas in panel (A). Colour scheme is the same as in panel (B). Fluorophore concentration was calculated from fluorescence intensity as described in Figure 6.8.

The quenching efficiency and the estimated concentration are spatially correlated in FLIM images, so these two types of data can be plotted against each other to describe the quenching behaviour of TR. **Figure 6.10a** shows the resulting QE vs C curve which combines all data sets obtained for electrophoresis of lipid bilayers containing TR. In addition to displaying the fluorophore concentration in mole/mole (bottom x-axis, **Figure 6.10a**), the concentration was converted to a number density based on the known molecular packing (fluorophores per 100 nm^2, equation 6.2) to provide a more tangible representation of the fluorophore concentration (top x-axis, **Figure 6.10a**). From this plot we can make several observations about the quenching behaviour of TR. Firstly, the QE vs C curves obtained from different samples are extremely consistent in terms of the trend which they reveal but each sample set covers a slightly different range of concentrations. Secondly, the amount of quenching initially increases steeply with concentration before the gradient begins to decrease. The quenching efficiency cannot increase past 1 (by definition) and therefore we expect this curve to saturate at higher concentrations (>10 % TR).

A well-known method to explore the kinetics of photophysical quenching is to plot a Stern-Volmer relationship[292], typically represented as:

$$\frac{F_0}{F} = 1 + k_{SV}Q \qquad \text{Eq. 6.14}$$

where F_0 is the fluorescence intensity in the absence of quenching, F is the fluorescence intensity due to quenching, and Q is the concentration of quenchers (traps). k_{SV} is referred to as the Stern-Volmer constant, and describes how the extent of fluorescence quenching changes with trap concentration. To assess the "molecularity" (i.e., how many molecules are involved) of trap formation, n, the Stern-Volmer relationship can be rewritten as:

$$\frac{F_0}{F} = 1 + k_{SV}C^n \qquad \text{Eq. 6.15}$$

where C is the concentration of fluorophores[269]. If the number of traps is proportional to the number of fluorophores, $Q \propto C$ and $n = 1$. Otherwise, if traps form from the interaction between a pairs of molecules (i.e., a dimer), then the number of traps would be proportional to the number of pairs of fluorophores, $Q \propto C^2$, and $n = 2$, and so forth for higher order kinetic processes.

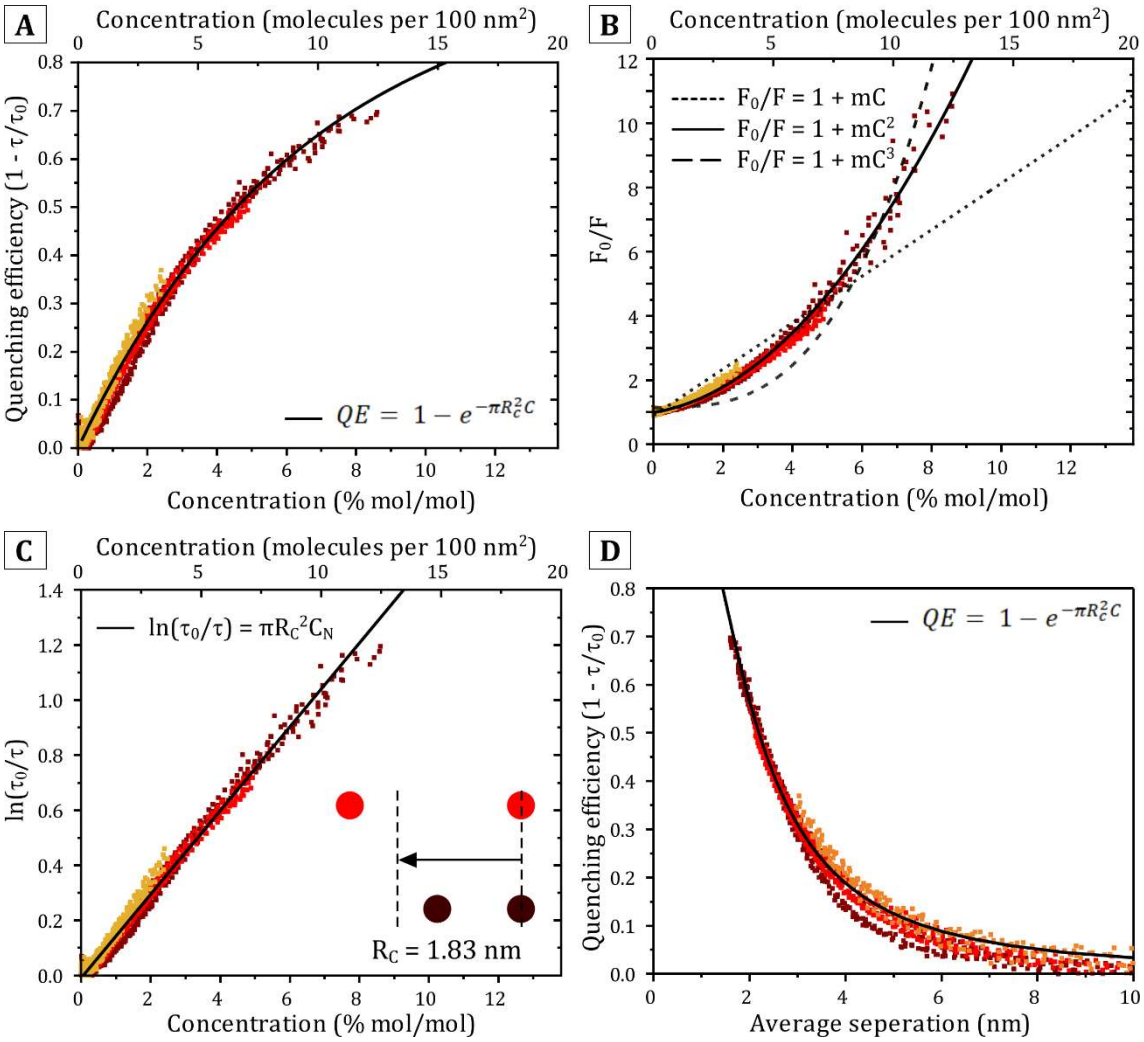

Figure 6.10: Multiple plots to show the relationship between fluorophore concentration, or average separation, and the amount of lifetime quenching for Texas Red. In all panels, *yellow* data shows the results of electrophoresis and analysis on bilayers initially containing 0.28 % (mol/mol) TR-DHPE, *light red* data shows the results from bilayers initially containing 0.56 % (mol/mol) TR-DHPE, and *dark red* data shows the results from bilayers initially containing 0.84 % (mol/mol) TR-DHPE. **(A)** Quenching efficiency, QE = 1 – τ/τ_0, versus concentration for TR fluorophores in lipid bilayers. The *solid black line* shows the theoretical quenching efficiency curve calculated using the critical radius determined from the linear fit in (C). **(B)** The same data as in (A) but plotted as the inverse relative intensity versus concentration. Three fits are attempted to the data, using equation 6.17, and by setting the molecularity to 1 (*short, dashed line*), 2 (*solid* line) and 3 (*long, dashed line*). **(C)** The same data as in (A) plotted as the semilogarithmic inverse lifetime vs concentration. A linear fit (*solid black line*) is used to obtain the critical radius for trap formation. **(D)** The same data as in (A) plotted as quenching efficiency versus average fluorophore separation. The *solid black line* shows the theoretical quenching efficiency curve calculated using the critical radius determined from the linear fit in (C).

To determine the molecularity of trap sites, F_0/F, was plotted against the fluorophore concentration, *C,* (**Figure 6.10b**) and multiple fits of were attempted to the Stern-Volmer plot using Equation 6.15 for multiple values of *n* (*short dashed, solid* and *long dashed* lines represent *n* = 1, 2 and 3, respectively). For *n* = 1 and *n* = 3 the quality of the fit was poor with large distances between the fitted line and the data points and low R-squared values (R^2 = 0.93 and 0.88 for *n* = 1 and 3, respectively). The best quality fit was achieved for *n* = 2 (R^2 = 0.98) and the fitted curve (*solid black line*, **Figure 6.10b**) overlays well with the data points for all concentrations. It therefore seems likely that the number of quenchers is proportional to the number of pairs of molecules in the system. This suggests that the fluorescent traps form as a function of dimer, rather than monomer, concentration, in apparent agreement with the concept of fluorescence quenching by the formation of non-fluorescent statistical pairs.

To test whether the data obtained from electrophoresis experiments was consistent with the relationships predicted for transfer-to-trap quenching, $\ln(\tau_0/\tau)$ versus C was plotted, as shown in **Figure 6.10c**, and fitted to the linear relationship derived in section 6.3.1, $ln(\tau_0/\tau) = \pi R_C^2 C_N$ (Equation 6.9). A linear fit (*black line*, **Figure 6.10c**) was found to overlay well with the experimental data points (R^2 = 0.95), showing that our data is consistent with the theory for transfer-to-trap quenching whereby traps form from some interaction between pairs of molecules. It is possible to characterise the quenching "strength" by using the gradient from the linear fit to calculate the "critical radius" (R_c) for trap formation. The gradient of linear fit (*black line,* **Figure 6.10c**) was found to be 10.49 ± 0.06 nm^2 and the R_C for TR was calculated to be 1.83 ± 0.01 nm. This result suggests that two fluorophores have to be separated by very small distances to form a fluorescent trap. It seems feasible that traps may form as the result of short-range excitonic interactions when two molecules diffuse into close proximity (through random 2-D Brownian motion). Finally, we wished to describe the quenching behaviour of TR in terms of the separation between any two TR fluorophores. The average centre-to-centre distance, R, was calculated from the number of molecules per nm^2, C_N, using equation 6.3, and the quenching efficiency (QE) was plotted against R (**Figure 6.10d**). The resulting plot shows that for R > 6 nm QE is minimal (<10%), before rapidly increasing up to 70% QE at an average separation of ~2 nm. As previously

described we expect QE to saturate at sufficiently small R and it is theoretically possible that at extremely low R (where $R \ll R_C$) all of the fluorophores may be part of non-fluorescent dimers. To confirm that the experimental data was consistent with theory in all plots, a theoretical curve for QE vs C and QE vs R was calculated using the experimentally obtained value for R_C = 1.83 nm (and the calculated value of R_0 = 5.71 nm, section 6.3.1). The calculated curves for QE versus C (*black line*, **Figure 6.10a**) and QE versus R (*black line*, **Figure 6.10d**) were found to be highly consistent with the experimental datapoints for all concentrations/separations. Overall, these results show that it is highly likely that TR fluorophores follow transfer-to-trap quenching, in which fluorophores form non-fluorescent dimers as a probabilistic function of concentration and excitons may migrate via FRET from excited monomers to dimeric trap sites where excitons are quenched (i.e. dissipated non-radiatively). In addition, the strength of TR quenching has been quantified in terms of the critical radius of trap formation in order to be able to compare the relative strengths of quenching of different fluorophores. This method of analysis was repeated for electrophoresis measurements of lipid membranes containing NBD, TR and BOD. These results are presented in the next section and the quenching behaviours of all three fluorophores are compared.

6.3.4 Comparison of quenching behaviour between TR, NBD and BOD

To be able to quantitatively compare the quenching behaviours of all three dyes, the analysis in section 6.3.3 was repeated for in-membrane electrophoresis experiments of NBD and BOD, and then compared to TR. The resulting QE vs C curve for all fluorophores are shown in **Figure 6.11a**. It can be seen that all three fluorophores follow the same overall trend, whereby QE increases with C but the gradient of the curve becomes increasingly shallow at high concentrations. From **Figure 6.11a** it is also apparent BOD (*blue*) self-quenches more strongly than TR (*red*) and NBD (*green*), as demonstrated by the steeper gradient of the QE vs C curves and greater amounts of quenching for similar concentrations. For example, in a bilayer containing 2.5% (mol/mol) of a specific fluorophore the fluorescence would be quenched by ~10% for NBD, ~30% for TR and ~ 50% for BOD.

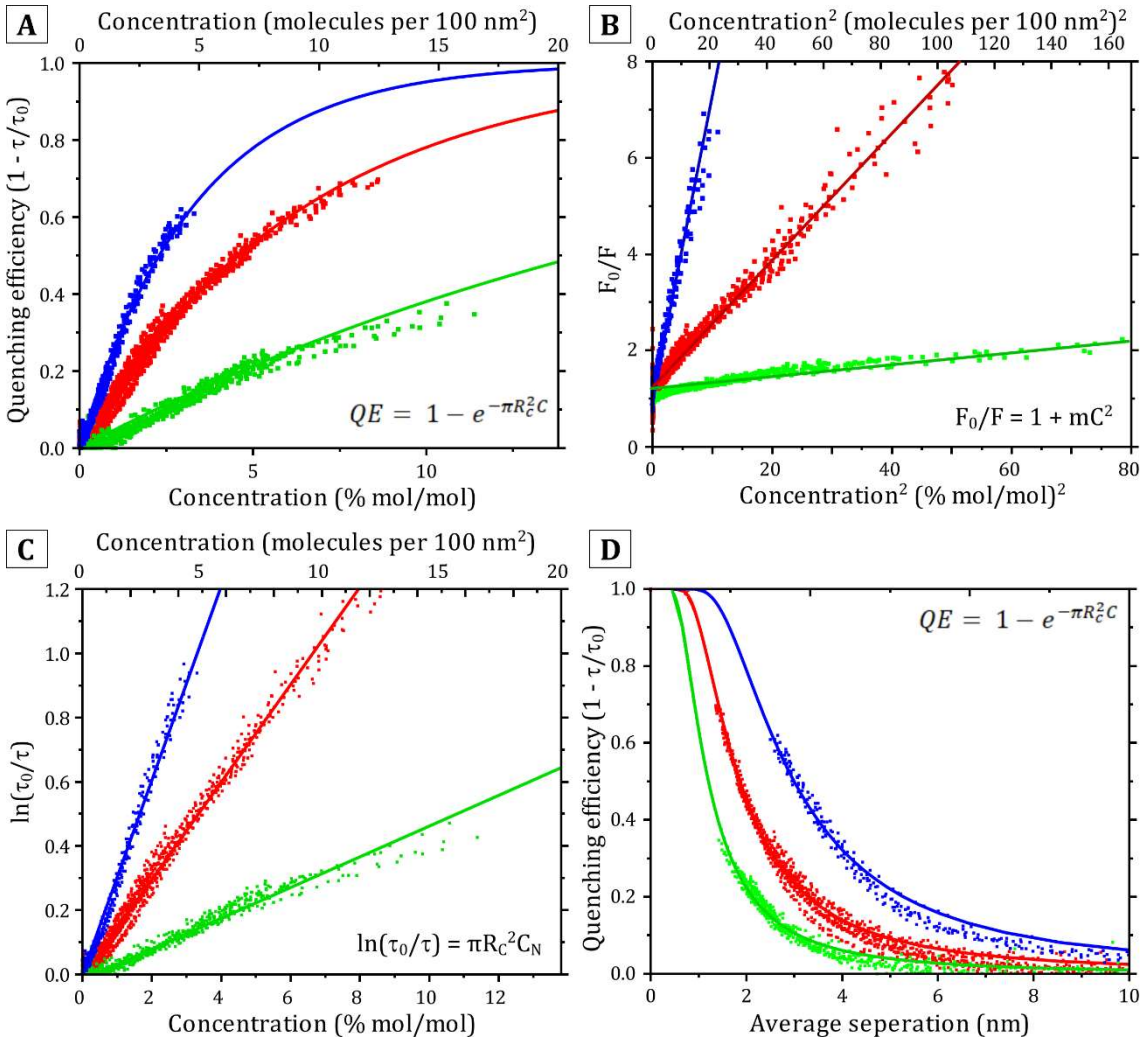

Figure 6.11: Graphs to compare the relationships for fluorophore quenching between TR, NBD and BOD. **(A)** Quenching efficiency versus concentration for all fluorophores in lipid bilayers. In all panels, *red* data shows the results of electrophoresis and analysis on lipid bilayers containing TR, *green* data shows the results from bilayers containing NBD, and *blue* data shows the results from bilayers containing BOD. The *solid lines* shows the theoretical quenching efficiency curves calculated using the critical radii determined from the linear fits in (C). **(B)** The same data as in (A) but plotted as the inverse relative lifetime versus concentration squared. The linear fit (*black*, *solid line*) shows that the amount of quenching is proportional to the dimer population in the membrane for all three dyes. **(C)** The same data as in (A) plotted as the semilogarithmic inverse lifetime vs concentration. Linear fits (*solid line*) are used to obtain the critical radius for trap formation for each dye. **(D)** The same data as in (A) plotted as quenching efficiency versus average fluorophore separation. The *black, solid line* shows the theoretical quenching efficiency curve calculated using the critical radii determined from the linear fits in (C).

To assess the molecularity of trap formation for each fluorophore, each data set was plotted as a Stern-Volmer plot testing $n = 2$, the condition representing dimers, and that $F_0/F = 1 + k_{SV}C^2$ (as determined to represent TR quenching). When plotting F_0/F versus C^2 (**Figure 6.11b**) we find that all three fluorophores can be fit to a linear relationship (*solid lines*, $R^2 > 0.99$) showing that the number of traps is proportional to the concentration of pairs of fluorophores, and suggesting that quenching is dominated by interacting dimers. Once again, the gradient of the BOD plot (*blue*) is significantly steeper than the gradients of the TR (*red*) and NBD (*green*) lines, and we hypothesise that BOD fluorophores form non-fluorescent dimers (traps) more readily than TR or NBD.

Next, to assess whether or not all three fluorophores follow transfer-to-trap quenching, each data set was plotted as $ln(\tau_0/\tau)$ versus C and fitted to a linear relationship, $ln(\tau_0/\tau) = \pi R_C^2 C_N$. For all three fluorophores the experimental data was strongly correlated to the theoretical model and followed the linear trend with high fidelity over all concentrations, suggesting that all three dyes undergo the same quenching mechanism (**Figure 6.16c**). Next, to compare the relative strengths of quenching, the critical radii for trap formation (R_C) were calculated from the gradient of the linear fits of these data. The gradient ($m = \pi R_C^2$) of each fit was found to be 20.7 ± 0.1, 10.5 ± 0.1 and 3.40 ± 0.02 nm^{-2} for BOD, TR and NBD, respectively, leading to critical radii for fluorophores of $R_{C(BOD)}$ = 2.57 ± 0.01, $R_{C(TR)}$ = 1.83 ± 0.01, $R_{C(NBD)}$ = 1.04 ± 0.01 nm**.** The critical radius represents the distance at which two fluorophores have a 63% likelihood to associate and form a trap, and, since the quenching mechanism is trap-limited, it is therefore a measure of the overall "strength" of quenching between fluorophores. Our results show that the quenching strength of BOD is 1.4 times greater than that of TR, which is in turn 1.8 times greater than that of NBD. The potential reasons for this relative strength is discussed in later sections. Our determined values for R_C (R_{BOD} = 2.57, R_{TR} = 1.83, R_{NBD} = 1.03 nm) corroborate values found in previous studies of NBD[268] and BOD[270] self-quenching (to the authors' best knowledge, there have been no previous attempts to determine R_C for TR), and show that this method for quantifying the strength of self-quenching in fluorophores is reliable and accurate. The ability to calculate the critical radius for trap formation for different fluorophores that have different chemistry and

different Förster radii, and obtain good fits, shows the utility of this experimental platform to assess photophysical differences for quite different systems.

To show how quenching may change as a function of average separation, QE vs R plots were generated for each fluorophore (**Figure 6.11d**). As expected, BOD (*blue*) begins to quench at much smaller separations than TR (*red*) and NBD (g*reen*) and reaches a quenching efficiency of 50% at ~3 nm, compared to 50% efficiency at ~ 2 nm for TR and ~1 nm for NBD. Within the plotted range (QE cannot be greater than 1), the QE continues to increase at decreasing separations, though this is expected to saturate at QE = 1 for very low separations. As before, theoretical quenching curves were generated using the calculated R_c and the known Förster radius and overlaid upon the experimental data. These calculated curves match well with both the QE versus C (*solid lines*, **Figure 6.11a**) and QE versus R (*solid lines*, **Figure 6.11d**) curves, with high fidelity to the data over the majority of C and R tested experimentally. A slight discrepancy is evident between the experimental data and theoretical curves at large separations (>5 nm), particularly for the BOD data, likely due to the fact that FRET simplification that $P_{FRET} \sim 1$ is no longer valid when the fluorophores are separated by distances larger than a few nanometers. Despite this, the clear correlation between experimental data and the theoretical relationship thought to represent self-quenching by the formation of non-fluorescent dimers (traps) and excitation migration throughout the membrane (transfer-to-trap) is very good evidence that this quenching mechanism does indeed occur for all three fluorophores.

6.4 Section summary and discussion

This chapter describes the use of electrophoresis to control the organization of charged fluorophores that are held within lipid membrane via their covalent bonding to lipids and the subsequent assessment of quenching that occurs as a function of the resultant fluorophore concentration. Direct Current electric fields were applied parallel to the long-axis of patterned lipid membranes containing either NBD, Texas Red (TR) or Bodipy (BOD) fluorophores, such that the fluorophores were displaced in the direction of the generated electromagnetic (Lorentz) force. Time-lapse FLIM measurements visualised the movement of

charged fluorophores and showing that all three fluorophores diffuse in response to the applied electric force, accumulating at the impenetrable edge of the membrane (shown by an increasing fluorescence intensity).

The increase in fluorescence intensity observed was correlated to a decrease in the average fluorescence lifetime, suggesting that fluorescence is quenched by increasing the fluorophore concentration. FLIM images taken of lipid bilayers containing NBD, TR and BOD in equilibrium in an electric field show that all three fluorophores experience concentration quenching, manifested as a gradient from short to long lifetimes correlated to the gradient from high to low concentrations across the membrane. By varying the initial in-membrane concentration of fluorophores (using fluorophore-to-lipid mole/mole fractions from 0.28 % to 0.84 % TR), we demonstrated the ability to modulate the maximum concentration of fluorophores reached during in-membrane electrophoresis from ~2 % to 7 % and therefore to control the maximum amount of quenching achieved from 31 % to 68 %. Membrane disruption at the highest concentration of fluorophores, likely caused by high local curvatures of the membrane[137], suggests that there is an experimental limit to the maximum fluorophore concentration (~10% mole/mole) that can be achieved in our patterned membranes. However, we note that other researchers were able to increase the fluorophore concentrate by up to 25-fold by using different membrane geometries or AC currents[145, 148]. It seems likely that the membrane disruption we observed could be overcome by changing the dimensions of the patterned template to provide more stability to highly curved membranes.

The evidence suggests that the quenching observed, for all fluorophores, is a combination of the concentration-dependent formation of a non-fluorescent dimers which act as trap sites and energy migration through the membrane which depends on FRET to reach these sites. This conclusion was based upon the excellent fit of our experimental data to theoretical models which were based upon numerous previous mathematical models (e.g., Perrin quenching) and adapted for our purposes[267, 268, 270, 272, 289]. We found that the overall quenching efficiency is generally limited by the fraction of traps occurring in the system rather than energy migration because energy migration between fluorophores is already extremely probable at the average separations required for trap formation.

A careful analysis of FLIM data was used convert the fluorescence intensity to a relative concentration and maintain the correlation to fluorescence lifetime in each pixel. This allowed the determination of the "quenching efficiency" of fluorophores correlated to their concentration. For NBD, TR and BOD the quenching efficiency increased with concentration before asymptotically tending towards unity at high concentrations. Here, theoretical plots of transfer-to-trap quenching were in excellent agreement our experimental data suggesting that this is the correct molecular explanation for quenching here. The important implication here is that self-quenching depends upon "statistical pairs" (Perrin quenching) which do not require any long-lived interactions. In other words, chemical (e.g., covalent) or physical (e.g., aggregation) interactions are not required for concentration quenching, which may explain why such quenching behaviour appears to be a general phenomenon for most pigments.

The critical radii for trap formation, representing the relative quenching strengths, were found to be R_{BOD} = 2.57 ± 0.01, R_{TR} = 1.83 ± 0.01, R_{NBD} = 1.03 ± 0.01 nm. These are in close agreement to those found in previous investigations of NBD[268] and BOD self-quenching[270] and give us a high level of confidence in in-membrane electrophoresis as a platform to quantify concentration quenching in lipid membranes. The critical radius of TR has been determined for the first time, as this has not previously been characterised (to our knowledge). Therefore, BOD undergoes concentration-dependent quenching most strongly, followed by TR at an intermediate level, and then NBD at a lowest level. A useful outcome of this type of characterisation is the potential for specific selection of the fluorescence quenching behaviour depending on experimental requirements. For example, a fluorophore with negligible/weak quenching (like NBD) may be better suited for experiments to detect the relative quantities of material through fluorescence emission measurements. Alternatively, multiple studies use self-quenched fluorophores as an assay to test for a decrease in the concentration of molecules, whereby the fluorescence intensity quantitatively increases as quenching effect is relieved (e.g., measuring the stability of liposomes[293]), and using a more strongly quenching fluorophore (e.g. BOD) would provide the greatest sensitivity.

6.5 Concluding remarks and future outlook

A particular advantage of in-membrane electrophoresis is the generation of a continuum of fluorophore concentrations, which avoids the need to prepare multiple samples at discrete concentrations, which could significantly increase the throughput of investigations into fluorescence quenching. Multiple studies using fluorescent probes may benefit from a standardised and streamlined platform to characterise the self-quenching of fluorophores, to aid in the interpretation of fluorescence measurements, e.g., to correct the fluorescence intensity measured to determine molecular concentration more accurately.[145] In addition to self-quenching, in-membrane electrophoresis could be also used to interrogate energy transfer between different types of fluorophores (i.e., typical donor-acceptor FRET), by maintaining one fluorophore at a fixed concentration (e.g., by surface tethering[80, 294]) and by modulating the concentration of the other fluorophore (which should be charged or otherwise mobile). This platform could provide a method for the rapid screening of potential FRET pairs (similar to those investigated in Chapter 5) and for optimising the concentrations of donors/acceptors to maximise the energy transfer efficiency of light-harvesting nanomaterials. In-membrane electrophoresis has previously been applied in order to separate multiple species of fluorophores by their different electrophoretic properties[147, 278, 280] and could be used to generate a system where energy transfer or electron generation could be selectively switched on/off by the respective mixing/unmixing of fluorophores or proteins.

Future studies could also involve modifying the array pattern of the template, for example, in an attempt to generate more extreme fluorophore concentrations (e.g., corral area/ shape/ aspect ratio). Reconstituting membrane proteins into lipid membranes at higher concentrations (which might better-represent natural biological membranes) has so far proved difficult, however, in-membrane electrophoresis has already been applied to achieve drastic increases in membrane protein concentration, e.g., a 25-fold increase in the concentration of the integral membrane protein proteorhodopsin[143, 148]. Furthermore, studies have used electrophoresis “traps” that prevent the redistribution of fluorophores once the electric field is removed.[144, 145] This approach, combined with lifetime or atomic force microscopy measurements, could provide a powerful platform in which to

study membrane proteins in close-to-native concentrations and within a lipid membrane environment that mimics natural lipid-protein interactions. Overall, our results in this chapter have demonstrated how in-membrane electrophoresis and FLIM can be used quantify the quenching behaviours of small-molecule organic fluorophores. In the final results chapter this method is applied to investigate the fluorescent quenching behaviour of Light Harvesting proteins, by using the hybrid membranes introduced in Chapter 4.

6.6 Chapter acknowledgements

In this chapter S. A. Meredith was responsible for the preparation and manipulation of patterned bilayers in electrophoresis experiments, acquisition and analysis of FLIM data and presentation of FLIM images. T. Yoneda and Y. Kusunoki were responsible for the fabrication of patterned polymerised templates. P. G. Adams, S. D. Connell and S. D. Evans are the academic supervisors of S. A. Meredith. K. Morigaki is the academic supervisor of T. Yoneda and Y. Kusunoki.

7 Using model membranes to investigate the self-quenching and energy transfer processes between Light-Harvesting proteins

7.1 Introduction

High-intensity sunlight has been shown to cause several deleterious effects to the growth of plants, if left unchecked, often referred to as photoinhibition[39, 40]. Photosynthetic organisms have different strategies that attempt to prevent this, collectively termed "photoprotection". This can be at the whole organism level or at the molecular level. The exact mechanism of non-photochemical quenching (NPQ) is still a contentious topic in the photosynthetic community. In the early 1990s Horton and co-workers proposed the aggregation model of quenching, in which changes to the local environment (pH or detergent removal) of purified LHCII complexes result in their aggregation and a transition from a fluorescent to a highly quenched state that resembles that spectroscopic signatures observed for NPQ in intact plants.[295] It was proposed that protein aggregation results in an internal conformation change in the complex and the formation of a quenching interaction between chlorophyll and xanthophyll pigments (though the precise site of this interaction is still unknown). An important issue is whether the LHCII antenna clustering is a primary cause of the quenching or simply a thermodynamic consequence of the inner conformational change within each timer/monomer that creates the quencher. This is particularly confusing due to the discovery that the aggregation of LHCII is not always required for the formation of a quenched state. Previous studies have shown that fluorescence quenching can be induced in isolated LHCII trimers,[54] and that individual trimers can undergo a phenomenon called fluorescence intermittency,[67, 68] whereby the complex "blinks" between a fluorescence or a dissipative state likely as the result of two distinct conformational states. It therefore appears that switching between light-harvesting and photoprotective states is an intrinsic property of LHCII trimers, which in turn raises the following question: does LHCII aggregation cause or stabilise the dissipative

energy state or does the conformational change associated with photo-protection alter protein-protein interactions in the membrane?

To address these questions, it would be useful to assess the effect of protein concentration/aggregation on fluorescence quenching. A small number of researchers have successfully used electric fields to direct the movement of membrane proteins in lipid bilayers, including a few studies on membrane-associated proteins[143, 144] and a single study on a transmembrane protein (proteorhodopsin)[148] and it seems feasible that mobile photosynthetic proteins may also be susceptible to in-membrane electrophoresis. In Chapter 4, "hybrid membranes" were introduced as an experimental platform in which to assess the organisation and photophysics of photosynthetic proteins within a lipid bilayer. It was demonstrated that the proteins within hybrid membranes are able to diffuse within the membrane (~80% mobility) and are at a sufficiently low concentration that protein-protein interactions (that may cause quenching) were unlikely to be present. Increasing the protein concentration in hybrid membranes, in the same manner as was done for lipids in Chapter 6, may result in the quenching of chlorophyll fluorescence intensity and lifetime (as depicted in the schematic in **Figure 7.1**). Quantification of this fluorescence quenching over a range of protein concentrations (using FLIM) may allow for the delineation of the role of protein aggregation in NPQ and a deepened understanding of energy transfer and quenching traps in photosynthetic membranes. This chapter documents the experimental development of this platform and presents results from the in-membrane electrophoresis of photosynthetic proteins in a native-like lipid environment.

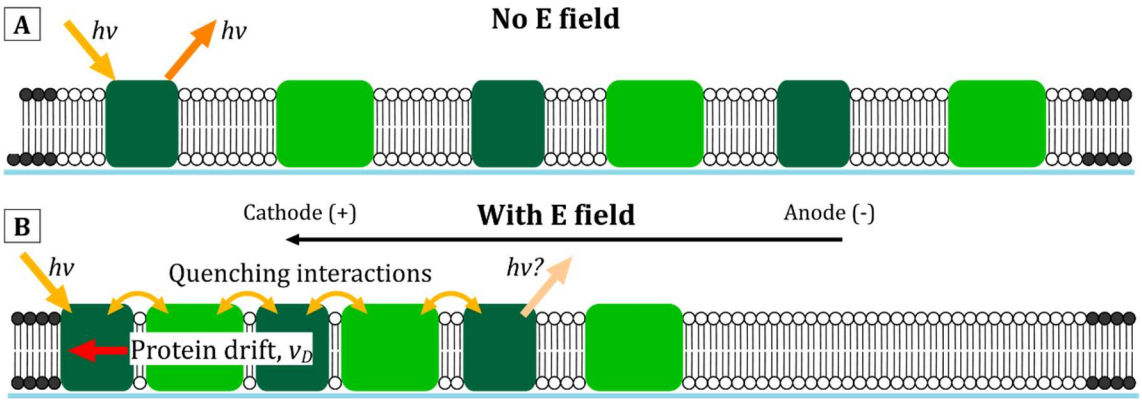

Figure 7.1: Proposed schematic for in-membrane electrophoresis of hybrid membranes **(A)** Schematic of a hybrid membrane in equillibirium in no electric field. Proteins are uniformly distributed throughout the membrane. **(B)** Proposed schematic of a hybrid membrane after being concentrated by an electric field, leading to quenching interactions between proteins.

7.2 In membrane electrophoresis of hybrid membranes to investigate energy transfer and self-quenching

7.2.1 Removing oxygen from the imaging buffer significantly reducing photobleaching during electrophoresis experiments

First, to avoid any unwanted alterations to the fluorescence lifetime measured during FLIM measurements (described in section 5.2.7) and avoid uncertainty in calculations of the protein concentration, it was important to ensure that any photodamage to proteins within the hybrid membranes was minimized. In photosynthetic systems, the majority of photodamage that occurs is believed to be caused by direct damage to the chlorophyll molecules by singlet oxygen and previous studies have used O_2-scavenging enzymes to remove the small amount of molecular oxygen which is typically dissolved in aqueous buffers from the protein's local environment to reduce the likelihood of photodamage.[56, 80] For in-membrane electrophoresis, this approach was deemed to be unpractical, due to the large volumes of buffer that are required per experiment and the prohibitive cost and preparation required for large quantities of such enzymes. Instead, oxygen was removed from the buffer by a freeze-evacuate-thaw process that has been shown to be effective at eliminating oxygen,[296] in which the buffer is flash frozen by immersion in liquid nitrogen and then thawed under vacuum at room temperature.

Photobleaching timelapse measurements were obtained of hybrid membranes (formed as described in methods section 3.3.6 and section 4.3.1) that had been washed into buffer that either had, or had not, been "degassed". To monitor the extent of photobleaching as a function of FLIM exposure, samples were imaged via FLIM for a prolonged acquisition (250 frames) and then the acquisition was digitally separated into images consisting of 25 frames each (**Figure 7.2a-b**). It is observed that the amount of photobleaching is significantly reduced when the hybrid membrane are washed into degassed buffer. **Figure 7.2a** shows FLIM images of a hybrid membrane in standard buffer (not degassed), where the Chl fluorescence intensity can be seen to steadily decrease with each FLIM image (25 frames). In contrast, the series of images in **Figure 7.2b** shows that the Chl intensity remains approximately constant when the hybrid membrane was prepared with a buffer that had been degassed. The number of counts per corral was measured for each image and plotted, shown in **Figure 7.2c**, and fit to a mono-exponential decay function. After 100 frames of acquisition, the sample washed into not-degassed buffer is photobleached to 71% of its initial intensity, compared to 96% of the initial intensity for the sample washed into degassed buffer (for the full 400 frames, the intensity decreases to 35% and 80%, respectively). Our results show that a combination of degassing the buffer and limiting the exposure time of each area to less than 100 frames is sufficient to limit the amount of photobleaching to acceptable levels (<5 % photodamage). With these measures we are able to ensure that the "active" protein concentration remains approximately consistent over the duration of each measurement, so that it is possible to correlate the concentration of proteins to their photophysical properties. All subsequent measurements in this chapter were obtained with samples in degassed buffers to minimise any photodamage and changes to the active protein concentration.

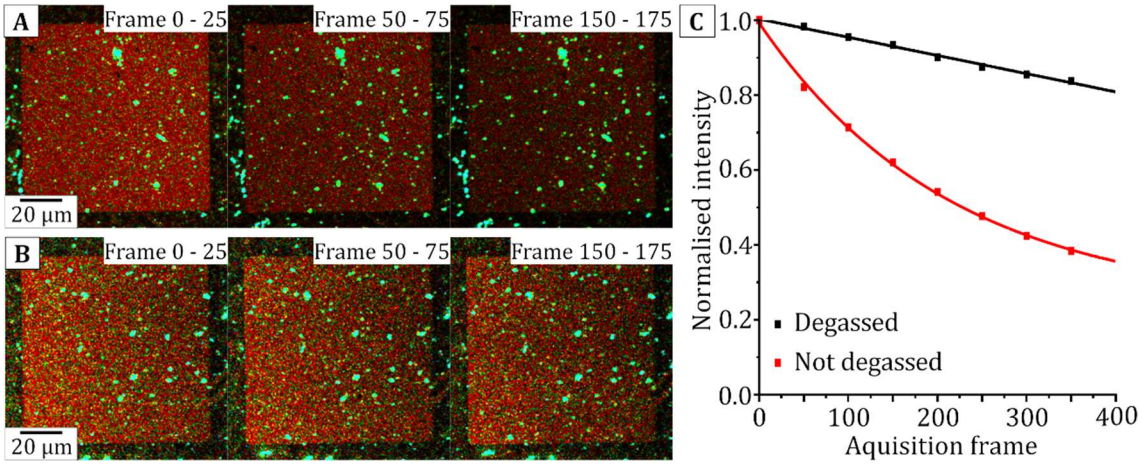

Figure 7.2: FLIM timelapse images of hybrid membranes imaged in buffer that had or had not been degassed. Removal of the oxygen results in significantly less protein photodamage. In both cases, the buffer was comprised of 50 mM KH_2PO_4, 10 mM NaCl, 2 mM $MgCl_2$, 330 mM sorbitol (pH 7.5) and the only difference was that the buffer used for (B) had gone through the freeze-vacuum-thaw process described in the text. **(A)** FLIM timelapse of a hybrid membranes imaged in buffer that had not been degassed. Each image shows photons detected in a group of 25 frames. **(B)** FLIM timelapse of hybrid membranes imaged in buffer that had been degassed. **(C)** Measured corral intensity versus frame number for hybrid membranes either in buffer that has not or has been degassed (*red* and *black*, respectively). Solid lines are a simple monoexponential decay function fitted to guide the eye.

7.2.2 Increasing the ratio of thylakoids to synthetic lipids increases the concentration of proteins in hybrid membranes

In Chapter 6, it was observed that a higher starting concentration of lipid-tagged fluorophores within lipid bilayers results in a higher maximum concentration of fluorophores accumulating at the end of the membrane by electrophoresis. Therefore, to test if it is possible to increase the initial concentration of proteins within the hybrid membrane during the self-assembly process, which would allow more control over the concentration range accessible with in-membrane electrophoresis, hybrid membranes were formed as described in sections 3.3.6 and 4.3.1, but briefly described here. Specifically, 100 × 100 µm Diyne-PC templates were incubated with an aqueous suspension of extracted thylakoids and synthetic lipid vesicles (DOPC) and the sample was washed with clean buffer solution. To modulate the protein concentration, the ratio of extracted thylakoids and DOPC vesicles incubated with the template was varied in a range from 1:3 to 5:3

(chlorophyll:DOPC in weight:weight) by keeping a standard concentration of liposomes and altering the quantity of thylakoids. In the subsequent figures, samples are referred to by the ratio of the components used in the self-assembly process, though this may not necessarily represent the final concentration of proteins/lipids in the membrane. In later stages, the concentration of proteins in each membrane is estimated and the sample notation is updated accordingly.

To compare the resulting composition of different types of hybrid membranes, FLIM was used to image hybrid membranes formed from the Chl:DOPC ratios described above. The FLIM microscope was optimised for the detection of chlorophyll (Chl) fluorescence (excitation: 640 nm laser, emission: 672 – 696 nm filter) at maximal temporal resolution and the imaging parameters were kept consistent between samples so that changes to the fluorescence intensity/lifetime can be assessed quantitatively and to allow for accurate analysis of concentration and quenching. FLIM images for 1:3, 2:3 and 3:3 (Chl:DOPC) hybrid membranes are show in **Figure 7.3a, b** and **c** respectively. Hybrid membranes did not form when using Chl:DOPC ratios higher than 3:3 (i.e., these had inhomogeneous intensity and no lateral mobility).

FLIM images of 1:3, 2:3 and 3:3 (Chl:DOPC) hybrid membranes show a mostly homogeneous fluorescence intensity that is largely restricted to the corral region (empty box generated by the Diyne-PC mesh) with far fewer fluorescent patches found on the peripheral template. The Chl fluorescence in the corral region has a long (~3 to 4 ns) lifetime, represented by *orange*/*red* pixels in the FLIM false colour scale, and there are very few pixels with a long fluorescence lifetime on the surrounding template. In all three samples, there are significant numbers of globular, *blue* (short lifetime) particles that occur non-specifically across both the corral and the template regions of the sample, which appear to represent thylakoid membranes that are loosely adsorbed to the sample (as first identified in Section 4.3.2). These adsorbed thylakoid membranes appear to be more numerous in hybrid membranes that are formed at a higher Chl:DOPC ratio, and it makes logical sense that a higher concentration of thylakoid membranes in solution results in a larger number of adsorbed membranes.

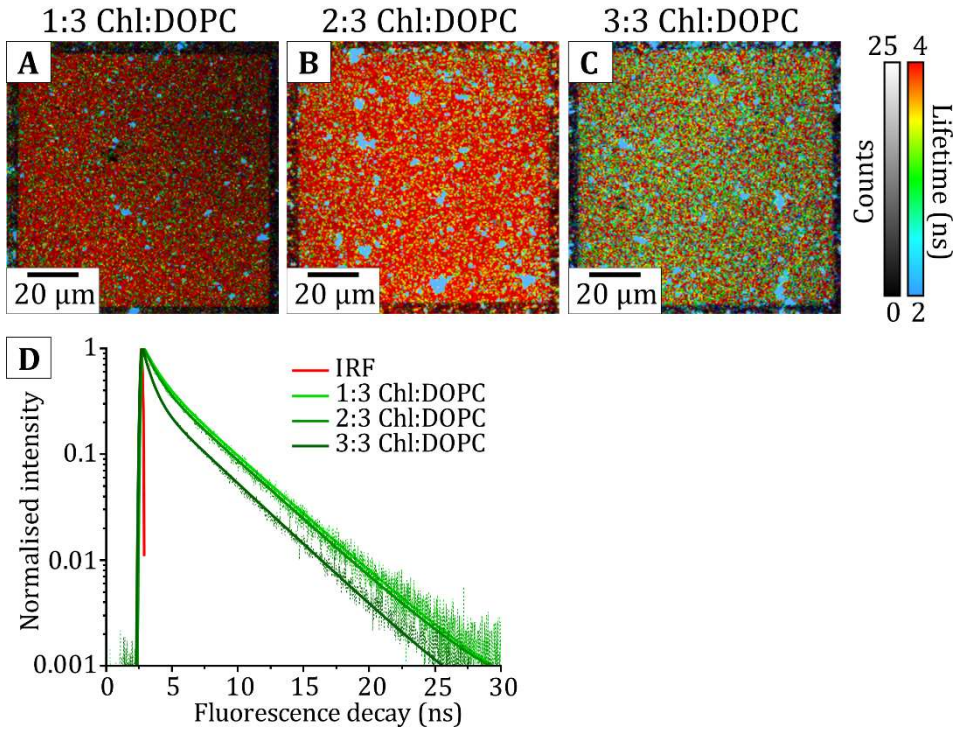

Figure 7.3: Hybrid membranes formed from different ratios of thylakoid extracts to DOPC liposomes (weight Chl to weight lipid). FLIM images of one example corral of hybrid membranes formed by incubating a **(A)** a 1:3 Chl:DOPC solution, **(B)** a 2:3 Chl:DOPC solution and **(C)** a 3:3 Chl:DOPC solution on polyermised lipid templates. Each solution was diluted to give a final concentration of 0.64 mM DOPC and then incubated with the substrate for 30 minutes before copiously washing it with buffer. 0.64 mM DOPC is approximately equivalent to 0.155 mg Chl/mL. **(D)** Fluorescence decay curves obtained from the membrane region of (a), (b) and (c). *Light* to *dark* green represents hybrid membranes formed from increasing ratios of Chl:DOPC.

Further washing these samples with buffer did not result in the further removal of adsorbed membranes, therefore, these objects were digitally removed (i.e. deselected from areas of analysis) for all subsequent comparisons of fluorescence intensity and lifetime so as not to skew the analysis of the underlying membranes. The fluorescence emission and lifetime of *orange/red* fluorescence inside the template region differs between the three different samples. Specifically, the average detected fluorescence intensity increases from ~17 to 25 counts/pix as the Chl:DOPC was increased from 1:3 to 2:3, and decreases to ~22 counts/pix for the hybrid membrane formed from a ratio of 3:3 Chl:DOPC. The initial increase in intensity may suggest a higher protein concentration in the 2:3 membrane compared to the 1:3 membrane. Correlated to the changes in fluorescence intensity, the fluorescence lifetime is decreased in membranes formed from higher ratios of Chl:DOPC relative to the fluorescence lifetime of a hybrid membrane formed from 1:3 Chl:DOPC. Fluorescence decay curves accumulated from photons detected in the template regions (excluding *blue* particles) are shown in **Figure 7.3d** and amplitude-weighted fluorescence lifetimes, $<\tau_{ratio}>$, were obtained for each sample by fitting an exponential decay to each decay curve. It was found that $<\tau_{ratio}>$ decreased from $<\tau_{1:3}> = 3.67 \pm 0.02$ ns to $<\tau_{2:3}> = 3.42 \pm 0.01$ ns to $<\tau_{3:3}> = 2.46 \pm 0.02$ ns as the ratio of Chl:DOPC was increased. A shortened fluorescence lifetime is a common manifestation of protein-protein interactions that may occur in photosynthetic membranes, and suggests the presence of an increased number of protein-protein interactions and higher protein concentrations in hybrid membranes assembled from a higher Chl:DOPC ratio.

The concentration of proteins in each hybrid membrane was estimated as described below (using the method described in full in section 4.3.3). The fluorescence intensity which represents a single LHCII complex was estimated in a multi-step process (stage 1) and then this was used to assess the fluorescence intensity of corrals of hybrid membranes that contain an unknown quantity of LHCII (stage 2). In stage 1, the fluorescence intensity which represents one LHCII was estimated using a control sample of LHCII proteoliposomes using the same FLIM settings as those for electrophoresis measurements of hybrid membranes. To do this, the number of LHCII per proteoliposome was estimated based on particle size measurements and known protein and lipid packing constraints (Table 7.1). Then,

using FLIM, the fluorescence intensity of these proteoliposomes (0.17 counts per liposome per frame) and their average fluorescence lifetime (1.88 ns) was measured. This FLIM data combined with the estimates for number of LHCII per proteoliposome allowed the number of fluorescence counts for a single LHCII to be estimated, for which a best-estimate and lower and upper estimate, to account for the uncertainty, was calculated (Table 7.2). In stage 2, these best, lower and upper estimates for fluorescence per LHCII were used as inputs into the final analysis of new hybrid membranes prepared with the range of Chl:DOPC, to calculate the number of LHCII per corral for each sample (Table 7.3). For hybrid membranes assembled from a ratio of 1:3, 2:3 and 3:3 Chl:DOPC, our best estimate for the number of trimers per corral is 1.06×10^6, 1.93×10^6, and 2.33×10^6 trimers/corral, respectively, corresponding to 0.53 %, 0.97 % and 1.23% of the membrane area being occupied by photosynthetic proteins. The result of these calculations show that the compositions of hybrid membranes can be directly modulated by adjusting the ratio of Chl to DOPC used in the self-assembly process. Through this modulation, it may be possible to exert some level of control over the amount of quenching that occurs when proteins are concentrated using in-membrane electrophoresis.

Scenario	D (nm)	L/P (mol/mol)	$A_{vesicle}$ (nm^2)	A_{lipid} (nm^2)	A_{LHCII} (nm^2)	n (LHCII /vesicle)
best estimate	130	2916	53093	0.67	50.3	51.7
min. estimate	127	2916	43005	0.65	38.5	49.4
max. estimate	143	2916	64242	0.70	78.5	60.7

Table 7.1: Calculations for the number of LHCII proteins found on average per proteoliposome (which has 0.36 μM LHCII and 1 mM thylakoid lipids), given the estimated dimensions for the protein, lipids and the vesicle.

D, average diameter measured via dynamic light scatterting measurements (DLS), 130 nm is the average but given the accuracy of DLS the low and high values shown represent reasonable low and high estimates (± 10 %);

L/P, the average lipid-to-LHCII trimer ratio, as determinated from ensemble absorption spectroscopy measurements and spectral decomposition analysis using published methodology[98];

$\mathbf{A_{vesicle}}$, calculated from $4\pi r^2$ (where, r= D/2);

$\mathbf{A_{lipid}}$, published value for DOPC headgroup area. Given the uncertainty values of 0.65 and 0.70 were used the low and high estimates;

$\mathbf{A_{LHCII}}$, estimation of the membrane area occupied by one LHCII, from the consideration of space-filling models of published protein structures and then approximation of LHCII as a circular area (πr^2) where r = 3.5, 4.0 or 5.0 for the low, medium and high estimates (range due to uncertain protein packing);

Area per vesicle approximates to the following equation (note, the factor 0.5 is due to 2 lipids one from each two monolayer togethe to form one bilayer and thus occuping an area of A_{lipid}):

$$A_{vesicle} = n[A_{LHCII} + 0.5(L/P)A_{lipid}] \quad \text{Eq. 7.1}$$

This expression was solved to calculate **n** using the values for **L/P**, $\mathbf{A_{vesicle}}$, $\mathbf{A_{lipid}}$ and $\mathbf{A_{LHCII}}$.

The minimum, maximum and best estimates are made using the different possible values shown for each term, as shown.

Est.	N_{LHCII} per vesicle (#)	$F_{vesicle}$ (cnts/ frame)	$\tau_{vesicle}$ (ns)	F_{LHCII} (cnts /frame)
best	51.7	0.17	1.88	0.0067
min.	43.6	0.17	1.88	0.0083
max.	60.7	0.17	1.88	0.0057

Table 7.2: Calculations for the non-quenched intensity of an LHCII trimer.

These use the average fluorescence counts measured by FLIM for an LHCII proteoliposome and converts to counts per LHCII protein, given the measured number of proteins within a typical proteoliposome (from **Table 7.1-7.2**). Consistent acquisition parameters were used to record FLIM images of both LHCII proteoliposomes and hybrid membranes.

$\mathbf{N_{LHCII/vesicle}}$, estimated number of LHCII-equivalents per proteoliposome (**n** from **Table 7.1**). This range from the minimum to the maximum considering our combined uncertainties;

$\mathbf{F_{vesicle}}$, estimated fluorescence intensity measured per proteoliposome per frame in FLIM measurements.

$\boldsymbol{\tau_{vesicle}}$, the measured mean fluorescence lifetime of a typical LHCII proteoliposme (mean of N=100 measured particles);

$\mathbf{F_{LHCII}}$, the FLIM counts expected per LHCII trimer per frame calculated for each possible $\mathbf{N_{LHCII/vesicle}}$, as follows. LHCII within proteoliposomes is known to self-quench, shortening the fluorescence lifetime due to the self-association of neighbouring LHCII.[56] The measured $\tau_{vesicle}$ of proteoliposomes of 1.88 ns (SD = 0.015 ns) implies significant quenching relative to isolated LHCII in detergent ($\tau_{DDM} \approx 4$ns), so to crudely take this into account the intensity is multiplied by the ratio of the lifetimes (4/1.88). Thus, the intensity of the proteins in the unquenched state is estimated as:

$$\mathbf{F_{LHCII}} = \frac{\mathbf{F_{vesicle}}}{\mathbf{N}_{\left(\frac{\mathbf{LHCII}}{\mathbf{vesicle}}\right)}} \times \left(\frac{\tau_{DDM}}{\tau_{vesicle}}\right) = \frac{0.17}{\mathbf{N}_{\left(\frac{\mathbf{LHCII}}{\mathbf{vesicle}}\right)}} \times \left(\frac{4}{1.88}\right) = \frac{0.36}{\mathbf{N}_{\left(\frac{\mathbf{LHCII}}{\mathbf{vesicle}}\right)}} \qquad \text{Eq. 7.2}$$

Sample	Est.	F_{LHCII} (cnts /frame)	F_{corral} (cnts /frame)	τ_{corral} (ns)	$F0_{corral}$ (cnts /frame)	N_{LHCII} per corral (# ×10^6)	$A_{\%}$ (%)
1:3 Chl:DOPC	best	0.0067	6200	3.67	7200	1.01	0.51
	min.	0.0083	6200	3.67	7200	0.97	0.37
	max.	0.0057	6200	3.67	7200	1.19	0.93
2:3 Chl:DOPC	best	0.0067	10600	3.42	13000	1.86	0.95
	min.	0.0083	10600	3.42	13000	1.78	0.68
	max.	0.0057	10600	3.42	13000	2.18	1.71
3:3 Chl:DOPC	best	0.0067	9600	2.46	16000	2.33	1.18
	min.	0.0083	9600	2.46	16000	2.24	0.86
	max.	0.0057	9600	2.46	16000	2.75	2.16

Table 7.3: Calculations for the number of proteins per corral, in terms of "LHCII-equivalents" for either 1:3, 2:3 or 3:3 hybrid membranes.

F_{LHCII}, the FLIM counts expected per LHCII trimer per frame (calculated in **Table 7.2**) which produce either our minimal, maximal, or "best" estimate.

F_{corral}, average fluorescence intensity measured in FLIM of hybrid membranes, as total counts within one corral per frame. This value is found from careful analysis of the corrals from many images of hybrid membranes similar to those shown in **Figure 7.3** (N = 4 corrals)

τ_{corral}, fitted fluorescence lifetime measured in FLIM of hybrid membranes. This value is found from careful analysis of the corrals from many images of hybrid membranes similar to those shown in **Figure 7.3** (N = 4 corrals)

$F0_{corral}$, the calculated "non-quenched" fluorescence intensity, as total counts per corral per frame. This is calculated from:

$$F0 = F \times \frac{\tau_0}{\tau_{corral}} \qquad \text{Eq. 7.3}$$

$N_{LHCII/corral}$ is the estimated number of LHCII trimers per corral, N = F_{corral} / F_{LHCII};

$A_{protein}$(%), estimated surface area fraction of the corral occupied by LHC and PS proteins:

$$A_{protein}(\%) = \frac{N_{LHCII}}{A_{corral}} \times A_{LHCII}(nm^2) \qquad \text{Eq. 7.4}$$

A_{LHCII} is the area occupied by a single trimeric LHCII protein complex, as estimated in **Table 7.1**;

A_{corral} is the area of a single corral (10,000 μm^2 = 10^{10} nm^2)

7.2.3 Calculating the mobility of proteins within hybrid membranes

Next, to confirm if photosynthetic proteins are mobile and able to be moved by the electric field, the mobility of proteins was assessed within hybrid membranes formed from the different ratios of Chl:DOPC described in previous sections. FRAP measurements were performed by deliberately photobleaching a circular region within one corral for each sample, and then monitoring the fluorescence recovery via a time-lapse series of FLIM images. To calculate the mobile fraction of the membrane, images taken immediately before bleaching and a long period after bleaching were compared (the same analysis method as in Section 4.3.4). If the mobile fraction of proteins is 100%, one expects the intensity of these two areas to tend towards the same value after a sufficiently long time after photobleaching. FRAP experiments show a high mobile fraction (typically ~80%) for all three membranes (1:3, 2:3 and 3:3 Chl:DOPC), as seen in the before versus after images (**Figure 7.4a,b,c**) where the fluorescence intensity appears to almost fully recover in the bleached area versus the non-bleached area. Note that, in examples where adsorbed thylakoids (*blue* globular particles) are located inside the bleached area, the intensity of these particles does not recover, demonstrating that these objects are not physically connected to the hybrid membrane. The calculated values for the mobile fraction are shown in **Table 7.4**, showing that the mobile fraction is similar for all three samples, but decreases slightly (from 83.3 % to 79.5 % as the ratio of Chl:DOPC for hybrid membrane self-assembly is increased from 1:3 to 3:3.

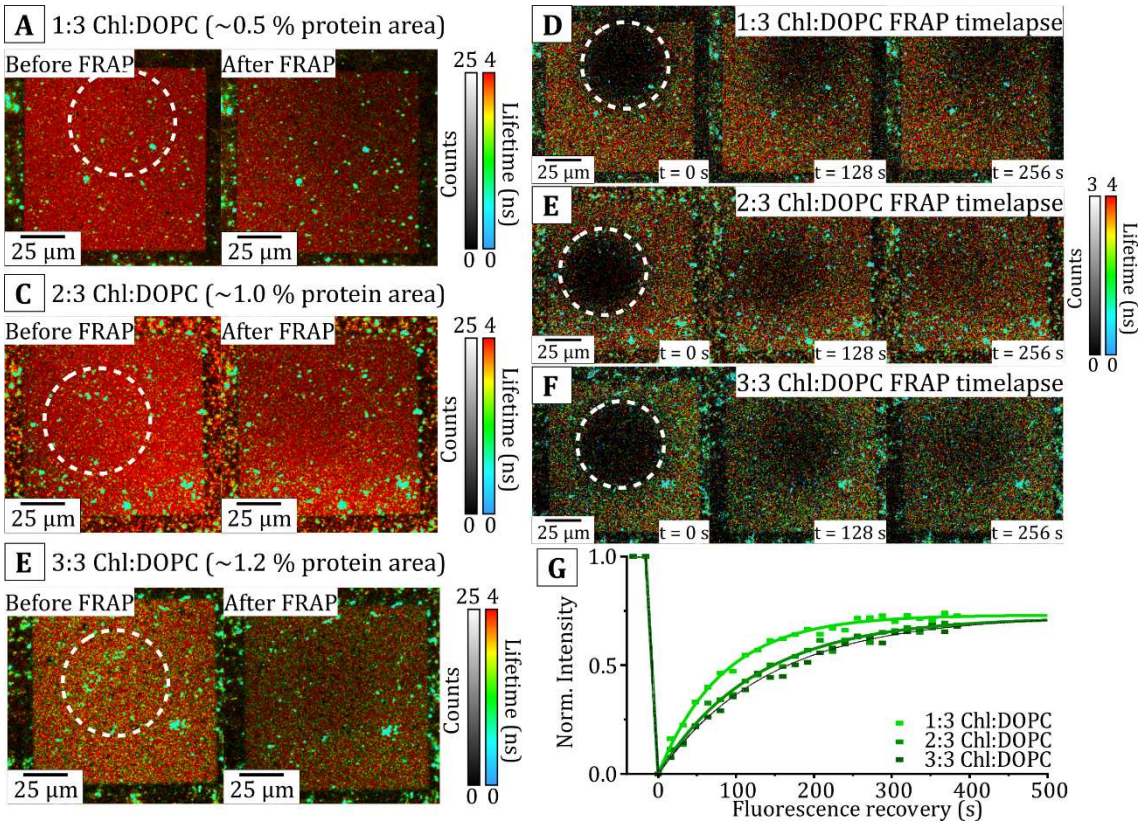

Figure 7.4: Fluorescence recovery after photobleaching (FRAP) experiments showing the mobility of proteins in patterened hybrid membranes containing different concentrations of protein. **(A)** FLIM images of hybrid membranes containing ~0.5% (of the total area) PS proteins acquired before photobleaching the *white, circular* region (*left*) versus at least 15 minutes after the initial bleach (*right*). **(B)** FLIM images of hybrid membranes containing ~1.0% PS proteins aquired before photobleaching versus after fluorescence recovery (*right*). **(C)** FLIM images of hybrid membranes containing ~1.2% PS proteins aquired before photobleaching versus after fluorescence recovery (*right*). **(D) (E) (F)** Timelapse FLIM series showing the fluorescence recovery of the bleached region in (a), (b) and (c), respectively. In (d), (e) and (f) each image represents all photons detected in a 16 s interval. Each timepoint represents the fluorescence measured in a 5-frame (16 s) interval, this interval was sufficient to obtain a measurable fluorescence signal (~5 counts/pix) whilst still ensuring reasonable temporal resolution to monitor the fluorescence recovery **(G)** Fluorescence recovery curves obtained from (d) (*light green*), (e) (*medium green*) and (f) (*dark green*). A mono-exponential fit, $F = F_0(1-e^{-kt})$, was used to obtain the "doubling time", $\tau = \ln(2)/k$, for each sample, from which the diffusion constant, $D = 0.22 \times R_{bleach}^2/\tau$, is calculated.

To determine the diffusion constant and protein mobility, a series of time-lapse FLIM images were obtained of the hybrid membrane immediately after photobleaching and the intensity of the bleached area was plotted as a function of time (**Figure 7.4d, e** and **f** for 1:3, 2:3 and 3:3 Chl:DOPC, respectively). Fluorescence recovery curves (**Figure 7.4g**) obtained from timelapse FLIM images show that all three membranes have an approximately similar rate of fluorescence recovery, but that the rate of recovery is slightly reduced for hybrid membranes containing a higher concentration of protein. The diffusion constant was calculated for each membrane is shown in **Table 7.4** and this data suggests that hybrid membranes containing a higher concentration of proteins may contain some nanoscale protein aggregates that diffuse throughout the membrane at a slower rate than individual protein trimers (generally, particle mobility is inversely proportional to the particle radius[297]). The possibility of these nano-aggregates is consistent with the shorter lifetime of higher concentration membranes observed in the previous section, and overall suggests that some form of protein-protein interactions occur in the membrane even at relatively low concentrations (~1 % protein area). Our FRAP results demonstrate that hybrid membranes formed from a variety of Chl:DOPC ratios contain mobile proteins and that samples prepared in this manner are suitable targets for in-membrane electrophoresis.

Sample description	Membrane conc. (area %)	Half recovery time (s)	Diffusion constant ($\mu m/s^2$)	Mobile fraction (%)
1:3 Chl:DOPC	~0.5	96.6 ± 9.8	1.56 ± 0.25	83.3 ± 5.3
2:3 Chl:DOPC	~1.0	125.6 ± 15.0	1.03 ± 0.12	82.9 ± 4.5
3:3 Chl:DOPC	~1.2	134.6 ± 6.4	0.97 ± 0.09	79.5 ± 8.3

Table 7.4: Summary of results from FRAP experiments on hybrid membranes assembled from different ratios of Chl:DOPC. Values with uncertainties represent the mean ± standard deviation from n=3 measurements.

7.2.4 Applying an E-field parallel to the membrane causes a reduction in the fluorescence intensity and lifetime, which indicates concentration quenching

To assess the electrophoretic effect and the resulting reorganisation of proteins in the membrane, time-lapse FLIM images were taken of hybrid membranes following the initial application of an electric field parallel to the plane of the membrane. A long FLIM acquisition (500 frames, 1600 s) was collected immediately after the electric field was switched on, and then digitally separated into individual images to monitor the emission and lifetime of the proteins as they were concentrated by the electric field. Each timepoint represents the photons collected over a 25 frame (80 s) interval, deemed to be the minimum period of time required to achieve a measurable number of counts and reasonable temporal resolution. **Figure 7.5a** shows a timelapse series for 3:3 Chl:DOPC hybrid membranes (~1.2 % protein concentration) acquired immediately after the application of a 45 V/cm electric field. Initially (t = 0 – 80 s) the fluorescence intensity and lifetime appear largely homogeneous across the square membrane area, and there is no discernible quenching effect that occurs within the first timepoint. This suggests that there is no instantaneous change or undesirable protein damage due to the E-field. In later timepoints, there is a decrease in fluorescence intensity correlated to a shortening of the fluorescence lifetime, a red-to-blue shift in the false colour scale, at the left side of the patterned membrane (closest to the positive electrode). Average intensity profiles (**Figure 7.5b**) drawn across the membrane area show that the fluorescence intensity decreased by ~3-fold at the left side of the membrane by t = 480-560 s as compared to t = 0 – 80 s. Correlated to the decrease in fluorescence intensity, the fluorescence lifetime also appears to decrease from ~4 ns to ~2 ns at the left edge of the membrane at later points in the timelapse (*black* to *red* curves represent increasing timepoints) suggesting fluorescent quenching. However, the low number of counts/pix in timelapse FLIM images of hybrid membranes results in a large uncertainty in the measured intensity and lifetime, indicated by large amounts of noise in profiles in **Figure7.5b**-**c**, and more rigorous analysis was reserved for data with a greater signal to noise ratio.

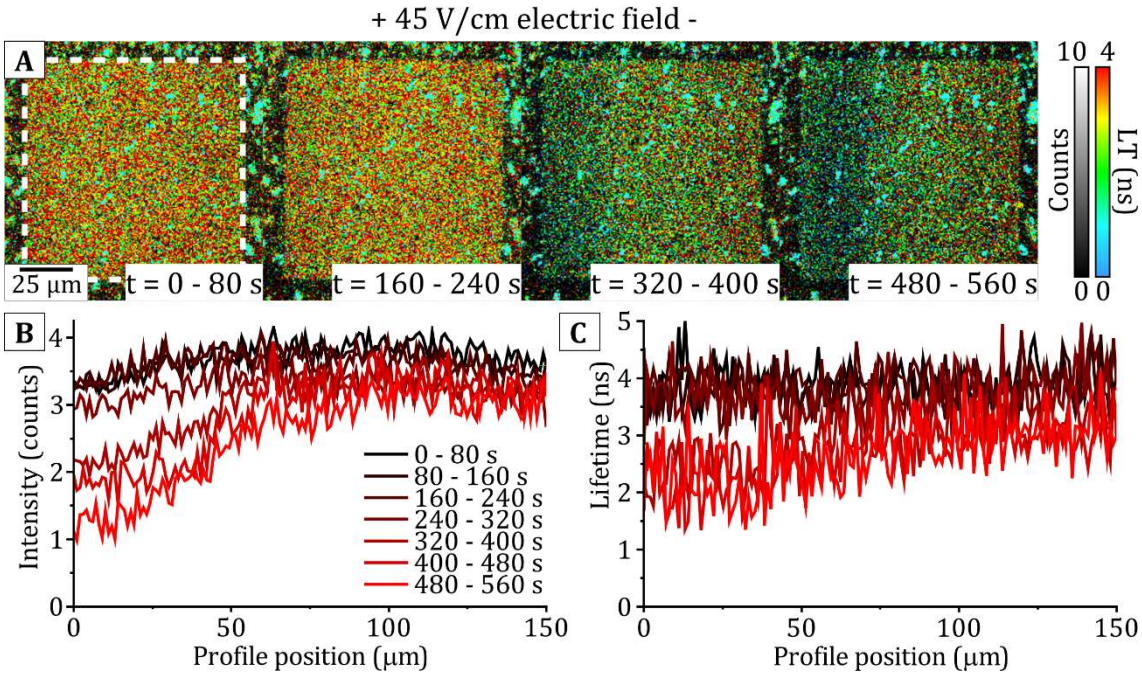

Figure 7.5: Timelapse analysis of in-membrane electrophoresis for a membrane containing ~1.2 % proteins (by area) with intensity and lifetime profiles showing the evolution of the membrane over time. **(A)** Timelapse series of FLIM images showing changes to the intensity and lifetime of Chl fluorescence of hybrid membranes immediately following the application of a 45 V/cm electric field. Each time point represents all photons accumulated in a 25 frame (80 s) period. **(B)** Average intensity profiles obtained from the *white, dashed* rectangle for each timepoint in (a). *Black* to *red* line represent later time points. **(C)** Average fluorescence lifetime profiles obtained from the *white, dashed* rectangle for each timepoint in (a). Colour scheme as in (b).

To better compare the result of electrophoresis for photosynthetic proteins, higher quality average intensity and lifetime profiles were obtained from FLIM images taken before electrophoresis and after the system had been allowed to reach equilibrium the in the E-field. These "steady-state" images did not require the acquisition of many images as for a timelapse series, and therefore each could be acquired for a longer period of time to increase the data quality (100 frames, 320 seconds). **Figure 7.6a** and **b** show representative images for 3:3 Chl:DOPC hybrid membranes (~1.2% protein concentration). The fluorescence intensity prior to electrophoresis (*blue profile*, **Figure 7.6c**) is similar across the entire width of the corral (~19 counts/pix), as would be expected for a homogeneous concentration of fluorophores that are randomly diffusing throughout the membrane.

In contrast, after electrophoresis (*red profile,* **Figure 7.6c**) the fluorescence intensity decreases from ~18 counts/pix at the right hand side of the membrane to ~7 counts at the left edge closest to the cathode. This is surprising when compared to intensity profiles obtained from electrophoresis of lipid-tagged fluorophores (section 6.2.2) where the fluorescence intensity generally increases as fluorophores accumulate at the edge of the membrane. On its own the intensity profile may be interpreted in one of two ways: either (i) the protein concentration has decreased at the left edge of the membrane because proteins are somehow dislodged/stripped from the membrane during electrophoresis, or (ii) the quenching strength of PS proteins is significantly stronger than that of lipid-tagged fluorophores and that, even at low concentrations (~1 %), photosynthetic proteins may quench each other so strongly that increasing the local protein concentration has a net negative effect on the fluorescence intensity.

An increased protein concentration would result in a greater likelihood of protein-protein interactions (which are known to cause fluorescent quenching[39]) and manifest as a decreased fluorescence lifetime and intensity. Therefore, to determine whether the reduced fluorescence intensity was caused by quenching interactions between proteins, the fluorescence intensity was considered in tandem with changes to the fluorescence lifetime that occur during in-membrane electrophoresis. FLIM images of the hybrid membrane during electrophoresis (**Figure 7.6b**) show that the decreased fluorescence intensity is correlated to a shortened fluorescence lifetime, as shown by a *red*-to-*blue* lifetime shift from right-to-left across the membrane. The average lifetime profiles (obtained from the *red dashed* region in **Figure 7.6b**) shows that the Chl fluorescence lifetime decreases from ~4 ns at x = 80 μm to ~1.5 ns at x = 0 μm (*red line*, **Figure 7.6d**), representing a distribution of non-quenched and heavily quenched Chl excited states across the membrane. The author acknowledges that the low number of counts (~ 8 counts/pix) at the left edge of the membrane results in a greater amount of noise in the fluorescent lifetime profile, and the noise in the lifetime profile increases between x = 80 μm to 0 μm. Despite this, the overall trend is clear and the decrease in fluorescent lifetime is strongly correlated to the decrease in fluorescent intensity. Our results suggest that proteins have migrated towards, and accumulated at, the left edge of the corral closest to the positive electrode and undergo significant

fluorescence quenching due to an increased protein concentration. Most significantly, this result represents the first use of in-membrane electrophoresis to control the organisation and function of photosynthetic proteins within a native-like lipid membrane. This proof of concept is the first step towards a full characterisation of quenching between photosynthetic proteins and a comprehensive interrogation of the role of protein concentration in photoprotection processes.

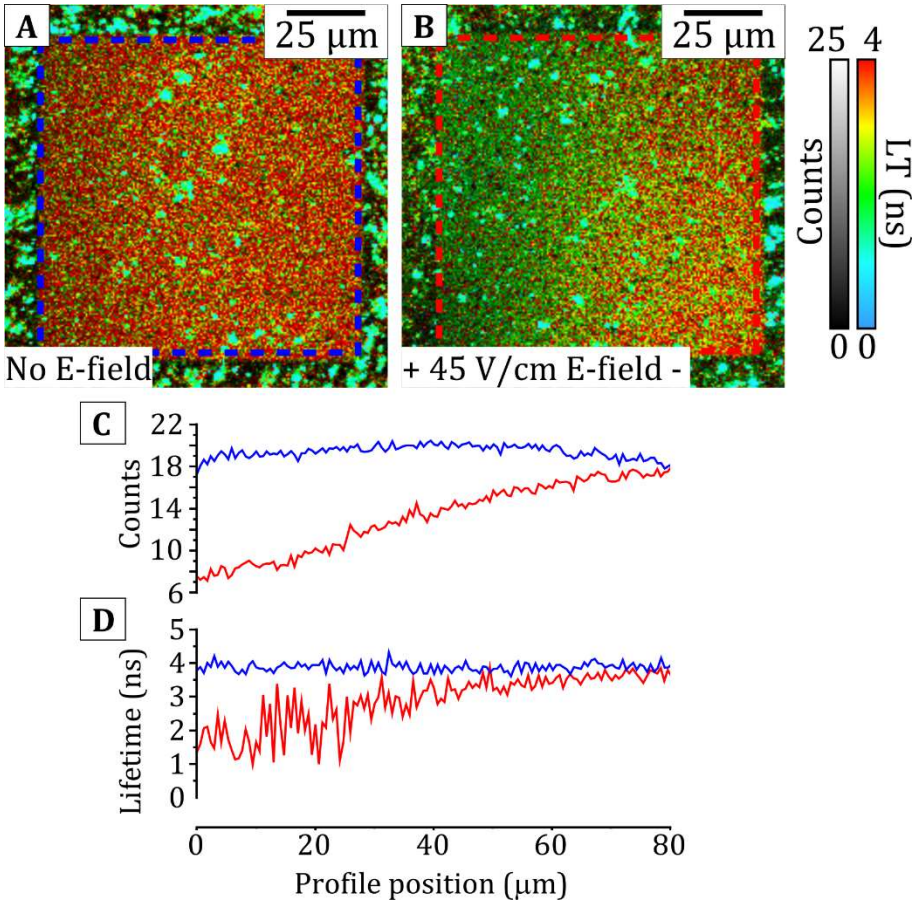

Figure 7.6: FLIM images comparing a hybrid membrane containing ~1.2 % photosynthetic proteins in equilibrium with and without an applied E-field. **(A)** FLIM image of a hybrid membrane prior to electrophoresis (0 V/cm equillibirum). **(B)** FLIM image of hybrid membrane during the application of a 45 V/cm electric field, after the sample had been left for at least an hour to equillibriate. In both (a) and (b) bright *blue* particles are digitally excluded (deselected) from the region of interest when measuring intensity/lifetime profiles. **(C)** Average intensity profiles measured in the *blue, dashed* region in (a) (*blue line*) and the *red, dashed* region in (b) (*red line*). **(D)** Average lifetime profiles measured in the *blue, dashed* region in (a) (*blue line*) and the *red, dashed* region in (b) (*red line*).

7.2.5 Hybrid membranes with a higher initial concentration are quenched more significantly during in-membrane electrophoresis

It is hypothesised that increasing the starting concentration of proteins within the membrane will increase the maximum concentration, and therefore maximum amount of quenching, achieved during in-membrane electrophoresis (as observed in membranes containing lipid-tagged fluorophores in section 6.2.4). Therefore, to describe the quenching behaviour of photosynthetic proteins over a large range of concentrations, in-membrane electrophoresis experiments were performed on hybrid membranes generated from different Chl:DOPC ratios and estimated to have a protein concentration of ~0.5, 1.0 and 1.2 % of overall membrane area (1:3 to 3:3 Chl:DOPC ratio).

Figure 7.7a shows the result of in-membrane electrophoresis on a membrane containing ~0.5 % proteins. Prior to electrophoresis, the fluorescence intensity and lifetime is homogeneous throughout the membrane, as previously described. At the 45 V/cm equilibrium both the fluorescence intensity and lifetime can be seen to be quenched at the left side of the membrane, likely as a result of protein-protein interactions that occur when the proteins accumulate at the edge of the membrane closest to the cathode. This effect is also observed for membranes containing ~1.0 % and ~1.2 % proteins, however, the reduction in fluorescence intensity and lifetime is more significant for membranes with a higher initial protein concentration. For example, the fluorescence lifetimes during electrophoresis are significantly shorter/*bluer* for membranes containing ~1.2 % proteins (**Figure 7.7c**) than for membranes containing ~1.0 % (**Figure 7.7b**) and ~0.5 % proteins (**Figure 7.7a**). Average intensity and lifetime profiles for each membrane are shown in **Figure 7.7d** and **7.7e**, respectively, to highlight this effect more clearly. In particular, the minimum fluorescence lifetime (at x = 0 μm) was found to decrease from ~4 ns to ~2 ns to ~1 ns for membranes containing ~0.5, 1.0 and 1.2 % proteins, respectively, suggesting that greater amounts of quenching are achieved in membranes containing a greater initial concentration of proteins.

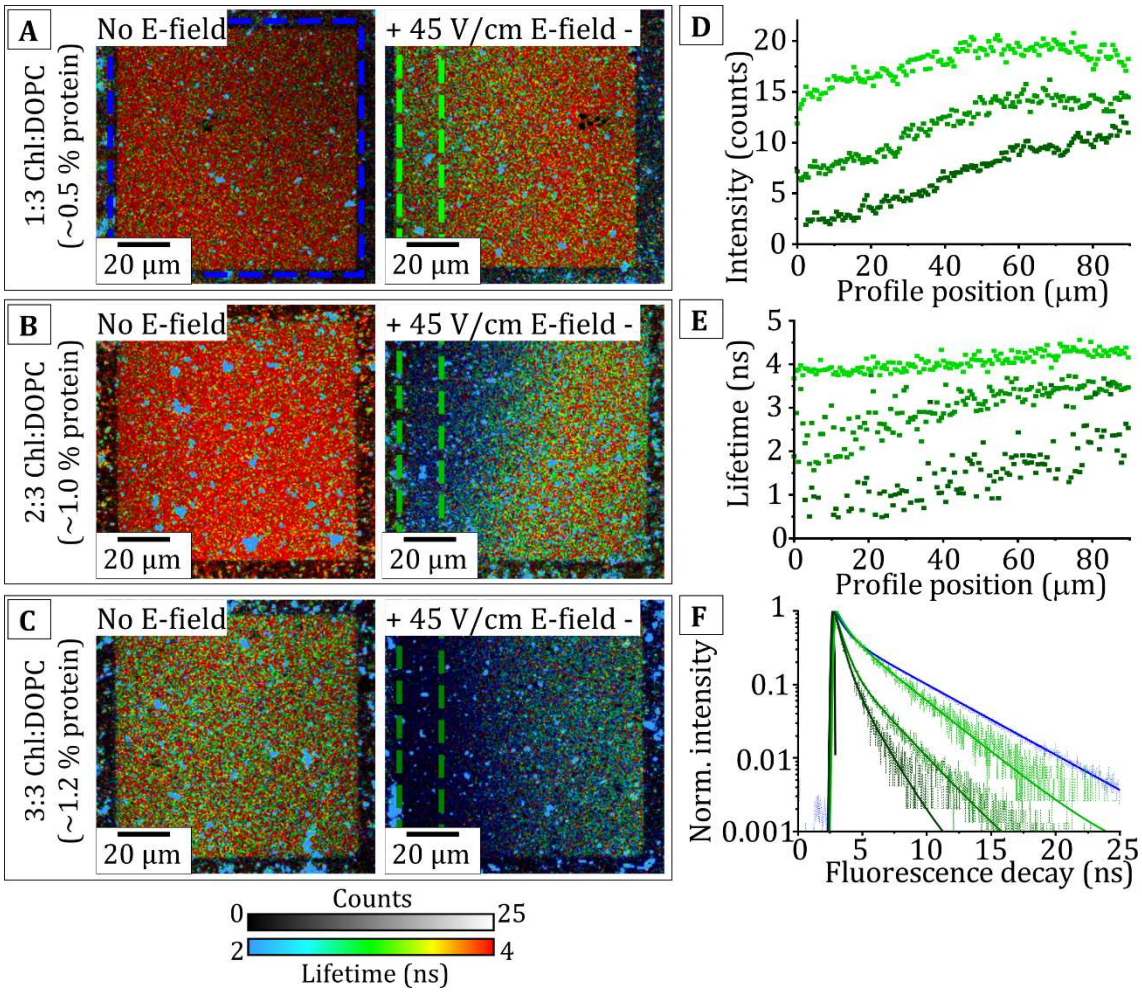

Figure 7.7: FLIM images of hybrid membranes containing ~0.5 %, ~1.0 % and ~1.5 % proteins comparing the amount of quenching that occurs during in-membrane electrophoresis. **(A)** FLIM images of hybrid membranes containing ~0.5% proteins before electrophoresis versus during 45 V/cm equillibirum. **(B)** FLIM images of hybrid membranes containing ~1.0% proteins before electrophoresis versus during 45 V/cm equillibirum. **(C)** FLIM images of hybrid membranes containing ~1.2% proteins before electrophoresis versus during 45 V/cm equillibirum. All FLIM images are on the same intensity and lifetime scale to allow for a qualitative comparison of the amount of quenching. **(D)** Average intensity profiles obtained for hybrid membranes containing an initial concentration of ~0.5 % (*light green*), 1.0 % (*medium green*) and 1.2 % (*dark green*) proteins obtained from the FLIM images during 45 V/cm equillibirum in (a) (b) and (c), respectively. **(E)** Average lifetime profiles obtained for hybrid membranes containing an initial concentration of ~0.5 % (*light green*), 1.0 % (*medium green*) and 1.2 % (*dark green*) proteins obtained from the FLIM images during 45 V/cm equillibirum in (a) (b) and (c), respectively. **(F)** Fluorescence decay curves obtained from accumulating all photons in the *coloured, dashed* regions in (a), (b) and (c). *Dashed lines* show raw fluorescence decay curves, whereas *solid lines* show the result of mono/bi-exponential fits to calculate the amplitude weighted lifetime.

To more accurately quantify the amount of quenching in each scenario, fluorescence decay curves were measured at the edge of each membrane by accumulating all the photons in the *green*, *dashed* regions in **Figure 7.7a, b** and **c. Figure 7.7f** shows the decay curves and fits for membranes containing ~0.5 % (*bright green*), ~1 % (*medium green*) and ~1.2 % (*dark green*) proteins; the fitted fluorescence lifetime at the end of the trap was calculated to be 2.83 ± 0.03 ns, 1.47 ± 0.14 ns and 0.96 ± 0.02 ns, respectively. As before, the maximum quenching efficiency, $QE = 1 - \frac{\tau}{\tau_0}$, was calculated for each type of membrane, where τ_0 = 4ns for LHCII in detergent. Membranes containing ~0.5 % proteins are quenched to a maximum efficiency of 29%, as compared to 63 % and 76 % QE for membranes containing ~1.0 % and ~1.2 % proteins, respectively, showing that it is possible to modulate the quenching effect by changing the starting composition of the hybrid membranes. This has the potential to be a powerful, yet simple, method to interrogate a wide range of quenching behaviours in photosynthetic membranes.

7.2.6 After electrophoresis the fluorescence lifetime is reduced suggesting the formation of aggregates

Finally, we wished to assess the organisation of the membrane following the removal of the electric field, and subsequent relaxation of protein-protein interactions. Monitoring the dissociation of possible protein aggregates (i.e. clusters of several proteins), when all other forces are removed, provides an indirect method to investigate the forces between proteins in a membrane environment and may provide insight to membrane reorganization that occurs within native thylakoids. To monitor the membrane relaxation, a series of FLIM images was obtained of the hybrid membrane immediately after the electric field was switched off. Due to relatively low fluorescence signal, FLIM images were obtained by accumulating 25 frames into a single timepoint. The result is a timelapse series with relatively poor temporal resolution, however it is still sufficient to observe the redistribution of fluorescence intensity throughout the corral. **Figure 7.8a** shows the "relaxation" FLIM timelapse for a hybrid membrane containing ~1.2 % photosynthetic proteins. At the start of the timelapse there is an asymmetrical distribution of fluorescence intensity and lifetime due to the accumulation and self-quenching of photosynthetic proteins at the left edge of the membrane.

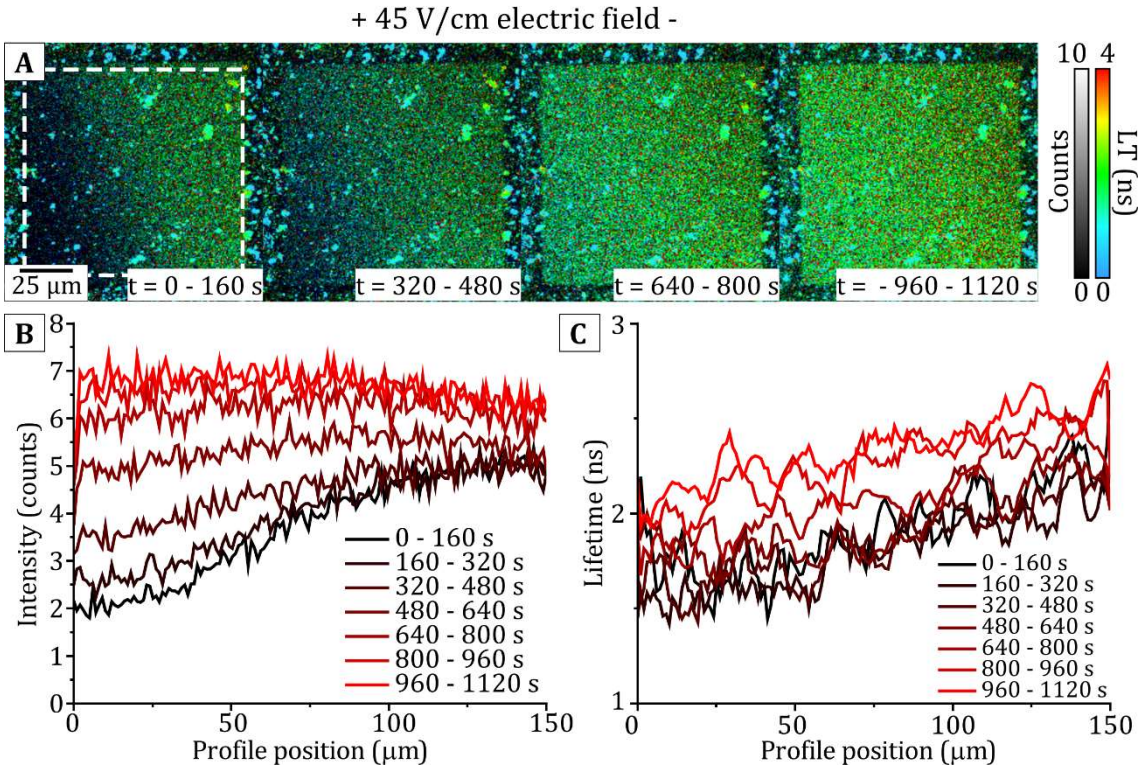

Figure 7.8: Timelapse FLIM series of the relaxation of a hybrid membrane containing 1.2 % proteins after removal of the electric field. **(A)** Timelapse series of FLIM images of the hybrid membrane taken immediately after the electric field is switched off. Each image represents photons accumulated in a 50-frame interval (160 seconds) **(B)** Average intensity profiles obtained from the *dashed* box region in (a) for all time points. *Black* to *red* lines represent later timepoints. **(C)** Average lifetime profiles obtained from the *dashed* box region in (a) for all time points. *Black* to *red* lines represent later timepoints.

The intensity profile at the start of the timelapse (*black line,* **Figure 7.8b**) shows that the number of counts increases from left to right, starting at ~2 counts/pix, and increasing to 5 counts/pix, correlated to an increase in the fluorescence lifetime (*black line*, **Figure 7.8c**) from ~1.5 ns to ~2.25 ns. At later timepoints, the fluorescence intensity can be seen to increase and return to a homogenous intensity, ~7 counts/pix, across the whole membrane at t = 960 - 1120 s (*bright red line*, **Figure 7.8b**). Similarly, the fluorescence lifetime increases at increasing timepoints (*black* to *red* lines represent later timepoints, **Figure 7.8c**) in the acquisition, however, does not return to a homogenous distribution of lifetimes within the duration of the timelapse. It is apparent that the disassociation of proteins is a slow process and that there is some weak attractive force between proteins that maintains quenching interactions for a long time after the electric field is removed.

In addition, the redistribution of fluorescence intensity suggests that that highly concentrated proteins will randomly disperse throughout the membrane (likely through Brownian motion) when there are no external forces to maintain their organisation.

To assess the "final state" of the hybrid membrane after allowing a long period of time for recovery post-electrophoresis, higher quality "steady-state" FLIM measurements were made of hybrid membranes after they had been allowed to return to equilibrium at least 2 hours after turning off the E-field following a standard electrophoresis experiment. The fluorescence signal was maximised by accumulating 100 FLIM frames into a single image (photobleaching was minimised as in section 7.2.1). To assess any changes to the fluorescence distribution or lifetimes, FLIM images obtained from hybrid membranes after electrophoresis were compared to FLIM images obtained from hybrid membranes before and during electrophoresis experiments. These images are shown in **Figure 7.9 a,c,e** for hybrid membranes containing ~0.5 %, ~1.0 % and ~1.2 % proteins respectively. It is observed that, for all three types of hybrid membrane, the Chl fluorescence lifetime is shorter (ie. *bluer* on the false colour scale) when compared to FLIM images acquired before electrophoresis. Fluorescence decay curves were generated from all the photons detected in the *dashed, box* regions in **Figure 7.9a,c,e** and are shown in **Figure 7.9b,d,f**, respectively. For all three concentrations (**Figure 7.9b,d,f**), the fluorescence decay curve prior to electrophoresis (*red data*) has a relatively shallow gradient, representing long fluorescence lifetimes, in contrast to the steep decay curve obtained from the edge of the membrane during electrophoresis (*orange data*) that suggests fluorescence quenching due to protein interactions. A long time after electrophoresis, the fluorescence decay curve (*blue data*) has a moderate gradient, and appears to have partially "recovered" to a midpoint between the other two decay curves. Fitted fluorescence lifetimes were calculated from exponential fits to each decay curve, and the fitted fluorescence lifetimes for all samples are shown in **Table 7.5**. The lifetime during electrophoresis is 77%, 43% and 39% of the lifetime prior to electrophoresis for membranes containing ~0.5% proteins, ~1.0% and 1.2% proteins, respectively. After the electric field is removed, the fluorescence lifetime is then 94%, 75% and 50% of the initial lifetime.

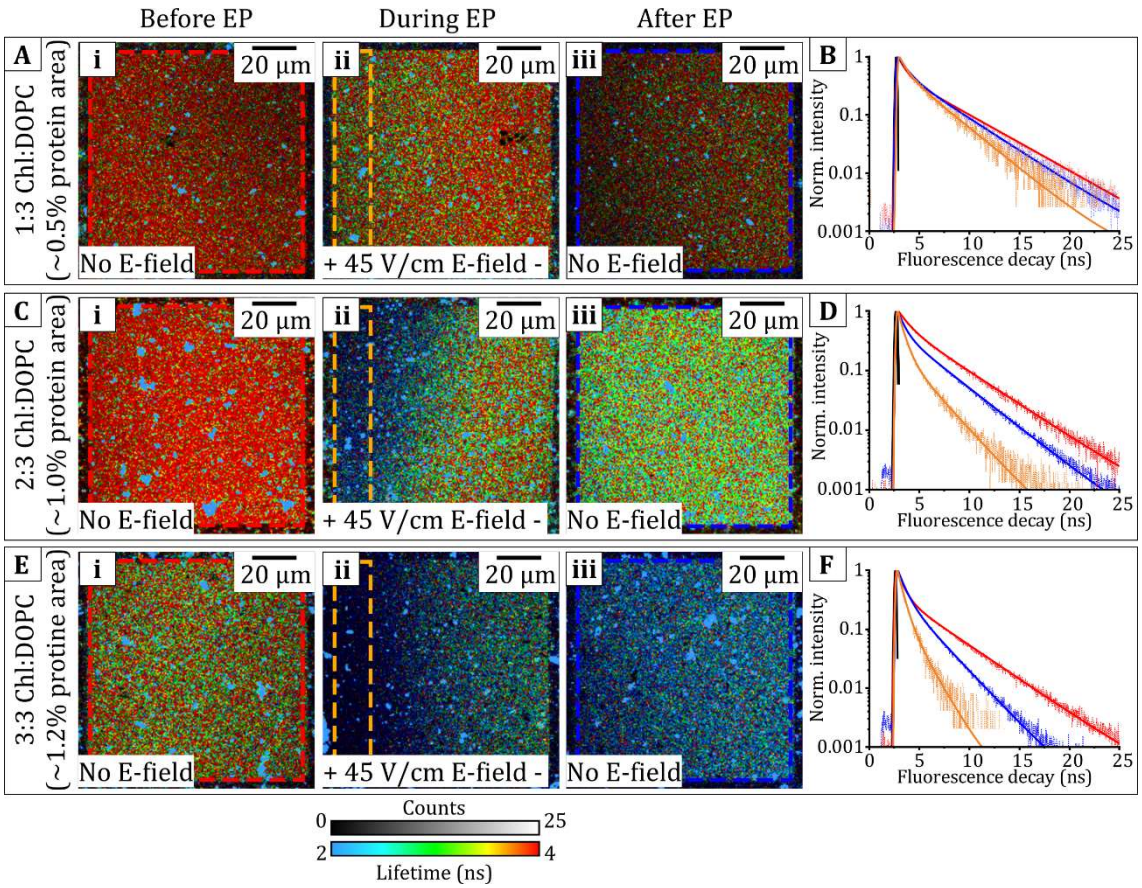

Figure 7.9: Comparison of hybrid membranes either before, during or after electrophoresis. **(A)** FLIM images of hybrid membranes containing ~0.5 % proteins aquired before (*left*), during (*middle*) and after (*right*) electrophoresis. **(B)** Fluorescence decay curves obtained from (a). *Red*: Accumulated from photons in the *red* dashed. *Orange*: Accumulated from photons in the *orange* dashed region. *Blue*: Accumulated from photons in the *blue* dashed region. *Black*: IRF **(C)** FLIM images of hybrid membranes containing ~1.0 % proteins aquired before (*left*), during (*middle*) and after (*right*) electrophoresis. **(D)** Fluorescence decay curves obtained from the *coloured, dashed* regions in (c). Colour scheme as in (b). **(E)** FLIM images of hybrid membranes containing ~1.2 % proteins aquired before (*left*), during (*middle*) and after (*right*) electrophoresis. **(F)** Fluorescence decay curves obtained from the *coloured, dashed* regions in (e). Colour scheme as in (b) and (d).

Membrane concentration (area %)	$\langle\tau_{before}\rangle$	$\langle\tau_{during}\rangle$	$\frac{\langle\tau_{during}\rangle}{\langle\tau_{before}\rangle}$	$\langle\tau_{after}\rangle$	$\frac{\langle\tau_{after}\rangle}{\langle\tau_{before}\rangle}$
~0.5	3.67 ± 0.02	2.83 ± 0.03	0.77	3.44 ± 0.02	0.94
~1.0	3.42 ± 0.01	1.47 ± 0.14	0.43	2.57 ± 0.10	0.75
~1.2	2.46 ± 0.02	0.96 ± 0.02	0.39	1.22 ± 0.08	0.50

Table 7.5: Analysis of fluorescence decay curves from FLIM images before/during/after electrophoresis. From the images shown in **Figure 7.9**. $\langle\tau_{before}\rangle$, $\langle\tau_{during}\rangle$, $\langle\tau_{after}\rangle$ shows fitted lifetimes obtained before, during or after electrophoresis, respectively.

The result show that protein organization within the membrane is altered during electrophoresis with only a partial reversibility, and that hybrid membranes with higher concentration of proteins experience greater quenching during electrophoresis followed by a smaller lifetime recovery once the electric field is removed. It is possible that protein aggregates, that quench the fluorescent lifetime, form when photosynthetic proteins are concentrated by the electric field and then do not entirely disassociate after the electric field has been removed. In addition, it seems likely that the number of aggregates that remain after electrophoresis is proportional to the number of aggregates that form during the electrophoretic concentration of proteins within the membrane (indicated by the greater amount of quenching during electrophoresis and smaller lifetime recovery after electrophoresis of ~1.2 % compared to ~0.5 % hybrid membranes).

Next to estimate the proportion of proteins in either a quenched (possibly aggregated) or non-quenched state in each hybrid membrane and at each stage in the electrophoresis experiment, a bi-exponential curve

$$A(t) = A_1 \exp\left(-\frac{t}{\tau_1}\right) + A_2 \exp\left(-\frac{t}{\tau_2}\right) \qquad \text{Eq. 7.5}$$

was fit to each fluorescence decay curve in **Figure 7.9b,d,f**. The lifetime components were fixed to those previously reported for quenched LHCII aggregates ($\tau_1 \sim 400$ ps) or non-quenched LHCII in detergent ($\tau_2 \sim 4$ ns) and the amplitude of each component, A_i, was optimised to achieve the best fit (a similar approach has been used by multiple researchers[55, 189, 298, 299]). These constrained fits were lower quality than the fits in **Figure 7.9b,d,f**, where both amplitudes and lifetime components were fitted, as shown by the χ^2 values in **Table 7.6**, but may still be used to approximate changes to the proportion of quenched or non-quenched proteins by assessing changes to the amplitude of the fast and slow lifetime components. It was found that for hybrid membranes containing ~0.5 %, ~1 % and ~1.2 % protein, the amplitude of the quenched component was initially 0.15, 0.30 and 0.41, respectively, suggesting that the minority of proteins are quenched but that the proportion of quenched proteins increases with the overall concentration of proteins in the membrane (in support of our lifetime analysis in section 7.2.2). During electrophoresis, the amplitude of the quenched component increases significantly to 0.54, 0.68 and 0.83 for ~0.5 %, ~1 % and ~1.2 % membranes, respectively. These

results imply that a large proportion of proteins switch from a light-harvesting to a photoprotective state during electrophoresis experiments and that in membranes with a higher overall protein concentration the proportion of quenched proteins is greater. Interestingly, the increase in relative increase in the quenched amplitude during electrophoresis is greater for ~0.5 % membranes (3.6× increase) than for ~1.2 % membranes (2.0× increase). This can be explained by considering that there is a larger proportion of proteins available to become quenched in low concentration membranes, compared to proteins in high concentration membranes that are more likely to be in a quenched state before electrophoresis. After electrophoresis, the amplitude of the ~400 ps component decreases to 0.24, 0.45 and 0.62 for ~0.5 %, ~1.0 % and ~1.2 % membranes, respectively, corresponding to an overall increase of 0.09, 0.15 and 0.21 when compared to the amplitude of the quenched component before electrophoresis. Overall, these results suggest that after electrophoresis a portion of the proteins return to a non-quenched and non-aggregated state (also shown by a correlated increase in the amplitude of the ~ 4 ns component). It also seems likely that the proportional of proteins that remain in a quenched state after electrophoresis is proportional to the overall concentration of proteins within the membrane.

Timing	Membrane concentration (area %)	τ_1	A_1	τ_2	A_2	τ_{avg}	chi^2
Before	~0.5	0.4	0.15 ± 0.04	4.0	0.85 ± 0.05	3.46 ± 0.08	1.61
	~1.0	0.4	0.30 ± 0.01	4.0	0.70 ± 0.06	2.92 ± 0.21	1.46
	~1.2	0.4	0.41 ± 0.01	4.0	0.59 ± 0.01	2.52 ± 0.05	1.55
During	~0.5	0.4	0.54 ± 0.04	4.0	0.46 ± 0.04	2.06 ± 0.16	1.75
	~1.0	0.4	0.68 ± 0.05	4.0	0.32 ± 0.05	1.55 ± 0.22	1.46
	~1.2	0.4	0.83 ± 0.01	4.0	0.17 ± 0.01	1.01 ± 0.04	1.75
After	~0.5	0.4	0.24 ± 0.03	4.0	0.76 ± 0.03	3.14 ± 0.13	1.35
	~1.0	0.4	0.45 ± 0.01	4.0	0.55 ± 0.01	2.38 ± 0.02	1.47
	~1.2	0.4	0.62 ± 0.04	4.0	0.38 ± 0.04	1.77 ± 0.11	1.54

Table 7.6: Analysis of fluorescence decay curves from FLIM images before/during/after electrophoresis to obtain the relative amplitudes of quenched or non-quenched lifetime components. τ_1 and τ_2 are fixed lifetime components corresponding to quenched or non-quenched LHCII, respectively. $A_1$and A_2 are the component amplitudes obtained by fitting a bi-exponential decay function to the fluorescence decay curves shown in **Figure 7.9b,d,f**.

7.2.7 FRAP measurements show that protein diffusion is also reduced after electrophoresis experiments

To investigate the possibility of long-lived protein aggregates, FRAP measurements were performed on hybrid membranes before versus after electrophoresis to determine any changes in the mobility of fluorescent proteins in the membrane. In general, the mobility of any particle is inversely proportional to its hydrodynamic radius[297], therefore the rate of fluorescence recovery will be reduced for nanoscale protein aggregates relative to protein trimers (scaling with the effective radius of the protein cluster). **Figure 7.10** shows the result of a FRAP experiments performed on hybrid membranes containing ~1.2 % proteins before and after electrophoresis. The mobile fraction of proteins within the membrane was calculated by analytically comparing FLIM images taken before versus after photobleaching, and it was determined that the majority of proteins are mobile within the membrane both before (79.5 ± 8.3%, **Figure 7.10a**) and after (73.3 ± 5.7%, **Figure 7.10b**) electrophoresis measurements (mean ± standard deviation, N = 3 measurements). FLIM timelapse measurements taken immediately after photobleaching the *white, circular* areas in **Figure 7.10c** and **d** were used to determine the rate of fluorescence recovery for hybrid membranes both before and after electrophoresis. Qualitatively it can be observed from images that the intensity of the bleached area recovers at a faster rate for FRAP experiments performed before electrophoresis (**Figure 7.10c**) compared to after electrophoresis (**Figure 7.10d**). To quantitatively compare the protein diffusivity, the intensity of the bleached region was plotted over time (**Figure 7.10e**), from which the diffusion constant was calculated (**Table 7.7**). For the corral shown, which is expected to contain ~1.2 % protein, the diffusion constant prior to electrophoresis was determined to be 0.97 ± 0.09 $\mu m^2/s$ and reduced significantly (by ~55%) after electrophoresis to 0.44 ± 0.08 $\mu m^2/s$. Similar experiments performed for hybrid membranes containing ~1.0 % proteins and ~0.5 % proteins showed that the diffusion constant decreased by 22 % and 3 % respectively. Since the diffusion constant is inversely proportional to the hydrodynamic radius of a diffusing particle, the reduced diffusivity of proteins supports our hypothesis for the formation of stable protein aggregates during electrophoresis and that these aggregates occur much more readily when the starting protein concentration is higher.

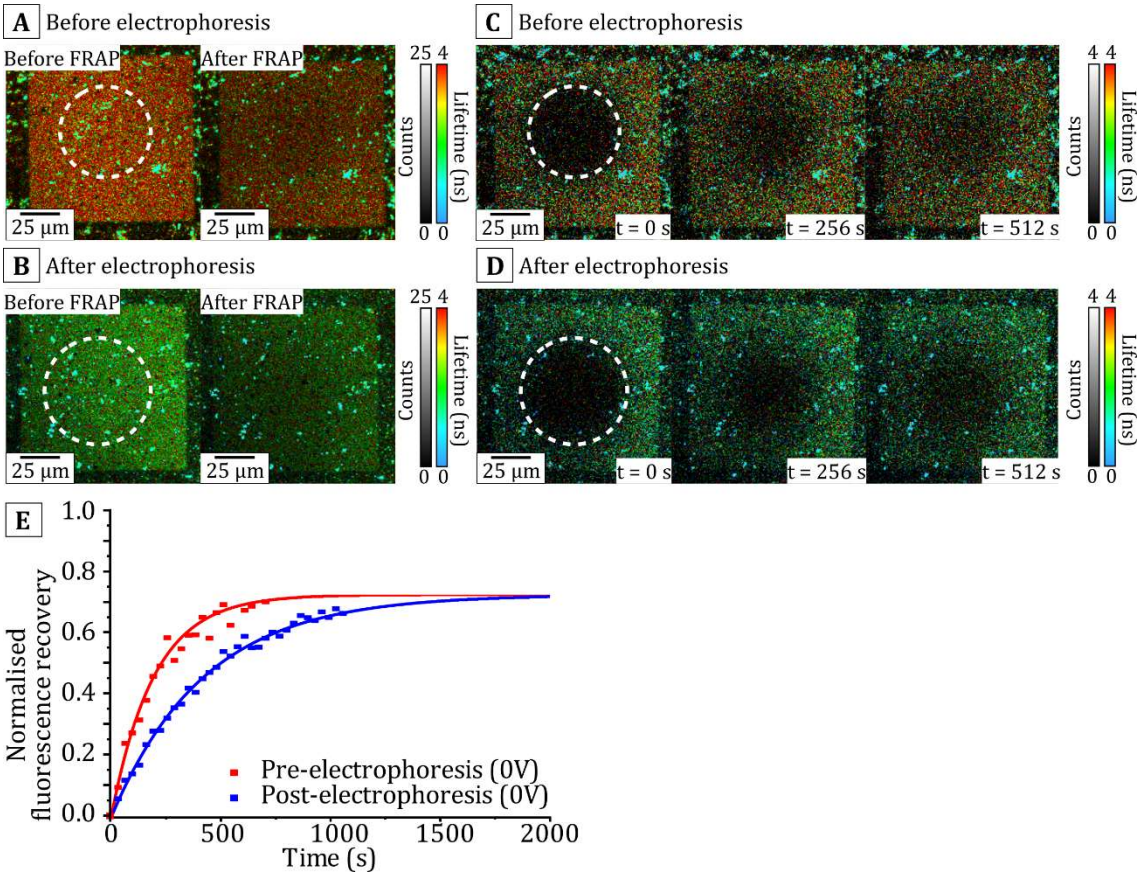

Figure 7.10: Comparison of FRAP measurements for hybrid membranes containing ~1.2% of proteins taken before electrophoresis versus after electrophoresis. FRAP methodology as described in Section 7.2.3. Before versus after (t = 15 min) FLIM images from a FRAP experiment performed on a hybrid membrane containing ~1.2 % proteins **(A)** before and **(B)** electrophoresis. FRAP experiment performed on a hybrid membrane containing ~1.2 % proteins **(C)** before and **(D)** after electrophoresis. The *white, circular* region is deliberately photobleached, and the fluorescence recovery is monitor over a timelapse series of FLIM images. **(E)** Fluorescence recovery curves obtained by monitoring the intensity in the *white, circular* regions of (c) (*red*) and (d) (*blue*). The *solid* lines are mono-exponential fits, $F = F_0(1-e^{-kt})$, used to calculate the diffusion constant for each data set.

	Before electrophoresis		**After electrophoresis**		
Membrane concentration (%)	Doubling time (s)	Diffusion constant (µm²/s)	Doubling time (s)	Diffusion constant (µm²/s)	ΔD (% diff)
~0.5	97 ± 10	1.56 ± 0.25	101 ± 7	1.51 ± 0.18	3.2 ± 2.4
~1.0	126 ± 15	1.03 ± 0.12	161 ± 4	0.80 ± 0.04	22.3 ± 1.0
~1.2	135 ± 6	0.97 ± 0.09	294 ± 3	0.44 ± 0.08	54.6 ± 0.9

Table 7.7: Summary of FRAP experiments performed on hybrid membranes either before or after electrophoresis measurements. *ΔD* is the percentage difference in the calculated diffusion constant after versus before electrophoresis.

Overall, these results and those in Section 7.2.6 imply that both large- and small-scale protein clusters form when the protein concentration is increased via electrophoresis and that some of the smaller (nanoscale) protein clusters remain at least partially intact when external (Lorentz) forces are removed. Hybrid membranes containing a higher concentration of proteins become more heavily quenched during electrophoresis as indicated by their much lower fluorescence lifetimes and also experience a greater reduction in the protein mobility which does not recover after the E-field is removed (so the fluorescence lifetime remains lower too). Therefore, it is reasonable to assume that a higher degree of protein aggregation during electrophoresis results in larger numbers and/or larger sizes of stable aggregates once the electric field is removed. Our results suggest that there may be a short-range attractive force between photosynthetic proteins that maintains protein-protein interactions, but does not cause proteins to form aggregates across large distances (greater than a few nm). In addition, our results show that concentration quenching between photosynthetic proteins in lipid bilayers is a reversible effect and that Chl fluorescence is restored when protein interactions/aggregates are disassociated. This may be considered a similar effect to the reversible reorganisation of proteins or supercomplexes that occurs in natural thylakoid membranes[40] and could suggest that the ability of proteins to quench and subsequently "un-quench" may play a vital role in photoprotective NPQ.

7.3 Quenching as a function of protein concentration for photosynthetic membranes

7.3.1 Development of quenching relationships for photosynthetic proteins in hybrid membranes

To understanding the quenching behaviour of photosynthetic proteins in hybrid membranes it would be useful to quantify the concentration-dependence. Therefore, as for the analysis of lipid-only systems analysed in Chapter 6, concentration versus "quenching efficiency" curves were generated from FLIM images obtained during electrophoresis. A short Python (v3.8) program was written to increase the throughput of image analysis, as described below.

First, the script separates each FLIM image into an intensity-only image and a lifetime-only image which are both cropped such that only the corral box region (and not the template region) is selected for analysis. An example FLIM image of a hybrid membrane containing ~1.2 % proteins during electrophoresis (45 V/cm equilibrium) is shown in **Figure 7.11a**, alongside the intensity-only matrix (**Figure 7.11b**) and lifetime-only matrix (**Figure 7.11c**). Next, an intensity threshold (>50 counts) is applied to the intensity-only matrix to exclude bright objects that represent multi-layered thylakoid membranes that are loosely adsorbed to the hybrid membrane (pixels above this threshold are highlighted in *red* in **Figure 7.11b** and *black* in **Figure 7.11c**). These pixels are excluded from all later stages in the analysis to prevent these bright objects from skewing measurements of intensity or lifetime. Next, average lifetime profiles (**Figure 7.11d**) and average intensity profiles (*red data*, **Figure 7.11e**) are obtained by calculating the mean of each vertical column of pixels (N ≥150 pixels), and plotting this average against the horizontal position. Due to the low number of counts there is typically significant fluctuation in the fluorescence lifetime profile (there is a discernible trend in the data and uncertainty across the entire data set will be reduced by analysis of many FLIM images).

In order to estimate the important property of protein concentration at each location, the non-quenched fluorescence intensity must be calculated using the intensity and lifetime at each location. Several other research groups report that an intrinsic property of LHCII is that the reduction in fluorescence emission is proportional to the reduction in the fluorescence lifetime, $\frac{F}{F_0} = \frac{\tau}{\tau_0}$, where τ_0 is the lifetime of LHCII in detergent[298-300]. This relationship was used to generate a non-quenched intensity profile, shown in *black* in **Figure 7.11e**. Next, to calculate the concentration of proteins at each location, non-quenched intensity was divided by the known intensity of an LHCII trimer (calculated to be 0.0067 counts/trimer/frame in **Table 7.2**) to estimate the number of trimers at each location and the estimated trimer density, C_N, in trimers/μm^2.

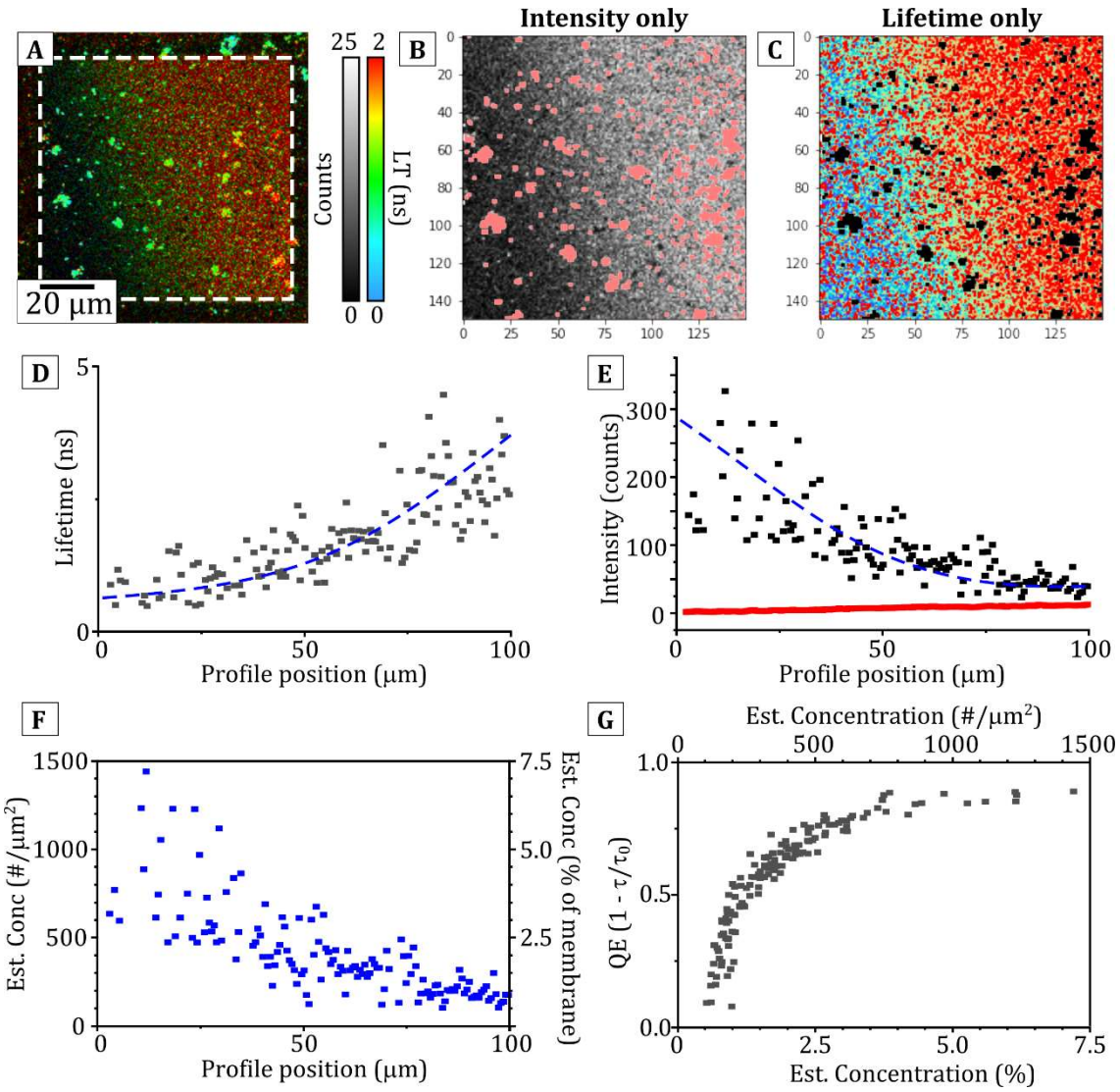

Figure 7.11: Results of the analysis of FLIM images to obtain quenching efficients vs concetration curves. **(A)** A FLIM image of a hybrid membrane containing ~1.2 % protiens during in-membrane electrophoresis. **(B)** An intensity-only image from the FLIM image in (a). *Red* pixels show those that are excluded from analysis using an intensity threshold. **(C)** A lifetime-only image from the FLIM image in (a). *Black* pixels show those that are excluded from analysis using an intensity threshold. **(D)** The average lifetime profile obtained from (c) showing the average fluorescence lifetime (N > 150 pixels) against the horizontal position in the membrane. **(E)** *Red:* the average intensity profile obtained from (b) showing the average measured intensity (N > 150 pixels) against the horizontal position in the membrane. *Black*: The non-quenched intensity profile, calculated as described in text. *Dashed, blue* lines to guide the eye. **(F)** The estimated protein concentration calculated using the non-quenched intensity for each position horizontal profile. **(G)** The final quenching efficiency versus concentration curve obtained for the FLIM image in (a).

The estimated protein concentration increases from right-to-left from ~1 % of the membrane area (200 trimers/μm^2) to ~5 % (1000 trimers/μm^2). The increase in protein concentration due to electrophoresis (~5-fold) is similar in magnitude to the increase observed for lipid-tagged fluorophores (~7-fold) in section 6.3.3. It is reassuring that the same size of hybrid membranes (100 μm^2) produces similar results for different types of fluorophores and gives us additional confidence in the estimated protein concentration. Finally, the quenching efficiency, $QE = 1 - \tau/\tau_0$, is plotted against the spatially-correlated concentration at each location to produce a characteristic quenching curve for photosynthetic proteins in hybrid membranes (**Figure 7.11g**). For the example FLIM image shown, it can be see that QE initially increases very steeply at low concentrations of proteins (<2.5 % membrane area) before beginning to plateau and approach unity at concentrations greater than ~4 %. To improve the accuracy of the quenching relationship and to reduce the effect of random noise/fluctuations, this method of analysis was repeated on multiple FLIM images (N > 4) and for hybrid membranes containing different concentrations of proteins (~0.5 %, ~1.0 % and ~1.2 % proteins). In the final sections of this thesis, the quenching curves obtained from all FLIM measurements of hybrid membrane electrophoresis are presented and discuss the implications of these relationships with regard to NPQ in native membranes.

7.3.2 Further analysis of quenching relationships for photosynthetic proteins

To quantify the quenching behaviour of photosynthetic proteins over a continuous range of concentrations, the analysis in section 7.3.1 was repeated for FLIM images of hybrid membranes containing ~0.5 %, ~1.0 % and ~1.2 % photosynthetic proteins in which proteins had been concentrated using in-membrane electrophoresis. Again, we make the simplification that all Chl-containing proteins that are present may be represented by the dimensions of an LHCII trimer. The resulting QE vs C curve for all samples is shown in **Figure 7.12a**, where data obtained from membranes containing ~0.5 %, ~1.0 % and ~1.2 % proteins is shown in *light green*, *medium green*, and *dark green*, respectively. Quenching curves obtained from different types of hybrid membranes were found to be highly reproducible with significant overlap between different data sets.

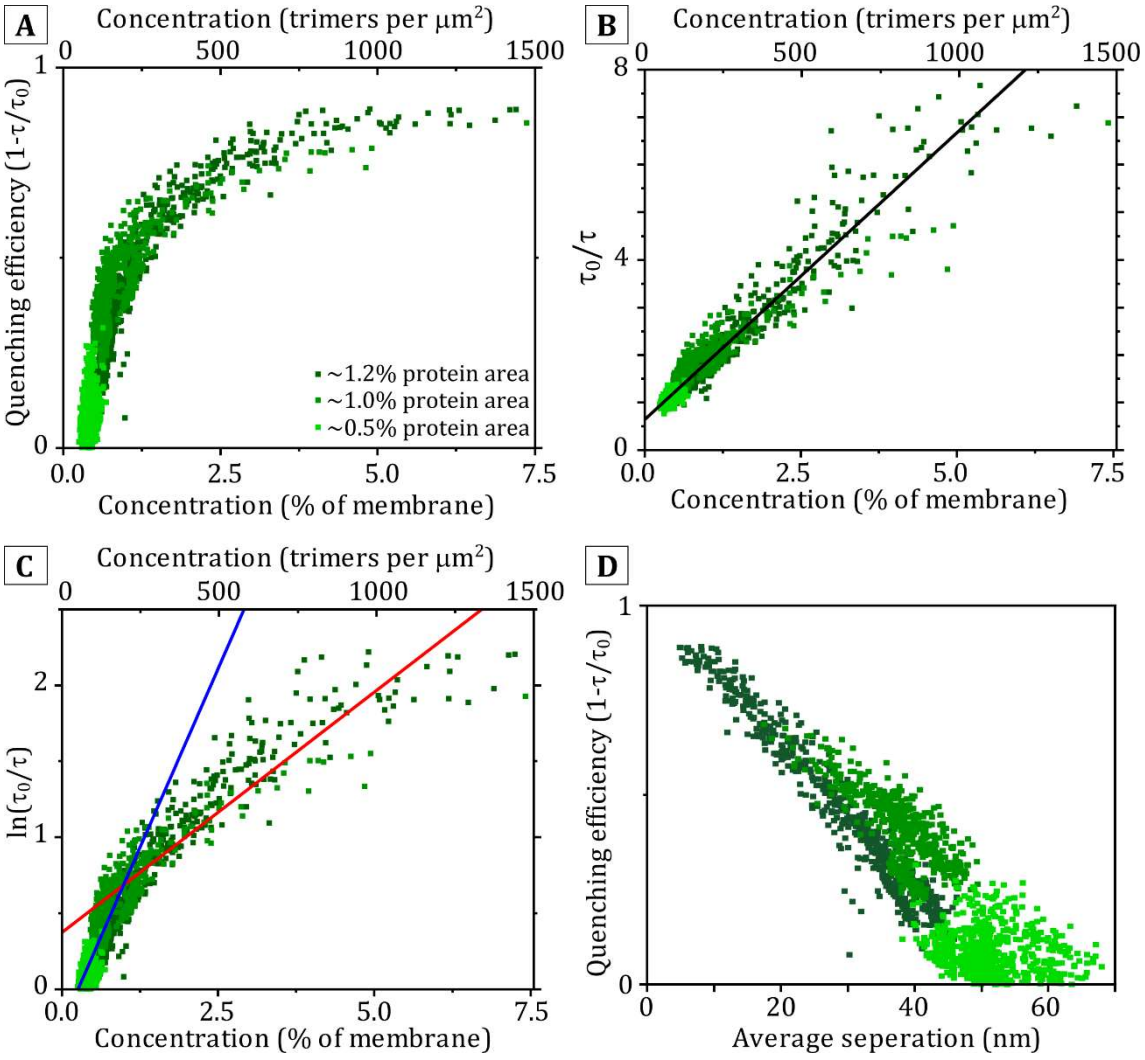

Figure 7.12: Multiple plots to show the relationship between protein concentration, or average separation, and the amount of quenching for photosynthetic proteins in hybrid membranes. **(A)** Quenching efficiency versus concentration curve obtained from multiple FLIM measurements (N = 16) of hybrid membranes during electrophoresis. Data obtained from hybrid membranes containing ~0.5 %, ~1.0 % and ~1.2 % is shown in *light green*, *medium green* and *dark green*, respectively. **(B)** The same data as in (a) but plotted as the inverse relative lifetime versus concentration. The linear fit (*red*, *solid line*) shows that the amount of quenching is proportional to the protein concentration. **(C)** The same data as in (a) plotted as the semilogarithmic inverse lifetime vs concentration. Linear fits (*solid line*) are used to obtain the critical radius for quenching for both a low concentration (<1%) and high concentration regime. **(D)** The same data as in (a) plotted as quenching efficiency versus average fluorophore separation.

There is a wider distribution of data points within the quenching curve when compared to QE curves obtained for lipid-tagged fluorophores (section 6.3.4) which is attributed to a lower signal to noise ratio in FLIM images of hybrid membranes and a greater uncertainty in lifetime measurements. Despite this, the overall trend in the data is clear and it can be seen that the quenching efficiency of the thylakoid proteins (likely to be mixtures of LHCII, PSII, PSI and LHCI) increases very steeply at low concentrations (~2.5 %) before tending asymptotically towards unity at higher concentrations (~5% of the membrane). At first glance, the shape of the QE vs concentration curve is similar to those produced for lipid-tagged fluorophores but with a much steeper gradient and a greater QE for all concentrations, showing that the quenching strength of PS proteins is significantly greater than that of the lipid-tagged fluorophores investigated in Chapter 6.

As discussed in section 6.3.3, Stern-Volmer relationships be used to determine the "molecularity" (ie. number of molecules involved) of trap formation by plotting the inverse relative intensity (F_0/F) against the concentration of quenchers (traps), Q:

$$\frac{F_0}{F} = 1 + k_{SV}Q \qquad \text{Eq. 6.14}$$

where k_{SV} is the Stern-volmer constant that descibes the relative change in quenching with Q (i.e., the strength of the traps). If Q is proportional to the concentration of LHCII-equivalents, C, this implies that only one trimer is requried to form a trap. Likewise, if Q is proportional to the concentration of pairs of trimers, C^2, then it is implies that the mechanism of trap formation involves two molecules (and so forth).

To determine the molecularity of trap formation and to be able to discuss potential quenching mechanisms, a Stern-Volmer plot (using τ_0/τ, rather than intesnity, versus concentration) was generated (**Figure 7.12b**) using data from the QE versus concentration curve. It is found that the relative lifetime, τ_0/τ, is proportional to the concentration of LHCII-equivalents, C, within the membrane. This is in contrast to the Stern-volmer plots observed for Bodipy, Texas Red and NBD, in which τ_0/τ is proportional to C^2. This result is particularly interesting, since it suggests that the number of traps is proportional to the number of trimers, rather than a single trap or dissipative state forming as a result of interactions between two, or more, trimers

(e.g. non-fluorescence dimers that quench fluorescence in lipid-tagged fluorophores). Our results imply that the trap state occurs within individual protein complexes rather than being than formed due to some excitonic interaction between multiple LH or photosystem complexes. One possibility is that traps form, or are stabilised, within LHCII trimers as a result of protein aggregation or other protein-protein interactions, and that the number of traps within a cluster of connected proteins is proportional to the number of proteins within that cluster. It may also be possible that the quenching occuring in LHCII aggregates is merely the result of an increased connectivity and a higher likelihood of exciton migration to short-lived, intermittent traps (fluorescence intermittency has been observed in individual trimers[68, 69]). A similar system has already been modelled by Valkunas and co-workers, in which excitons may migrate through a PSII/LHCII supercomplex and a single trap was sufficient to cause the quenching.[301] Likewise, another study by Belgio et al. indicates that the quenching mechanism may be associated with an overall increase in the connectivity of multiple antennas.[302]

Next, to compare the strength of quenching for photosynthetic membranes to the strength of quenching for lipid-tagged monochromatic fluorophores, semilogarithmic plots were plotted to show the relationship between $\ln(\tau_0/\tau)$ and concentration. As before, the gradient extracted from fitting this graph was used to calculate the critical radius and estimate the relative quenching strength. It was found that the relationship between $\ln(\tau_0/\tau)$ and concentration is non-linear, in contrast to similar plots for lipid-tagged fluorophores, and suggests that the quenching mechanism of photosynthetic proteins follows a different mechanism (i.e.. is not due to the formation of non-fluorescent statistical pairs). Instead, it appears that the semilogarithmic plot follows two distinct regimes: (i) at low concentrations (<1%), $\ln(\tau_0/\tau)$ increases sharply with concencetration and has a large gradient (ii) at moderate to high concentrations (>1%), the gradient of $\ln(\tau_0/\tau)$ is shallower, and the quenching stregnth is weaker. The relative quenching stregnth of each regime was estimated by fitting a linear gradient to (i) and (ii), shown by *blue* and *red* lines, respectively. The critical radius of quenching was found to be R_i = 38.7 ± 0.1 nm for low concentrations of proteins (<1%), and R_{ii} = 22.2 ± 0.1 nm for moderate-high concentrations of proteins (>1%). This result suggests that quenching between photosynthetic proteins may be 10-15 times stronger than

quenching between lipid-tagged monochromatic fluorophores (R_{BOD} = 2.5 nm, R_{TR} = 1.6 nm, R_{NBD} = 1.1 nm) and that interactions that lead to quenching may occur over distances much larger than the effective radius of the protein trimer ($R_{LHCII} \sim 4$ nm). It is possible there may be an attractive force between proteins that occurs over several nanometres and leads to protein aggregation/quenching when two or more proteins are separated by a distance less than R_i. The biphasic behaviour of photosynthetic quenching, in which the quenching effect is stronger for low concentrations (<1%) than for high concentrations (>1%), is more challenging to interpret. This "turning point" may represent a critical concentration of protein aggregation at which proteins associate into large aggregates and the quenching effect of each additional protein is reduced. Further structural characterisation (e.g. AFM topography) is required to test this hypothesis, however, optimisation of AFM measurements during electrophoresis was not possible within the timescale of this project.

Finally, to describe photosynthetic quenching in terms of the average distance between trimers, the average separation, r, for each data point was calculated using the following equation (already described in chapter 6):

$$\text{Effective area per molecule} = \frac{1}{C_N} = \pi r^2 \qquad \text{Eq. 6.3}$$

where C_N is the number of LHCII-equivalents per μm^2. Assuming proteins with interact via peripheral chlorophyll pigments, the average separation was then converted to an edge-to-edge distance by subtracting the radius of each LHCII trimer (~4 nm). The result is the QE versus edge-to-edge separation graph shown in **Figure 7.12d**. It is observed that quenching occurs at even large separations (e.g. QE = 0.5 at edge-to-edge separations of ~20 nm) and increases up to 0.9 at an average separation of ~5 nm. It seems extremely unlikely that exciton energy migration and quenching would occur over distances larger than a few nanometres. Instead, it may be possible that the distribution of proteins at a high concentration in the membrane is non-uniform and that the average edge-to-edge distance may actually represent a mixture of protein aggregates and large areas of lipid-only membrane. Indeed, multiple authors have suggested that photosynthetic proteins in lipid bilayers preferentially partition into semi-crystalline domains[79, 120, 124]. Once again,

structural measurements from microscopy (e.g., AFM) or other techniques would allow this hypothesis to be tested.

Overall, the result of this analysis suggests the following conclusions: (i) there is a weak attractive force between photosynthetic proteins in lipid membranes, that maintains protein-protein interactions in the absence of the applied electric field (section 7.2.6) and may contribute to the quenching behaviour of proteins by encouraging aggregation over short-to-moderate average distances (tens of nanometres) (**Figure 7.12d**), (ii) fluorescent traps appear to occur within individual LH/PS protein complexes, rather than traps which require multiple complexes to come together (**Figure 7.12b**; not a "higher-order" relationship with concentration), (iii) the quenching efficiency begins to saturate at relatively low concentrations (when only ~5% of the membrane is occupied by proteins), and increasing the concentration beyond this point may have a limited effect on the fluorescence lifetime and energy dissipation (**Figure 7.12a**). There are still many unknowns surrounding the roles of specific proteins and components in NPQ, however this study represents the first comprehensive characterisation of the quenching behaviour of photosynthetic proteins across a continuum of concentrations and within a native-like lipid environment, and the first use of in-membrane electrophoresis to moderate and interrogate the function of light-harvesting proteins.

7.4 Section summary and discussion

This chapter describes the use of in-membrane electrophoresis correlated with fluorescence lifetime measurements to investigate concentration quenching effects of photosynthetic proteins. 2D-micro-patterned hybrid membranes were assembled from a mixture of thylakoid extracts and synthetic lipids, and increasing the ratio of Chl to DOPC lipids was found to increase the concentration of photosynthetic proteins that incorporated into the membrane (estimated range from 0.5 – 1.2 % of the total membrane area). FRAP measurements confirmed that proteins in all hybrid membranes consisted of a majority of mobile proteins (~80 % mobile fraction) and that the diffusion constant of membranes with a higher concentration of proteins was slightly reduced, suggesting the formation of

nanoscale protein aggregates. Applying a 45 V/cm direct electric field to the membrane was found to result in a reduction in fluorescence intensity and lifetime at the edge of the membrane closest to the positive cathode, suggesting fluorescence quenching and the formation of protein-protein interactions as the protein concentration is increased. In addition, in-membrane electrophoresis of hybrid membranes containing a higher concentration of proteins was found to result in a higher degree of quenching (up to 76%), likely due to a higher maximum protein concentration accumulating at the edge of the confined membrane. Altogether, this demonstrates that it is possible to control the movement of photosynthetic proteins using electric fields and that the outcomes of in-membrane electrophoresis can be modulated through simple changes to the starting membrane composition.

A careful manual analysis of FLIM images of hybrid membranes during electrophoresis was used to determine the quenching efficiency (QE) of photosynthetic proteins correlated to their concentration. It was found that QE increases rapidly with protein concentration, before asymptotically tending towards unity for concentrations greater than ~5% of the membrane area. It seems likely that photosynthetic proteins may form aggregates within the membrane rather than being uniformly distributed, resulting in a heterogeneous distribution of proteins aggregates and areas of lipid-only membrane. One could speculate that attractive interactions could lead to a positive feedback loop that enriches such a sub-population leading to an accumulation of LH proteins. Indeed, following the removal of the electric field a portion of the densely-packed proteins appear to disassociate into smaller aggregates (indicated by the maintenance of quenched fluorescence and lower fluorescence mobility). This suggests the presence of short-range attractive forces between proteins that maintain some degree of nanoscale protein aggregates in the absence of other forces and may induce further protein aggregation at moderate/high concentrations (>1%). These aggregates must be both two-dimensional and nanoscale because no new microscale features are visible within the membrane. This is in contrast to some previous studies in which ill-defined and 3-D aggregates of LHCII are generated by the removal of detergent from purified proteins[40, 55, 189].

Our group has previously made direct measurements of the structural organisation and average fluorescence lifetimes of LHCII trimers,[56] where it was observed that in tightly-packed LHCII aggregates (average centre-to-centre separation of ~10 nm) the quenching efficiency was ~81 %. However, in our in-membrane electrophoresis study it is found that QE approaches unity at much larger average separations (QE ~ 80% at an average centre-to-centre separation of ~25 nm). This discrepancy may be due to the comparison between relatively homogeneous protein aggregates that appear to assemble on mica,[56] as compared to an unknown nanoscale organisation of proteins within a lipid membrane (here). It is possible that the concentrated hybrid membranes described in this chapter may contain a mixture of sizes of protein aggregates together with non-interacting proteins, which results in a mixture of highly quenched states and unquenched states, respectively. It is also possible to compare our data on fluorescence quenching caused by electrophoresis-induced protein clusters with previous studies of fluorescence quenching in proteoliposomes. Multiple authors have reconstituted purified LHCII into proteoliposomes, where it has been shown that at sufficiently low lipid-to-protein ratios LHCII spontaneously clusters to form aggregates, potentially appearing as phase-separated domains within the membrane, which results in reduction in the fluorescence lifetime[79].

A side-by-side comparison of our results to multiple previous datasets is shown in **Figure 7.13** [79, 98, 105, 303]. The large discrepancy between our data and proteoliposome studies is surprising and asserts the need to verify of our estimations of protein concentration with other techniques. However, there are several considerations that may also contribute to the difference in quenching that is observed. Firstly, it is possible that the forced migration of proteins in the E-field may increase the likelihood of protein aggregation beyond that of expected average separation distance expected for a given overall concentration (i.e., shorter protein-protein distances than the most-spaced expectation due to inhomogeneity). This could occur due to attractive interactions, for example, due to changes in the electrostatic interactions between proteins and lipids. It is also feasible that the process of concentrating proteins against a confined edge may result in proteins that are more often closely-associated than proteins that have randomly assembled during proteoliposome self-assembly. Another possible source of discrepancy arises

from possible variations across a proteoliposome population due to fluctuations and randomization of the self-assembly process. It has recently been shown that proteoliposome preparations may result in multiple sub-populations of particles, ranging from almost entirely "empty" (i.e., lipid only) proteoliposomes to large protein-only oligomers[105, 119]. This same study also highlighted the procedural challenges of separating proteoliposomes with highly-aggregated LHCII or less-aggregated LHCII. It is possible that this overall sample heterogeneity, in addition to the multiple different states of LHCII that may exist within a single proteoliposome, contribute to a skewed, or underestimated QE in proteoliposome measurements. Despite the discrepancy between our results and previous literature, **Figure 7.13** also highlights the abundance of data that can be obtained from in-membrane electrophoresis that is not possible through ensemble analysis of proteoliposomes. Reinforcing our results through AFM and spectroscopy measurements may provide a platform with which to comprehensively describe photosynthetic quenching, rather than extrapolating trends from only a handful of data points.

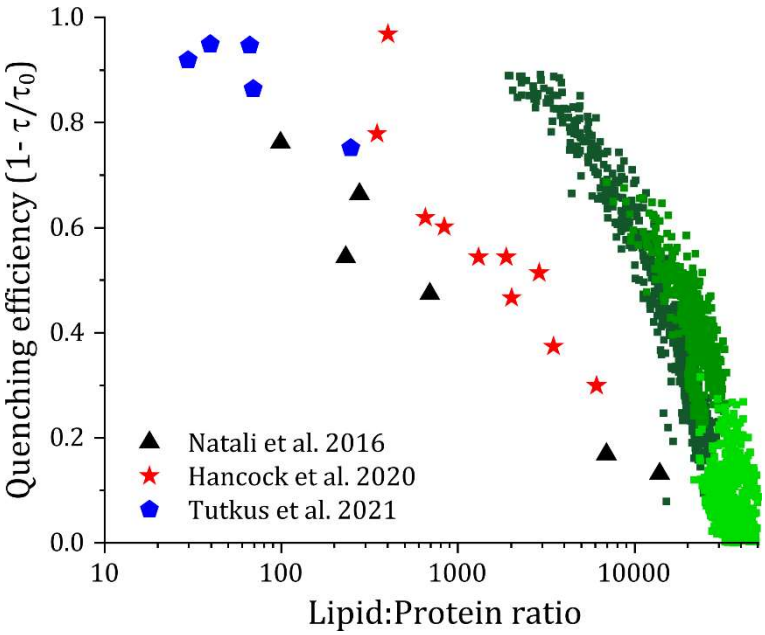

Figure 7.13: The quenching efficiency versus lipid:protein ratio for LHCII reconstituted into proteoliposomes as determined by previous studies, compared to those found using in-membrane electrophoresis. *Green*: Data obtained from in-membrane electrophoresis experiments on hybrid membranes, as labelled in **Figure 7.12**. *Black*: Data obtained by Natali et al (2016) from LHCII and thylakoid lipid proteoliposomes[79]. *Red*: Data obtained by Hancock et al (2020) from LHCII and thylakoid lipid proteoliposomes[98, 303]. *Blue*: Data obtained by Tutkus et al (2021) from LHCII and PEGylated PE lipid proteoliposomes[105].

Our calculations of the "molecularity" of photosynthetic quenching suggests that the trap site occurs within single protein units (e.g., LHCII trimers), rather than requiring two, or more, proteins to form a fluorescent trap (i.e., energy dissipative state). This is in stark contrast to the formation of non-fluorescent dimers that is predicted to cause self-quenching in lipid-tagged monochromatic fluorophores (in Chapter 6) and self-quenching of freely-diffusing chlorophylls observed by other researchers[267]. An implication of the quenching molecularity is that the number of traps scales linearly to the number of LHCII-equivalents. Exciton quenching in light-harvesting complexes results from their ability to switch intermittently from light-harvesting to quenched state[65, 68], and previous researchers have hypothesised that in large aggregates the probability of there being at least one intermittently quenched state increases with the number of constituting complexes[102, 298]. In addition, by modelling exciton migration to traps within a PSII/LHCII supercomplex, Valkunas et al found that a single quenching site was sufficient to account for a 0.4 ns lifetime, and that the addition of further quenching sites reduced the lifetime to well below those observed in nature[39, 301]. Our results, in context with these studies, could suggest that in large protein aggregates a small number of deep (possibly intermittent) traps may be sufficient to quench excitons and that the number of these traps scales with antenna concentration.

These experiments represent the first time that in-membrane electrophoresis has been used to control the organisation of photosynthetic proteins in a lipid membrane, and has been shown to induce a correlated change to the photophysical state. It has been well documented and experimentally proven that aggregation of LH proteins leads to a quenching state[41, 55, 56, 105]. In addition, it has also been demonstrated that quenching can occur within individual and isolated LHCII trimers, possibly due to conformational changes within the proteins[62, 65, 67, 68]. In this chapter we have, for the first time, shown experimentally that the dynamic concentration of LH proteins in a lipid membrane leads to the formation of a quenched state whilst *also* showing that quenching is dominated by single trimers on a fundamental level. Previously it has been hard to reconcile these two processes as they may seem inherently contradictory and because one is often based upon measurements of single proteins whereas the other is based measurements of multiple interacting proteins. Furthermore, it has been demonstrated that in-

membrane electrophoresis of LH proteins is a partially reversible process and that proteins can be "un-quenched" by the removal of the electric field and the disaggregation of proteins as they redisperse through the membrane. By measuring the quenching properties of proteins over a continuum of concentrations and by assessing the molecularity of the quenching process, we have effectively been able to bridge the gap in the current knowledge of the photophysics of LH proteins, as relates to the protective process of NPQ in nature, and have demonstrated in-membrane electrophoresis as a powerful platform with which to interrogate photosynthesis.

7.5 Concluding remarks and future outlook

In-membrane electrophoresis of photosynthetic proteins has several advantages compared to other methods to test how protein clustering can cause quenching. Firstly, proteins are maintained within consistent lipid environment at all concentrations, whereas previous studies have required the introduction of lipids[56], detergent[80] or ions[189] (pH) to induce protein aggregation. It has been shown that individual LHCII trimers exhibit subtle conformational differences when measured in detergent versus lipids[62, 109] and one cannot rule out the possibility that fluorescence quenching reported in previous studies may have contributions from changes to protein/lipid or protein/detergent interactions. Secondly, in-membrane electrophoresis offers the opportunity to assess a range of protein concentrations and photophysical states on a single sample, as well as presenting the opportunity to directly image the reorganisation of proteins in real time. This provides significantly more data from which to infer the biological implications of photosynthetic self-quenching, rather than relying on many discrete samples.

There are several outstanding questions that need to be addressed before it is possible to fully describe concentration quenching in hybrid membranes. First, the exact composition of the hybrid membrane is still unknown and to comprehensively describe photosynthetic quenching it would be useful to quantify the protein populations present in hybrid membranes. This factor is particularly important when considering quenching interactions that may occur between different species of proteins (e.g. quenching may be different in LHCII only aggregates versus

LHCII/PSII supercomplexes). Previous publications have used in-membrane electrophoresis to separate multiple species of proteins by taking advantage of their different electrophoretic properties (termed “electrophoretic focussing”, a similar strategy to traditional SDS-PAGE)[147], and it may be possible to apply this technique to separate and quantify mixtures of photosynthetic proteins. Alternatively, it would be possible albeit time consuming, to extract (e.g., washing the surfaces with detergent) and quantify the membrane material from multiple hybrid membrane preparations via gel-electrophoresis or size exclusion chromatography[225, 226].

AFM could also be used for a more complete analysis of protein dimensions and species[72] and to confirm our estimations of protein concentration from FLIM images. In addition, AFM may also reveal the organisation of the proteins within aggregates or supercomplexes that may form during in-membrane electrophoresis and help to resolve the discrepancy between our results and other investigations. In addition, correlating FLIM and AFM in this manner may allow for the theoretical modelling of lifetimes that are expected from various arrangements of proteins and the comparison of these models to experimental results, to test the current theoretical understanding of energy dissipation and transfer between multiple proteins. However, obtaining AFM measurements of hybrid membranes that have been concentrated with in-membrane electrophoresis may require significant changes to the current procedure. Proteins were shown to re-disperse throughout the membrane following the removal of the electric field and so, to obtain AFM measurements of proteins at high concentrations, it may be necessary to modify the electrophoresis flow cell to provide access for the AFM probe or to “freeze” the proteins in-place during electrophoresis so that the sample can be removed from the flow cell and imaged after electrophoresis. It may be possible to limit protein mobility by increasing the rigidity of the surrounding lipid membranes by reducing the temperature[229], inducing phase transitions in lipids[230, 231] or by chemically cross-linking lipids[134, 142, 164]. Alternatively, it may be possible to alter the dimensions of the patterned membrane and to design “electrophoresis traps” that prevent the backflow of proteins once the electric field is removed[144, 148].

Finally, it is important to determine if protein denaturation occurs as a result of in-membrane electrophoresis. It is possible that proteins become damaged by the

electrophoretic force and that that may result in changes to the fluorescence lifetime that are falsely interpreted as quenching. To confirm that no damage has occurred, and that the quenching observed during electrophoresis experiments is a genuine effect, spectroscopy measurements should be used to assess any changes to the absorption and/or emission spectra of the sample that would indicate changes to the pigment energy levels and/or pigment configurations[56, 79]. This could be achieved by comparing solution-based spectroscopy measurements of hybrid membrane material that has or has not been subjected to electrophoresis experiments or by using a surface-based spectrophotometer to observe changes to the spectra within a single sample.

7.6 Chapter acknowledgements

In this chapter S. A. Meredith was responsible for the preparation and manipulation of hybrid membranes using in-membrane electrophoresis, the acquisition and analysis of FLIM data and presentation of FLIM images, with assistance from A. M. Hancock. Y. Kusunoki was responsible for the fabrication of patterned polymerised templates. P. G. Adams, S. D. Connell and S. D. Evans are the academic supervisors of S. A. Meredith. K. Morigaki is the academic supervisor of Y. Kusunoki.

8 Conclusions and future outlook

The four results chapters (Ch. 4-7) have detailed the development and application of self-assembled and modular systems to assess the energy transfer between artificial fluorophores and photosynthetic proteins in lipid membranes and to quantify self-quenching between identical molecules.

Chapter 4 investigated the structural and photophysical properties of a new model platform "hybrid membranes", which consist of patterned lipid membranes that are self-assembled from a mix of synthetic DOPC lipids and thylakoid membrane extracts. This characterisation was essential before we could use hybrid membranes as a platform for further experiments. A combination of FLIM and AFM was used to determine the structure of hybrid membranes and to infer information about the concentration of proteins and protein-protein interactions that may occur within the system. It was found that hybrid membranes are much larger, flatter and more stable than thylakoid extracts and are therefore more amenable to microscopy studies as a controllable platform. Chl-containing proteins were found to be highly mobile and to occupy ~1 % of the membrane area. This concentration is significantly lower than that of native membranes (~60-70 %), and we hypothesise that the proteins in thylakoid membranes are diluted by the addition of synthetic lipids during hybrid membrane self-assembly. The dilution of proteins, and the disassociation of protein aggregates/interactions, was correlated to an increase in the chlorophyll (Chl) fluorescence lifetime from ~0.4 ns (in thylakoid extracts) to ~4 ns (in hybrid membranes). Finally, photochemical assays, designed to measure the electron generation of PSII[203-206], suggested that hybrid membranes are capable of electron generation and that it may be possible to incorporate this platform into existing nanotechnologies for light-harvesting[258-260].

Chapter 5 detailed the development of two light-harvesting nanomaterials in which the synthetic fluorophore, Texas Red (TR), was interfaced with photosynthetic proteins in a lipid membrane: (i) light-harvesting proteoliposomes containing TR and the photosystem II antenna protein (LHCII), (ii) hybrid membranes containing a mixture of photosynthetic proteins (PSII, LHCII, etc) and TR. In both systems, TR was found to be capable of energy transfer to Chl due to their complementary

spectra, manifesting as a quenched TR fluorescence and an enhanced Chl emission. In proteoliposomes, with fixed TR content (6.50 μM), it was shown that increasing the LHCII concentration from 0.00 μM to 3.50 μM results in the decrease in the relative TR emission to as low as 2 % (compared to its level in the absence of LHCII). In proteoliposomes with fixed LHCII content (0.7 μM), increasing the TR concentration resulted in an increase in the relative LHCII emission up to 300 %. Both of these effects are strong indicators of the successful energy transfer from TR to LHCII. FLIM measurements of individual proteoliposomes showed that >90 % of proteoliposomes had successfully incorporated both components, and population statistics revealed a monodisperse population of fluorescence lifetimes for each sample, suggesting that proteoliposomes self-assemble in a consistent manner and that there are few/negligible aggregates that may skew ensemble analysis. Overall, our results show a highly consistent and modular system in which the energy transfer efficiency (ETE) can be selectively tuned or increased to ETEs >90 %. In hybrid membranes containing TR, the extent of energy transfer was calculated by comparing the fluorescence lifetime of TR in hybrid membranes to TR in the absence of Chl, and by comparing the enhanced Chl emission when excited in the "green gap" of low absorbance. The ETE from TR-to-Chl was calculated to be 50% and Chl emission was effectively enhanced by 108 % of its initial intensity, providing a "proof of concept" for this method of enhancing light-harvesting and electron generation.

Chapter 6 detailed the development of "in-membrane electrophoresis" combined with FLIM measurements as a platform to interrogate the self-quenching that occurs between fluorophores at high concentrations. In this chapter, direct current electric fields were applied parallel to patterned lipid membranes containing either TR, NBD or Bodipy (BOD) fluorophores, such that the fluorophores experience a force, migrate in the direction of the field and increase in concentration at the membrane edge. In our patterned membranes (100 × 100 μm squares) the maximum fluorophore concentration was ~7-fold greater than the concentration of fluorophores prior to electrophoresis, and increasing the initial concentration of fluorophores from 0.28 % to 0.94 % (mol/mol) resulted in maximum concentrations of 2 % and 7 %, respectively. Lifetime measurements of lipid bilayers during electrophoresis showed that increasing the fluorophore concentration resulted in

fluorescence quenching (i.e., a shortened fluorescent lifetime), and by correlating the concentration and lifetime at each location it was possible to produce quenching efficiency versus concentration curves for each fluorophore. Using these curves it was possible to predict the quenching behaviour over a continuous range of concentrations and to determine the mechanism of self-quenching. It was found that quenching is most likely caused by the formation of quasi-stable non-fluorescent dimers, that form when two fluorophores are separated by the "critical radius of trap formation", R_C. From quenching efficiency curves, we were able to determine R_C for each fluorophore (R_{BOD} = 2.57 ± 0.01, R_{TR} = 1.83 ± 0.01, R_{NBD} = 1.03 ± 0.01 nm) and found these to be in agreement to previous studies[268, 270]. Our results show that this platform is sensitive to nanoscale differences in parameters that may dictate quenching, and that the results are reliable and accurate when compared to other methods to quantify quenching.

In chapter 7, in-membrane electrophoresis and correlated FLIM measurements were used to quantify the quenching that occurs as a result of interactions between or aggregation of photosynthetic proteins. First, hybrid membranes were self-assembled from a mixture of thylakoid extracts and synthetic lipids, and increasing the concentration of thylakoid extracts in the self-assembly process was found to increase the concentration of proteins that incorporated into the membrane (in a range of 0.5 % - 1.2 % of the membrane area). Applying an electric field parallel to the plane of patterned (100 × 100 μm square) hybrid membranes resulted in the migration of photosynthetic proteins towards the positive electrode, correlated to the quenching of the fluorescence lifetime (from ~ 4 ns to as little as ~0.8 ns) as the concentration of proteins increased at the membrane edge. Removal of the electric field resulted in the redistribution of Chl fluorescence, until it was homogenous throughout the membrane, and a correlated "un-quenching" of Chl fluorescence as the protein concentration decreases and protein aggregates disassociate. Both FRAP measurements (showing a reduce diffusivity of proteins after versus before electrophoresis experiments) and fluorescence lifetime measurements (showing a slightly reduced fluorescence lifetime after versus before electrophoresis) indicate that protein interactions do not entirely disassociate once the electric field is removed and that there may be some nanoscale protein aggregates that are maintained by some weak attractive force. Overall, we have demonstrated the first

application of in-membrane electrophoresis to control the organisation and photophysics of photosynthetic proteins in a lipid membrane, and our results show that the proteins can be reversibly switched between an energy dissipative or light-harvesting state by increasing or decreasing the protein concentration, respectively. Careful analysis of FLIM images was used to generate quenching efficiency versus concentration curves to quantify the overall strength of quenching and to reveal information about the mechanism of photosynthetic quenching over a continuous range of concentrations. The quenching strength between photosynthetic proteins was found to be 10-15 fold greater than the quenching strength of freely diffusing pigments (BOD, NBD, or TR), possibly due to attractive forces between proteins that may lead to sustained protein interactions. Finally, the "molecularity" (i.e. number of proteins required to form an energy trap) was assessed. It was found that the number of traps was proportional to the concentration of proteins and suggests that quenching traps are dominated by individual trimers on a fundamental level, possibly due to conformational changes of those trimers due to interactions or forces between proteins. This is the first time (to the Author's knowledge) that the protein aggregation model[41, 55, 105] and later observations of quenching in individual proteins[68, 69] (two models that appear inherently contradictory) have been reconciled in a single experiment.

Overall, in all four chapters, we have demonstrated that both proteoliposomes and hybrid membranes are a powerful experimental platform for correlated AFM and FLIM measurements for which to interrogate excitation energy transfer and fluorescence quenching between small-molecule fluorophores and photosynthetic proteins. Whilst it is not unusual for photosynthetic proteins to be reconstituted into lipid bilayers[74, 79, 98, 105, 120], or otherwise studied in a native thylakoid lipid environment[53, 72, 169, 304], the ability to incorporate multiple types of photosynthetic proteins into a series of discrete patterned membranes allows this single experimental platform to be applied to a broader range of applications than either native thylakoid extracts or non-patterned lipid membranes (liposomes or SLBs) alone. The self-assembly process of hybrid membranes (and liposomes) was harnessed to incorporate complementary chromophores into close proximity to photosynthetic proteins to enhance their absorption spectra, and was able to reach energy transfer efficiencies comparable to those reported in literature for the direct

covalent attachment of chromophores to light-harvesting proteins[237, 239, 240, 305]. The ability to do this within a surface patterned system (i.e. hybrid membranes) is another advance, because these may be also capable of electron transfer, opening the possibility of utilising "enhanced hybrid membranes" alongside other 2D micro/nanoscale electronics that already exist[258-260]. The configuration of hybrid membranes as being surface-supported (in contrast to solution-based vesicles) also means that they are flexible and compatible with many experimental techniques, such as in-membrane electrophoresis, and amenable to surface-based microscopy, such as AFM and FLIM. By taking advantage of these properties, significant steps were made towards a comprehensive understanding of fluorescence self-quenching between identical fluorophores and the quenching that occurs between photosynthetic proteins as the direct result of protein interactions/aggregation. Our findings allow us to make convincing conclusions regarding the nature and mechanism of protective non-photochemical quenching in photosynthesis, and have wider implications for the use of fluorophores, and opportunities to characterise and take advantage of fluorescence quenching, in both the model membrane and other photosynthesis research communities.

A promising next step for this research would be to apply in-membrane electrophoresis to a wider range of photosynthetic samples in order to delineate the effects of different components and conditions on non-photochemical quenching. Other researchers have already demonstrated the ability to form model lipid bilayers containing LHCII[74, 98, 105] or PSII[129, 306, 307] and it is feasible that these membranes could be deposited into patterned templates to make them compatible with in-membrane electrophoresis. It would be particularly interesting to compare concentration-induced quenching in LHCII-only membranes, PSII-only membranes and hybrid membranes to generate quenching efficiency versus concentration curves for each protein and to determine their relative contributions to energy dissipation and photoprotective NPQ. Numerous researchers report changes to thylakoid membrane structure and photophysics as a result of pH[39, 40, 189, 308] and it would also be possible to perform in-membrane electrophoresis in a variety of aqueous environments. Specifically, it would be interesting to determine if the quenching efficiency of concentrated proteins is increased in different pH or ionic conditions, or if proteins organize into different supercomplexes as a result of

changes to electrostatic interactions. In addition, the stability of protein aggregates could be indirectly measured in a variety of electrostatic conditions by concentrating proteins via electrophoresis and then monitoring the redistribution of proteins once the electric field is removed. It would also be highly revealing to investigate the specific role of PsbS protein, which may be the gatekeeper of inducing the quenched state of LHCII[174, 309, 310], using LHCII-PsbS model membranes and electrophoresis.

Finally, it has been shown that it is possible to create multi-bilayer stacks of model membranes by exploiting electrostatic attractions between anionic lipids and cationic polymers,[200, 235] divalent cations,[236] or protein-protein interactions (including LHCII-LHCII).[74] It may also be possible to generate multi-layered hybrid membranes for use in in-membrane electrophoresis experiments to assess whether energy transfer between stacked membranes may contribute to NPQ and whether protein diffusion within stacked membranes results in different membrane organisations. Through a methodical screening of various conditions and membrane compositions, it may be possible to delineate the network of complicated interactions and photoprotective processes that occur native thylakoid membranes.

9 References

1. Blankenship, R. E., *Molecular Mechanisms of Photosynthesis*. John Wiley & Sons: Chichester, UK, 2014.

2. Thekaekara, M. P., Solar irradiance: total and spectral and its possible variations. *Appl. Opt.* **1976,** *15* (4), 915-920.

3. Higuchi-Takeuchi, M.; Numata, K., Marine Purple Photosynthetic Bacteria as Sustainable Microbial Production Hosts. *Frontiers in Bioengineering and Biotechnology* **2019,** *7* (258), 11.

4. Hoffert, M. I.; Caldeira, K.; Benford, G.; Criswell, D. R.; Green, C.; Herzog, H.; Jain, A. K.; Kheshgi, H. S.; Lackner, K. S.; Lewis, J. S.; Lightfoot, H. D.; Manheimer, W.; Mankins, J. C.; Mauel, M. E.; Perkins, L. J.; Schlesinger, M. E.; Volk, T.; Wigley, T. M., Advanced technology paths to global climate stability: energy for a greenhouse planet. *Science* **2002,** *298* (5595), 981-7.

5. IPPC; V. Masson-Dolmotte; P. Zhai; A. Pirani; S. L. Connors; C. Pean; S Berger; N. Caud; Y. Chen; L. Goldfarb; M. I. Gomis; M. Huang; K. Leitzell; E. Lonnoy; J. B. R. Matthews; T. K. Maycock; T. Waterfield; O. Yelekci; R. Yu; Zhou, B., Climate Change 2021: The Physical Science Basis. Contribution of Working Group I to the Sixth Assessment Report of the Intergovernmental Panel on Climate Change. *Cambridge University Press* **2021**.

6. Long, S. P.; Zhu, X.-G.; Naidu, S. L.; Ort, D. R., Can improvement in photosynthesis increase crop yields? *Plant, Cell & Environment* **2006,** *29* (3), 315-330.

7. Cavalier-Smith, T., Membrane heredity and early chloroplast evolution. *Trends Plant Sci* **2000,** *5* (4), 174-182.

8. Daum, B.; Kuhlbrandt, W., Electron Tomography of Plant Thylakoid Membranes. *J. Exp. Bot.* **2011,** *62* (7), 2393-2402.

9. Johnson, M. P., Photosynthesis. *Essays Biochem* **2016,** *60* (3), 255-273.

10. Pribil, M.; Labs, M.; Leister, D., Structure and dynamics of thylakoids in land plants. *J Exp Bot* **2014,** *65* (8), 1955-1972.

11. Dekker, J. P.; Boekema, E. J., Supramolecular Organization of Thylakoid Membrane Proteins in Green Plants. *Biochim. Biophys. Acta-Bioenerg.* **2005,** *1706* (1-2), 12-39.

12. Rozak, P. R.; Seiser, R. M.; Wacholtz, W. F.; Wise, R. R., Rapid, reversible alterations in spinach thylakoid appression upon changes in light intensity. *Plant, Cell & Environment* **2002,** *25* (3), 421-429.

13. Allen, J. F., State Transitions--a Question of Balance. *Science* **2003,** *299* (5612), 1530.

14. Trissl, H.-W.; Wilhelm, C., Why do thylakoid membranes from higher plants form grana stacks? *Trends Biochem.Sci.* **1993,** *18* (11), 415-419.

15. Vallon, O.; Bulte, L.; Dainese, P.; Olive, J.; Bassi, R.; Wollman, F. A., Lateral redistribution of cytochrome b6/f complexes along thylakoid membranes upon state transitions. *Proceedings of the National Academy of Sciences* **1991,** *88* (18), 8262.

16. Albertsson, P.-Å., A quantitative model of the domain structure of the photosynthetic membrane. *Trends Plant Sci* **2001,** *6* (8), 349-354.

17. Wood, W. H. J.; MacGregor-Chatwin, C.; Barnett, S. F. H.; Mayneord, G. E.; Huang, X.; Hobbs, J. K.; Hunter, C. N.; Johnson, M. P., Dynamic Thylakoid Stacking Regulates the Balance between Linear and Cyclic Photosynthetic Electron Transfer. *Nat. Plants* **2018,** *4* (6), 391-391.

18. Mirkovic, T.; Ostroumov, E. E.; Anna, J. M.; van Grondelle, R.; Govindjee; Scholes, G. D., Light Absorption and Energy Transfer in the Antenna Complexes of Photosynthetic Organisms. *Chem. Rev.* **2017,** *117* (2), 249-293.

19. Lubitz, W.; Chrysina, M.; Cox, N., Water oxidation in photosystem II. *Photosynth Res* **2019,** *142* (1), 105-125.

20. Croce, R.; van Amerongen, H., Natural strategies for photosynthetic light harvesting. *Nature Chemical Biology* **2014,** *10* (7), 492-501.

21. Grossman, A. R.; Schaefer, M. R.; Chiang, G. G.; Collier, J. L., The phycobilisome, a light-harvesting complex responsive to environmental conditions. *Microbiological reviews* **1993,** *57* (3), 725-749.

22. Standfuss, R.; van Scheltinga, A. C. T.; Lamborghini, M.; Kuhlbrandt, W., Mechanisms of Photoprotection and Nonphotochemical Quenching in Pea Light-harvesting Complex at 2.5A Resolution. *EMBO J.* **2005,** *24* (5), 919-928.

23. Barros, T.; Royant, A.; Standfuss, J.; Dreuw, A.; Kuhlbrandt, W., Crystal structure of plant light-harvesting complex shows the active, energy-transmitting state. *Embo J* **2009,** *28* (3), 298-306.

24. Liu, Z.; Yan, H.; Wang, K.; Kuang, T.; Zhang, J.; Gui, L.; An, X.; Chang, W., Crystal structure of spinach major light-harvesting complex at 2.72 Å resolution. *Nature* **2004,** *428* (6980), 287-292.

25. Wei, X. P.; Su, X. D.; Cao, P.; Liu, X. Y.; Chang, W. R.; Li, M.; Zhang, X. Z.; Liu, Z. F., Structure of spinach photosystem II-LHCII supercomplex at 3.2 angstrom resolution. *Nature* **2016,** *534* (7605), 69-74.

26. Barzda, V.; Gulbinas, V.; Kananavicius, R.; Cervinskas, V.; van Amerongen, H.; van Grondelle, R.; Valkunas, L., Singlet-Singlet Annihilation Kinetics in Aggregates and Trimers of LHCII. *Biophys. J.* **2001,** *80* (5), 2409-2421.

27. Şener, M.; Strümpfer, J.; Hsin, J.; Chandler, D.; Scheuring, S.; Hunter, C. N.; Schulten, K., Förster energy transfer theory as reflected in the structures of photosynthetic light-harvesting systems. *Chemphyschem* **2011,** *12* (3), 518-31.

28. Forster, T., Delocalization excitation and excitation transfer. *Modern Quantum Chemistry* **1965**.

29. Loura, L. M., Simple estimation of Förster Resonance Energy Transfer (FRET) orientation factor distribution in membranes. *Int J Mol Sci* **2012,** *13* (11), 15252-70.

30. van Grondelle, R., Excitation energy transfer, trapping and annihilation in photosynthetic systems. *Biochimica et Biophysica Acta (BBA) - Reviews on Bioenergetics* **1985,** *811* (2), 147-195.

31. Schuler, B.; Eaton, W. A., Protein folding studied by single-molecule FRET. *Curr. Opin. Struct. Biol.* **2008,** *18* (1), 16-26.

32. van Amerongen, H.; Croce, R., Light harvesting in photosystem II. *Photosynth Res* **2013,** *116* (2), 251-263.

33. Croce, R.; van Amerongen, H., Light-harvesting and structural organization of Photosystem II: From individual complexes to thylakoid membrane. *Journal of Photochemistry and Photobiology B: Biology* **2011,** *104* (1), 142-153.

34. Fleming, G. R.; Schlau-Cohen, G. S.; Amarnath, K.; Zaks, J., Design principles of photosynthetic light-harvesting. *Faraday Discussions* **2012,** *155* (0), 27-41.

35. Krieger-Liszkay, A., Singlet oxygen production in photosynthesis. *J Exp Bot* **2004,** *56* (411), 337-346.

36. Ruban, A. V., Nonphotochemical Chlorophyll Fluorescence Quenching: Mechanism and Effectiveness in Protecting Plants from Photodamage. *Plant Physiol* **2016,** *170* (4), 1903-1916.

37. Demmig-Adams, B.; Cohu, C. M.; Muller, O.; Adams, W. W., Modulation of photosynthetic energy conversion efficiency in nature: from seconds to seasons. *Photosynth Res* **2012,** *113* (1), 75-88.

38. Weis, E.; Berry, J. A., Quantum efficiency of Photosystem II in relation to 'energy'-dependent quenching of chlorophyll fluorescence. *Biochimica et Biophysica Acta (BBA) - Bioenergetics* **1987,** *894* (2), 198-208.

39. Duffy, C. D. P.; Ruban, A. V., Dissipative Pathways in the Photosystem-II Antenna in Plants. *J. Photochem. Photobiol., B* **2015,** *152*, 215-226.

40. Ruban, A. V.; Johnson, M. P.; Duffy, C. D. P., The photoprotective molecular switch in the photosystem II antenna. *Bba-Bioenergetics* **2012,** *1817* (1), 167-181.

41. Horton, P.; Ruban, A. V.; Rees, D.; Pascal, A. A.; Noctor, G.; Young, A. J., Control of the Light-Harvesting Function of Chloroplast Membranes by Aggregation of the Lhcii Chlorophyll Protein Complex. *Febs Lett* **1991,** *292* (1-2), 1-4.

42. Noctor, G.; Ruban, A. V.; Horton, P., Modulation of Delta-Ph-Dependent Nonphotochemical Quenching of Chlorophyll Fluorescence in Spinach-Chloroplasts. *Biochim Biophys Acta* **1993,** *1183* (2), 339-344.

43. Yamamoto, H. Y.; Kamite, L., The effects of dithiothreitol on violaxanthin de-epoxidation and absorbance changes in the 500-nm region. *Biochimica et Biophysica Acta (BBA) - Bioenergetics* **1972,** *267* (3), 538-543.

44. Demmigadams, B., Carotenoids and Photoprotection in Plants - a Role for the Xanthophyll Zeaxanthin. *Biochim Biophys Acta* **1990,** *1020* (1), 1-24.

45. Frank, H. A.; Cogdell, R. J., Carotenoids in Photosynthesis. *Photochem Photobiol* **1996,** *63* (3), 257-264.

46. Li, X. P.; Bjorkman, O.; Shih, C.; Grossman, A. R.; Rosenquist, M.; Jansson, S.; Niyogi, K. K., A pigment-binding protein essential for regulation of photosynthetic light harvesting. *Nature* **2000,** *403* (6768), 391-395.

47. Ilioaia, C.; Johnson, M. P.; Horton, P.; Ruban, A. V., Induction of Efficient Energy Dissipation in the Isolated Light-harvesting Complex of Photosystem II in the Absence of Protein Aggregation. *J Biol Chem* **2008,** *283* (43), 29505-29512.

48. Dominici, P.; Caffarri, S.; Armenante, F.; Ceoldo, S.; Crimi, M.; Bassi, R., Biochemical Properties of the PsbS Subunit of Photosystem II Either Purified from Chloroplast or Recombinant*. *J Biol Chem* **2002,** *277* (25), 22750-22758.

49. Johnson, M. P.; Ruban, A. V., Restoration of rapidly reversible photoprotective energy dissipation in the absence of PsbS protein by enhanced DeltapH. *J Biol Chem* **2011,** *286* (22), 19973-81.

50. Jahns, P.; Krause, G. H., Xanthophyll cycle and energy-dependent fluorescence quenching in leaves from pea plants grown under intermittent light. *Planta* **1994,** *192* (2), 176-182.

51. Havaux, M.; Dall'Osto, L.; Bassi, R., Zeaxanthin Has Enhanced Antioxidant Capacity with Respect to All Other Xanthophylls in Arabidopsis Leaves and Functions Independent of Binding to PSII Antennae. *Plant Physiol* **2007,** *145* (4), 1506-1520.

52. Kouril, R.; Dekker, J. P.; Boekema, E. J., Supramolecular Organization of Photosystem II in Green Plants. *Biochim. Biophys. Acta-Bioenerg.* **2012,** *1817* (1), 2-12.

53. Johnson, M. P.; Goral, T. K.; Duffy, C. D. P.; Brain, A. P. R.; Mullineaux, C. W.; Ruban, A. V., Photoprotective Energy Dissipation Involves the Reorganization of Photosystem II Light-Harvesting Complexes in the Grana Membranes of Spinach Chloroplasts. *Plant Cell* **2011,** *23* (4), 1468-1479.

54. van Oort, B.; van Hoek, A.; Ruban, A. V.; van Amerongen, H., Equilibrium between quenched and nonquenched conformations of the major plant light-harvesting complex studied with high-pressure time-resolved fluorescence. *J Phys Chem B* **2007,** *111* (26), 7631-7637.

55. van Oort, B.; van Hoek, A.; Ruban, A. V.; van Amerongen, H., Aggregation of Light-Harvesting Complex II leads to Formation of Efficient Excitation Energy Traps in Monomeric and Trimeric Complexes. *FEBS Lett.* **2007,** *581* (18), 3528-3532.

56. Adams, P. G.; Vasilev, C.; Hunter, C. N.; Johnson, M. P., Correlated Fluorescence Quenching and Topographic Mapping of Light-Harvesting Complex II within Surface-assembled Aggregates and Lipid Bilayers. *Biochim. Biophys. Acta-Bioenerg.* **2018,** *1859* (10), 1075-1085.

57. Mascoli, V.; Liguori, N.; Xu, P.; Roy, L. M.; van Stokkum, I. H. M.; Croce, R., Capturing the Quenching Mechanism of Light-Harvesting Complexes of Plants by Zooming in on the Ensemble. *Chem* **2019,** *5* (11), 2900-2912.

58. Son, M.; Schlau-Cohen, G. S., Flipping a Protein Switch: Carotenoid-Mediated Quenching in Plants. *Chem* **2019,** *5* (11), 2749-2750.

59. Son, M.; Pinnola, A.; Bassi, R.; Schlau-Cohen, G. S., The Electronic Structure of Lutein 2 Is Optimized for Light Harvesting in Plants. *Chem* **2019,** *5* (3), 575-584.

60. Gelzinis, A.; Chmeliov, J.; Ruban, A. V.; Valkunas, L., Can red-emitting state be responsible for fluorescence quenching in LHCII aggregates? *Photosynth Res* **2018,** *135* (1-3), 275-284.

61. Chmeliov, J.; Bricker, W. P.; Lo, C.; Jouin, E.; Valkunas, L.; Ruban, A. V.; Duffy, C. D. P., An 'All Pigment' Model of Excitation Quenching in LHCII. *Phys. Chem. Chem. Phys.* **2015,** *17* (24), 15857-15867.

62. Son, M., Pinnola, A., Gordon, S.C., Bassi, R., Schlau-Cohen, G.S., Observation of dissipative chlorophyll-to-carotenoid energy transfer in light-harvesting complex II in membrane nanodiscs. *Nat Commun* **2020,** *11*, 1295.

63. Müh, F.; Madjet, M. E.-A.; Renger, T., Structure-based simulation of linear optical spectra of the CP43 core antenna of photosystem II. *Photosynth Res* **2012,** *111* (1), 87-101.

64. Ruban, A. V.; Berera, R.; Ilioaia, C.; van Stokkum, I. H. M.; Kennis, J. T. M.; Pascal, A. A.; van Amerongen, H.; Robert, B.; Horton, P.; van Grondelle, R., Identification of a mechanism of photoprotective energy dissipation in higher plants. *Nature* **2007,** *450* (7169), 575-578.

65. Schlau-Cohen, G. S.; Yang, H.-Y.; Krüger, T. P. J.; Xu, P.; Gwizdala, M.; van Grondelle, R.; Croce, R.; Moerner, W. E., Single-Molecule Identification of Quenched and Unquenched States of LHCII. *The Journal of Physical Chemistry Letters* **2015,** *6* (5), 860-867.

66. Kondo, T.; Chen, W. J.; Schlau-Cohen, G. S., Single-Molecule Fluorescence Spectroscopy of Photosynthetic Systems. *Chem. Rev.* **2019,** *119* (7), 4817-4817.

67. Krüger, T. P. J.; Wientjes, E.; Croce, R.; van Grondelle, R., Conformational switching explains the intrinsic multifunctionality of plant light-harvesting complexes. *Proceedings of the National Academy of Sciences* **2011,** *108* (33), 13516.

68. Krüger, T. P. J.; Ilioaia, C.; Valkunas, L.; van Grondelle, R., Fluorescence Intermittency from the Main Plant Light-Harvesting Complex: Sensitivity to the Local Environment. *The Journal of Physical Chemistry B* **2011,** *115* (18), 5083-5095.

69. Kruger, T. P. J.; Ilioaia, C.; Johnson, M. P.; Ruban, A. V.; Papagiannakis, E.; Horton, P.; van Grondelle, R., Controlled Disorder in Plant Light-Harvesting Complex II Explains Its Photoprotective Role. *Biophys J* **2012,** *102* (11), 2669-2676.

70. Valkunas, L.; Chmeliov, J.; Krüger, T. P. J.; Ilioaia, C.; van Grondelle, R., How Photosynthetic Proteins Switch. *The Journal of Physical Chemistry Letters* **2012,** *3* (19), 2779-2784.

71. Duffy, C. D. P.; Valkunas, L.; Ruban, A. V., Light-harvesting processes in the dynamic photosynthetic antenna. *Phys. Chem. Chem. Phys.* **2013,** *15* (43), 18752-18770.

72. Johnson, M. P.; Vasilev, C.; Olsen, J. D.; Hunter, C. N., Nanodomains of Cytochrome b_6f and Photosystem II Complexes in Spinach Grana Thylakoid Membranes. *Plant Cell* **2014,** *26* (7), 3051-3061.

73. Zhao, L. S.; Huokko, T.; Wilson, S.; Simpson, D. M.; Wang, Q.; Ruban, A. V.; Mullineaux, C. W.; Zhang, Y. Z.; Liu, L. N., Structural Variability, Coordination and Adaptation of a Native Photosynthetic Machinery. *Nat. Plants* **2020,** *6* (7), 882.

74. Seiwert, D.; Witt, H.; Ritz, S.; Janshoff, A.; Paulsen, H., The Nonbilayer Lipid MGDG and the Major Light-Harvesting Complex (LHCII) Promote Membrane Stacking in Supported Lipid Bilayers. *Biochem.* **2018,** *57* (15), 2278-2288.

75. MacGregor-Chatwin, C.; Sener, M.; Barnett, S. F. H.; Hitchcock, A.; Barnhart-Dailey, M. C.; Maghlaoui, K.; Barber, J.; Timlin, J. A.; Schulten, K.; Hunter, C. N., Lateral Segregation of Photosystem I in Cyanobacterial Thylakoids. *Plant Cell* **2017,** *29* (5), 1119-1136.

76. Liu, L. N.; Scheuring, S., Investigation of Photosynthetic Membrane Structure using Atomic Force Microscopy. *Trends in Plant Sci.* **2013,** *18* (5), 277-286.

77. Zhao, L. S.; Huokko, T.; Wilson, S.; Simpson, D. M.; Wang, Q.; Ruban, A. V.; Mullineaux, C. W.; Zhang, Y. Z.; Liu, L. N., Structural variability, coordination and adaptation of a native photosynthetic machinery. *Nat Plants* **2020,** *6* (7), 869-882.

78. Daum, B.; Nicastro, D.; Il, J. A.; McIntosh, J. R.; Kuhlbrandt, W., Arrangement of Photosystem II and ATP Synthase in Chloroplast Membranes of Spinach and Pea. *Plant Cell* **2010,** *22* (4), 1299-1312.

79. Natali, A.; Gruber, J. M.; Dietzel, L.; Stuart, M. C. A.; van Grondelle, R.; Croce, R., Light-harvesting Complexes (LHCs) Cluster Spontaneously in Membrane Environment Leading to Shortening of Their Excited State Lifetimes. *J. Biol. Chem.* **2016,** *291* (32), 16730-16739.

80. Vasilev, C.; Johnson, M. P.; Gonzales, E.; Wang, L.; Ruban, A. V.; Montano, G.; Cadby, A. J.; Hunter, C. N., Reversible Switching between Nonquenched and Quenched States in

Nanoscale Linear Arrays of Plant Light-Harvesting Antenna Complexes. *Langmuir* **2014,** *30* (28), 8481-8490.

81. Boardman, N. K.; Anderson, J. M., Fractionation of the photochemical systems of photosynthesis. II. Cytochrome and carotenoid contents of particles isolated from spinach chloroplasts. *Biochim Biophys Acta* **1967,** *143* (1), 187-203.

82. Sane, P. V.; Goodchild, D. J.; Park, R. B., Characterization of chloroplast photosystems 1 and 2 separated by a non-detergent method. *Biochim Biophys Acta* **1970,** *216* (1), 162-78.

83. Albertsson, P.-Å.; Andreasson, E.; Stefánsson, H.; Wollenberger, L., [45] Fractionation of thylakoid membrane. In *Methods in Enzymology*, Academic Press: 1994; Vol. 228, pp 469-482.

84. Berthold, D. A.; Babcock, G. T.; Yocum, C. F., A highly resolved, oxygen-evolving photosystem II preparation from spinach thylakoid membranes. *Febs Lett* **1981,** *134* (2), 231-234.

85. Anderson, J. M.; Boardman, N. K., Fractionation of the photochemical systems of photosynthesis. I. Chlorophyll contents and photochemical activities of particles isolated from spinach chloroplasts. *Bibl Laeger* **1966,** *112* (3), 403-21.

86. Kouřil, R.; Oostergetel, G. T.; Boekema, E. J., Fine structure of granal thylakoid membrane organization using cryo electron tomography. *Biochimica et Biophysica Acta (BBA) - Bioenergetics* **2011,** *1807* (3), 368-374.

87. Mustárdy, L. s.; Buttle, K.; Steinbach, G. b.; Garab, G. z., The Three-Dimensional Network of the Thylakoid Membranes in Plants: Quasihelical Model of the Granum-Stroma Assembly. *The Plant Cell* **2008,** *20* (10), 2552-2557.

88. Bumba, L.; Vácha, F. E., Electron microscopy in structural studies of Photosystem II. *Photosynth Res* **2003,** *77* (1), 1-19.

89. Kirchhoff, H.; Lenhert, S.; Buchel, C.; Chi, L. F.; Nield, J., Probing the organization of photosystem II in photosynthetic membranes by atomic force microscopy. *Biochemistry-Us* **2008,** *47* (1), 431-440.

90. Sznee, K.; Dekker, J. P.; Dame, R. T.; van Roon, H.; Wuite, G. J. L.; Frese, R. N., Jumping mode atomic force microscopy on grana membranes from spinach. *The Journal of biological chemistry* **2011,** *286* (45), 39164-39171.

91. Cuello, J.; Quiles, M. J., Fractionation of Thylakoid Membranes Into Grana and Stroma Thylakoids. In *Photosynthesis Research Protocols*, Carpentier, R., Ed. Humana Press: Totowa, NJ, 2004; pp 1-9.

92. Pashayeva, A.; Wu, G.; Huseynova, I.; Lee, C.-H.; Zulfugarov, I. S., Role of Thylakoid Protein Phosphorylation in Energy-Dependent Quenching of Chlorophyll Fluorescence in Rice Plants. *International journal of molecular sciences* **2021,** *22* (15), 7978.

93. Bressan, M.; Dall'Osto, L.; Bargigia, I.; Alcocer, M. J. P.; Viola, D.; Cerullo, G.; D'Andrea, C.; Bassi, R.; Ballottari, M., LHCII can substitute for LHCI as an antenna for photosystem I but with reduced light-harvesting capacity. *Nat. Plants* **2016,** *2* (9), 16131.

94. Grinzato, A.; Albanese, P.; Marotta, R.; Swuec, P.; Saracco, G.; Bolognesi, M.; Zanotti, G.; Pagliano, C., High-Light versus Low-Light: Effects on Paired Photosystem II Supercomplex Structural Rearrangement in Pea Plants. *International journal of molecular sciences* **2020,** *21* (22), 8643.

95. Kouřil, R.; Wientjes, E.; Bultema, J. B.; Croce, R.; Boekema, E. J., High-light vs. low-light: Effect of light acclimation on photosystem II composition and organization in Arabidopsis thaliana. *Biochimica et Biophysica Acta (BBA) - Bioenergetics* **2013,** *1827* (3), 411-419.

96. Kirchhoff, H.; Horstmann, S.; Weis, E., Control of the photosynthetic electron transport by PQ diffusion microdomains in thylakoids of higher plants. *Biochimica et Biophysica Acta (BBA) - Bioenergetics* **2000,** *1459* (1), 148-168.

97. Daum, B.; Nicastro, D.; Austin, J., 2nd; McIntosh, J. R.; Kühlbrandt, W., Arrangement of photosystem II and ATP synthase in chloroplast membranes of spinach and pea. *The Plant cell* **2010,** *22* (4), 1299-1312.

98. Hancock, A. M.; Meredith, S. A.; Connell, S. D.; Jeuken, L. J. C.; Adams, P. G., Proteoliposomes as Energy Transferring Nanomaterials: Enhancing the Spectral Range of Light-harvesting Proteins using Lipid-linked Chromophores. *Nanoscale* **2019,** *11* (35), 16284-16292.

99. Nield, J.; Orlova, E. V.; Morris, E. P.; Gowen, B.; van Heel, M.; Barber, J., 3D map of the plant photosystem II supercomplex obtained by cryoelectron microscopy and single particle analysis. *Nat. Struct. Biol.* **2000,** *7* (1), 44-47.

100. Barros, T.; Kuhlbrandt, W., Crystallisation, structure and function of plant light-harvesting Complex II. *Bba-Bioenergetics* **2009,** *1787* (6), 753-772.

101. Balevičius, V.; Duffy, C. D. P., Excitation quenching in chlorophyll–carotenoid antenna systems: 'coherent' or 'incoherent'. *Photosynth Res* **2020,** *144* (3), 301-315.

102. Chmeliov, J.; Gelzinis, A.; Songaila, E.; Augulis, R.; Duffy, C. D. P.; Ruban, A. V.; Valkunas, L., The Nature of Self-Regulation in Photosynthetic Light-Harvesting Antenna. *Nat. Plants* **2016,** *2* (5), 7.

103. Kell, A.; Feng, X.; Lin, C.; Yang, Y.; Li, J.; Reus, M.; Holzwarth, A. R.; Jankowiak, R., Charge-Transfer Character of the Low-Energy Chl a Q(y) Absorption Band in Aggregated Light Harvesting Complexes II. *J Phys Chem B* **2014,** *118* (23), 6086-6091.

104. Tietz, C.; Jelezko, F.; Gerken, U.; Schuler, S.; Schubert, A.; Rogl, H.; Wrachtrup, J., Single molecule spectroscopy on the light-harvesting complex II of higher plants. *Biophys J* **2001,** *81* (1), 556-562.

105. Tutkus, M.; Chmeliov, J.; Trinkunas, G.; Akhtar, P.; Lambrev, P. H.; Valkunas, L., Aggregation-related quenching of LHCII fluorescence in liposomes revealed by single-molecule spectroscopy. *Journal of Photochemistry and Photobiology B: Biology* **2021,** *218*, 112174.

106. Kruger, T. P. J.; Ilioaia, C.; Johnson, M. P.; Ruban, A. V.; van Grondelle, R., Disentangling the Low-energy States of the Major Light-harvesting Complex of Plants and their Role in Photoprotection. *Biochim. Biophys. Acta-Bioenerg.* **2014,** *1837* (7), 1027-1038.

107. Kruger, T. P. J.; Novoderezhkin, V. I.; Ilioaia, C.; van Grondelle, R., Fluorescence Spectral Dynamics of Single LHCII Trimers. *Biophys J* **2010,** *98* (12), 3093-3101.

108. Schaller, S.; Latowski, D.; Jemiola-Rzeminska, M.; Dawood, A.; Wilhelm, C.; Strzalka, K.; Goss, R., Regulation of LHCII aggregation by different thylakoid membrane lipids. *Bba-Bioenergetics* **2011,** *1807* (3), 326-335.

109. Ogren, J. I.; Tong, A. L.; Gordon, S. C.; Chenu, A.; Lu, Y.; Blankenship, R. E.; Cao, J. S.; Schlau-Cohen, G. S., Impact of the lipid bilayer on energy transfer kinetics in the photosynthetic protein LH2. *Chem Sci* **2018,** *9* (12), 3095-3104.

110. Nogueira, E.; Gomes, A. C.; Preto, A.; Cavaco-Paulo, A., Design of liposomal formulations for cell targeting. *Colloids Surf B Biointerfaces* **2015,** *136*, 514-26.

111. Shashi, K.; Satinder, K.; Bharat, P. In *A complete review on: Liposomes*, 2012.

112. Ollivon, M.; Lesieur, S.; Grabielle-Madelmont, C.; Paternostre, M. t., Vesicle reconstitution from lipid–detergent mixed micelles. *Biochimica et Biophysica Acta (BBA) - Biomembranes* **2000,** *1508* (1), 34-50.

113. Richter, R. P.; Bérat, R.; Brisson, A. R., Formation of solid-supported lipid bilayers: an integrated view. *Langmuir* **2006,** *22* (8), 3497-505.

114. Demchenko, A. P.; Mély, Y.; Duportail, G.; Klymchenko, A. S., Monitoring Biophysical Properties of Lipid Membranes by Environment-Sensitive Fluorescent Probes. *Biophys J* **2009,** *96* (9), 3461-3470.

115. Kaiser, H.-J.; Lingwood, D.; Levental, I.; Sampaio, J. L.; Kalvodova, L.; Rajendran, L.; Simons, K., Order of lipid phases in model and plasma membranes. *Proceedings of the National Academy of Sciences* **2009,** *106* (39), 16645.

116. Bitounis, D.; Fanciullino, R.; Iliadis, A.; Ciccolini, J., Optimizing Druggability through Liposomal Formulations: New Approaches to an Old Concept. *ISRN Pharmaceutics* **2012,** *2012*, 738432.

117. Malhotra, K.; Alder, N. N., Advances in the use of nanoscale bilayers to study membrane protein structure and function. *Biotechnology and Genetic Engineering Reviews* **2014,** *30* (1), 79-93.

118. Liguori, N.; Periole, X.; Marrink, S. J.; Croce, R., From light-harvesting to photoprotection: structural basis of the dynamic switch of the major antenna complex of plants (LHCII). *Sci Rep* **2015,** *5*, 15661.

119. Tutkus, M.; Akhtar, P.; Chmeliov, J.; Gorfol, F.; Trinkunas, G.; Lambrev, P. H.; Valkunas, L., Fluorescence Microscopy of Single Liposomes with Incorporated Pigment-Proteins. *Langmuir* **2018,** *34* (47), 14410-14418.

120. Crisafi, E.; Pandit, A., Disentangling Protein and Lipid Interactions that Control a Molecular Switch in Photosynthetic Light harvesting. *Biochim. Biophys. Acta, Biomembr.* **2017,** *1859* (1), 40-47.

121. Zhou, F.; Liu, S.; Hu, Z. H.; Kuang, T. Y.; Paulsen, H.; Yang, C. H., Effect of Monogalactosyldiacylglycerol on the Interaction between Photosystem II Core Complex and its Antenna Complexes in Liposomes of Thylakoid Lipids. *Photosynth. Res.* **2009,** *99* (3), 185-193.

122. Yang, C.; Boggasch, S.; Haase, W.; Paulsen, H., Thermal stability of trimeric light-harvesting chlorophyll a/b complex (LHCIIb) in liposomes of thylakoid lipids. *Biochim Biophys Acta* **2006,** *1757* (12), 1642-8.

123. Li, M.; Khan, S.; Rong, H.; Tuma, R.; Hatzakis, N. S.; Jeuken, L. J. C., Effects of membrane curvature and pH on proton pumping activity of single cytochrome bo(3) enzymes. *Biochim Biophys Acta Bioenerg* **2017,** *1858* (9), 763-770.

124. Moya, I.; Silvestri, M.; Vallon, O.; Cinque, G.; Bassi, R., Time-resolved fluorescence analysis of the photosystem II antenna proteins in detergent micelles and liposomes. *Biochemistry-Us* **2001,** *40* (42), 12552-12561.

125. Rouck, J. E.; Krapf, J. E.; Roy, J.; Huff, H. C.; Das, A., Recent advances in nanodisc technology for membrane protein studies (2012-2017). *Febs Lett* **2017,** *591* (14), 2057-2088.

126. Swainsbury, D. J. K.; Proctor, M. S.; Hitchcock, A.; Cartron, M. L.; Qian, P.; Martin, E. C.; Jackson, P. J.; Madsen, J.; Armes, S. P.; Hunter, C. N., Probing the local lipid environment of the Rhodobacter sphaeroides cytochrome bc(1) and Synechocystis sp. PCC 6803 cytochrome b(6)f complexes with styrene maleic acid. *Biochim Biophys Acta Bioenerg* **2018,** *1859* (3), 215-225.

127. Bhaduri, S.; Zhang, H.; Erramilli, S.; Cramer, W. A., Structural and functional contributions of lipids to the stability and activity of the photosynthetic cytochrome b (6) f lipoprotein complex. *J Biol Chem* **2019,** *294* (47), 17758-17767.

128. Zhou, F.; Liu, S.; Hu, Z.; Kuang, T.; Paulsen, H.; Yang, C., Effect of monogalactosyldiacylglycerol on the interaction between photosystem II core complex and its antenna complexes in liposomes of thylakoid lipids. *Photosynth Res* **2009,** *99* (3), 185-93.

129. Feng, X. Y.; Jia, Y.; Cai, P.; Fei, J. B.; Li, J. B., Coassembly of Photosystem II and ATPase as Artificial Chloroplast for Light-Driven ATP Synthesis. *ACS Nano* **2016,** *10* (1), 556-561.

130. Schaller, S.; Latowski, D.; Jemiola-Rzeminska, M.; Dawood, A.; Wilhelm, C.; Strzalka, K.; Goss, R., Regulation of LHCII Aggregation by Different Thylakoid Membrane Lipids. *Biochim. Biophys. Acta-Bioenerg.* **2011,** *1807* (3), 326-335.

131. Deme, B.; Cataye, C.; Block, M. A.; Marechal, E.; Jouhet, J., Contribution of Galactoglycerolipids to the 3 Dimensional Architecture of Thylakoids. *Faseb J.* **2014,** *28* (8), 3373-3383.

132. van Oudenaarden, A.; Boxer, S. G., Brownian ratchets: Molecular separations in lipid bilayers supported on patterned arrays. *Science* **1999,** *285* (5430), 1046-1048.

133. Okazaki, T.; Morigaki, K.; Taguchi, T., Phospholipid Vesicle Fusion on Micropatterned Polymeric Bilayer Substrates. *Biophys. J.* **2006,** *91* (5), 1757-1766.

134. Morigaki, K.; Baumgart, T.; Jonas, U.; Offenhausser, A.; Knoll, W., Photopolymerization of Diacetylene Lipid Bilayers and its Application to the Construction of Micropatterned Biomimetic Membranes. *Langmuir* **2002,** *18* (10), 4082-4089.

135. Oliver, A. E.; Parikh, A. N., Templating Membrane Assembly, Structure, and Dynamics using Engineered Interfaces. *Biochim. Biophys. Acta. Biomembr.* **2010,** *1798* (4), 839-850.

136. Hovis, J. S.; Boxer, S. G., Patterning and Composition Arrays of Supported Lipid Bilayers by Microcontact Printing. *Langmuir* **2001,** *17* (11), 3400-3405.

137. Adams, P. G.; Swingle, K. L.; Paxton, W. F.; Nogan, J. J.; Stromberg, L. R.; Firestone, M. A.; Mukundan, H.; Montano, G. A., Exploiting Lipopolysaccharide-Induced Deformation of Lipid Bilayers to Modify Membrane Composition and Generate Two-Dimensional Geometric Membrane Array Patterns. *Sci. Reports* **2015,** *5*.

138. Castellana, E. T.; Cremer, P. S., Solid supported lipid bilayers: From biophysical studies to sensor design. *Surface Science Reports* **2006,** *61* (10), 429-444.

139. Groves, J. T.; Boxer, S. G., Micropattern formation in supported lipid membranes. *Accounts of Chemical Research* **2002,** *35* (3), 149-157.

140. Yee, C. K.; Amweg, M. L.; Parikh, A. N., Membrane Photolithography: Direct Micropatterning and Manipulation of Fluid Phospholipid Membranes in the Aqueous Phase Using Deep-UV Light. *Advanced Materials* **2004,** *16* (14), 1184-1189.

141. Heath, G. R.; Roth, J.; Connell, S. D.; Evans, S. D., Diffusion in Low-Dimensional Lipid Membranes. *Nano Lett* **2014,** *14* (10), 5984-5988.

142. Morigaki, K.; Kiyosue, K.; Taguchi, T., Micropatterned composite membranes of polymerized and fluid lipid bilayers. *Langmuir* **2004,** *20* (18), 7729-7735.

143. Han, X.; Cheetham, M. R.; Sheikh, K.; Olmsted, P. D.; Bushby, R. J.; Evans, S. D., Manipulation and charge determination of proteins in photopatterned solid supported bilayers. *Integrative Biology* **2009,** *1* (2), 205-211.

144. Cheetham, M. R.; Bramble, J. P.; McMillan, D. G. G.; Bushby, R. J.; Olmsted, P. D.; Jeuken, L. J. C.; Evans, S. D., Manipulation and sorting of membrane proteins using patterned diffusion-aided ratchets with AC fields in supported lipid bilayers. *Soft Matter* **2012,** *8* (20), 5459-5465.

145. Bao, P.; Cheetham, M. R.; Roth, J. S.; Blakeston, A. C.; Bushby, R. J.; Evans, S. D., On-Chip Alternating Current Electrophoresis in Supported Lipid Bilayer Membranes. *Analytical Chemistry* **2012,** *84* (24), 10702-10707.

146. Groves, J. T.; Boxer, S. G., Electric field-induced concentration gradients in planar supported bilayers. *Biophys J* **1995,** *69* (5), 1972-1975.

147. Liu, C.; Monson, C. F.; Yang, T.; Pace, H.; Cremer, P. S., Protein Separation by Electrophoretic–Electroosmotic Focusing on Supported Lipid Bilayers. *Analytical Chemistry* **2011,** *83* (20), 7876-7880.

148. Bao, P.; Cartron, M. L.; Sheikh, K. H.; Johnson, B. R. G.; Hunter, C. N.; Evans, S. D., Controlling transmembrane protein concentration and orientation in supported lipid bilayers. *Chemical Communications* **2017,** *53* (30), 4250-4253.

149. Monson, C. F.; Pace, H. P.; Liu, C.; Cremer, P. S., Supported bilayer electrophoresis under controlled buffer conditions. *Analytical chemistry* **2011,** *83* (6), 2090-2096.

150. Boreham, A.; Brodwolf, R.; Walker, K.; Haag, R.; Alexiev, U., Time-Resolved Fluorescence Spectroscopy and Fluorescence Lifetime Imaging Microscopy for Characterization of Dendritic Polymer Nanoparticles and Applications in Nanomedicine. *Molecules* **2017,** *22* (1).

151. Becker, W., Introduction to Multi-dimensional TCSPC. In *Advanced Time-Correlated Single Photon Counting Applications*, Becker, W., Ed. Springer International Publishing: Cham, 2015; pp 1-63.

152. Hanson, K. M.; Barry, N. P.; Behne, M. J.; Mauro, T. M.; Gratton, E.; Clegg, R. M., Two-photon fluorescence lifetime imaging of the skin's stratum corneum pH gradient. *Biophys J* **2002,** *82* (1), 494A-494A.

153. Levchenko, S. M.; Pliss, A.; Qu, J. L., Fluorescence lifetime imaging of fluorescent proteins as an effective quantitative tool for noninvasive study of intracellular processes. *Journal of Innovative Optical Health Sciences* **2018,** *11* (1).

154. Shimolina, L. E.; Izquierdo, M. A.; Lopez-Duarte, I.; Bull, J. A.; Shirmanova, M. V.; Klapshina, L. G.; Zagaynova, E. V.; Kuimova, M. K., Imaging tumor microscopic viscosity in vivo using molecular rotors. *Sci Rep-Uk* **2017,** *7*.

155. Kuimova, M. K.; Yahioglu, G.; Levitt, J. A.; Suhling, K., Molecular rotor measures viscosity of live cells via fluorescence lifetime imaging. *Journal of the American Chemical Society* **2008,** *130* (21), 6672-+.

156. Okabe, K.; Inada, N.; Gota, C.; Harada, Y.; Funatsu, T.; Uchiyama, S., Intracellular temperature mapping with a fluorescent polymeric thermometer and fluorescence lifetime imaging microscopy. *Nature Communications* **2012,** *3*.

157. Skala, M. C.; Riching, K. M.; Gendron-Fitzpatrick, A.; Eickhoff, J.; Eliceiri, K. W.; White, J. G.; Ramanujam, N., In vivo multiphoton microscopy of NADH and FAD redox states, fluorescence lifetimes, and cellular morphology in precancerous epithelia. *P Natl Acad Sci USA* **2007,** *104* (49), 19494-19499.

158. Kalinina, S.; Breymayer, J.; Schafer, P.; Calzia, E.; Shcheslavskiy, V.; Becker, W.; Ruck, A., Correlative NAD(P)H-FLIM and oxygen sensing-PLIM for metabolic mapping. *Journal of Biophotonics* **2016,** *9* (8), 800-811.

159. Luo, T.; Lin, D. Y.; Zhou, T.; Lu, Y.; Liu, S. X.; Qu, J. L., Identification and characterization of different tissues in blood vessel by multiplexed fluorescence lifetimes. *Analyst* **2018,** *143* (10), 2243-2248.

160. Bergmann, A.; Becker, W., Multiwavelength fluorescence lifetime imaging by TCSPC. In *Advanced Photon Counting Techniques*, Becker, W., Ed. 2006; Vol. 6372.

161. Grant, D. M.; Zhang, W.; McGhee, E. J.; Bunney, T. D.; Talbot, C. B.; Kumar, S.; Munro, I.; Dunsby, C.; Neil, M. A. A.; Katan, M.; French, P. M. W., Multiplexed FRET to Image Multiple Signaling Events in Live Cells. *Biophys J* **2008,** *95* (10), L69-L71.

162. Yoneda, T.; Tanimoto, Y.; D., T.; Morigaki, K., Photosynthetic Model Membranes of Natural Plant Thylakoid Embedded in a Patterned Polymeric Lipid Bilayer. *Langmuir* **2020,** *36* (21), 5863-5871.

163. Grab, O.; Abacilar, M.; Daus, F.; Geyer, A.; Steinem, C., 3D-Membrane Stacks on Supported Membranes Composed of Diatom Lipids Induced by Long-Chain Polyamines. *Langmuir* **2016,** *32* (39), 10144-10152.

164. Morigaki, K.; Baumgart, T.; Offenhausser, A.; Knoll, W., Patterning Solid-supported Lipid Bilayer Membranes by Lithographic Polymerization of a Diacetylene Lipid. *Angew. Chem. Int.* **2001,** *40* (1), 172-174.

165. Murphy, D. J.; Woodrow, I. E., Lateral heterogeneity in the distribution of thylakoid membrane lipid and protein-components and its implications for the molecular-organization of photosynthetic membranes. *Biochim Biophys Acta* **1983,** *725* (1), 104-112.

166. Kirchhoff, H., Structure-function Relationships in Photosynthetic Membranes: Challenges and Emerging Fields. *Plant Sci.* **2018,** *266*, 76-82.

167. Sener, M.; Strumpfer, J.; Singharoy, A.; Hunter, C. N.; Schulten, K., Overall Energy Conversion Efficiency of a Photosynthetic Vesicle. *eLife* **2016,** *5*, e09541.

168. Cartron, M. L.; Olsen, J. D.; Sener, M.; Jackson, P. J.; Brindley, A. A.; Qian, P.; Dickman, M. J.; Leggett, G. J.; Schulten, K.; Hunter, C. N., Integration of Energy and Electron Transfer

Processes in the Photosynthetic Membrane of *Rhodobacter Sphaeroides*. *Biochim. Biophys. Acta-Bioenerg.* **2014,** *1837* (10), 1769-1780.

169. Goral, T. K.; Johnson, M. P.; Duffy, C. D. P.; Brain, A. P. R.; Ruban, A. V.; Mullineaux, C. W., Light-harvesting antenna composition controls the macrostructure and dynamics of thylakoid membranes in Arabidopsis. *Plant J.* **2012,** *69* (2), 289-301.

170. Scheuring, S.; Sturgis, J. N., Chromatic Adaptation of Photosynthetic Membranes. *Science* **2005,** *309* (5733), 484-487.

171. Escalante, M.; Lenferink, A.; Zhao, Y. P.; Tas, N.; Huskens, J.; Hunter, C. N.; Subramaniam, V.; Otto, C., Long-Range Energy Propagation in Nanometer Arrays of Light Harvesting Antenna Complexes. *Nano Lett.* **2010,** *10* (4), 1450-1457.

172. Huang, X.; Vasilev, C.; Hunter, C. N., Excitation Energy Transfer between Monomolecular Layers of Light Harvesting LH2 and LH1 Reaction Centre Complexes Printed on a Glass Substrate. *Lab Chip* **2020,** *20* (14), 2529-2538.

173. Liu, C.; Gao, Z. M.; Liu, K.; Sun, R. X.; Cui, C. B.; Holzwarth, A. R.; Yang, C. H., Simultaneous Refolding of Denatured PsbS and Reconstitution with LHCII into Liposomes of Thylakoid Lipids. *Photosynth. Res.* **2016,** *127* (1), 109-116.

174. Wilk, L.; Grunwald, M.; Liao, P. N.; Walla, P. J.; Kuhlbrandt, W., Direct Interaction of the Major Light-Harvesting Complex II and PsbS in Nonphotochemical Quenching. *Proc. Natl. Acad. Sci. U. S. A.* **2013,** *110* (14), 5452-5456.

175. Morigaki, K.; Tanimoto, Y., Evolution and Development of Model Membranes for Physicochemical and Functional Studies of the Membrane Lateral Heterogeneity. *Biochim. Biophys. Acta. Biomembr.* **2018,** *1860* (10), 2012-2017.

176. Asgari, M.; Biria, A., Free Energy of the Edge of an Open Lipid Bilayer based on the Interactions of its Constituent Molecules. *Int. J. Nonlin. Mech.* **2015,** *76*, 135-143.

177. Dewa, T.; Sumino, A.; Watanabe, N.; Noji, T.; Nango, M., Energy Transfer and Clustering of Photosynthetic Light-harvesting Complexes in Reconstituted Lipid Membranes. *Chem. Phys.* **2013,** *419*, 200-204.

178. Uragami, C.; Sugai, Y.; Hanjo, K.; Sumino, A.; Fujii, R.; Nishioka, T.; Kinoshita, I.; Dewa, T.; Nango, M.; Gardiner, A. T.; Cogdell, R. J.; Hashimoto, H., Observation of Hybrid Artificial Photosynthetic Membranes using Peripheral and Core Antennae from Two Different Species of Photosynthetic Bacteria by AFM and Fluorescence Micro-spectroscopy. *J. Photochem. Photobiol., A* **2015,** *313*, 60-71.

179. Sumino, A.; Dewa, T.; Kondo, M.; Morii, T.; Hashimoto, H.; Gardiner, A. T.; Cogdell, R. J.; Nango, M., Selective Assembly of Photosynthetic Antenna Proteins into a Domain-Structured Lipid Bilayer for the Construction of Artificial Photosynthetic Antenna Systems: Structural Analysis of the Assembly Using Surface Plasmon Resonance and Atomic Force Microscopy. *Langmuir* **2011,** *27* (3), 1092-1099.

180. Bittner, T.; Irrgang, K. D.; Renger, G.; Wasielewski, M. R., Ultrafast excitation-energy transfer and exciton-exciton annihilation processes in isolated light-harvesting complexes of photosystem-II (LHC-II) from spinach. *J Phys Chem-Us* **1994,** *98* (46), 11821-11826.

181. Gillbro, T.; Sandstrom, A.; Spangfort, M.; Sundstrom, V.; Vangrondelle, R., Excitation-energy annihilation in aggregates of chlorophyll a/b complexes. *Biochim Biophys Acta* **1988,** *934* (3), 369-374.

182. Wentworth, M.; Ruban, A. V.; Horton, P., The Functional Significance of the Monomeric and Trimeric States of the Photosystem II Light Harvesting Complexes. *Biochem.* **2004,** *43* (2), 501-509.

183. Caffarri, S.; Tibiletti, T.; Jennings, R. C.; Santabarbara, S., A Comparison Between Plant Photosystem I and Photosystem II Architecture and Functioning. *Curr Protein Pept Sc.* **2014,** *15* (4), 296-331.

184. Johnson, M. P.; Ruban, A. V., Photoprotective Energy Dissipation in Higher Plants Involves Alteration of the Excited State Energy of the Emitting Chlorophyll(s) in the Light Harvesting Antenna II (LHCII). *J. Biol. Chem.* **2009,** *284* (35), 23592-23601.

185. Lakowicz, J. R., Energy Transfer. In *Principles of Fluorescence Spectroscopy*, 3rd ed.; Springer: Boston, MA, 2006; pp 443-475.

186. Broess, K.; Borst, J. W.; van Amerongen, H., Applying Two-photon Excitation Fluorescence Lifetime Imaging Microscopy to Study Photosynthesis in Plant Leaves. *Photosynth. Res.* **2009,** *100* (2), 89-96.

187. Farooq, S.; Chmeliov, J.; Wientjes, E.; Koehorst, R.; Bader, A.; Valkunas, L.; Trinkunas, G.; van Amerongen, H., Dynamic Feedback of the Photosystem II Reaction Centre on Photoprotection in Plants. *Nat. Plants* **2018,** *4* (4), 225-231.

188. Chukhutsina, V. U.; Holzwarth, A. R.; Croce, R., Time-resolved Fluorescence Measurements on Leaves: Principles and Recent Developments. *Photosynth. Res.* **2019,** *140* (3), 355-369.

189. Petrou, K.; Belgio, E.; Ruban, A. V., pH Sensitivity of Chlorophyll Fluorescence Quenching is Determined by the Detergent/Protein Ratio and the State of LHCII Aggregation. *Biochim. Biophys. Acta-Bioenerg.* **2014,** *1837* (9), 1533-1539.

190. Hills, R. D.; McGlinchey, N., Model Parameters for Simulation of Physiological Lipids. *J. Comput. Chem.* **2016,** *37* (12), 1112-1118.

191. Bagatolli, L. A., To see or not to see: Lateral organization of biological membranes and fluorescence microscopy. *Bba-Biomembranes* **2006,** *1758* (10), 1541-1556.

192. Bagatolli, L. A., The Lateral Structure of Lipid Membranes as Seen by Fluorescence Microscopy. In *Fluorescence Spectroscopy in Biology: Advanced Methods and their Applications to Membranes, Proteins, DNA, and Cells*, Hof, M.; Hutterer, R.; Fidler, V., Eds. Springer Berlin Heidelberg: Berlin, Heidelberg, 2005; pp 150-159.

193. Sackmann, E., Supported membranes: scientific and practical applications. *Science* **1996,** *271* (5245), 43-8.

194. Chiho, H.; Tinglu, Y.; Sho, K.; Paul, S. C.; Siegfried, M. M., Effect of Average Phospholipid Curvature on Supported Bilayer Formation on Glass by Vesicle Fusion. *Biophys J* **2006,** *90* (4), 1241-1248.

195. Zhang, H.-Y.; Hill, R. J., Concentration dependence of lipopolymer self-diffusion in supported bilayer membranes. *J R Soc Interface* **2011,** *8* (54), 127-143.

196. Attwood, S. J.; Choi, Y.; Leonenko, Z., Preparation of DOPC and DPPC Supported Planar Lipid Bilayers for Atomic Force Microscopy and Atomic Force Spectroscopy. *Int. J. Mol. Sci.* **2013,** *14* (2), 3514-3539.

197. Alberts, B.; Johnson, A.; Lewis, J.; al., E., *Molecular Biology of the Cell: Membrane Proteins*. Garland Science;: New York:, 2002; Vol. 4th edition.

198. Langmuir, I., The Adsorption of Gases on Plane Surfaces of Glass, Mica and Platinum. *J. Am. Chem. Soc.* **1918,** *40*, 1361-1403.

199. Gabdoulline, R. R.; Wade, R. C., Protein-protein association: Investigation of factors influencing association rates by Brownian dynamics simulations. *J. Mol. Biol.* **2001,** *306* (5), 1139-1155.

200. Heath, G. R.; Li, M. Q.; Rong, H. L.; Radu, V.; Frielingsdorf, S.; Lenz, O.; Butt, J. N.; Jeuken, L. J. C., Multilayered Lipid Membrane Stacks for Biocatalysis Using Membrane Enzymes. *Adv. Funct. Mater.* **2017,** *27*, 1606265.

201. Zhang, J. Z.; Reisner, E., Advancing Photosystem II Photoelectrochemistry for Semi-Artificial Photosynthesis. *Nat. Rev. Chem.* **2020,** *4* (1), 6-21.

202. Ryu, D.; Kim, Y. J.; Kim, S. I.; Hong, H.; Ahn, H. S.; Kim, K.; Ryu, W., Thylakoid-Deposited Micro-Pillar Electrodes for Enhanced Direct Extraction of Photosynthetic Electrons. *Nanomaterials* **2018,** *8* (4), 189.

203. Longatte, G.; Fu, H. Y.; Buriez, O.; Labbe, E.; Wollman, F. A.; Amatore, C.; Rappaport, F.; Guille-Collignon, M.; Lemaitre, F., Evaluation of Photosynthetic Electrons Derivation by Exogenous Redox Mediators. *Biophys. Chem.* **2015,** *205*, 1-8.

204. Karukstis, K. K., Chlorophyll Fluorescence Analyses of Photosystem-II Reaction Center Heterogeneity. *J. Photochem. Photobiol., B* **1992,** *15* (1-2), 63-74.

205. Farias, M. E.; Martinazzo, E. G.; Bacarin, M. A., Chlorophyll Fluorescence in the Evaluation of Photosynthetic Electron Transport Chain Inhibitors in the Pea. *Rev. Cienc. Agron.* **2016,** *47* (1), 178-186.

206. Dewez, D.; Ali, N. A.; Perreault, F.; Popovic, R., Rapid Chlorophyll a Fluorescence Transient of *Lemna gibba* Leaf as an Indication of Light and Hydroxylamine Effect on Photosystem II Activity. *Photochem. Photobiol. Sci.* **2007,** *6* (5), 532-538.

207. Prasil, O.; Kolber, Z. S.; Falkowski, P. G., Control of the Maximal Chlorophyll Fluorescence Yield by the Q_B Binding Site. *Photosynthetica* **2018,** *56* (1), 150-162.

208. Cheniae, G. M.; Martin, I. F., Effects of Hydroxylamine on Photosystem-II Photoreversal of NH_2OH Destruction of O2 Evolution. *Plant Physiol.* **1972,** *50* (1), 94.

209. Beck, W. F.; Brudvig, G. W., Reactions of Hydroxylamine with the Electron-donor Side of Photosystem-II. *Biochem.* **1987,** *26* (25), 8285-8295.

210. Debus, R. J., The manganese and calcium-ions of photosynthetic oxygen evolution. *Biochim Biophys Acta* **1992,** *1102* (3), 269-352.

211. Ghanotakis, D. F.; Babcock, G. T., Hydroxylamine as an Inhibitor between Z and P680 in Photosystem-II. *FEBS Lett.* **1983,** *153* (1), 231-234.

212. Kruger, T. P. J.; van Grondelle, R., The Role of Energy Losses in Photosynthetic Light Harvesting. *J. Phys. B: At., Mol. Opt. Phys.* **2017,** *50* (13), 14.

213. Ostroumov, E. E.; Goetze, J. P.; Reus, M.; Lambrev, P. H.; Holzwarth, A. R., Characterization of fluorescent chlorophyll charge-transfer states as intermediates in the excited state quenching of light-harvesting complex II. *Photosynth Res* **2020,** *144* (2), 171-193.

214. Cupellini, L.; Calvani, D.; Jacquemin, D.; Mennucci, B., Charge transfer from the carotenoid can quench chlorophyll excitation in antenna complexes of plants. *Nature Communications* **2020,** *11* (1), 662.

215. Ramanan, C.; Ferretti, M.; van Roon, H.; Novoderezhkin, V. I.; van Grondelle, R., Evidence for coherent mixing of excited and charge-transfer states in the major plant light-harvesting antenna, LHCII. *Phys. Chem. Chem. Phys.* **2017,** *19* (34), 22877-22886.

216. Nagata, M.; Amano, M.; Joke, T.; Fujii, K.; Okuda, A.; Kondo, M.; Ishigure, S.; Dewa, T.; Iida, K.; Secundo, F.; Amao, Y.; Hashimoto, H.; Nango, M., Immobilization and Photocurrent Activity of a Light-Harvesting Antenna Complex II, LHCII, Isolated from a Plant on Electrodes. *Acs Macro Letters* **2012,** *1* (2), 296-299.

217. Kondo, M.; Matsuda, H.; Noji, T.; Nango, M.; Dewa, T., Photocatalytic activity of the light-harvesting complex of photosystem II (LHCII) monomer. *J. Photochem. Photobiol. A-Chem.* **2021,** *406*.

218. Macdonald, G. M.; Steenhuis, J. J.; Barry, B. A., A difference fourier-transform infrared spectroscopy study of chlorophyll oxidation in hydroxlamine-treated photosystem-II. *J Biol Chem* **1995,** *270* (15), 8420-8428.

219. Yocum, C. F.; Yerkes, C. T.; Blankenship, R. E.; Sharp, R. R.; Babcock, G. T., Stoichiometry, inhibitor sensitivity and organization of manganese associated with photosynthetic oxygen evolution. *P Natl Acad Sci-Biol* **1981,** *78* (12), 7507-7511.

220. Rashid, A.; Popovic, R., Requirement of manganese for the photooxidation of hydroxylamine by photosystem-II. *J Photoch Photobio B* **1992,** *13* (3-4), 323-326.

221. Kretschmann, H.; Pauly, S.; Witt, H. T., Evidence for a chemical-reaction of hydroxylamine with the photosynthetic water splitting enzyme-s in the dark - possible states of manganese and water in the s-cycle. *Biochim Biophys Acta* **1991,** *1059* (2), 208-214.

222. Wexler, P., Encyclopedia of toxicology (Second edition). **2005**, 557-558.

223. Bao, P.; Cartron, M. L.; Sheikh, K. H.; Johnson, B. R. G.; Hunter, C. N.; Evans, S. D., Controlling Transmembrane Protein Concentration and Orientation in Supported Lipid Bilayers. *Chem. Commun.* **2017,** *53* (30), 4250-4253.

224. Jonsson, P.; Gunnarsson, A.; Hook, F., Accumulation and Separation of Membrane-Bound Proteins Using Hydrodynamic Forces. *Anal. Chem.* **2011,** *83* (2), 604-611.

225. Lichtenberg, D.; Ahyayauch, H.; Alonso, A.; Goni, F. M., Detergent solubilization of lipid bilayers: a balance of driving forces. *Trends Biochem.Sci.* **2013,** *38* (2), 85-93.

226. Lichtenberg, D.; Ahyayauch, H.; Goni, F. M., The Mechanism of Detergent Solubilization of Lipid Bilayers. *Biophys J* **2013,** *105* (2), 289-299.

227. Heath, G. R.; Scheuring, S., High-speed AFM height spectroscopy reveals μs-dynamics of unlabeled biomolecules. *Nat Commun* **2018,** *9* (1), 4983.

228. Matin, T. R.; Heath, G. R.; Huysmans, G. H. M.; Boudker, O.; Scheuring, S., Millisecond dynamics of an unlabeled amino acid transporter. *Nature Communications* **2020,** *11* (1), 5016.

229. Tserkovnyak, Y.; Nelson, D. R., Conditions for extreme sensitivity of protein diffusion in membranes to cell environments. *Proceedings of the National Academy of Sciences* **2006,** *103* (41), 15002-15007.

230. Briones, R.; Aponte-Santamaría, C.; de Groot, B. L., Localization and Ordering of Lipids Around Aquaporin-0: Protein and Lipid Mobility Effects. *Front Physiol* **2017,** *8*, 124.

231. Vaz, W. L.; Kapitza, H. G.; Stümpel, J.; Sackmann, E.; Jovin, T. M., Translational mobility of glycophorin in bilayer membranes of dimyristoylphosphatidylcholine. *Biochemistry-Us* **1981,** *20* (5), 1392-6.

232. Tamura, F.; Tanimoto, Y.; Nagai, R.; Hayashi, F.; Morigaki, K., Self-Spreading of Phospholipid Bilayer in a Patterned Framework of Polymeric Bilayer. *Langmuir* **2019,** *35* (45), 14696-14703.

233. de Bianchi, S.; Betterle, N.; Kouril, R.; Cazzaniga, S.; Boekema, E.; Bassi, R.; Dall'Osto, L., Arabidopsis Mutants Deleted in the Light-Harvesting Protein Lhcb4 Have a Disrupted Photosystem II Macrostructure and Are Defective in Photoprotection. *The Plant Cell* **2011,** *23* (7), 2659-2679.

234. Alboresi, A.; Dall'Osto, L.; Aprile, A.; Carillo, P.; Roncaglia, E.; Cattivelli, L.; Bassi, R., Reactive oxygen species and transcript analysis upon excess light treatment in wild-type

Arabidopsis thaliana vs a photosensitive mutant lacking zeaxanthin and lutein. *BMC Plant Biology* **2011,** *11* (1), 62.

235. Heath, G. R.; Li, M.; Polignano, I. L.; Richens, J. L.; Catucci, G.; O'Shea, P.; Sadeghi, S. J.; Gilardi, G.; Butt, J. N.; Jeuken, L. J. C., Layer-by-Layer Assembly of Supported Lipid Bilayer Poly-L-Lysine Multilayers. *Biomacromolecules* **2016,** *17* (1), 324-335.

236. Adams, P. G.; Lamoureux, L.; Swingle, K. L.; Mukundan, H.; Montano, G. A., Lipopolysaccharide-Induced Dynamic Lipid Membrane Reorganization: Tubules, Perforations, and Stacks. *Biophys. J.* **2014,** *106* (11), 2395-2407.

237. Gundlach, K.; Werwie, M.; Wiegand, S.; Paulsen, H., Filling the "green gap" of the major light-harvesting chlorophyll a/b complex by covalent attachment of Rhodamine Red. *Bba-Bioenergetics* **2009,** *1787* (12), 1499-1504.

238. Harris, M. A.; Jiang, J. B.; Niedzwiedzki, D. M.; Jiao, J. Y.; Taniguchi, M.; Kirmaier, C.; Loach, P. A.; Bocian, D. F.; Lindsey, J. S.; Holten, D.; Parkes-Loach, P. S., Versatile design of biohybrid light-harvesting architectures to tune location, density, and spectral coverage of attached synthetic chromophores for enhanced energy capture. *Photosynth Res* **2014,** *121* (1), 35-48.

239. Yoneda, Y.; Noji, T.; Katayama, T.; Mizutani, N.; Komori, D.; Nango, M.; Miyasaka, H.; Itoh, S.; Nagasawa, Y.; Dewa, T., Extension of Light-Harvesting Ability of Photosynthetic Light-Harvesting Complex 2 (LH2) through Ultrafast Energy Transfer from Covalently Attached Artificial Chromophores. *Journal of the American Chemical Society* **2015,** *137* (40), 13121-13129.

240. Springer, J. W.; Parkes-Loach, P. S.; Reddy, K. R.; Krayer, M.; Jiao, J. Y.; Lee, G. M.; Niedzwiedzki, D. M.; Harris, M. A.; Kirmaier, C.; Bocian, D. F.; Lindsey, J. S.; Holten, D.; Loach, P. A., Biohybrid Photosynthetic Antenna Complexes for Enhanced Light-Harvesting. *Journal of the American Chemical Society* **2012,** *134* (10), 4589-4599.

241. Schmitt, F. J.; Maksimov, E. G.; Hatti, P.; Weissenborn, J.; Jeyasangar, V.; Razjivin, A. P.; Paschenko, V. Z.; Friedrich, T.; Renger, G., Coupling of different isolated photosynthetic light harvesting complexes and CdSe/ZnS nanocrystals via Forster resonance energy transfer. *Bba-Bioenergetics* **2012,** *1817* (8), 1461-1470.

242. Werwie, M.; Xu, X. X.; Haase, M.; Basche, T.; Paulsen, H., Bio Serves Nano: Biological Light-Harvesting Complex as Energy Donor for Semiconductor Quantum Dots. *Langmuir* **2012,** *28* (13), 5810-5818.

243. Sahin, T.; Harris, M. A.; Vairaprakash, P.; Niedzwiedzki, D. M.; Subramanian, V.; Shreve, A. P.; Bocian, D. F.; Holten, D.; Lindsey, J. S., Self-Assembled Light-Harvesting System from Chromophores in Lipid Vesicles. *J Phys Chem B* **2015,** *119* (32), 10231-10243.

244. De Leo, V.; Catucci, L.; Falqui, A.; Marotta, R.; Striccoli, M.; Agostiano, A.; Comparelli, R.; Milano, F., Hybrid Assemblies of Fluorescent Nanocrystals and Membrane Proteins in Liposomes. *Langmuir* **2014,** *30* (6), 1599-1608.

245. Lukashev, E. P.; Knox, P. P.; Gorokhov, V. V.; Grishanova, N. P.; Seifullina, N. K.; Krikunova, M.; Lokstein, H.; Paschenko, V. Z., Purple-bacterial photosynthetic reaction centers and quantum-dot hybrid-assemblies in lecithin liposomes and thin films. *J Photoch Photobio B* **2016,** *164*, 73-82.

246. Lord, S. J.; Lu, Z.; Wang, H.; Willets, K. A.; Schuck, P. J.; Lee, H.-l. D.; Nishimura, S. Y.; Twieg, R. J.; Moerner, W. E., Photophysical Properties of Acene DCDHF Fluorophores: Long-Wavelength Single-Molecule Emitters Designed for Cellular Imaging. *The Journal of Physical Chemistry A* **2007,** *111* (37), 8934-8941.

247. Geertsma, E. R.; Nik Mahmood, N. A.; Schuurman-Wolters, G. K.; Poolman, B., Membrane reconstitution of ABC transporters and assays of translocator function. *Nat Protoc* **2008,** *3* (2), 256-66.

248. Schubert, R., Liposome Preparation by Detergent Removal. In *Methods in Enzymology*, Academic Press: 2003; Vol. 367, pp 46-70.

249. Croce, R.; Mozzo, M.; Morosinotto, T.; Romeo, A.; Hienerwadel, R.; Bassi, R., Singlet and triplet state transitions of carotenoids in the antenna complexes of higher-plant Photosystem I. *Biochemistry-Us* **2007,** *46* (12), 3846-3855.

250. Subramanian, V.; Zurek, N. A.; Evans, D. G.; Shreve, A. P., Predictive modeling of broad wavelength light-harvesting performance in assemblies of multiple chromophores. *Journal of Photochemistry and Photobiology A: Chemistry* **2018,** *367*, 105-114.

251. Yaghoubi, H.; Schaefer, M.; Yaghoubi, S.; Jun, D.; Schlaf, R.; Beatty, J. T.; Takshi, A., A ZnO nanowire bio-hybrid solar cell. *Nanotechnology* **2017,** *28* (5), 054006.

252. Csiki, R.; Drieschner, S.; Lyuleeva, A.; Cattani-Scholz, A.; Stutzmann, M.; Garrido, J. A., Photocurrent generation of biohybrid systems based on bacterial reaction centers and graphene electrodes. *Diamond and Related Materials* **2018,** *89*, 286-292.

253. Friebe, V. M.; Frese, R. N., Photosynthetic reaction center-based biophotovoltaics. *Current Opinion in Electrochemistry* **2017,** *5* (1), 126-134.

254. Kang, M.; Tuteja, M.; Centrone, A.; Topgaard, D.; Leal, C., Nanostructured Lipid-based Films for Substrate Mediated Applications in Biotechnology. *Adv Funct Mater* **2018,** *28*.

255. Milano, F.; Punzi, A.; Ragni, R.; Trotta, M.; Farinola, G. M., Photonics and Optoelectronics with Bacteria: Making Materials from Photosynthetic Microorganisms. *Advanced Functional Materials* **2019,** *29* (21), 1805521.

256. Hubbard, J. A. M.; Evans, M. C. W., Electron Acceptors in Photosystem II. In *Techniques and New Developments in Photosynthesis Research*, Barber, J.; Malkin, R., Eds. Springer US: Boston, MA, 1989; pp 237-239.

257. Zhang, J. Z.; Sokol, K. P.; Paul, N.; Romero, E.; van Grondelle, R.; Reisner, E., Competing charge transfer pathways at the photosystem II–electrode interface. *Nature Chemical Biology* **2016,** *12* (12), 1046-1052.

258. Roy, S.; Gao, Z., Direct-write fabrication of a nanoscale digital logic element on a single nanowire. *Nanotechnology* **2010,** *21* (24), 245306.

259. Le Thai, M.; Chandran, G. T.; Dutta, R. K.; Li, X.; Penner, R. M., 100k Cycles and Beyond: Extraordinary Cycle Stability for MnO2 Nanowires Imparted by a Gel Electrolyte. *ACS Energy Letters* **2016,** *1* (1), 57-63.

260. Zhang, A.; Lieber, C. M., Nano-Bioelectronics. *Chem Rev* **2016,** *116* (1), 215-57.

261. Ravi, S. K.; Yu, Z.; Swainsbury, D. J. K.; Ouyang, J.; Jones, M. R.; Tan, S. C., Enhanced Output from Biohybrid Photoelectrochemical Transparent Tandem Cells Integrating Photosynthetic Proteins Genetically Modified for Expanded Solar Energy Harvesting. *Advanced Energy Materials* **2017,** *7* (7), 1601821.

262. Ciesielski, P. N.; Faulkner, C. J.; Irwin, M. T.; Gregory, J. M.; Tolk, N. H.; Cliffel, D. E.; Jennings, G. K., Enhanced Photocurrent Production by Photosystem I Multilayer Assemblies. *Advanced Functional Materials* **2010,** *20* (23), 4048-4054.

263. Lubart, Q.; Hannestad, J. K.; Pace, H.; Fjällborg, D.; Westerlund, F.; Esbjörner, E. K.; Bally, M., Lipid vesicle composition influences the incorporation and fluorescence properties of the lipophilic sulphonated carbocyanine dye SP-DiO. *Phys. Chem. Chem. Phys.* **2020,** *22* (16), 8781-8790.

264. Jensen, K. H.; Berg, R. W., CLARITY-compatible lipophilic dyes for electrode marking and neuronal tracing. *Sci Rep* **2016,** *6*, 32674.

265. Kirst, H.; Gabilly, S. T.; Niyogi, K. K.; Lemaux, P. G.; Melis, A., Photosynthetic antenna engineering to improve crop yields. *Planta* **2017,** *245* (5), 1009-1020.

266. Anemaet, I. G.; Bekker, M.; Hellingwerf, K. J., Algal photosynthesis as the primary driver for a sustainable development in energy, feed, and food production. *Mar Biotechnol (NY)* **2010,** *12* (6), 619-29.

267. Boulu, L. G.; Patterson, L. K.; Chauvet, J. P.; Kozak, J. J., Theoretical investigation of fluorescence concentration quenching in two-dimensional disordered systems. Application to chlorophyll a in monolayers of dioleylphosphatidylcholine. *The Journal of Chemical Physics* **1987,** *86* (2), 503-507.

268. Brennan, J. D.; Brown, R. S.; Krull, U. J., Self-quenching of nitrobenzoxadiazole labeled phospholipids in lipid membranes. *Biophys J* **1996,** *70* (2), MP321-MP321.

269. MacDonald, R. I., Characteristics of self-quenching of the fluorescence of lipid-conjugated rhodamine in membranes. *J Biol Chem* **1990,** *265* (23), 13533-13539.

270. Dahim, M.; Mizuno, N. K.; Li, X.-M.; Momsen, W. E.; Momsen, M. M.; Brockman, H. L., Physical and Photophysical Characterization of a BODIPY Phosphatidylcholine as a Membrane Probe. *Biophys J* **2002,** *83* (3), 1511-1524.

271. Brown, R. S.; Brennan, J. D.; Krull, U. J., Self-quenching of nitrobenzoxadiazole labeled phospholipids in lipid membranes. *The Journal of Chemical Physics* **1994,** *100* (8), 6019-6027.

272. Knoester, J.; Van Himbergen, J. E., Monte Carlo simulations on concentration self-quenching by statistical traps. *The Journal of Chemical Physics* **1987,** *86* (6), 3577-3582.

273. Knoester, J.; Van Himbergen, J. E., On the theory of concentration self-quenching by statistical traps. *The Journal of Chemical Physics* **1987,** *86* (6), 3571-3576.

274. Watson, W. F.; Livingston, R., Self-Quenching and Sensitization of Fluorescence of Chlorophyll Solutions. *The Journal of Chemical Physics* **1950,** *18* (6), 802-809.

275. Dexter, D. L.; Schulman, J. H., Theory of Concentration Quenching in Inorganic Phosphors. *The Journal of Chemical Physics* **1954,** *22* (6), 1063-1070.

276. Baumann, J.; Fayer, M. D., Excitation transfer in disordered two-dimensional and anisotropic three-dimensional systems: Effects of spatial geometry on time-resolved observables. *The Journal of Chemical Physics* **1986,** *85* (7), 4087-4107.

277. Zumofen, G.; Blumen, A., Energy transfer as a random walk. II. Two-dimensional regular lattices. *The Journal of Chemical Physics* **1982,** *76* (7), 3713-3731.

278. Daniel, S.; Diaz, A. J.; Martinez, K. M.; Bench, B. J.; Albertorio, F.; Cremer, P. S., Separation of Membrane-Bound Compounds by Solid-Supported Bilayer Electrophoresis. *Journal of the American Chemical Society* **2007,** *129* (26), 8072-8073.

279. van Weerd, J.; Krabbenborg, S. O.; Eijkel, J.; Karperien, M.; Huskens, J.; Jonkheijm, P., On-Chip Electrophoresis in Supported Lipid Bilayer Membranes Achieved Using Low Potentials. *Journal of the American Chemical Society* **2014,** *136* (1), 100-103.

280. Nabika, H.; Takimoto, B.; Murakoshi, K., Molecular separation in the lipid bilayer medium: electrophoretic and self-spreading approaches. *Analytical and Bioanalytical Chemistry* **2008,** *391* (7), 2497-2506.

281. Poyton, M. F.; Cremer, P. S., Electrophoretic Measurements of Lipid Charges in Supported Bilayers. *Analytical Chemistry* **2013,** *85* (22), 10803-10811.

282. Tian, H.; Chen, K., Solvent effect on the triplet lifetime of some rhodamine dyes. *Dyes and Pigments* **1994,** *26* (3), 167-174.

283. Lin, S.; Struve, W. S., Time-resolved fluorescence of nitrobenzoxadiazole-aminohexanoic acid: effect of intermolecular hydrogen-bonding on non-radiative decay. *Photochem Photobiol* **1991,** *54* (3), 361-5.

284. Raghuraman, H.; Shrivastava, S.; Chattopadhyay, A., Monitoring the looping up of acyl chain labeled NBD lipids in membranes as a function of membrane phase state. *Biochimica et Biophysica Acta (BBA) - Biomembranes* **2007,** *1768* (5), 1258-1267.

285. Karolin, J.; Johansson, L. B. A.; Strandberg, L.; Ny, T., Fluorescence and Absorption Spectroscopic Properties of Dipyrrometheneboron Difluoride (BODIPY) Derivatives in Liquids, Lipid Membranes, and Proteins. *Journal of the American Chemical Society* **1994,** *116* (17), 7801-7806.

286. Brismar, H.; Trepte, O.; Ulfhake, B., Spectra and fluorescence lifetimes of lissamine rhodamine, tetramethylrhodamine isothiocyanate, texas red, and cyanine 3.18 fluorophores: influences of some environmental factors recorded with a confocal laser scanning microscope. *J Histochem Cytochem* **1995,** *43* (7), 699-707.

287. Farsad, K.; De Camilli, P., Mechanisms of membrane deformation. *Curr. Opin. Cell Biol.* **2003,** *15* (4), 372-381.

288. Skaug, M. J.; Longo, M. L.; Faller, R., The Impact of Texas Red on Lipid Bilayer Properties. *The Journal of Physical Chemistry B* **2011,** *115* (26), 8500-8505.

289. Chandrasekhar, S., Stochastic Problems in Physics and Astronomy. *Reviews of Modern Physics* **1943,** *15* (1), 1-89.

290. Zhang, X.-F.; Zhu, J., BODIPY parent compound: Fluorescence, singlet oxygen formation and properties revealed by DFT calculations. *Journal of Luminescence* **2019,** *205*, 148-157.

291. Wu, P. G.; Brand, L., Resonance Energy Transfer: Methods and Applications. *Analytical Biochemistry* **1994,** *218* (1), 1-13.

292. Gehlen, M. H., The centenary of the Stern-Volmer equation of fluorescence quenching: From the single line plot to the SV quenching map. *Journal of Photochemistry and Photobiology C: Photochemistry Reviews* **2020,** *42*, 100338.

293. Dalgarno, P. A.; Juan-Colás, J.; Hedley, G. J.; Piñeiro, L.; Novo, M.; Perez-Gonzalez, C.; Samuel, I. D. W.; Leake, M. C.; Johnson, S.; Al-Soufi, W.; Penedo, J. C.; Quinn, S. D., Unveiling the multi-step solubilization mechanism of sub-micron size vesicles by detergents. *Sci Rep-Uk* **2019,** *9* (1), 12897.

294. Lauterbach, R.; Liu, J.; Knoll, W.; Paulsen, H., Energy transfer between surface-immobilized light-harvesting chlorophyll a/b complex (LHCII) studied by surface plasmon field-enhanced fluorescence spectroscopy (SPFS). *Langmuir* **2010,** *26* (22), 17315-21.

295. Horton, P.; Ruban, A.; Rees, D.; Pascal, A. A.; Noctor, G.; Young, A., Control of the light-harvesting function of chloroplast membranes by aggregation of the LHCII chlorophyll—protein complex. *Febs Lett* **1991,** *292* (1-2), 1-4.

296. Guerrero-Sanchez, C.; Keddie, D. J.; Saubern, S.; Chiefari, J., Automated Parallel Freeze–Evacuate–Thaw Degassing Method for Oxygen-Sensitive Reactions: RAFT Polymerization. *ACS Combinatorial Science* **2012,** *14* (7), 389-394.

297. Einstein, A., On the movement of particles suspended in stationary liquids required by the molecular kinetic theory of heat. *Annalen der Physik* **1905,** *322* (8), 549-560.

298. Lambrev, P. H.; Schmitt, F.-J.; Kussin, S.; Schoengen, M.; Várkonyi, Z.; Eichler, H. J.; Garab, G.; Renger, G., Functional domain size in aggregates of light-harvesting complex II and thylakoid membranes. *Biochimica et Biophysica Acta (BBA) - Bioenergetics* **2011,** *1807* (9), 1022-1031.

299. Lambrev, P. H.; Miloslavina, Y.; Jahns, P.; Holzwarth, A. R., On the relationship between non-photochemical quenching and photoprotection of Photosystem II. *Biochimica et Biophysica Acta (BBA) - Bioenergetics* **2012,** *1817* (5), 760-769.

300. Müller, P.; Li, X.-P.; Niyogi, K. K., Non-Photochemical Quenching. A Response to Excess Light Energy1. *Plant Physiol* **2001,** *125* (4), 1558-1566.

301. Valkunas, L.; Trinkunas, G.; Chmeliov, J.; Ruban, A. V., Modeling of exciton quenching in photosystem II. *Phys. Chem. Chem. Phys.* **2009,** *11* (35), 7576-7584.

302. Belgio, E.; Kapitonova, E.; Chmeliov, J.; Duffy, C. D. P.; Ungerer, P.; Valkunas, L.; Ruban, A. V., Economic photoprotection in photosystem II that retains a complete light-harvesting system with slow energy traps. *Nature Communications* **2014,** *5* (1), 4433.

303. Hancock, A. M. Development of novel energy transferring nanomaterials which enhance the photophysical properties of light-harvesting proteins. University of Leeds 2020.

304. Wood, W. H. J.; Barnett, S. F. H.; Flannery, S.; Hunter, C. N.; Johnson, M. P., Dynamic Thylakoid Stacking Is Regulated by LHCII Phosphorylation but Not Its interaction with PSI. *Plant Physiol* **2019,** *180* (4), 2152-2166.

305. Harris, M. A.; Sahin, T.; Jiang, J. B.; Vairaprakash, P.; Parkes-Loach, P. S.; Niedzwiedzki, D. M.; Kirmaier, C.; Loach, P. A.; Bocian, D. F.; Holten, D.; Lindsey, J. S., Enhanced Light-Harvesting Capacity by Micellar Assembly of Free Accessory Chromophores and LH1-like Antennas. *Photochem Photobiol* **2014,** *90* (6), 1264-1276.

306. Sun, R.; Liu, K.; Dong, L.; Wu, Y.; Paulsen, H.; Yang, C., Direct energy transfer from the major antenna to the photosystem II core complexes in the absence of minor antennae in liposomes. *Biochim Biophys Acta* **2015,** *1847* (2), 248-261.

307. Sprague, S. G.; Camm, E. L.; Green, B. R.; Staehelin, L. A., Reconstitution of light-harvesting complexes and photosystem II cores into galactolipid and phospholipid liposomes. *J Cell Biol* **1985,** *100* (2), 552-7.

308. Krause, G. H., Changes in chlorophyll fluorescence in relation to light-dependent cation transfer across thylakoid membranes. *Biochimica et Biophysica Acta (BBA) - Bioenergetics* **1974,** *333* (2), 301-313.

309. Sylak-Glassman, E. J.; Malnoe, A.; De Re, E.; Brooks, M. D.; Fischer, A. L.; Niyogi, K. K.; Fleming, G. R., Distinct roles of the photosystem II protein PsbS and zeaxanthin in the regulation of light harvesting in plants revealed by fluorescence lifetime snapshots. *P Natl Acad Sci USA* **2014,** *111* (49), 17498-17503.

310. Nicol, L.; Croce, R., The PsbS protein and low pH are necessary and sufficient to induce quenching in the light-harvesting complex of plants LHCII. *Sci Rep-Uk* **2021,** *11* (1), 7415.

Appendix for

“Model Lipid Membranes To Assess The Organization And Photophysical Properties Of Synthetic Pigments And Light-Harvesting Proteins”

Sophie A. Meredith

Submitted in accordance with the requirements for the degree of Doctorate of Philosophy
on the programme of the “BBSRC White Rose DTP in Mechanistic Biology”

University of Leeds

School of Physics and Astronomy
Faculty of Biological Sciences

September 2021

Appendix 1: Optimising the excitation fluence for FLIM measurements of photosynthetic samples

Prior to any characterisation of photosynthetic samples, it was necessary to ensure that the parameters selected for FLIM measurements did not introduce lifetime artefacts into our analysis of photosynthetic samples. Singlet-singlet annihilation (SSA) is a mechanism of fluorescence quenching induced by Forster-type energy transfer between two fluorophores while they are both in their first excited singlet state (S1S1), and may result in the unintentional truncation of the fluorescence lifetime, and misinterpretation of the photophysical properties of photosynthetic systems, or a sub-optimal fluorescence signal. SSA is very likely to occur in photosynthetic light harvesting complexes,[1] due to the high density of pigments within photosynthetic proteins, and the probability of SSA is increased by increasing the concentration of excitons (or exciton flux) within the system, e.g. by increasing the intensity of exciting light.[2, 3] Therefore, it was necessary to de-couple effects of SSA or to limit experimental parameters to a regime where SSA is unlikely to occur.

Experiments were performed to select an appropriate excitation fluence for future protein measurements, and to characterise the extent of annihilation at a range of other fluences. To quantify SSA in photosynthetic systems, multiple measurements of LHCII fluorescence lifetime were obtained using a wide range of excitation fluences above and below the level where SSA was expected to occur (0.001 mJ/cm^2 to 0.373 mJ/cm^2). LHCII was excited using a 485 nm pulsed laser source, operating at a repetition rate of 10 MHz, with a FWHM of ~70 ps. To calculate the amount of energy delivered per unit area, the laser fluence was calculated from the average power, as shown in **Table A1.1**. The total exposure time was adjusted for each measurement, such that the net delivered excitation remained constant.

Average Laser power output (AU) P_{AU}	Average laser power output (uW) $P_{\mu W} = K \times P_{AU}$	Average laser power output (W) $P_W = P_{\mu W} \times 10^{-6}$	Average Intensity (W/cm2) $I = P_W / A$	Peak power (W = J/s) $P_{PEAK} = P_W / (FWHM \times R_{rep} \times 10^6)$	Fluence (J/m2) $F_{SI} = P_{PEAK} \times FWHM / A$	Fluence (mJ/cm2) $F = F_{SI}/10$	Fluence after obj. (mJ/cm2) $F' = F \times E$
1.5E+04	2.3E+01	2.3E-05	4.5E+03	2.5E-02	4.5	0.45	0.38
1.5E+04	2.2E+01	2.2E-05	4.4E+03	2.5E-02	4.4	0.44	0.37
1.5E+04	2.3E+01	2.3E-05	4.5E+03	2.5E-02	4.5	0.45	0.38
2.0E+04	2.4E+01	2.4E-05	4.9E+03	3.5E-02	4.9	0.49	0.42
5.5E+04	7.5E+01	7.5E-05	1.5E+04	8.4E-02	15.0	1.50	1.27
5.5E+04	8.3E+01	8.3E-05	1.6E+04	0.2E-02	16.4	1.64	1.40

Table A1.1 – Method of calculating the excitation fluence from the average laser power output.

K is the conversion constant for the 485 nm laser and the 485/560 dichroic mirror. K = 0.00147. **A** is the laser spot area. For the 485 nm laser, this is 5.03 $\times 10^{-13}$ m^2. **FWHM** is the full width at half maximum of the laser pulse, 90 ps for the 485 nm laser. $\mathbf{R_{rep}}$ is the repetition rate of the laser pulse. For the 485 nm laser, this is typically set to be 10MHz but can vary depending on the application. **E** is the efficiency of the objective lens at the laser wavelength. From the manufacturers specifications, this is estimated to be 0.85 (85%).

K, A, FWHM will vary as a result of changing laser heads, or using different dichroic mirrors. A complete list of these parameters is provided at the end of the chapter. $\mathbf{R_{rep}}$ is specific to the requirements of each experiment, and is selected by the user. Fluences were recalculated for each iteration of these parameters such that SSA effects were avoided (unless deliberately introduced) in all experiments in subsequent chapters.

The likelihood of SSA may also increase as a result of system connectivity, so the presence of SSA was assessed in a variety of systems with various degrees of protein aggregation. Firstly, fluorescence decay curves were obtained for LHCII diluted in buffer containing 0.3% α-DDM detergent (a system with no interactions between proteins) using a range of excitation fluences. Fluorescence decay curves obtained using low excitation fluences (*black* curve, **Figure A1.1a**) have a significantly slower decay than those obtained using high excitation fluences (*bright green* curve, **Figure A1.1a**), as shown by the relative gradients of the each fluorescence decay curve. Each lifetime decay curve was used to calculate a fitted fluorescence lifetime, by reconvolution of the lifetime signal from the IRF (*red* curve, **Figure A1.1a**). For LHCII in detergent, the fitted lifetime (*green*, **Figure A1.1b**) remained approximately constant (~3.6 ± 0.04 ns) at low to medium excitation (0.0010 to 0.0026 mJ/cm^2) before decreasing exponentially (note the semi-logarithmic scale on **Figure A1.1b**) as the excitation fluence increased from 0.0026 to 0.373 mJ/cm^2. Our results are in agreement to similar studies, showing the dependency of the fluorescence lifetime on the excitation power.

Next, to generate a system with large amounts of LHCII aggregation, LHCII was deposited in solution onto a clean, atomically flat mica substrate. In this scenario, trimeric LHCII self-assembles into tightly packed domains of various sizes, where the luminal or stromal surface of the LHCII is loosely associated with the mica substrate.[4] After a period of incubation, and copious washing, the fluorescence lifetime of these adsorbed LHCII aggregates was measured at low fluence (0.002 mJ/cm^2) where no SSA should occur. The fluorescence lifetime of LHCII aggregates was found to be extremely quenched (0.31 ± 0.01 ns) relative to the lifetime of LHCII in detergent (3.60 ± 0.04 ns). This result shows that there is a high degree of quenching is present in the LHCII deposited on mica in this way, suggesting the presence of protein-protein interactions (that are known to quench LHCII fluorescence) and a highly aggregated network of LHCII trimers.

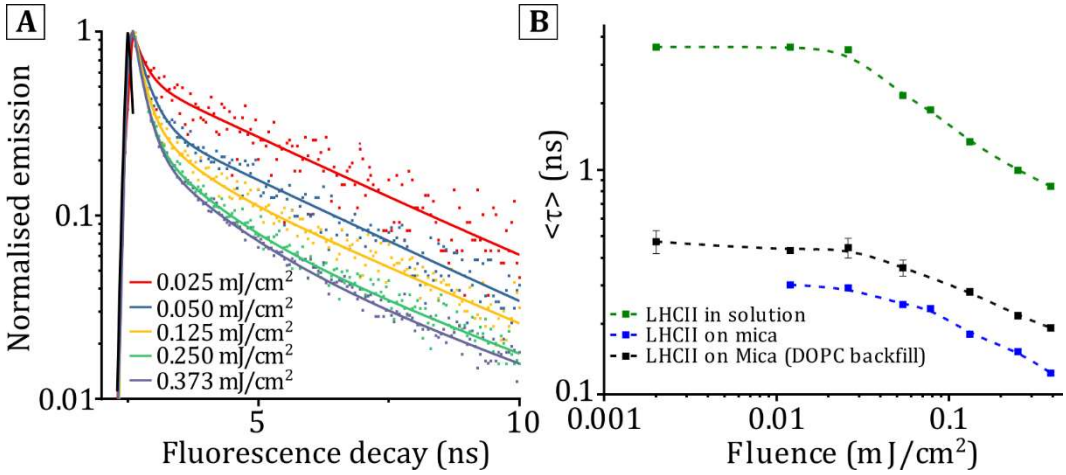

Figure A1.1: Control measurements to limit non-linear fluorescence effects that may result in FLIM artefacts. **(A)** Fluorescence lifetime decay curves for LHCII in detergent solution (0.3% α-DDM 20 mM HEPES). Measurements were taken at a range of excitation fluences (0.002 to 0.338 mJ/cm2, increasingly green curves indicate increasing fluence). **(B)** Fitted fluorescence lifetimes for LHCII samples in a variety of aggregated states: No aggregation, ie. in detergent solution (green), Loosely aggregated, ie. deposited on mica and backfilled with DOPC (black), and Densely aggregated, ie. deposited on mica (blue). The red, shaded region represents a range of moderate to high fluences (> 0.026 mJ/cm2) where the increased excitation fluence causes shortening of the fitted fluorescence lifetime.

Fluence after obj. (mJ/cm2)	LHCII in detergent <τ> (ns)	LHCII + DOPC on mica <τ> (ns)	LHCII on mica <τ> (ns)
0.002	3.60 ± 0.04	0.47 ± 0.06	0.31 ± 0.01
0.012	3.60 ± 0.01	0.43 ± 0.01	0.30 ± 0.01
0.026	3.50 ± 0.02	0.44 ± 0.05	0.29 ± 0.01
0.054	2.17 ± 0.03	0.36 ± 0.03	0.25 ± 0.01
0.078	1.87 ± 0.04	0.31 ± 0.04	0.24 ± 0.01
0.132	1.34 ± 0.24	0.27 ± 0.01	0.18 ± 0.01
0.251	1.00 ± 0.03	0.22 ±0.01	0.15 ± 0.01
0.388	0.84 ± 0.02	0.20 ± 0.01	0.14 ± 0.02

Table A1.2: Fitted lifetimes for multiple LHCII aggregation states as a function of excitation fluence.

It has previously been reported that the addition of lipids to LHCII aggregates causes a rearrangement of the LHCII, resulting in a system with less fluorescent quenching.[4] So, to generate a sample with moderate amounts of aggregation LHCII deposited on mica was incubated with a 0.5 mg/ml DOPC liposome solution, such that the liposomes rupture onto the hydrophilic surface, and the DOPC lipids associate with the hydrophobic transmembrane segments of the LHCII. Following copious washing to remove any loosely adsorbed material, the fluorescence lifetime of LHCII on mica was measured, and found to have increased due to the presence of lipids from 0.31 ± 0.01 ns to 0.47 ± 0.06 ns. The change in the fluorescence lifetime reveals that the addition of lipids has indeed reduced the level of quenching by LHCII, and suggests that the LHCII in this arrangement is more loosely aggregated with fewer protein-protein interactions (relative to LHCII on mica with no addition of lipids).

Annihilation measurements for LHCII in both aggregated states (LHCII on mica, and LHCII with DOPC on mica) show the same SSA onset fluence as LHCII in detergent solution. For all three aggregation states, the fitted fluorescence lifetime remained approximately constant (<10% variation) at fluences below 0.0026 mJ/cm^2, before rapidly decreasing at fluences above 0.0026 mJ/cm^2. The results show that the fluence at which annihilation effects become significant is not dependant on the aggregated state of the protein, or altered by potential interactions between the substrate and the proteins. Therefore, the same fluence can be used to obtain lifetime measurements for LHCII in a range of systems. After this series of experiments, a fluence of 0.0026 mJ/cm^2 was used for all subsequent FLIM measurements of the photosynthetic systems (unless annihilation effects were the target of an experiment). This medium-low fluence was chosen to allow for the collection of data with moderate speed and high signal, whilst also minimising the effect of SSA on the fitted fluorescent lifetimes. In subsequent chapters, this series of measurements gives us a high confidence in the analysis of the fluorescence lifetimes, and subsequent interpretation of the photophysical state of LH and PS proteins in a variety of conditions.

Appendix references

1. Bittner, T.; Irrgang, K. D.; Renger, G.; Wasielewski, M. R., Ultrafast excitation-energy transfer and exciton-exciton annihilation processes in isolated light-harvesting complexes of photosystem-II (LHC-II) from spinach. *J Phys Chem-Us* **1994,** *98* (46), 11821-11826.

2. Barzda, V.; Gulbinas, V.; Kananavicius, R.; Cervinskas, V.; van Amerongen, H.; van Grondelle, R.; Valkunas, L., Singlet-Singlet Annihilation Kinetics in Aggregates and Trimers of LHCII. *Biophys. J.* **2001,** *80* (5), 2409-2421.

3. Gillbro, T.; Sandstrom, A.; Spangfort, M.; Sundstrom, V.; Vangrondelle, R., Excitation-energy annihilation in aggregates of chlorophyll a/b complexes. *Biochim Biophys Acta* **1988,** *934* (3), 369-374.

4. Adams, P. G.; Vasilev, C.; Hunter, C. N.; Johnson, M. P., Correlated Fluorescence Quenching and Topographic Mapping of Light-Harvesting Complex II within Surface-assembled Aggregates and Lipid Bilayers. *Biochim. Biophys. Acta-Bioenerg.* **2018,** *1859* (10), 1075-1085.